Lyman Alpha Emission from Low-Redshift Star-Forming Galaxies as a Probe for Lyman Continuum Escape

by

Keith Redwine

A dissertation submitted to The Johns Hopkins University in conformity with the requirements for the degree of Doctor of Philosophy.

Baltimore, Maryland

April, 2018

Abstract

The goal of this thesis is to analyze far-ultraviolet spectra from nearby star-forming galaxies and investigate how the hydrogen Lyman alpha (Lyα) line at 1216 Å is related to the host's environmental parameters that determine Lyman continuum (LyC) escape. It has been suggested that Lyα can be used as a proxy for the escape of LyC radiation from UV-bright regions of nearby galaxies. LyC is of particular interest with respect to reionization of neutral atomic hydrogen in the universe over a redshift range from z $\sim$ 6 to z $\sim$ 12, which was highly dependent on the flux of ionizing LyC photons in the intergalactic medium. Expanding our understanding of the dynamics of the Lyα escape fraction ($f_{Ly\alpha}$) from the local neutral hydrogen environment around star formation could be key to guiding searches for measurement of a total LyC escape fraction (f_{LyC}) across all morphologies of galaxies. We will describe multiple Lyα projects to do this, including a *Hubble Space Telescope* (HST) observation program with the *Cosmic Origins Spectrograph* (COS) in Cycle 22 to complete a far-UV survey of nearby star-forming galaxies as an analog to early galaxies driving reionization, as well as a launch of an ultraviolet spectrograph built by the Johns Hopkins sounding

ABSTRACT

rocket group. This concludes with identification of galaxy candidates that indicate neutral hydrogen columns suggestive of high LyC escape fractions, as well as defining methodology for future observations to identify LyC leak galaxies with inexpensive observation programs.

Primary Reader: Stephan R. McCandliss

Secondary Reader: Paul D. Feldman

Secondary Reader: David Neufeld

Secondary Reader: Anand Sivaramakrishnan

Secondary Reader: Sabine Stanley

Acknowledgements

This thesis is a culmination of efforts not only by me but also by many supporting people in my personal and professional life. I entered graduate school excited to study physics but unqualified for real research work, and the faculty, support staff, and fellow graduate students were more than patient in fixing my shortcomings. Special thanks must go to Steve McCandliss, who guided everything I did in both science and lab work. Brian Fleming was accommodating in showing me how the FORTIS systems worked and upon his graduation handing them off to me without concern for how I would use or abuse them. Russ Pelton is a miracle worker and he made my life demonstrably easier in the lab, while never letting my silly mistakes become big ones. I became close to this group as we worked at JHU and in the field, which made my work much more enjoyable than it probably had any reason to be.

I've made many close friends at JHU and will always value my experiences here, from intramural softball championships to Friday happy hours. It is a close community of graduate students in the Physics department, which is more important than we give it credit for, and I would run out of space listing the peers here with whom I

have been lucky to both struggle through class and unwind after.

Finally, I'd like to acknowledge my family. They are always interested and engaged, even when I am deep in the minutiae of lab work. And I could not have made it to this degree without my wife Lisa, who is always willing to hear me struggle through a practice talk, read a first draft paper, or just keep me going after a rough week.

Contents

CONTENTS

CONTENTS

CONTENTS

List of Tables

List of Figures

Chapter 1

Introduction

The question of how Lyman continuum escapes from star-forming galaxies is one that holds many implications for the formation of the universe. Immediately following the Big Bang, the universe consisted of a homogeneous, isotropic plasma of hydrogen and helium nuclei and free electrons. As the universe cooled and expanded the temperature dropped enough for the nuclei to combine with free electrons and form the first neutral atoms. At this point, high-energy electromagnetic radiation was strongly attenuated by absorption and scattering by these neutral atoms, almost entirely preventing these photons from surviving into subsequent stages of the universe's development. Over time, this matter formed the first significant gravitational structures, tending to clump together. As certain localized regions of space became increasingly dense, fusion in the first stars was ignited, and the first galaxies formed.

Currently, the oldest luminous objects we have observed are at redshifts of z $\sim$

11. These galaxies do not have any observed flux below the hydrogen Lyman alpha line at $\lambda = 1216$ Å, implying that the flux in this region is fully absorbed by neutral hydrogen along the line of sight. From this we infer that at z $\sim$ 11 most of the hydrogen in the intergalactic medium (IGM) is still neutral.

Evidence of a neutral hydrogen IGM is found in spectra of quasars exhibiting a distinct Gunn-Peterson trough (1), shown in Figure 1.1, where the spectral energy distribution shows a sharp cutoff of flux below the rest frame Lyman alpha, suggesting the existence of a large column of neutral atomic hydrogen along the line of sight to the emitting object (2). However, this phenomenon becomes progressively less pronounced in similar objects at redshifts $\lesssim 6$, and the far-ultraviolet (FUV) photons are able to penetrate the IGM, implying that at this point the hydrogen along the lines of sight is fully ionized. This period of transition from neutral H I to ionized H II is referred to as reionization, and marks an important step in evolution for the universe.

The energy sources responsible for reionization are subject to some debate. Candidate sources for H I ionizing radiation below $\lambda = 912$ Å, include flux from quasars and from star-forming regions of galaxies. Quasars produce a high-energy photons capable of ionizing H I, but the resulting intensity derived from their observed spectral energy distributions and their luminosity function is most likely too low to fully provide the required photons for reionization (3; 4). Some recent formulations (5) of ionizing radiation production models, following the Planck Collaboration's con-

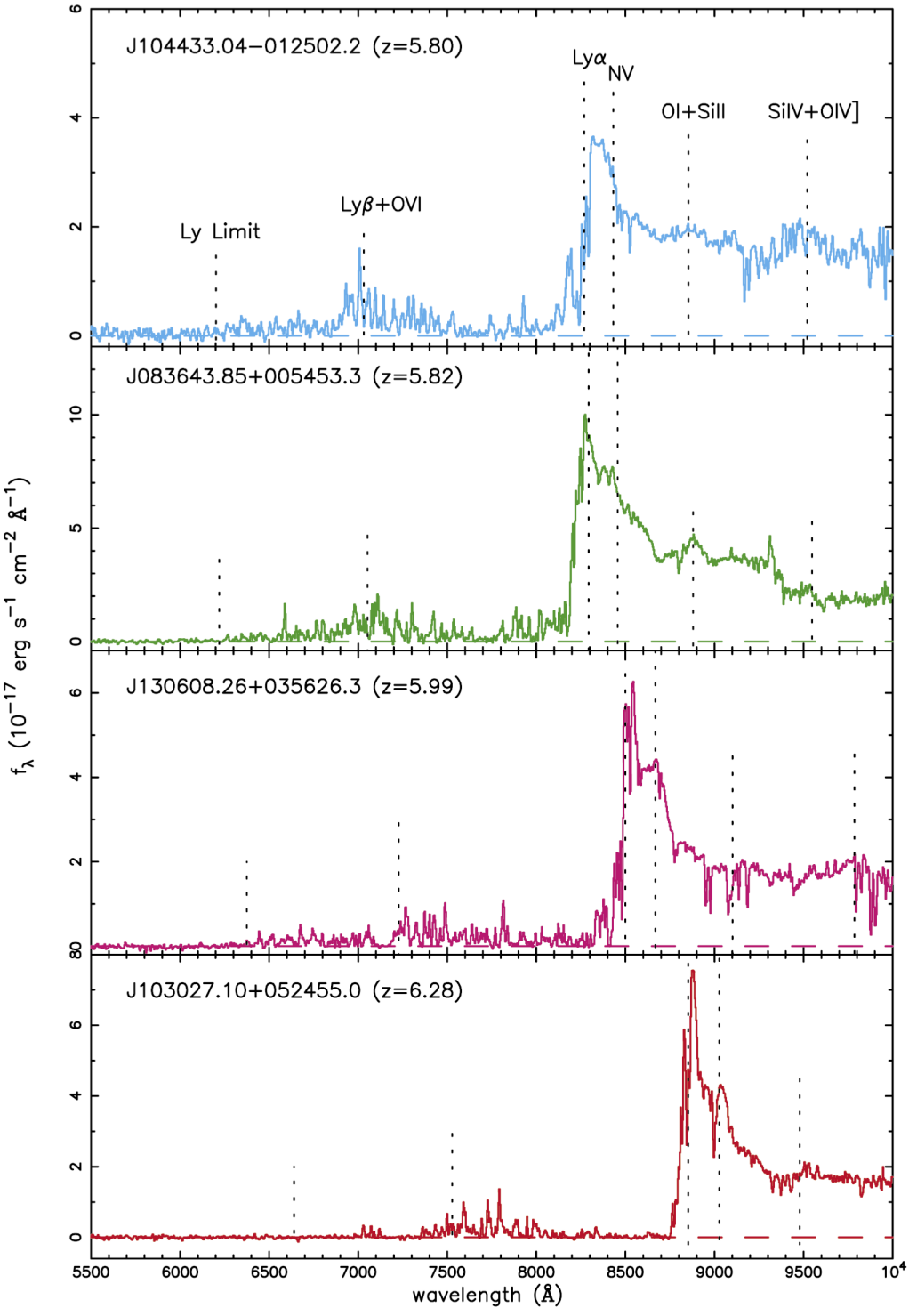

Figure 1.1: Visible spectra from Keck/ESI of four quasars in the observed frame, with rest frame spectra features labeled as dotted lines. The Gunn-Peterson troughs shortward of the dropoff at rest frame Lyα is apparent (2).

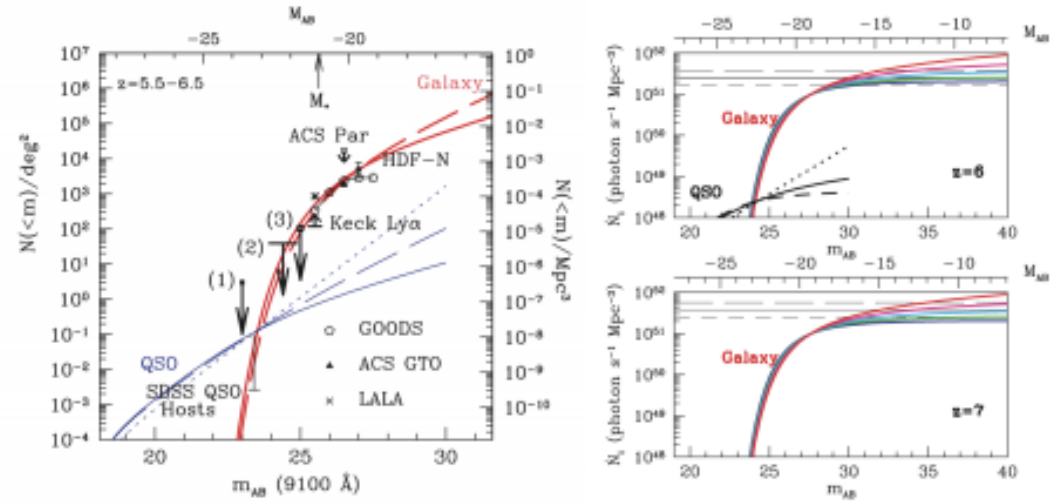

Figure 1.2: **Left:** Luminosity functions for both quasars and galaxies at 5.5 < z < 6.5 (8). **Right:** Photon production from galaxies and quasars at z=6 and from galaxies at z=7 (9). The three horizontal lines at the top of the plot indicate the critical photon production for universe ionization at clumping factors of C=20, 30, and 40.

straints on Thomson scattering optical depth at high redshift (6), have constructed a framework where AGN sources can drive ionizing photon production. However, most estimates predict that AGN may contribute to the overall ionizing photon flux but, as shown in Figure 1.2, they will not be the dominant source unless the early quasar population is severely underestimated by current measurements (7).

Ionizing emission from hot young stars in the early universe is the most promising contender for driving the reionization, but the how the light from star-forming regions of galaxies propagates through the universe is largely unknown, and depends on a few important parameters that we have not measured. The luminosity function of star-forming galaxies is known relatively well from visible and infrared measurements out to a redshift z$\sim$ 8 (10) (see Figure 1.3), allowing for predictive models of star formation

throughout most of the reinization epoch. This expected population of star-forming galaxies could produce enough ionizing photons to drive early-universe reionization of H I, but this still depends on a number of parameters. For this to occur, the total ionizing photon production density $\dot{n}_{ion}$ is generally given by

$$\dot{n}_{ion} = f_{esc}\xi_{ion}\varrho_{SFR}, \tag{1.1}$$

where f_{esc} is the fraction of ionizing photons produced by hot stars that escape to the IGM, ξ_{ion} is the number of ionizing photons produced per unit star-formation rate density per time, and ϱ_{SFR} is the average star-formation rate density of the universe. Fiducial values for f_{esc} and ξ_{ion} motivated by survey data at a given redshift are often used, and for early galaxies at $z \sim$ 7-8 (7), f_{esc}=0.2 (11) and $\log_{10}(\xi_{ion})$=53 ionizing photons s^{-1} $M_{\odot}^{-1}$ yr. The star-formation rate density is determined from surveys of bright galaxies and relating the star-formation rate of a galaxy in $M_{\odot}$ yr^{-1} to its far-UV luminosity by (12)

$$SFR = \mathcal{K}_{FUV} \times L_{\nu}(FUV) \tag{1.2}$$

where $L_{\nu}(FUV)$ is the intrinsic (dust-corrected) FUV luminosity in ergs s^{-1} Hz^{-1}. $\mathcal{K}_{FUV}$ depends on star-formation history, metallicity, and the choice of initial mass function (IMF) of the galaxy, which is the relative distribution of stellar masses within the galaxy's total stellar population. FUV luminosity is dominated by high-mass hot

(O- and B-type) stars, so $\mathcal{K}_{FUV}$ will depend on the high-mass end of the IMF. For a Salpeter IMF (13) in the mass range 0.1-100 $M_\odot$ and constant star-formation, which are typical for UV-bright galaxies, stellar population models (14; 15) predict $\mathcal{K}_{FUV}$ will span $\sim$1 to 1.5×10^{-28} $M_\odot$ yr^{-1} ergs^{-1} s Hz for metallicities ($\log Z/Z_\odot$) spanning -1 to +0.2. Selecting a $\mathcal{K}_{FUV}$ in the middle of this range for this analysis for simplicity, we can establish a star-formation rate density as a function of redshift with available galaxy survey datasets out to high redshift (z$\sim$8). Some of these rest-frame UV galaxy survey datasets are shown in Figure 1.3 and Figure 1.4, showing a sample UV luminosity functions and correspondinging star-formation rate density as a function of redshift. These data put strong constraints on f_{esc}, assuming that minimum ionizing flux of one photon per neutral hydrogen atom in the IGM is necessarily produced in star-formation and propagated out of the host galaxy in order to drive reionization. The best-fit given by (12), and presented as the solid green line in Figure 1.4, is

$$\varrho_{SFR} = 0.015 \frac{(1+z)^{2.7}}{1+[(1+z)/2.9]^{5.6}} M_\odot \text{ yr}^{-1} \text{ Mpc}^{-3} \tag{1.3}$$

Defining the ionized IGM fraction as $Q_{ion}(z)$, its evolution over time can be described by an ionizing photon flux offset by recombination, as

$$\dot{Q}_{ion}(z) = \frac{\dot{n}_{ion}}{\langle n_H \rangle} - \frac{Q_{ion}(z)}{t_{rec}}, \tag{1.4}$$

where $\langle n_H \rangle$ is the comoving hydrogen density and t_{rec} is the IGM recombination time.

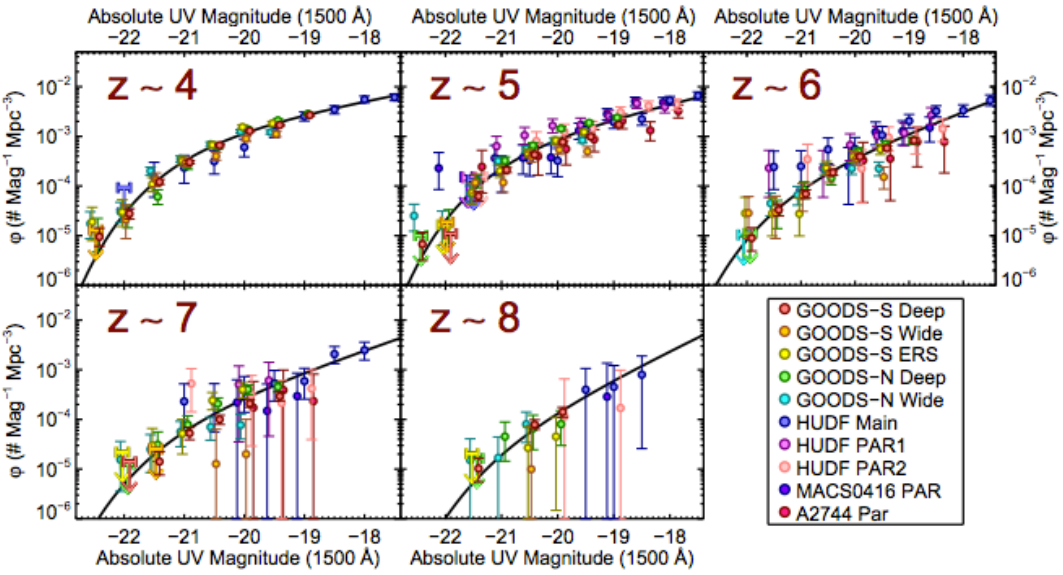

Figure 1.3: Rest-frame UV luminosity functions for redshifts $4 < z < 8$ in the CANDELS/GOODS fields from Finkelstein et al (10).

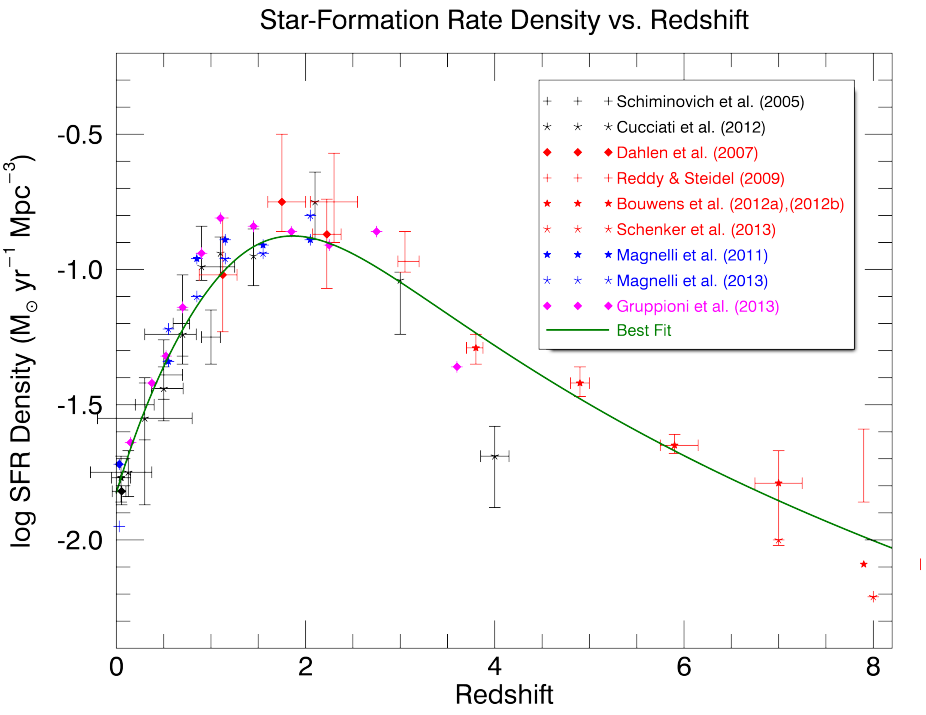

Figure 1.4: A series of star-formation rate densities as a function of redshift derived from galaxy survey data (16; 17; 18; 19; 20; 21; 22; 23; 24; 25; 26; 27).

$\langle n_H \rangle = X_p \Omega_b \rho_c$, where X_p is the hydrogen mass fraction, Ω_b is the baryon density, and ρ_c is the critical density. The rcombination time t_{rec} depends on the thermal properties and density of ionized hydrogen in the IGM, and is given by

$$t_{rec} = \left(C_{ion}\alpha_B(T)(1 + Y_p/4X_p)\langle n_H \rangle (1+z)^3\right)^{-1} \approx 3.2 \text{ Gyr} \left(\frac{1+z}{7}\right)^{-3} C_{ion}^{-1}, \quad (1.5)$$

where C_{ion} is the clumping fraction of the ionized gas (28; 29), defined as

$$C_{ion} = \frac{\langle n_{ion}^2 \rangle}{\langle n_{ion} \rangle^2}, \quad (1.6)$$

and is often set equal to three as an average determined from numerical simulations (28). The recombination time is also dependent on $\alpha_B(T)$, the Case B (discussed later (30)) recombination coefficient , addressed in a later section) and Y_p, the baryonic mass fraction of helium. The approximate expression of t_{rec} as a function of only C_{ion} and redshift is given for a gas temperature of 2×10^4 K. This, coupled with equation 1.1 provides a framework for relating the average ionizing radiation escape fraction necessary for escaping ionizing radiation from galaxies to drive reionization for a given instantaneous star-formation rate across redshift history, which is given by (31),

$$\rho_{cr}^{SFR} = (0.018 \text{M}_\odot \text{ yr}^{-1} \text{ Mpc}^{-3}) \left[\frac{(1+z)}{8}\right]^3 \left[\frac{C_{ion}/3}{f_{esc}/0.2}\right] \left[\frac{0.004}{\xi_{ion}}\right] T^{-0.845} \quad (1.7)$$

The clumping factor, stellar initial mass function, metallicity, and IGM properties are all important factors in this reionization calculation, and can be estimated from high-redshift observables and evolution models. The mean escape fraction of ionizing radiation, f_{esc}, is however very difficult to measure and remains a fairly unconstrained parameter, especially at high redshift. There have recently been a few direct detections of ionizing radiation (32; 33; 34; 35), also known as Lyman Continuum (LyC), at low redshift, with a resulting f_{esc} generally below 10%, but this search is ongoing. In order to have enough star formation for reionization at high redshifts and also explain the low measurements of f_{esc} of nearby galaxies, Haardt & Madau (36) treats the mean f_{esc} value as an evolving value over redshift:

$$f_{Lesc} = 1.8 \times 10^{-4}(1+z)^{3.4}$$

This predicts a negligible f_{esc} at very low redshifts, but simulations of the distribution of column densities of H I in the local IGM, supported by Cosmic Origins Spectrograph observations, require a factor of ~ 5 higher ionizing photon production rate at z ~ 0 than predicted (37). This low-redshift disparity can be accounted for by setting f_{esc} ≈ 0.15. However, in this case the density of ionizing photon for redshifts up to z = 4 is overestimated by a factor of ~ 3 . Clearly our understanding of the production and escape of LyC is incomplete, and a deeper investigation of f_{esc} is necessary to resolve this problem.

1.1 Lyman Continuum Escape

Directly measuring the LyC escape from galaxies is very difficult. Absorption at wavelengths below the Lyman break is very strong due to the clouds of neutral hydrogen surrounding star formation, such that in most cases very little of it propagates far enough to be observed on earth, especially at high redshifts where the IGM is mostly neutral. The mean IGM transmission function by calculating a mean optical depth (38; 39; 40) for photons at a given observed wavelength λ and source redshift z_s by:

$$\langle \tau_\lambda(z_s) \rangle = \int_0^{z_s} \int_0^{\infty} \frac{\partial^2 n}{\partial z \partial N_{HI}} (1 - e^{-\tau_{obs}}) \, \mathrm{d}N_{HI} \, \mathrm{d}z \tag{1.8}$$

where $\partial^2 n / \partial z / \partial N_{HI}$ is the distribution of absorbers in the IGM and $\tau_{obs} \equiv \sigma_\lambda^{HI} N_{HI}$ is the H I column density multiplied by the absorption cross-section. Using the IGM distribution function detailed in Inoue & Iwata (41), that depends on redshift, this mean optical depth can be numerically calculated. The expected IGM transmission function for redshifts out to $z_s = 3.5$ is shown in Figure 1.5, demonstrating the dramatic drop in LyC transmission through the IGM at high redshift, even up to wavelengths of 4000 Å. From this we can infer that any measurement of LyC needs to be done at low redshift.

The difficulty of direct observation compels us to explore options for LyC escape proxies. Recent work done in this regard has shown that tracking the escape of

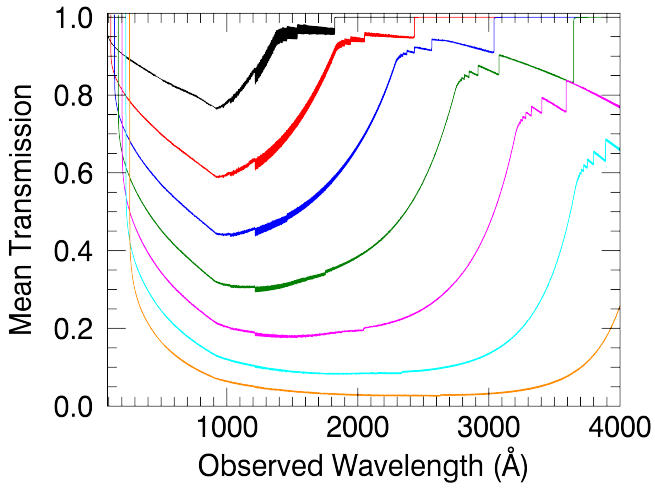

Figure 1.5: Observation-frame IGM mean transmission functions for emitting sources at redshifts of z = (0.5, 1.0, 1.5, 2.0, 2.5, 3.0, 3.5) progressing from black to orange, using the model from Inoue & Iwata (41).

emission lines of recombining atomic hydrogen provides bright lines that are much more visible in observations than LyC. When LyC is emitted from a bright source into the local H I in the nearby ISM, the fraction of LyC that does not escape will ionize the gas. This H II will subsequently recombine and the captured electron will eventually transition all the way down to the ground state, emitting radiation in a set of lines given by the hydrogen spectral series.

In particular, we focus on the Lyα line, where the electron moves from the first excited state to the ground state, emitting a photon with a wavelength of 1216 Å. Lyα is of note because it is strongly represented in the spectrum of a recombining hydrogen atom, and because it is susceptible to absorption by H I and its emission will therefore track the H I present in a galaxy, which will inform the potential for

LyC leakage. However unlike LyC, as it propagates through the IGM Lyα is able to redshift into the line wings where the scattering cross-section quickly decreases, allowing it to be observed more easily.

When a neutral hydrogen atom in a galaxy's ISM is ionized by a LyC photon, it will eventually recombine back to neutral hydrogen. During recombination it emits energy in the form of photons equal to the energy transitions of the electron as it spontaneously moves down the energy ladder to the ground state. The relative probabilities are given by quantum mechanics, and are reflected in relative intensities of the line fluxes observed in the galaxy. In two limiting cases of the ISM, low optical depth neutral hydrogen (Case A) and high optical depth neutral hydrogen (Case B) (30), different line intensity ratios are produced because of repeated re-absorption of higher order Lyman series photons (transitions to the ground-state) by neutral hydrogen, preferentially producing Lyα. For example, a Lyβ photon that would freely escape the galaxy in Case A will readily be absorbed by H I in Case B (n=1 $\rightarrow$ n=3) , and may re-emit two photons on its transition to the ground state, Hα (n=3 $\rightarrow$ n=2) and Lyα (n=2 $\rightarrow$ n=1). Lyα light is also re-absorbed in a Case B scenario, but there is only one path down the energy ladder from the first excited state to the ground state. Thus for each Lyα photon absorbed, a new Lyα photon is re-emitted, in the process of resonant scattering.

In the low optical depth Case A scenario, the H I emission lines formed from recombination after ionization will freely escape the galaxy to be observed from Earth.

The relative flux of these lines will be weighted by the canonical hydrogen atom transition probabilities. The intrinsic flux (before reddening) will be expected to have a ratio of Lyα to Hα ($n = 3$ to $n = 2$) to Hβ ($n = 4$ to $n = 2$) of 32.7 : 2.86 : 1 (30), to be observed from outside the galaxy. Lyα in its rest frame is still susceptible to scattering by clouds of H I between emission and observation, but redshifting will move it into the longer line wings where the scattering cross-section is significantly smaller. In the high optical depth Case B scenario, higher order transitions in the Lyman series (Lyβ, Lyγ, etc.) will be continually absorbed and reemitted, pushing more and more of the emission into Lyα and Hα. In this sitation, we expect the ratio of ratio of Lyα to Hα to Hβ to be 23.1 : 2.87 : 1 (30). Calculating the relative line strengths of the observed emission can establish the Case A vs. Case B nature of the star-forming region of the host galaxy, but the effect is small in the strong Lyman series lines, and only in the Paschen line series (produced downward transitions to the third excited state) does the distinction in line strength ratios become significant. Thus while these intrinsic line ratios are model-dependent and do inform our interpretation of observed line ratios, the discrepancy between Case A and Case B does not significantly affect the escape fraction calculation.

The fraction of LyC that ionizes H I in the ISM after correcting for scattering by dust is simply given by $1 - f_{esc}$, and from measuring Lyα flux resulting from recombination after photoionization, constraints can be placed on f_{esc} (42). Of course, along with the expected increase in Lyα emission, its own associated escape fraction,

$f_{Ly\alpha}$ needs to be defined and measured. Henceforth in this thesis, we will abandon the ambiguous f_{esc} and refer to the escape fraction of ionizing radiation as f_{LyC} and the escape fraction of Lyα as $f_{Ly\alpha}$. To calculate the intrinsic flux of Lyα from stars we measure line strengths of Hα (6563 Å) and Hβ (4861 Å), which track the recombination rate in the local region around star formation, since they will not resonantly scatter off ambient H I. The ratio of these two line strengths at emission is known from recombination theory, which we can use to correct the whole spectrum for dust reddening. This allows for a dust-corrected recombination rate, providing an intrinsic Lyα flux that we can compare to the measured Lyα flux to calculate an escape fraction.

For a total luminosity of ionizing photons produced by the host galaxy Q, the Lyα flux we see as a result of LyC ionizing H I in the ISM is given by the formula (43):

$$L_{Ly\alpha} \propto Q(1 - f_{LyC}) f_{Ly\alpha} \tag{1.9}$$

The constant of this proportionality will depend on the local environment, and has been calculated to be near 0.67 at a local temperature of 10,000 K (30). This provides a framework for a direct relationship between f_{LyC} and $f_{Ly\alpha}$, and could allow for a pathway to have $f_{Ly\alpha}$ measurements proxy for f_{LyC}. The first step is better understanding the relationship between local host galaxy properties and its Lyα escape, requiring new observation programs in the far-UV.

For the analysis of star-forming galaxies, the high gas densities necessary for stars

to form imply that in general the Case B environment is likely for the propagation of light from stars to the IGM, providing a baseline for an expected intrinsic Lyα flux to which to compare measurements.

In addition to IGM effects, as reviewed in Finkelstein et al 2014 (10), the environmental differences between types of galaxies should have a significant effect on how LyC and Lyα escapes from them, as the chemical composition, ionization fraction, clumping factor of the matter, and look angle in the local region will vary. The few direct measurements of compact low-redshift galaxies have given disparate results for f_{LyC} and f_{α} across a limited morphological set of galaxies (32; 33; 34), leaving much to be desired in achieving a good sample for really understanding the escape processes. The transport of Lyα photons through the ISM is a complicated process (44), and the total path length for a single Lyα photon that escapes following production in a star can be very long as it experiences many resonant scatterings off neutral hydrogen. At any point in this scattering process the photon can be destroyed by dust (resulting in dust heating) or by collisional de-excitations of excited hydrogen atoms, so Lyα escape should be more strongly attenuated by dust as the effective path length of an escaping photon is significantly greater than that of leaking photons that are not resonantly scattered, like LyC. Lyα can also be absorbed by warm molecular H_2 in the ISM, driving H_2 spectral line emission. Taken in sum, the Lyα escape fraction will depend greatly on the dust content and H 2 column within the galaxy, which will be considered in this thesis, but it will also be subject to effects from H_2 and

multiphase properties of the ISM of the emitting galaxy (45). Characterizing the details of these effects on Lyα escape is beyond the scope of this thesis, but we hope to capture a statistical idea of Lyα escape across a sample of galaxies with far-UV emission dominated by star-formation.

By measuring the Lyα escape of star-forming galaxies, in relation to LyC escape, coupled with other line features from the far-UV and those from archival SDSS visible spectra, we can compile statistical data to measure how the local properties of these galaxies affect Lyα escape, and confirm or deny $f_{Ly\alpha}$ as a viable proxy for f_{LyC}. We summarize below our observational and instrumental efforts to enable such studies.

1.2 Lyα with the Cosmic Origins Spectrograph

The far-ultraviolet sensitivity of of the *Cosmic Origins Spectrograph* allows for many interesting studies at the Lyman edge for neaby analogs to early galactic sources of ionizing photons. A direct measurement of f_{LyC} for a particularly bright, compact object (SDSS J092159.38+450912.3) at a redshift of z=0.235 was just published (32), and there is a window for observation of a similar sources.

The HST Cycle 22 SNAP proposal titled "High Efficiency SNAP survey for Lyman Alpha Emitters at Low Redshift" (Stephan McCandliss PI) was accepted and 33 of the 75 target galaxies at a redshift $0.02 < z < 0.24$ were observed by G140L mode of

COS, spanning a bandpass of 1100 Å $< \lambda <$ 2400 Å. The main thrust of this project is to provide a previously unavailable survey of star-forming galaxies in this redshift range, allowing investigation into the factors that determine the Lyα emission at these low redshifts. With the full set of targets we can begin to compile a statistical analysis of the relationship between Lyα emission and the physical properties of the galaxies, such as the gas-to-dust ratio. We can measure these properties with ancillary visible spectra from the *Sloan Digital Sky Survey* (SDSS) Data Release 7 (46), compare them to stellar evolution simulations from Starburst99 (47), and form a composite analysis of these target galaxies. This process is described in Chapter 2.

1.3 Far-Ultraviolet Off-Rowland Circle Telescope for Imaging and Spectroscopy

The Far-Ultraviolet Off-Rowland Circle Telescope for Imaging and Spectroscopy is an instrument built by the sounding rocket group at Johns Hopkins University for multi-object spectroscopy in the far-UV. In this group, we trailblaze utilization of new space technologies to explore previously unseen astrophysical sources. FORTIS is uniquely designed for measuring the Lyα escape from nearby galaxies. It is sensitive to the far-UV in two redundant spectral channels and one imaging channel. This is made possible by ruling the diffraction grating directly onto the secondary mirror, while also limiting the number of optical elements in the light path of the telescope.

Reflectivity of our mirror coatings, as well as the QE of the microchannel plate (MCP) detector, in the far-UV is limited to a maximum of around 40%, so minimizing the number of bounces in the optical path is important to increase efficiency. The ability to perform multi-object spectroscopy is provided by a prototype micro-shutter array at the focus of the primary mirror; similar arrays were designed and manufactured for use on the NIRSPEC instrument on the James Webb Space Telescope. Work on FORTIS as well as future plans for the Next-Generation FORTIS instrument are described in Chapter 5.

1.4 Other Work

In Chapters 3 and 4, I will discuss efforts in instrumentation to enable new science in UV astrophysics and contribute to the UV observation infrastructure in observational astrophysics. Chapter 3 describes an effort to calibrate a new observation mode for the COS G140L grating that moves the far-UV portion of the spectrum onto one detector channel and decreases astigmatism at shorter wavelengths than is achievable in any other existing science setting for G140L. This mode is in the process of being certified and offocially added to the COS Exposure Time Calculator for use by Cycle 22 proposers. Chapter 4 explains a prototype design for a narrow-band Lyα filter that could be used in ultraviolet telescopes in Earth orbit in order to eliminate geocoronal Lyα transmission, as Lyα photons originating from ambient hydrogen recombination

is a very large source of background radiation. The test apparatus and results of the lab experiment, where Lyα transmission is eliminated, are described.

Chapter 2

33 Low-Redshift UV-Bright Star-Forming Galaxies in Cosmic Origins Spectrograph Snap Survey

We report on a *Hubble Space Telescope* SNAP program that observed the Lyman alpha (Lyα) profiles of 33 far-UV bright galaxies in a redshift range of $0.023 < z < 0.186$, using the CENWAVE=1105 mode of the G140L grating of the *Cosmic Origins Spectrograph* (COS). The goal of the program was to assemble a significant sample of star-forming galaxies and correlate spectra features like Lyα emission, dust content, morphology, age, metallicity, star-formation rate, and atomic line features. We find a range of *Ly*α features in the dataset, with twenty distinct emitters and sixteen absorbers. Of the twenty emitters two show resolved P Cygni profiles. Two of the

targets show high ionization indicative of active galactic nuclei, including a very strong C IV signature, as well as small LyC leakage. We have used supplemental optical data from SDSS DR7 to determine metallicities and derive Balmer decrement based dust extinction corrections, and to build composite spectra across the bandpass from ∼1100 Å to ∼9000 Å. In addition to Lyα features, there are absorption lines in the galactic spectra, including He II, C II, C IV, N V, Si II, Si III, O I, and O V lines. Calculated Lyα escape fractions for each emitting galaxy will be presented, as well as relations between Lyα escape and the metallicity, power-law spectral index, and other emission line strengths. While a wide population of line features were found across the sample as a whole, it was difficult to achieve statistical significance for the majority of the lines, as few individual species were resolved in most of the target spectra. We also investigate the role of the observed Lyα emission peak velocity offset in determining H I column density in the host galaxy, which could guide future observations in the search for Lyman Continuum (LyC) escape.

2.1 Science Goals of Lyα Survey Program

The luminosity function of star-forming galaxies is known relatively well from visible and infrared measurements out to a redshift z $\sim$ 8 (10), allowing for predictive models of star-formation throughout most of the reinization epoch. This expected population of star-forming galaxies may produce enough ionizing photons to drive

early-universe reionization of H I (3; 4), but this inference depends on a number of parameters, most crucially the escape fraction of ionizing photons from the hot stars, f_{esc}^{LyC} (48). This is a difficult value to measure observationally, as emission at this wavelength is very susceptible to absorption by intervening neutral H I atoms along the line of sight from the galaxy to the Milky Way. Only a handful of LyC-emitting galaxies have been observed at low redshfit using COS (32; 33; 34; 35). However, Lyα emission may be viable as a proxy measurement for understanding LyC escape (49; 50; 51). Understanding the dynamics of Lyα escape in nearby star-forming galaxies, used as a proxy for star-forming galaxies in the early universe, can constrain theories of photon production responsible for reionization.

We focus on Lyα partly because it is strongly represented in the spectrum of a recombining hydrogen atom, and because as it propagates through the IGM it redshifts into the line wings where the scattering cross-section sharply decreases, allowing for a relatively unimpeded path to observation once escaping from the host galaxy. While still in the host galaxy however, a Lyα photon experiences similar absorption by dust kinematics as a LyC photon does, and the Lyα photon is more susceptible to H I kinematics, density, and spatial distribution along its path. The Lyα line is a resonant line, and it is very sensitive to H I along the path out of the dense galaxy. The structure of this H I can have a strong effect on the observed emission curve, often resulting in an asymmetric and even double-peaked profile(52; 53). Measuring these detailed profile effects requires a high spectral resolution, which

in this survey we sacrificed for a higher sensitivity in order to accommodate the short exposure times. However, it has been suggested that the red offset of the full Lyα profile, even if a double peak cannot be resolved, can indicate H I column density (49). Coupled with ancillary visible spectra from the SDSS DR7 data archive of our targets, these data exhibit the dynamics that dictate Lyα emission and escape as a function of intrinsic galaxy properties like metallicity and dust, derived from line emission across the whole spectrum, especially Hα (6563 Å) and Hβ (4861 Å).

2.2 HST Snapshot Program

The HST Snapshot Program was developed in order to make use of lost time in the observing schedule between scheduled observations (54). The HST scheduling team creates a Long Range Plan of targets for each cycle well in advance of its start, but there are often changes made in real-time as programs are adjusted. These changes, along with other anomalies in the schedule, open up gaps between selected programs' observations that can be up to an orbit or more in duration. The incidence of SNAP opportunites has steadily dropped over the lifetime of HST, but there were still 8-10 gaps in the schedule per week in Cycle 18. The rate of SNAP target execution in previous cycles has depended strongly on the total duration of the requested observation, and we tuned our requested time of 600 second observation to give the best chance for high execution rate. Each observation includes an acquisition image with

NUV detector, adding 500-600 seconds to the total SNAP time. Adding on the 300 seconds of observation with each of the FP-POS=3 and FP-POS=4 COS modes (55), this results in a total SNAP time of ∼21 minute, which has historically had an execution rate of >50%. Our goal was to maximize the number of targets with adequate signal-to-noise to enable a statistical investigation into the Lyα emission and absorption properties of these star-forming galaxies. There is no guarantee of any particular SNAP target observation, but we were able to have 34 of the 75 total galaxies on our target list scheduled for observation in Cycle 22 and 23.

Following a peak-up on the target with a 96-second exposure in the NUV, COS transitioned into FUV observing with the G140L grating, the same used in the new COS observing mode discussed in Chapter 3. The grating mode was set to CENWAVE=1105 for targets where Lyα emission was less than or equal to ∼1280 Å($z \leq 0.053$) and to CENWAVE=1280 for Lyα emission longward of ∼1280 Å, in order to place the LyC line feature in the Segment B channel of COS, to open a chance of directly measuring especially bright LyC emission. The observation only makes use of two focus position settings, FP-POS=3 and FP-POS=4, for these observations. COS collects data from each target for 300 seconds for each Fpos setting, resulting in a 600 second total science data time for each of the 34 galaxies that made it into the final SNAP observing schedule.

2.3 SNAP Target Spectra

The SNAP galaxies targeted in this search, detailed in Table 2.1, were chosen by querying the SDSS seventh data release (DR7) merged with the *Galaxy Evolution Explorer* (GALEX) (56) sixth data release UV catalogue. Our SNAP targets were chosen primarily to measure Lyα escape fractions in star-forming galaxies, but also to allow future investigations into relationships between Lyα and LyC escape. Consequently, targets were selected to have a minimum redshift of $z \geq 0.02$ and a minimum continuum flux at the Lyman edge of 3×10^{-15} erg cm^{-2} s^{-1} Å^{-1}, as was estimated by a power law extrapolation of GALEX FUV and NUV images,

$$F_\lambda = F_{1530} \left(\frac{\lambda}{1530\text{Å}} \right)^\beta , \tag{2.1}$$

parametrized by the exponent β and scaled by the measured flux at the GALEX FUV Band effective wavelength of 1530 Å (57). Using a conservative Case A recombination model that assumes a low column density scattering of UV light from star-forming regions of the targets (resulting in an intrinsic flux ratio of Lyα:Hα:Hβ equal to 32.7:2.86:1 (30)), we verified that the estimated Lyα line flux of each target added to its estimated continuum flux at the redshifted Lyα wavelength didn't surpass the countrate limits of COS (55).

The observed targets show a variety of features, both in line emission and continuum effects. Two of them (LY08 and LY34) were flagged in the SDSS library as

Target	**RA**	**Dec**	**z**	**E(B-V)$^{a}_{gas}$**	**E(B-V)$^{b}_{stars}$**	Z^{c}
LY00	7:43:50.60	+43:52:2.07	0.046	0.18	0.14	8.27
LY01	8:38:41.98	+35:43:49.95	0.042	0.33	0.25	0.00
LY02	8:47:23.82	+11:21:54.93	0.030	0.23	0.19	8.66
LY03	9:4:18.12	+26:1:6.38	0.098	0.25	0.12	8.77
LY04	9:17:59.45	+1:57:51.00	0.093	0.12	0.29	8.64
LY05	9:20:33.98	+52:38:37.40	0.132	0.29	0.30	8.65
LY06	9:26:0.41	+44:27:36.17	0.181	-0.11	0.06	8.48
LY08	9:39:22.90	+37:9:43.99	0.186	0.16	0.13	0.00
LY09	9:54:34.58	+51:35:8.04	0.129	0.25	0.10	8.63
LY12	10:2:33.54	-0:54:33.47	0.047	0.32	0.19	8.50
LY13	10:7:21.66	+52:12:50.67	0.042	0.16	0.05	8.15
LY21	10:55:36.51	+44:54:50.40	0.038	0.27	0.13	8.77
LY24	11:10:2.63	+36:56:4.96	0.027	0.17	0.10	8.15
LY25	11:14:39.20	+60:54:18.36	0.053	0.08	0.20	8.27
LY28	11:33:59.80	+18:31:0.93	0.033	0.21	0.29	8.21
LY32	11:48:14.31	+27:13:25.96	0.134	0.21	0.18	8.64
LY34	11:53:46.15	+56:19:35.37	0.129	0.04	0.12	0.00
LY38	12:27:20.16	+51:39:24.36	0.044	0.10	0.15	8.53
LY39	12:38:29.93	+19:59:21.36	0.049	0.28	0.21	8.71
LY41	12:57:29.54	+6:26:9.62	0.048	0.42	0.27	8.82
LY42	12:57:34.43	+15:22:29.22	0.067	0.14	0.08	8.59
LY46	13:29:13.77	+62:18:33.13	0.042	0.22	0.19	8.65
LY49	13:45:31.50	+4:42:32.71	0.030	0.17	0.19	8.09
LY52	13:59:50.92	+57:26:22.97	0.034	0.08	0.10	8.62
LY54	14:2:10.50	+56:36:53.45	0.041	0.24	0.05	8.61
LY57	14:32:16.48	+40:27:42.92	0.023	0.37	0.23	9.08
LY59	14:42:53.50	+52:36:20.85	0.036	0.23	0.05	8.40
LY61	14:50:56.59	+48:37:26.28	0.092	0.08	0.18	8.52
LY63	15:12:6.38	+33:30:0.29	0.059	0.32	0.31	8.58
LY65	15:23:32.19	+29:31:12.08	0.068	0.00	0.13	7.96
LY67	15:34:11.68	+52:18:35.64	0.029	0.13	0.09	8.64
LY68	15:34:24.56	+34:53:53.98	0.057	0.37	0.30	8.82
LY69	15:39:0.12	+1:47:19.57	0.100	0.49	0.15	8.89
LY74	17:3:5.09	+25:31:47.64	0.031	0.30	0.30	8.68

Table 2.1: Observed SNAP Targets. ^{a}E(B-V)$_{gas}$ is determined from the Balmer decrement (58; 59; 60; 61). ^{b}E(B-V)$_{stars}$ assumes an intrinsic starburst stellar power law parametrized by the exponent $\beta = -2.5$ (62; 47). ^{c}Metallicity $Z \equiv 12+\log(\mathrm{O/H})$ is extracted from the SDSS DR7 database (63). Solar metallicity $Z_{\odot} = \sim 8.69$ (64)

quasars (65), and one (LY06) is a Green Pea galaxy. Twenty show clear Lyα emission and seventeen show Lyα absorption, with four galaxies having both - a relatively narrow Lyα emission line within a broad absorption trough. A few (up to four, most notably LY01) have a P Cygni Lyα line profile. The details of Lyα emission across the sample will be addressed in a following section.

All the spectra can be seen in Appendix A in the observer frame of reference. Line features are labeled, and the fitted continuum curve is plotted over the spectrum in red. The continuum curve is described by a two element piece-wise power law relation of the form shown in Equation 2.1, pinned together at $\sim$1400 Å to be continuous. Gaussian fits to the geocoronal Lyα and O I λ1302 filled-aperture emission found in the spectra are added to this continuum curve. Both the archival SDSS images and the COS acquisition images are shown for each target. The COS acquisition images have circles overlaid on the NUV image, describing the COS science aperture over the target for both the sky location requested in the proposal (in red, derived from SDSS images) and the peak-up centroid (in black) that is utilized for the final science observation. The difference between the SDSS and COS centroids vary by an average of $0\farcs33$ and a maximum of $0\farcs96$. The only exception in the dataset is LY52, for which the 96-second acquisition failed, resulting in the observation settling on the position requested in the proposal.

2.3.1 Geocoronal Features

The geocoronal features are stronger when the sun is not occulted behind the Earth during the observation, and also depend on the angle between the sun and the target galaxy. Figure 2.1 shows how the sun altitude above the Earth's limb and the separation of the target galaxy and the sun affect geocoronal Lyα and O I λ1302 brightness. When the sun is present in the sky HST is situated in a bath of atomic hydrogen and oxygen that is being excited by incident sunlight, and the line emission by resulting resonant scattering produces a bright background spectrum. This introduces some spectral confusion between the intrinsic signal from the galaxy and the geocoronal emission, which for two targets (LY42 and LY65), obscures the galactic Lyα signal behind a geocoronal O I λ1302 emission peak. For a few of the observations with very bright geocoronal emission, the O I λ1356 appears as a broad line, and can overlap with intrinsic galactic O I λ1302, most notably with target LY13.

2.3.2 Stacked Spectra

Stacking the normalized spectra on one another can be useful for seeing bulk trends in line features, and plotting teh standard deviation of these stacked spectra at a given wavelength can inform as to at which wavelengths the galaxies significantly vary. This has been done for very large datasets in the infrared over this rest-frame

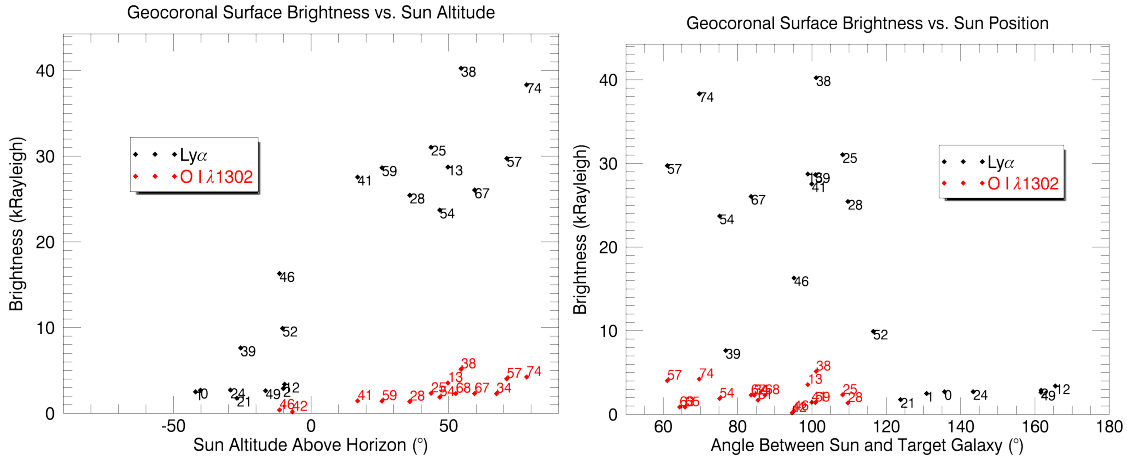

Figure 2.1: **(Left:)** Geocoronal emission as a function of sun altitude. The altitude has a significant effect on geocoronal Lyα emission, but does not strongly affect the O I. Note that for observations with the sun below the horizon, however, there was no discernible O I. **(Right:)** The same emission over angular separation of the target galaxy from the sun, for targets where the sun altitude is not greater than 50° below the horizon. As expected, targets nearer to the sun showed a brighter geocoronal signal in their spectra.

wavelength range (66; 67; 68), and using similar procedures we can define these mean spectra and corresponding standard deviation plot, shown in Figure 2.2. The sample sees a range of Lyα features, denoted by strong emission in the mean spectrum and also a large bump in the standard deviation. The only other line with a very strong signal in the standard deviation is C IV λ1549, which will a strong feature in average high-ionization ISM galaxies. The high variability of this line indicates that the SNAP sample as a mix of both high- and low-ionization galaxies, with the strongest C IV features in galaxies with AGN. Finally, there is a rise in spectra variability shortward of Lyα, but we expect a less coherent spectrum in this range as the geocoronal Lyα corrections will be spread here due to the redshift spread of the sample as a whole.

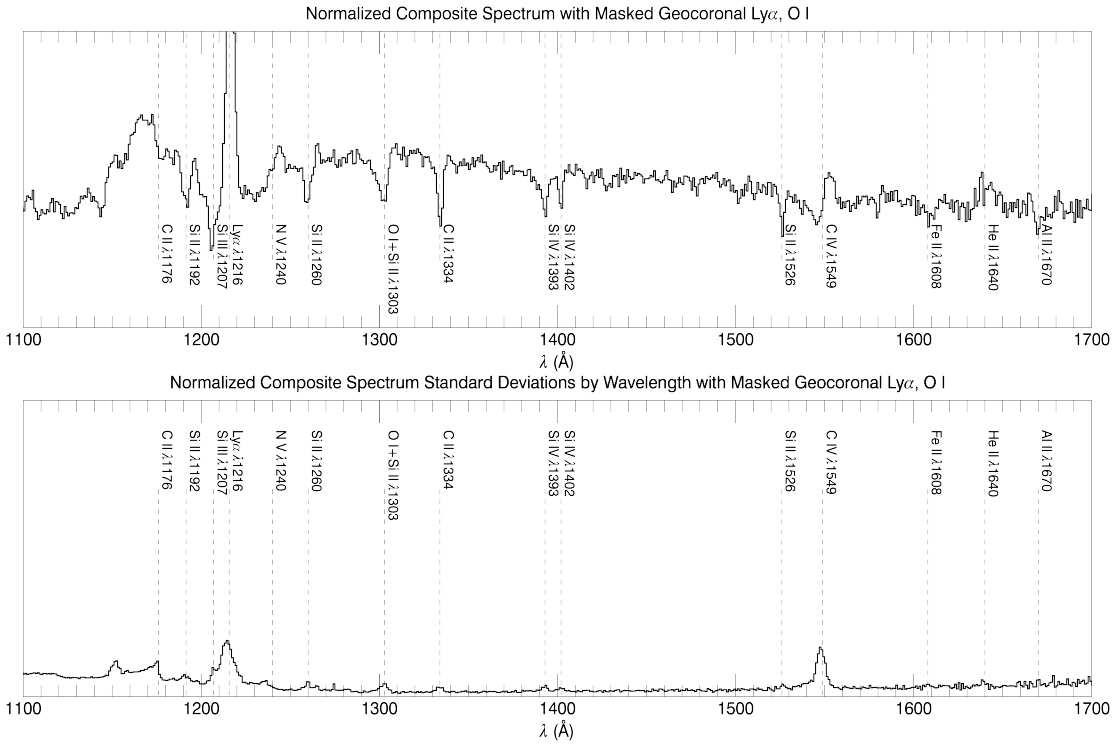

Figure 2.2: **(Top:)** Mean spectra in the sample, with lines of interest marked. Wavelengths are set by the target galaxy's rest frame, with geocoronal features in individual spectra blocked by a linear fit between flux on either side of the emission line before blue-shifting to rest frame. Each target is normalized to total flux between 1400 Å and 1500 Å. **(Bottom:)** The standard deviation in normalized flux for each 0.5 Å bin in the top mean spectrum.

2.4 SDSS Spectra

Sloan Digital Sky Survey (SDSS) Data Release 7 (DR7) (46), provides a spectroscopic survey of 10^6 galaxies found in the photometric imaging survey. SDSS uses a 2.5 meter f/5 modified Ritchey-Chrétien telescope, allowing for an especially wide field of view (3°). A distortion-free image is achieved by two corrector lenses and a large secondary mirror. For spectroscopic measurements, a fiber plug-plate is indi-

vidually drilled for targets in a particular region of the sky, and inserted in the focal plane. Up to 320 fiberoptic cables are inserted for galaxies and quasars of interest as well as for calibration stars and other unusual objects, leaving enough space between fibers to prevent spectral crosstalk. These 320 cables are fed to a beam splitter, and two CCD arrays are illuminated with images of the full array of fiber light. Between the two detectors there is an active wavelength range of 3900-9100 Å. The resolution of the SDSS spectra is 1850-2200, roughly the minimum to capture galactic and quasar absorption lines and capable of measuring velocities of $\sim \pm 20$ km s^{-1} across a galaxy spectrum (46).

The diameter of each fiber in the SDSS field of view is 3 arcseconds on the sky, compared to the 2.5 arcsecond diamater aperture used on COS. This could introduce errors to relative fluxes and require filling factor corrections, but in the COS acquisition image each target is free of nearby background objects, and each object is fully contained by the $2.5^{'}$ aperture, rendering this correction unnecessary. For extended objects in the COS aperture, the transmission on the edges (radius from center greater than $\sim 1^{'}$) the transmission does drop (69), which could introduce a small discrepancy between absolute flux measurements between SDSS and COS observations of the same object.

2.5 Dust Correction

The dust reddening will depend on the absorption and scattering properties of the dust grains in the ISM of the target galaxy and how this dust is distributed around the ISM. This reddening in the FUV spectra of star-forming galaxies is a significant effect, and there have been both empirical and simulated studies in the literature (58; 59; 60; 61) to account for this. For this SNAP dataset we followed the procedure detailed in Leitherer et al (62) using a composite piece-wise Fitzpatrick-Massa (70) (UV region) and Cardelli, Clayton, and Mathis (71) (visible) dust model. The dust correction model is parametrized by $E(B-V)$, the color excess of the host stellar population. $E(B-V)_{stars}$ acn theoretically be calculated assuming an unobscured intrinsic power law spectrum corresponding to a purely starburst galaxy where hot O-type stars completely dominate the spectrum, and $\beta \approx -2.5$ (62; 47). However, directly measuring the reddening of emission lines with intrinsic flux ratios is a more reliable way of calculating extinction on the spectrum as a whole (58; 59) Thus $E(B-V)_{stars}$ is determined by measuring the Balmer decrement in the spectra of each target. We assume a Case B recombination model (30), where the first two Balmer emission lines in the hydrogen spectrum, $H\alpha$ λ6562 and $H\beta$ λ4861 have an intrinsic luminosity ratio of 2.86. By measuring the observed reddening in the flux ratio of these two lines from SDSS DR7 spectra in the visible wavelength range, we can determine the $E(B-V)_{gas}$ (58; 59), which is related to the continuum emission

$E(B-V)_{stellar}$ (58; 59) by,

$$E(B-V)_{stellar} = 0.44E(B-V)_{gas} \tag{2.2}$$

This $E(B-V)_{stellar}$ is the scaling parameter for the dust extinction, which is reflected in the SB99 model spectra in Appendix B. Dust extinction is given by A_v, where for observed flux F_o and intrinsic flux F_i:

$$A(\lambda) \equiv -2.5 \log \left(\frac{F_o(\lambda)}{F_I(\lambda)} \right) \tag{2.3}$$

$A(\lambda)$ is constructed in different ways in the literature, but is generally scaled by the reddening $E(B-V)$ and an extinction curve $k(\lambda)$ that depends on wavelength. The ratio of $A(V)/E(B-V)$, denoted by R_v, is what scales the attenuation and is often set equal to 3.1 to match observations in the diffuse interstellar medium (71). The choice of R_v is thought to be dependent on the grain size of dust particles in the attenuating field, especially affecting attenuation at wavelengths less than 1600 Å, but for this analysis we use the standard ISM $R_v = 3.1$. The Cardelli, Clayton, and Mathis construction (71) treats the mean $A(\lambda)$ as:

$$\left\langle \frac{A(\lambda)}{A(V)} \right\rangle = a(x) + b(x)/R_v, \tag{2.4}$$

where x is given by $1/\lambda$ in inverse microns, and $a(x)$ and $b(x)$ are polynomials fit to empirical extinction measurements and the extinction at high wavelengths ($\lambda \gtrsim$ 3000Å) is fairly independant of R_v. The Fitzpatrick-Massa 1990 (70) construction has a very similar result, but applies its parameters differently. An extinction curve $k(x)$ is defined (x is still $1/\lambda$ in inverse microns) such that $A(\lambda) = (k(x)/R_v + 1)A_v$, and:

$$k(x) = c_1 + c_2 x + c_3 D(x; \gamma, x_0) + c_4 F(x). \tag{2.5}$$

This extinction curve includes a Drude term $D(x; \gamma, x_0)$, which is a Lorentzian-like profile matching the 2175 Å extinction bump (72; 73; 74),

$$D(x; \gamma, x_0) = \frac{x^2}{(x^2 - x_0^2)^2 + x^2\gamma^2} \tag{2.6}$$

and a far-UV curvature term $F(x)$ for wavelengths shorter than ∼1695 Å:

$$F(x) = \begin{cases} 0.5392(x - 5.9)^2 + 0.05644(x - 5.9)^3 & x \geq 5.9\,\mu\mathrm{m}^{-1} \\ 0 & x < 5.9\,\mu\mathrm{m}^{-1} \end{cases} \tag{2.7}$$

Fitzpatrick and Massa fit the constants in this equation to IUE UV extinction curves, and found good agreement between this formulation and the data.

Due to its construction into physical components, the Fitzpatrick Massa (FM) law is simpler to adjust to match far-UV spectral data, which is more suceptible to errors

due to grain size and limited signal, However, as it was fit to IUE data it is only valid in the ultraviolet, and the Cardelli, Clayton, and Mathis (CCM) law is necessary to correct in the SDSS wavelength range. For this analysis, we used a composite of the CCM and FM extinction curves. They almost exactly agree at $\lambda = 3045$ Å regardless of choice of R_v, making the implementation of the piecewise extinction curve over the COS and SDSS bandpass straightforward.

At wavelengths shorter than 1695 Å the FM extinction curve is strongly affected by its coefficient c_4, which sets the scale for a cubic polynomial. In the literature this value is set to $c_4 = 0.531$ to match the average of a large set of observed objects, but this often does not well match the extinction seen in the individual spectral data, potentially due to dust grain size discrepancies that become a more dominant effect as wavelength decreases (71). For this reason, we vary the c_4 value to match the continuum behavior of the COS SNAP spectra over the far-UV bandpass, excluding strong line features of intrinsic Lyα and geocoronal Lyα and O I. These optimized c_4 values cover a wide range, and while our dataset is not large enough to make general conclusions about the dust extinction laws, it is suggestive that the uncertainties of the behavior of dust in these far-UV regimes are significant.

2.6 Composite Spectra with SDSS and Galex Fit to Starburst99 Model

We have assembled composite spectra of the SNAP targets in a large wavelength range using the archival SDSS data and flux measurements through GALEX's NUV and FUV filters. The long wavelength component of the composite spectra were provided by SDSS DR7 (46). Using line features from the SDSS spectra, instantaneous star-formation Starburst99 (47) models of emission from starforming galaxies were dust-reddened and normalized to the target spectra between ∼1100 Å and ∼9000 Å, providing a baseline expected flux across the bandpass.

2.6.1 Starburst99 Models

Starburst99 (47) (SB99) is a set of synthesized spectral and photometric observables (as well as related properties) for active starforming galaxies. These models have long been a useful baseline tool for understanding the cumulative nature of stellar evolution on the spectrophotometric properties of a stellar population as a whole. The models begin with a population of new stars, given by an initial mass function (IMF) describing the relative population of different mass stars, and track the spectral evolution of the galaxy from 10^6 to 10^9 years. Galaxies without AGN are dominated by the very massive stellar population, and stellar atmosphere and evolution numerical models including rotation are applied to an input population of stars, parametrized by

mass function, metallicity, and nebular properties. Star-forming galaxies with All the SB99 models include stellar mass loss and stellar atmospheres, but any contributions to the spectral energy distributions by gas and dust in the ISM are not accounted for, requiring a separate correction for these features.

The model can include instantaneous star-formation, where all stars are presumed to be created at the start of the evolution model, or continuous star-formation where new stars are added to the population over time at a constant rate. As we expect our targets to be the result of intense starbursts we chose to fit to a model with instantaneous star-formation. The stellar initial mass function (IMF) is a power law between 1 $M_\odot$ and 100 $M_\odot$, with an exponent of $\alpha = 2.35$, similar to the Salpeter IMF (13). The Salpeter mass function was the first mass function calculated for a stellar mass range including stars larger than the Sun and corrections have been made to this baseline, but the large-mass region of the distribution well-constrained and since the UV-bright galaxies we observed in the COS sample are dominated by young, bright, massive stars, the Salpeter IMF is sufficient. SB99 has models that adjust this α exponent, as well as truncate the IMF to remove high mass stars from the modeling, but since large OB stars are relevant in our bright UB target galaxies, for this analysis we only considered the Salpeter formulation. Metallicities of Z=0.040, 0.020 (=$Z_\odot$), 0.008, 0.004, and 0.001 are available, for the stellar evolutionary models, and for this analysis the metallicity Z=0.020 were used to match the average observed metallicities described in Section 2.8, equal to solar metallicity. Nebular continuum

effects, an optional feature in the SB99 models, were included in our analysis because while the nebular effects are only a significant effect longward of the UV, we expect important nebular features in the SDSS spectra of our targets where the fitting of the SB99 spectrum is performed. A sample of a SB99 spectral energy distribution is shown in Figure 2.3.

The age of the model spectrum fit was determined by matching the 4000 Å Balmer break in SDSS spectra to the SB99 models, and normalizing to a line-feature-free region at 4050Å in the rest-frame continuum, leaving the far-UV portion of the model unconstrained. While SB99 has data for models across a variety of input parameters, instantaneous star-formation models were applied to each target in this analysis, as nearby UV-bright galaxies dominated by OB stars can be closely modeled by brief starfomation periods (75). A compilation of these composite spectra for all observed targets in this SNAP survey can be seen in Appendix B. It should be noted that for a few targets the SB99 fit does not describe the spectrum well at all, especially for the two galaxies with AGN (LY08 and LY34), which is expected as SB99 does not account for AGN emission in its models. These SB99 models are a useful diagnostic tool for evaluating the status of a target galaxy as a true starburst object, and a UV spectrum that varies significantly from a SB99 model that fits in the SDSS bandpass indicates that star-formation is not the dominant emission process and thus the galaxy is a less suitable candidate for studying escape of far-UV light sourced from star-formation.

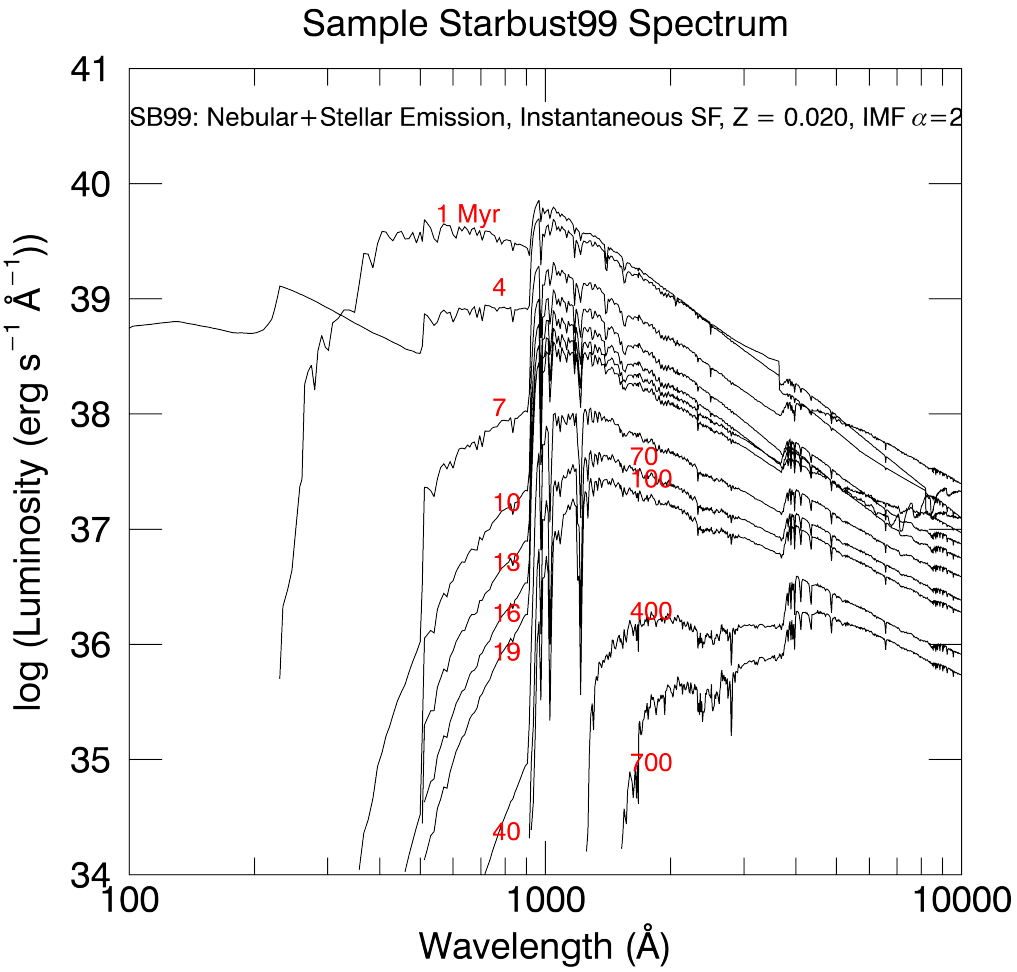

Figure 2.3: Example of spectral energy distributions for a given SB99 model from ages of 1 Myr to 1 Gyr. The model follows instantaneous star-formation with a Salpeter IMF, Z=0.020 (solar), and included nebular continuum (47). The luminosity is scaled for a inital total mass of 10^6 $M_\odot$.

2.7 Lyα Escape

Seventeen of the observed galaxy spectra have clear Lyα emission above the continuum background, some within a larger absorption trough. However, a strong column of H I is expected along the line of sight to the bright regions of the target galaxies, resulting in a deep absorption line at Lyα. This absorption can be estimated by a relation to the measured extinction parameter E(B-V) by $N_H/E(B-V) = 5.8 \times 10^{21}$ H cm^{-2} mag^{-1} (76) for a typical diffuse local ISM. This value was derived empirically from a far-UV spectral survey of a bandpass straddling Lyα for $\sim$100 stars in the local milky way using the *Orbiting Astronomical Observatory* (or *Copernicus*). This analysis by Bohlin et al (77) found a close relationship between hydrogen column and extinction E(B-V), varying by less than a factor of 1.5 from the linear fit, independent of line of sight. A small proportion of this hydrogen column was molecular H_2, but as the star-forming regions of our target galaxies are generally highly ionized regions due to the presence of very bright, hot stars, we will assume that all molecular hydrogen in the target galaxy ISM is dissociated into H I. This assumption will potentially slightly overestimate the absorbing H I column along the line of sight, but in all cases, even in the Bohlin study of our local stellar population, the hydrogen column should not be dominated by molecular hydrogen.

Using the Starburst99 as a baseline spectrum for emission without an absorbing ISM allows for a calculation of intrinsic absorption due to ISM H I column from the E(B-V) derived in section 2.5. Because this absorption profile, an example of which

is shown for LY00 in Figure 2.4, tends to be very deep, even observed galaxies that do not show Lyα emission above the continuum background will show an observed Lyα excess flux above the absorption trough.

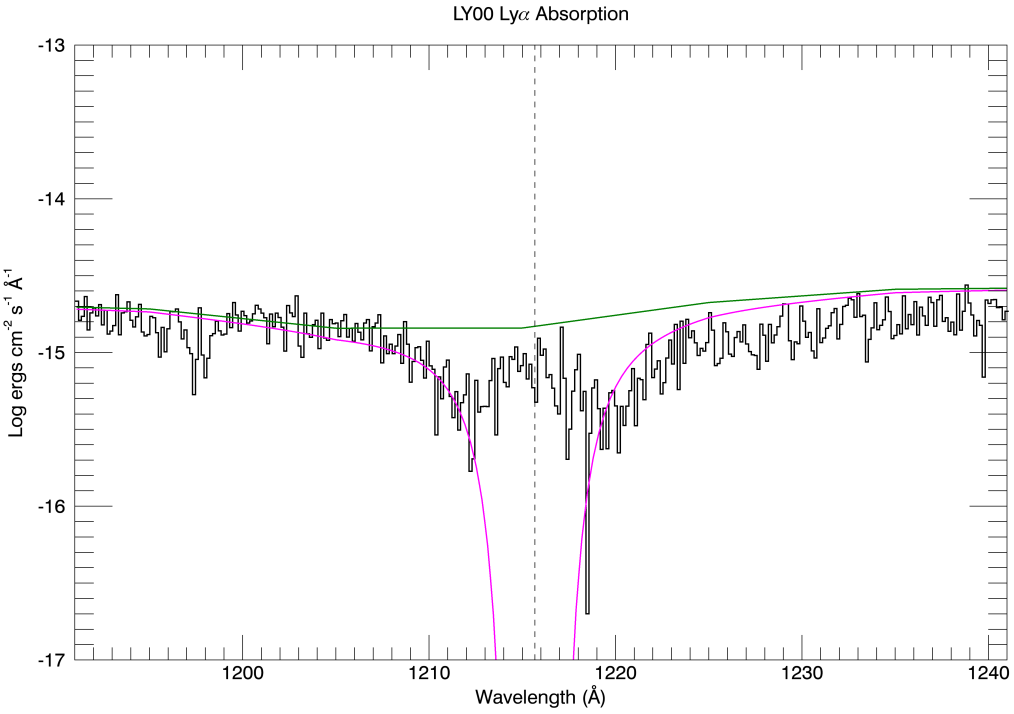

Figure 2.4: LY00 COS data (black) with normalized and fitted Starburst99 continuum (green). When the Zubko (76) H I column is calculated from the Balmer decrement, the resulting Lyα absorption added to the SB99 spectrum is shown in purple. This is a very deep trough that suppresses essentially 100% of the Lyα photons near its center.

To calculate the Lyα escape fraction we first correct the observed Hα excess flux for dust extinction using the Balmer Decrement procedure outlined in section 2.5. We then determine an intrinsic Lyα flux from the target galaxy based on a Case B recombination model (30), where the the ratio between Hα and Lyα flux from the

galaxy is assumed to be equal to 8.7. The escape fraction $f_{esc}^{Ly\alpha}$ is given by:

$$f_{esc}^{Ly\alpha} \equiv \frac{F_{observed}^{Ly\alpha}}{F_{emitted}^{Ly\alpha}} = \frac{F_{observed}^{Ly\alpha}}{8.7 \times F_{observed}^{H\alpha}} \tag{2.8}$$

The results can be seen in Table 2.2, showing a wide spread of escape fractions across the sample. We can compare the relationship between these escape fractions to other properties of the galaxy, as can be seen in Figure 2.5. The relationship between the Lyα emission line equivalent width and the escape fraction is strong, with the exception of one target LY24, which is a starforming galaxy at a redshift of $z \sim 0.027$. Looking closer at this particular object, we can determine in the COS target acquisition image that it has an unusual profile, with many bright emitting loci. This atypical structure indicates a collision event between two or more smaller galaxies, making it a morphological outlier. The single sample seen here is not sufficient to establish general relationship, but it is suggestive that atypical, decentralized morphologies of starforming galaxies can foster Lyα escape. The target galaxies with a higher E(B-V) extinction and higher metallicity tend to have a lower escape fraction, indicating that dust does play a significant role in the dynamics that dictate Lyα escape.

The average Lyα escape fraction for SNAP targets without notable AGN is $\sim$17.4% above the calculated H I absorption and $\sim$9.9% above the continuum, defining a reasonable range for Lyα escape depending on H I presence in the local ISM. Even at the low end of the range, this significant escape that indicates that bright UV galaxies

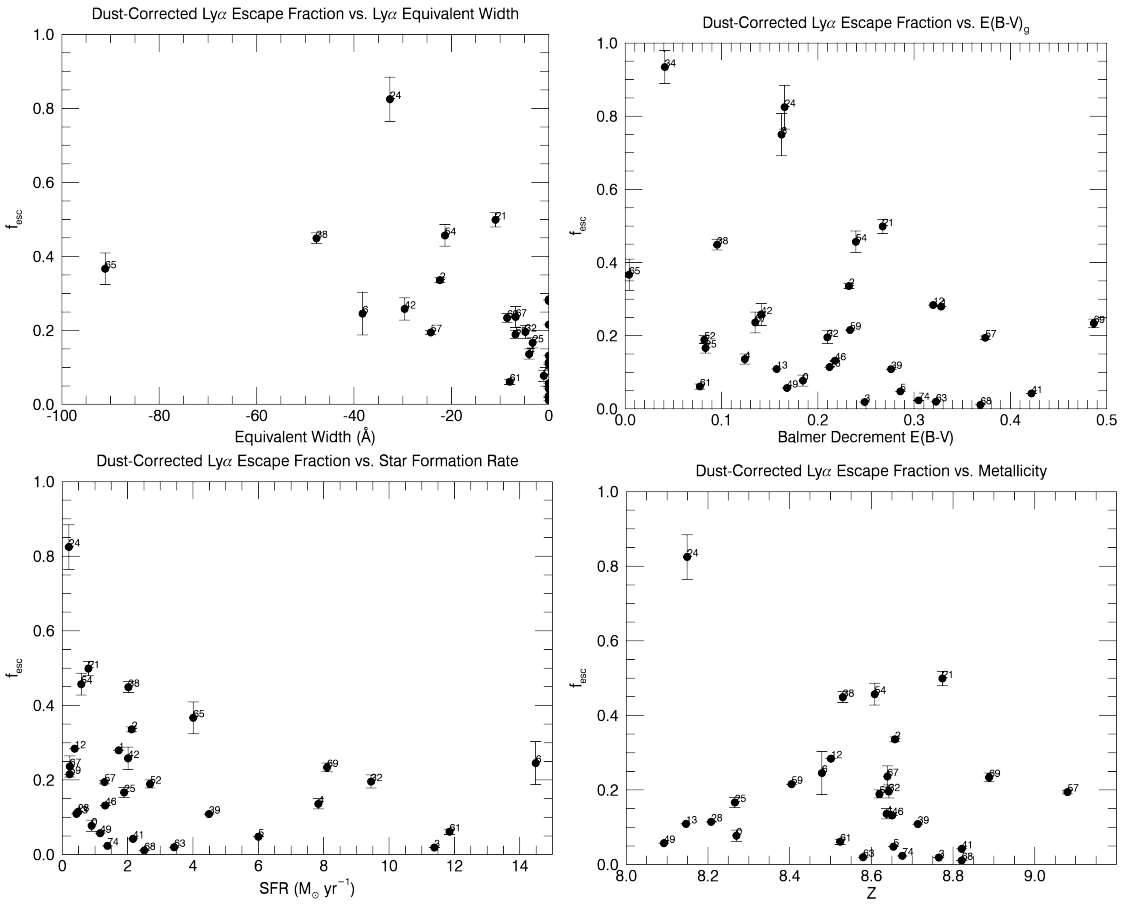

Figure 2.5: **(Top Left)** $f_{esc}^{Ly\alpha}$ vs. Lyα emission equivalent width, **(Top Right)** $f_{esc}^{Ly\alpha}$ plotted against E(B-V) calculated from the Balmer decrement, **(Bottom Left)** $f_{esc}^{Ly\alpha}$ vs. the star-formation rate derived from Hα luminosity (78), and **(Bottom Right)** $f_{esc}^{Ly\alpha}$ escape plotted against galaxy metallicity (63).

will show Lyα leakage at low redshifts, which is in conflict with studies showing a close relation between redshift and bulk Lyα escape fraction where escape is almost fully extinguished at $z <\sim 1$ (79). This relationship has been recently challenged (80). This is shown in Figure 2.6, where Lyα escape fractions out to z=7 are show to follow calculated curve by Hayes et al (79). This relationship breaks down for a recent sample of $z = 0.3$ Lyα emitting galaxies (80), and the SNAP sample of emitters in this analysis even further deviate from the relation that predicts very little Lyα leakage at low redshift, demonstrating (albeit with a small sample) that much more Lyα leakage is possble than predicted by Hayes (79).

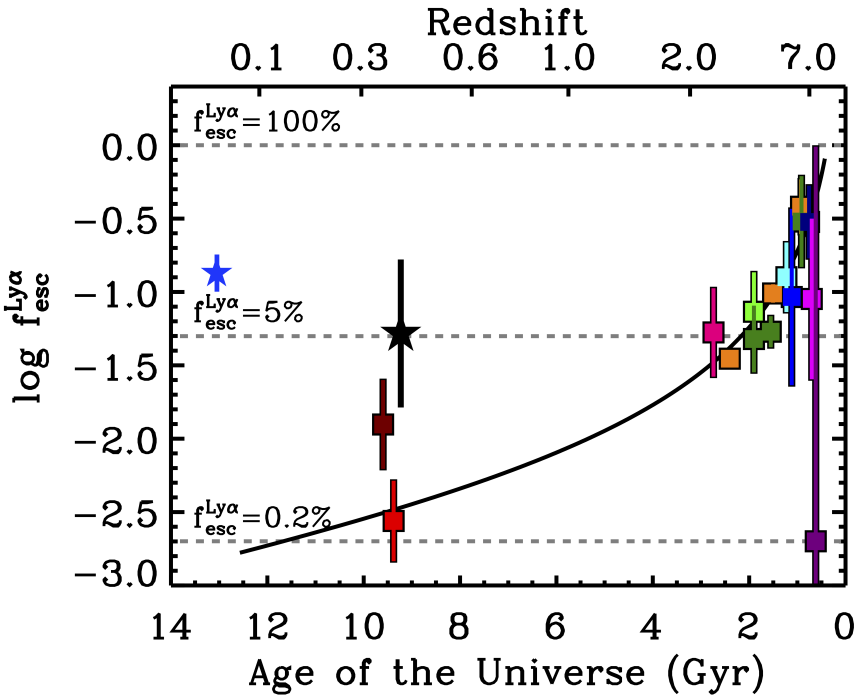

Figure 2.6: A dataset of average Lyα escape fractions from Lyα emitting galaxies as a function of redshift (79). A recent survey of z=0.3 galaxies is denoted by the black star (80), suggesting that the escape fraction does not drop to near zero at low redshift as an extrapolation of the high-z relation would indicate. The SNAP average is given by the blue star.

2.8 Metallicity

As the target galaxies are fairly bright low-redshift objects, measurements of their metallicities have been done in previous surveys using visible and infrared spectroscopic data, most notably for star-forming galaxies by Tremonti et al (63) and Brinchmann et al (81). Tremonti et al compiled a statistical model using data from strong emission lines O II, Hβ, O III, Hα, N II, and S II. Spectral data from many star-forming galaxies were fitted to metallicity using stellar synthesis models (15) and CLOUDY photoionization models (82), and a library of the resulting metallicities of SDSS DR7 galaxies was compiled and consulted for the purposes of this SNAP program analysis. Line features, likes those from He II, C II, C IV, N V, O I, O V, Si II, Si III, and Si IV are evident across the dataset, but not consistently for each individual galaxy target, shown in the tiled Figures in Appendix C for both low-ionization-state lines and high-ionization-state lines. Due to the insufficient signal-to-noise across the whole dataset to determine the species relative abundancies, we rely on the Tremonti metallicity values.

Of course there are other methods to determine metallicities; a summary of various useful methods can be found in Kewley & Ellison (83). These models are parametrized by emission line strength ratios in the SDSS bandpass for starforming galaxies, de-

Target	**H I Column**[a] (cm^{-2})	**Lyα Luminosity**[b] ($10^6 L_\odot$)	**Lyα EW** (Å)	$f_{esc}^{Ly\alpha}$	**Lyα Red Offset** (km s^{-1})
LY34	1.05e+20	3322.51	-124.12	0.93	10.51
LY24	4.22e+20	47.58	-27.68	0.82	-455.79
LY08	4.14e+20	6227.08	-48.48	0.75	-39.95
LY21	6.82e+20	114.08	-11.15	0.50	277.74
LY54	6.11e+20	75.83	-19.54	0.46	358.72
LY38	2.44e+20	259.82	-52.29	0.45	186.78
LY65	1.03e+19	420.79	-79.31	0.37	449.24
LY02	5.93e+20	204.27	-21.43	0.34	235.70
LY12	8.16e+20	30.76	14.90	0.28	-
LY01	8.37e+20	138.16	-2.83	0.28	-
LY42	3.60e+20	148.62	-42.11	0.26	417.58
LY06	0.e+0	1017.75	-43.09	0.25	221.61
LY67	3.44e+20	15.67	-6.80	0.24	376.22
LY69	1.24e+21	542.44	-4.78	0.23	135.37
LY59	5.96e+20	13.93	10.31	0.22	-
LY32	5.36e+20	529.53	-3.96	0.20	275.67
LY57	9.54e+20	71.82	-24.47	0.19	460.18
LY52	2.10e+20	145.33	15.79	0.19	12.41
LY25	2.13e+20	90.24	-1.47	0.17	505.99
LY04	3.17e+20	304.96	18.95	0.14	183.34
LY46	5.56e+20	49.43	22.69	0.13	-
LY28	5.42e+20	15.60	13.41	0.11	-
LY13	4.01e+20	13.60	9.70	0.11	-
LY39	7.04e+20	139.51	22.71	0.11	-
LY00	4.71e+20	19.87	14.68	0.08	-1371.43
LY61	1.98e+20	207.23	8.11	0.06	396.06
LY49	4.29e+20	18.97	22.16	0.06	-
LY05	7.29e+20	82.04	23.38	0.05	-
LY41	1.08e+21	26.08	18.28	0.04	-
LY74	7.78e+20	9.23	26.28	0.02	-
LY63	8.23e+20	19.31	10.29	0.02	-
LY03	6.34e+20	61.32	14.08	0.02	-
LY68	9.41e+20	7.92	6.41	0.01	-
LY09	6.47e+20	0.00	0.00	0.00	-

Table 2.2: Lyα line information for the sample. [a]Derived from calculated E(B-V) (76). [b]Above absorption due to H I column.

noted as $N2$, $O3N2$, and R_{23} (see Equations 2.9-2.11(83; 84; 85; 86; 87)).

$$N2 \equiv \log\left(\frac{[\text{N II}]\lambda 6584}{H\alpha}\right) \tag{2.9}$$

$$O3N2 \equiv \log\left(\frac{[\text{O III}]\lambda 5007/H\beta}{[\text{N II}]\lambda 6584/H\alpha}\right) \tag{2.10}$$

$$R_{23} \equiv \log\left(\frac{[\text{O II}]\lambda 3727 + [\text{O III}]\lambda\lambda 4959, 5007}{H\beta}\right) \tag{2.11}$$

These line ratio proxy relations to metallicities of the host emitting galaxies are determined via both empirical studies and stellar synthesis and photoionization models. We did a brief diagnostic of some of the models relating metallicity to these line strength ratios, as described in Kewley & Ellison (83), shown in Figure 2.7, relative to the archival Tremonti 2004 values. The sample size is not sufficient to make any strong statement about the validity of these metallicity models, but they do show a fairly robust correlation, especially with respect to diagnostic $N2$ (84). For the remaining analysis of this dataset, we use the Tremonti values (63) as the target metallicites.

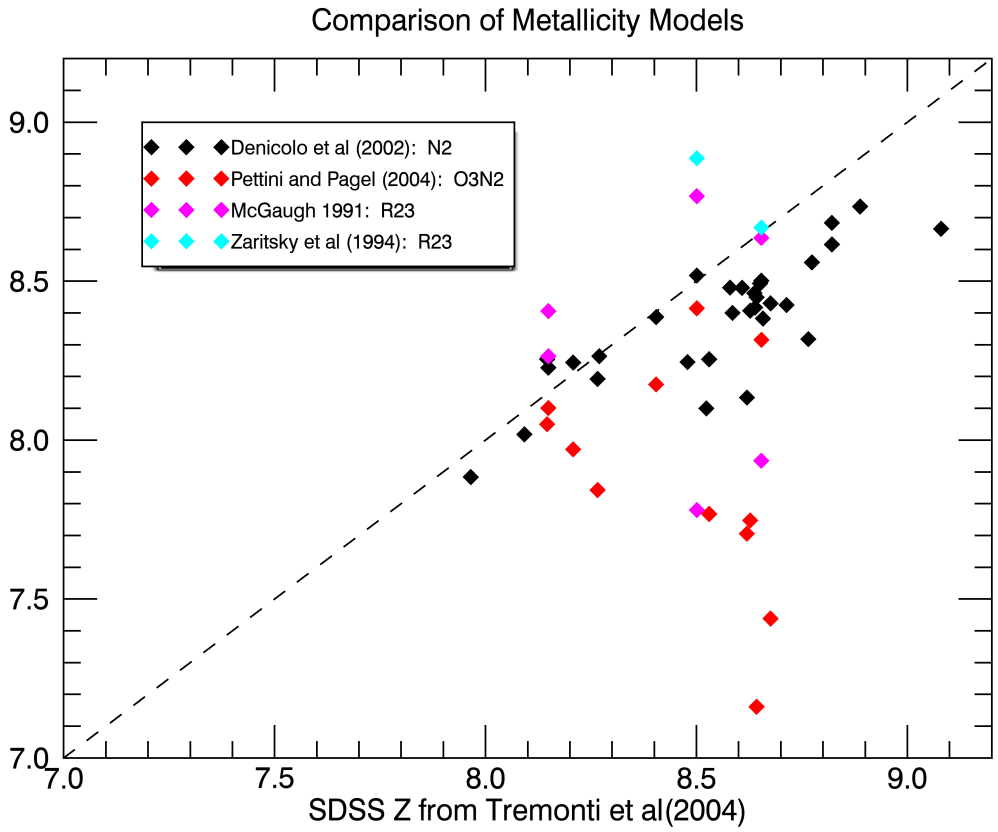

Figure 2.7: Comparison of metallicity models (83), within the redshift and metallicity bounds of their model effectiveness using Tremonti 2004 metallicities as abscissa.

2.9 BPT Diagram Outliers

A common tool to evaluate galaxy types from visible line features available in the SDSS archive is the Baldwin, Phillips & Terlevich (BPT) diagram (88), which diagnoses galaxy types from ratios of high and low ionization state lines. Two ratios detailed in Kewley et al (89) compare the ratio of S II λ6718,6733 ([S II]) and N II λ6585 ([N II]) to O III λ5007 ([O III]), with distinct lobes in a scatterplot of galaxies for normal H II regions, low-ionization nuclear emission-line regions (LINERs) (90),

and Seyfert-type galaxies (high-ionization species). The oxygen line strength is scaled by Hα and the sulfur and nitrogen lines are scaled by Hβ in order to limit the effect of dust reddening. The SNAP targets are shown in these BPT configurations in Figure 2.8. These galaxies generally track as H II regions, with a few outliers, most notably LY08. The fact that both clear AGN objects in the sample (as well as a few additional AGN candidates) do not fall into the AGN region of the BPT diagrams is not too concerning, as the sample of target galaxies for observation in this SNAP program was biased specifically to avoid typical quasars. However, despite LY08 and LY34 having broad emission lines suggesting AGN emission, their weak O III and O II typical of the uncommon narrow-line Seyfert 1 AGN type (91), allowed them to fall through the selection criteria of this project. The existence of the strong AGN signals from these objects explains the poor fit with the SB99 model, which only considers stellar evolution and stellar winds in its spectral synthesis. The SNAP sample is too small, especially considering the strict sampling biases in compiling the target set, to make broad conclusions about line feature anomalies like LY08, but the Lyα escape denoted by the symbol size in Figure 2.8 is spread fairly uniformly across the paramaeter space, which suggests that the escape is not strongly dependent on the ionization state of the non-hydrogen elements in the host galaxy.

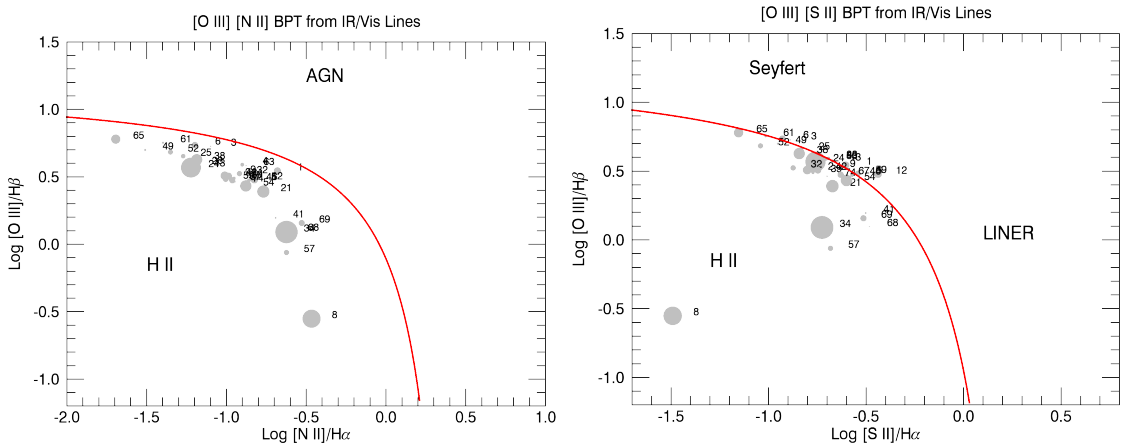

Figure 2.8: BPT Diagrams for the targets in the NSAP survey. The size of the points is given by the relative Lyαescape fraction of each galaxy. Red lines separate normal H II regions from LINER objects (89). **(Left)** BPT Diagram of [O III] vs. [N II]. **(Right)** BPT Diagram of [O III] vs. [S II].

2.10 Lyα Escape as a Proxy for LyC Ionizing Escape

While the COS observing mode used for this dataset is ostensibly sensitive down to 900 Å, the signal-to-noise acquired from the short SNAP observations isn't nearly high enough to see LyC escape, even if f_{esc}^{LyC} was higher than expected. However, there have been models (49) suggesting that the structure of the Lyα emission line can indicate a H I column density, based solely on the offset of the Lyα emission peak wavelength from the nominal redshifted Lyα center. Galaxies with high column densities along lines of sight outward will have Lyα peaks shifted more redward, as in the resonant scattering process in the dense medium the majority of photons that can escape are

those in the longward line wings, where the scattering cross-section sharply decreases. There is less of this scattering redward in galaxies with low column densities, where the f_{esc}^{LyC} is lower. These theoretical methods for Lyα line profile matching to LyC escape are better constrained at a high spectral resolution where the double-peaked emission profile can be seen. This requires a higher spectral resolution than provided by this SNAP program; for an example see Yang et al (92) for an analysis of a Green Pea galaxy spectral survey with data using the G160M COS grating, which has a resolution $\sim$10 times higher than that of the G140L grating. However, we can still track H I column density by measuring the redward shift of the overall flux of the Lyα line; galaxies with a redward shift of less than $\sim$150 km s^{-1} from the nominal redshifted Lyα line are suggested to have lower H I densities (49), making them good candidates for LyC leakage. Of the Lyα emitters in this SNAP sample (with Lyα line profiles shown in Figure 2.9, four satisfy this requirement after fitting the emission curve to a gaussian profile to determine a central wavelength, with all offset velocities listed in Table 2.2. Two of them (LY08 and LY34) are the previously mentioned AGN, which have offset velocities near zero (-22.2 km s^{-1} and 10.5 km s^{-1}, respectively). This is consistent with the expected highly ionized environment in the interior of these objects – a very low H I column density would result in very little reddening of the Lyα peak as the photons propagate outwards in the resonant scattering process. The two remaining emitters that indicate LyC leakage are LY52 and LY69, with offset velocities of 12.4 km s^{-1} and 135.4 km s^{-1} respectively. These galaxies make good

candidates for follow-up deep observations to search for LyC leakage. Furthermore, slightly loosening the requirements from Verhamme et al (49) qualifies LY04 (183.3 km s^{-1} red offset) and LY38 (186.8 km s^{-1} red offset) for potential LyC leakage.

Using this SNAP program, or similar short-exposure observations, is useful as a guide for future deep observations of Lyα emitters in order to find signatures of LyC escape. The LyC search requires long exposure time on a given target, and a method for evaluating potential LyC leakage using short COS observations of Lyα line profiles with a high FUV effective area grating like G140L on nearby starforming galaxies shows promise in expediting direct LyC observation. This SNAP survey demonstrates that reliable measurement of the red offset of the peak Lyα emission curve, which indicates H I column density (49), is achievable in short observations of target galaxies with the far- and extreme-ultraviotet sensitive G140L grating on COS. Larger surveys of these observations can be a pathfinding tool for further deep observations of LyC leaking galaxies.

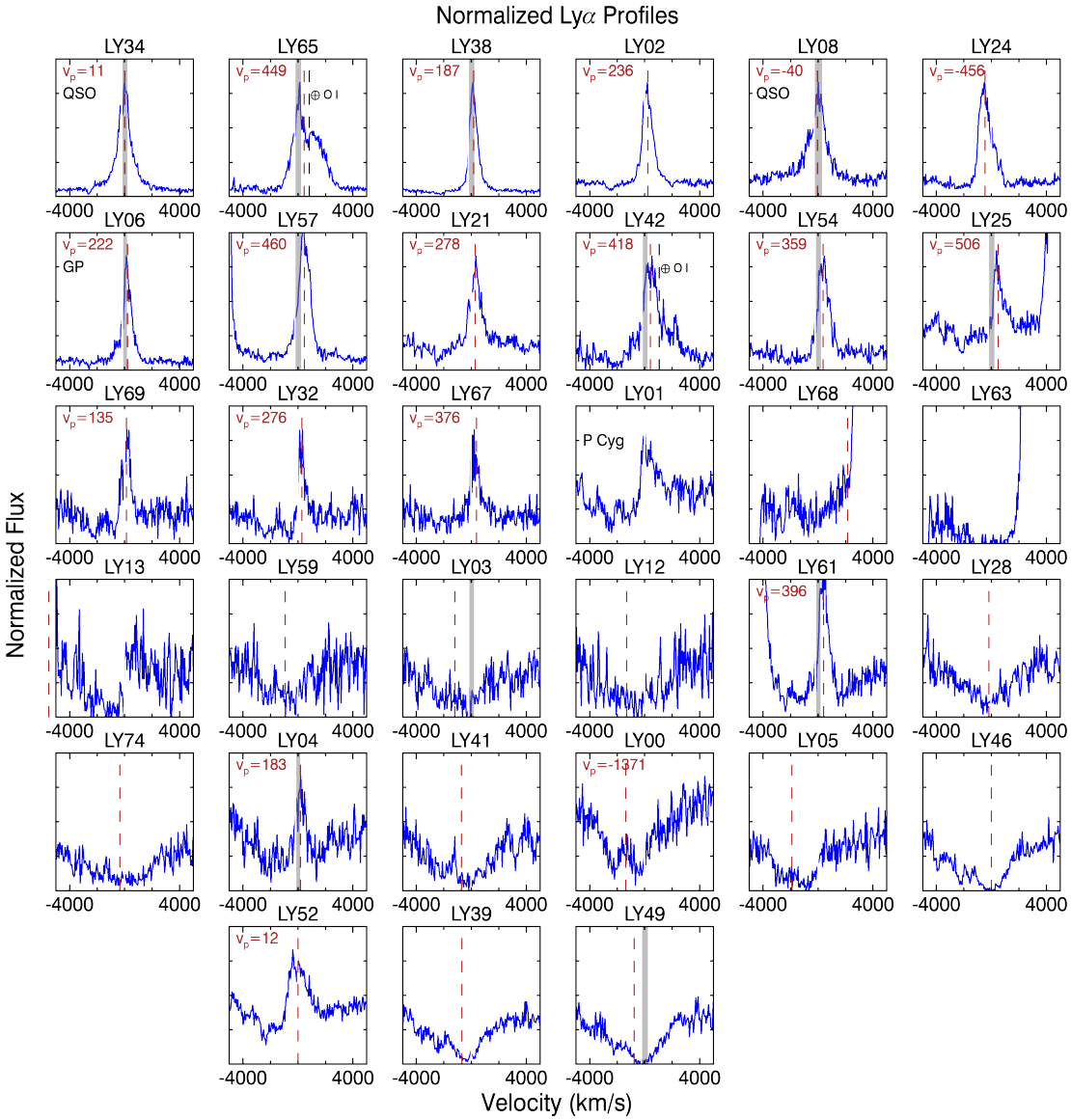

Figure 2.9: Lyα emission line profiles for each emitting SNAP target, in descending order by equivalent width, given in angstroms. Note that a few (LY04, LY52, LY61, and especially LY00) have emission embedded within a broader absorption profile. Quasars are labeled, as is the sole Green Pea Galaxy. If the geocoronal O Iλ1302 line encroaches on the Lyα profile, it is labeled with a $\oplus$ symbol.

Chapter 3

New Gapless COS G140L Mode Proposed for Background-Limited Far-UV Observations

3.1 Goals of Observation

The demonstrated sensitivity of COS (93; 94) G140L mode to wavelengths below 1150 Å(95) has opened a new window to the universe previously inaccessible to Hubble, and enabled a number of compelling science investigations, one of which is the search for ionizing hydrogen Lyman continuum (LyC) photons from star-forming galaxies at low redshift in order to characterize the escape process (10). To take full advantage of the FUV capabilities of COS, we proposed and calibrated a new observ-

ing mode where the CENWAVE setting, the nominal shortest wavelength to appear at the short wave end of the Segment A detector, was set to 800 Å, providing contiguous wavelength coverage from 900 Å to 1850 Å on the Segment A detector. This new mode has three significant advantages: 1) a contiguous spectral coverage on a single detector segment, which will simplify tracking of flux, wavelength and flat-field calibrations; 2) a $\sim$2 times lower background from reduced astigmatism at the short wavelength end where the effective area is lowest, which will boost the signal-to-noise of background limited observations; and 3) a more efficient use of observing time for programs requiring the full far-UV wavelength coverage by eliminating the need for a grating change.

We describe the flux and wavelength calibration of the new mode, using the calibration target AV 243, a stable O6V star in the Small Magellanic Cloud. We observed AV 243 in Cycle 19, and also utilized archival spectra (96) of AV 243 previously acquired by the *Far-Ultraviolet Spectroscopic Explorer* (FUSE) (97), the Faint Object Spectrograph (FOS) (98) once aboard HST, and the *International Ultraviolet Explorer* (IUE) (99), which guided our analysis of the new CENWAVE=800 mode of COS G140L. We determine the best focus position and characterize the astigmatism as a function of wavelength, as well as providing a wavelength calibration and effective area calculation.

3.2 Data

In order to establish this new mode, the selected source needed to have a high density of relatively narrow atomic and molecular absorption lines to determine focus and a wavelength solution. It was also required to be bright enough to supply a high enough signal-to-noise over the allotted orbit sweeps and be dim enough to not violate the bright object protection of COS (55). The integrated flux from AV 243 is known from previous observations by FUSE and FOS. A global count rate of 11141.1 counts s^{-1} was observed in the COS extraction window in this program, which was below the global limit of 15000 counts s^{-1} but high enough to provide a good volume of data.

We were granted time for three orbits of integration time in cycle 19 (HST Proposal ID #12501) on the target. Over the course of the observation, with a central wavelength setting rotated to 800 Å, the spectrum was moved to the four different FP-POS positions. Each of the focus settings used, Fpos = -370, -770, -870, -970, -1070, -1170, moved the focus of the spectrum across the detector in the dispersion direction. Note that these focus shifts given by Fpos are distinct from the FP-POS settings; in a typical COS observation the FP-POS will cycle through each setting, shifting the entire spectrum in the dispersion direction in order to preserve consistent sensitivity across the detector. The Fpos settings are not generally adjusted over an observation, and shift the position of the most sharply focused point of the spectrum, while not moving the spectrum itself. An example of the raw images and resulting

spectrum is shown in Figure 3.1.

One-dimensional spectra were extracted, using an optimal method for determining a summation envelope following the astigmatism. For a column containing N counts on the detector, we set symmetric bounds around the centroid of the column such that the bounds exclude a proportion of $\sqrt{\frac{1}{N}}$ of the data. The counts are then simply totaled for each column, resulting in a one-dimensional spectrum. In Figure 3.1, these bounds are explicitly drawn onto four of the two-dimensional COS spectra, along with the resulting one-dimensional extraction for the best focus position. For columns with lower count rates the extraction region is larger, exhibited by the larger regions contained by the bounds of the extraction regions of the spectra. This procedure assumes a symmetric cross-dispersion profile, which isn't strictly the case, but the error due to asymmetry from a small misalignment of the aperture with the microchannel plate detector is minimal.

We can compare the astigmatism in this new mode with those for existing G140L CENWAVE settings in order to track the astigmatism improvements of the new CENWAVE=800 mode in the FUV. In Figure 3.2 we define astigmatisms as extraction window widths that contain 95% of the on-target counts in each column in the geometrically corrected data, and plot them as a function of wavelength. This figure shows a minimum width of these extraction windows at a shorter wavelength ($\sim$1250 Å) for CENWAVE=800 than that for CENWAVE=1280 ($\sim$1550 Å).

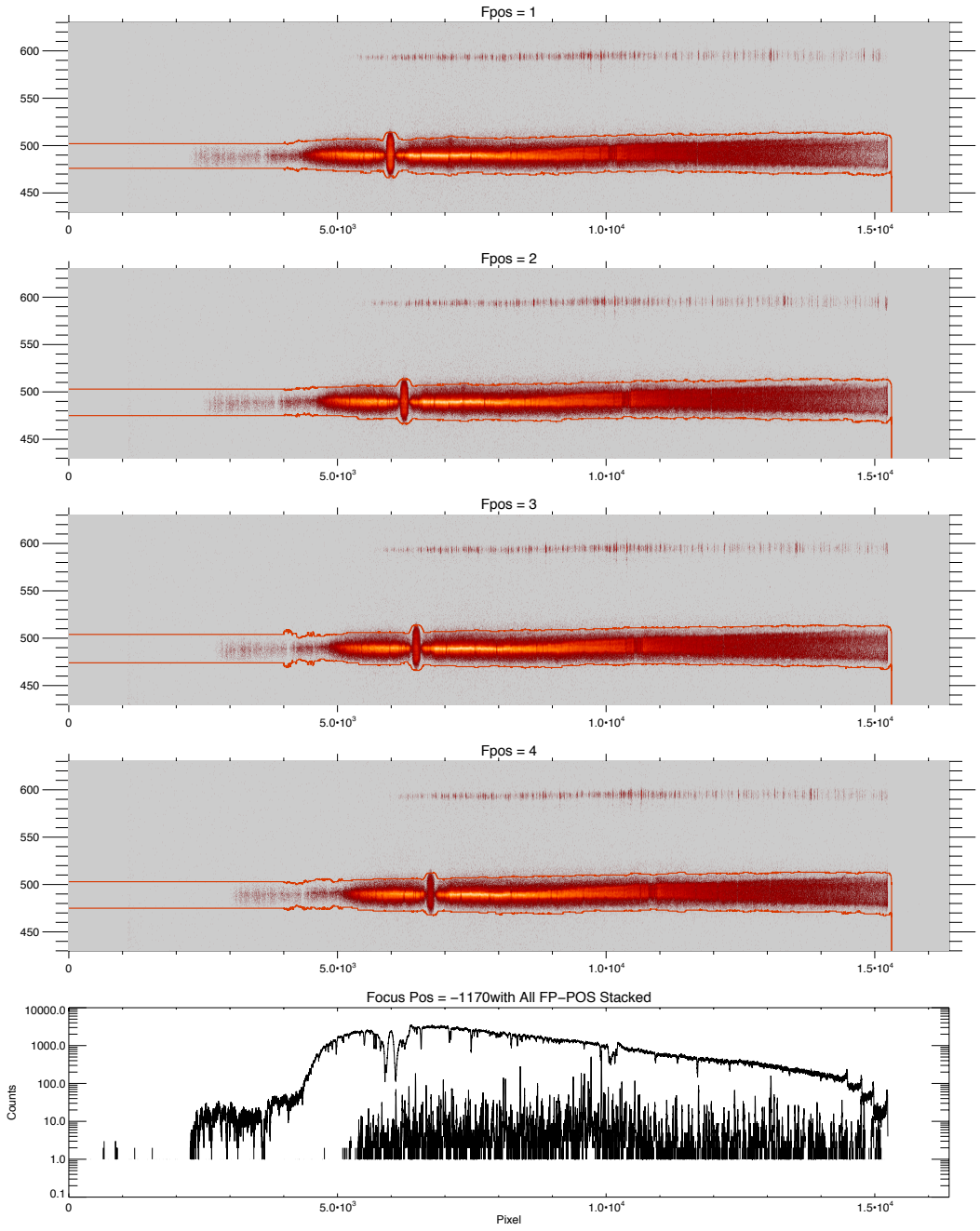

Figure 3.1: Calibrated spectra of four FP-POS positions, in Fpos=-1170 focus setting, with a one extracted one-dimensional spectrum of the on-target region and the PtNe lamp region of the detector. The red lines in the two-dimensional windows show the extraction windows for calculation of the one-dimensional spectrum.

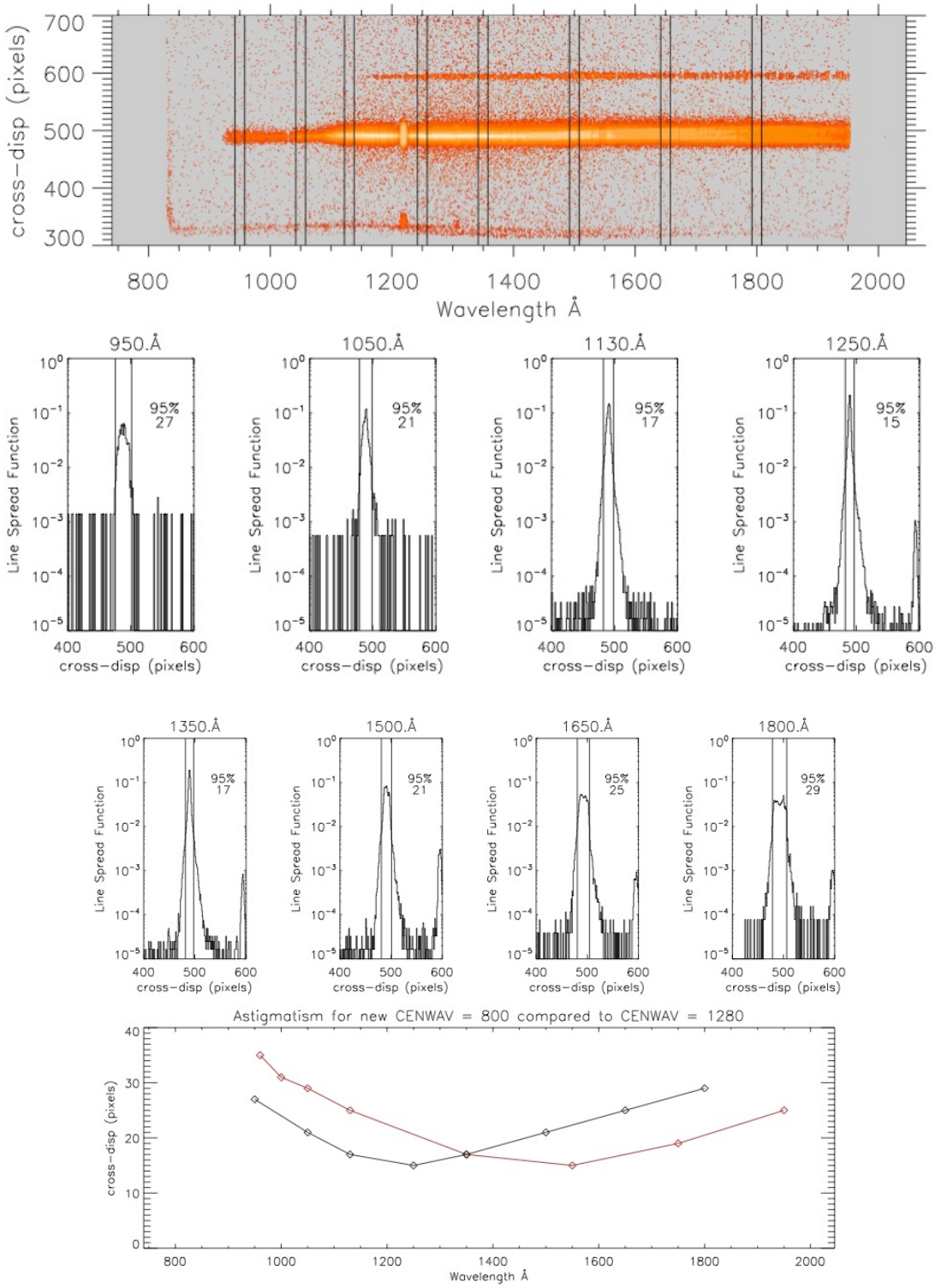

Figure 3.2: **Top:** A geometrically corrected data image with vertical lines delineating windows for calculating astigmatisms at various wavelengths. **Center:** These astigmatism window widths within 100 Åof the center wavelength, defined as containing 95% of the on-target counts in pixel space. **Bottom:** We plot these 95% pixel-widths (black) with the equivalent calculation for the G140L mode CENWAVE=1280 (red).

3.3 Calibration

Turning a raw measured spectrum of AV 243 into a wavelength solution and effective area curve for the new mode involves several steps. The onboard Platinum-Neon lamp spectrum was used to develop a wavelength calibration across the bandpass above $\sim$ 1200 Å. Wavelength positions were determined by calculating centroids on individual emission lines in the one-dimensional spectrum. We found that a second order calibration solution was suitable, along with a single-frequency sinusoidal offset. With this solution, residuals of the centroid positions to the documented PtNe lamp emission lines were limited to less than 0.1 Å.

Using this wavelength calibration as a starting point, we then matched the FUSE and FOS spectra of AV 243 to a theoretical absorption model of continuum emission from the star. We found strong populations of absorbing material responsible for significant absorption features in the spectrum. These included H I, H_2, Ar I, N I, N II, Si II, Fe II, and Fe III. The species present are typical of sight lines through the SMC including both warm and cold gas. We fitted the absorption lines, producing a model spectrum with absorption complexes (modeled as single Gaussians for our purposes) centered at v_{helio} = +20 and +140 km/s, consistent with expectations for the Milky Way and SMC. We compared the theoretical model with the observed COS G140L spectrum to derive the wavelength calibration at wavelengths below 1200 Å. We considered individual features in the G140L spectrum and performed centroid calculations similar to those used for the lamp spectra at longer wavelengths.

Parameter	**Value**
A	731.589
B	0.07912
C	3.9229×10^{-8}
D	0.1171
ω	6.274
ϕ	3.34969

Table 3.1: Parameters of the wavelength calibration.

With these offsets, we were able to fit the remaining short-wavelength region of the wavelength domain, from ∼950 Å to ∼1800 Å. This resulting calibration function matched the observed spectrum with residuals less than 0.2 Å. In Figure 3.3 we plot the mapping from pixel to wavelength with the quadratic solution and the sinusoid, with residuals for each step. The final wavelength calibration parameters are shown in Table 3.1, corresponding to the pixel-to-wave mapping in the form:

$$\lambda = A + Bp + Cp^2 + D\sin(\omega p - \phi)$$

This calibrated COS spectrum with the FUSE/FOS reference and the theoretical absorption spectra can be seen in Figure 3.4.

After linearizing the spectrum using this function, the total effective area of the new COS mode can be calculated by simply dividing the two spectra at any given wavelength. We used the reference spectra previously described of the target. We found it varied slightly between different instruments. Figure 3.5 shows these archival

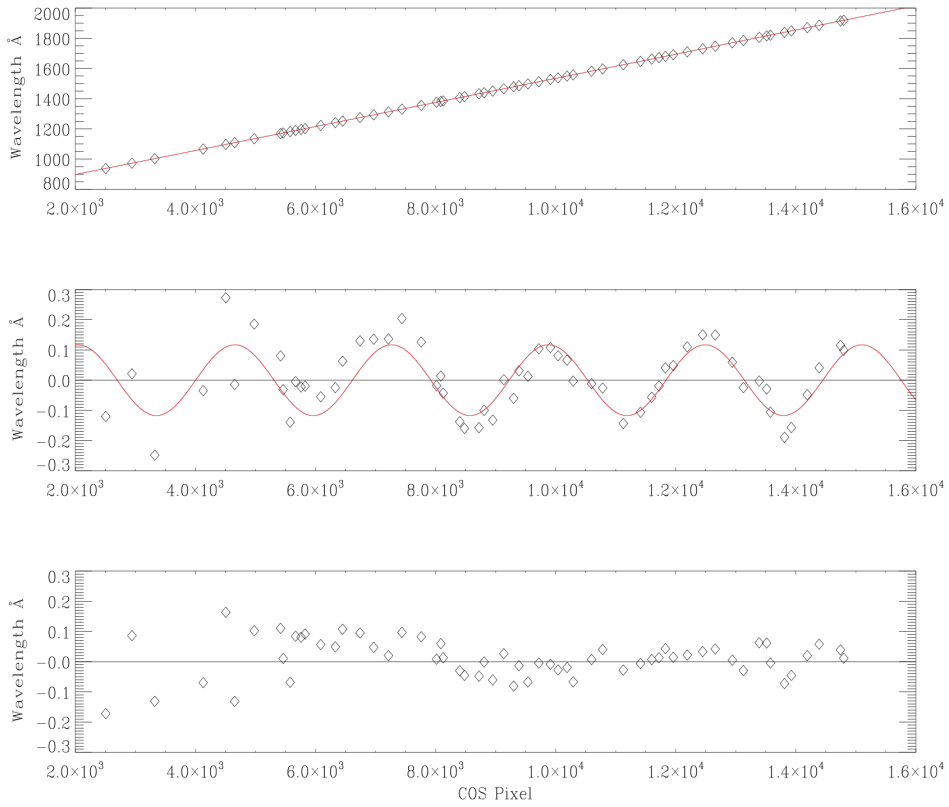

Figure 3.3: **Top:** The COS pixel to wavelength relationship for sixty absorption lines is plotted explicitly, with the second-order polynomial fit overplotted in red. **Center:** The same sixty points, but in this case the polynomial values at the data abscissa are subtracted from the measured wavelengths, and the residuals from this polynomial fit are plotted on the same wavelength scale. The sinusoidal dependence of these residuals is clear, and the fit to account for this is again overplotted in red. **Bottom:** Once again the same sixty points with both the polynomial and the sinusoid fit subtracted from the measured wavelength values for each of the sixty selected pixels. Errors are limited below 0.2 Å.

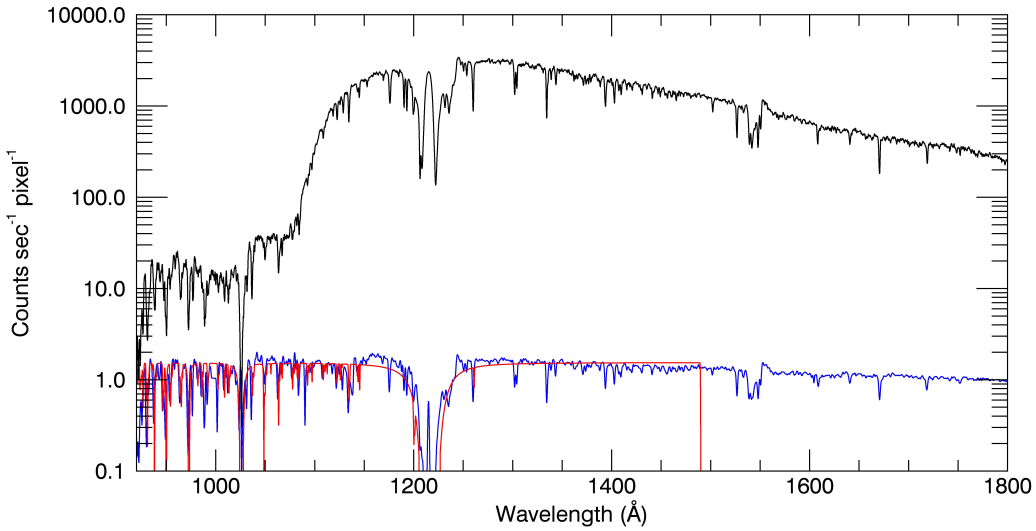

Figure 3.4: Wavelength calibrated COS spectrum (black) with the FUSE/FOS reference (blue) and theoretical absorption (red) spectra.

data of the calibration target, with each providing a different effective area curve. Figure 3.6 provides the final effective area calculations for reference spectra of FUSE/FOS and IUE data, along with the G140L effective area from the COS handbook for when the observation was made.

3.4 Results

Through this calibration effort, we have achieved a successful wavelength and flux calibration. The wavelength solution is consistent with similar solutions for other modes, and suitably maps pixel space to wavelength space with errors of less than 0.2 Å, which is a factor of ∼3 less than the minimum resolution limit of the G140L

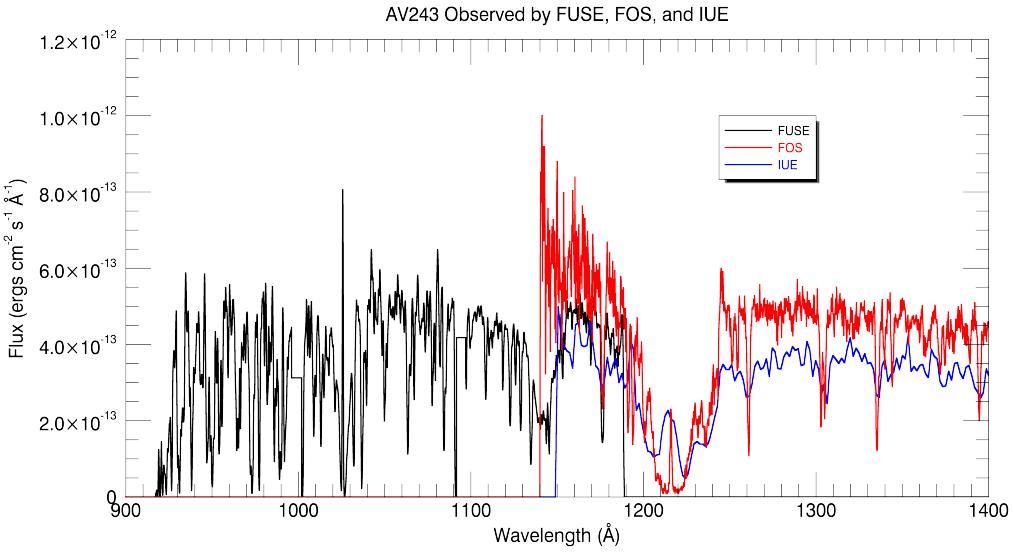

Figure 3.5: Spectra of the target AV 243 by FUSE, FOS, and IUE.

grating (55), $R_{min} = \frac{\lambda}{\Delta\lambda} = 1500$. The resolution, $\Delta\lambda$ (FWHM) at the minimum useable wavelengths, $\lambda \approx 900$ Å, is therefore $\Delta\lambda \approx 0.6$ Å. The throughput, defined as the ratio of the wavelength-dependent effective area to the total collecting area of the telescope, is necessary for the exposure time calculator that guides exposure time requests in proposals and similar to that for exisitng COS G104L modes. This throughput is shown in Figure 3.7. While final calibrations will be performed by the *Space Telescope Science Institute*, especially considering that the lifetime positions on the COS detector have changed since this observation, these flux and wavelength calibrations are useful guides to estimate the

Figure 3.8 shows a background equivalent flux for the extraction window used to define the on-target region of the detector and calculate the one-dimensional spec-

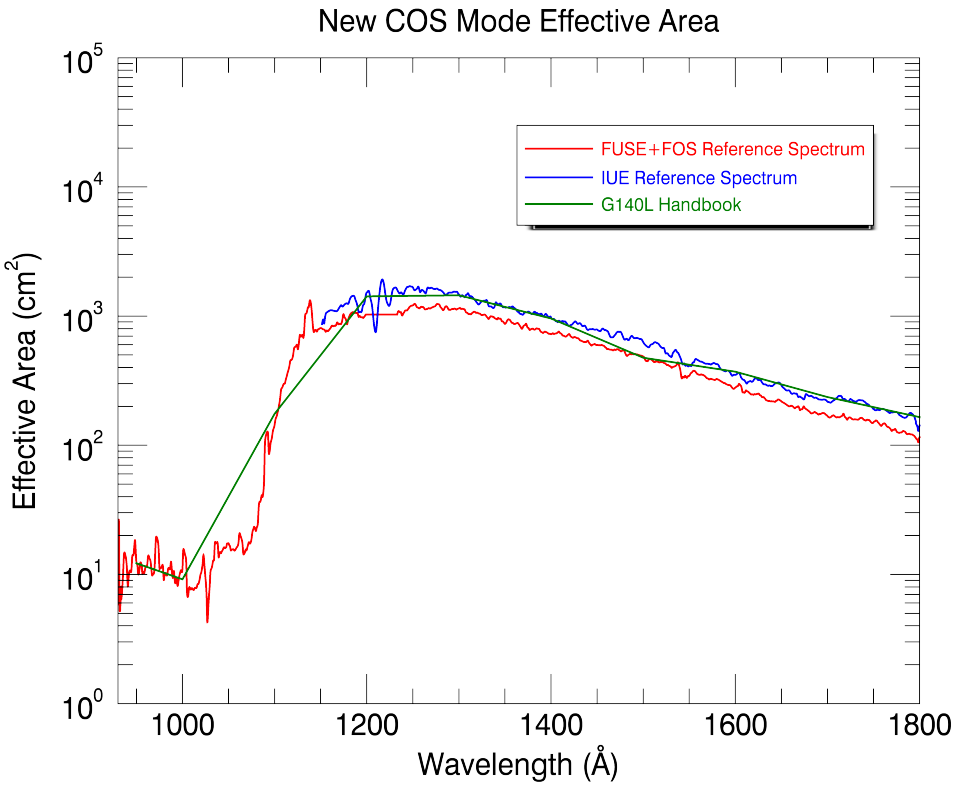

Figure 3.6: Effective areas for a FUSE/FOS reference spectrum, an IUE reference spectrum, and the archival effective area for the G140L grating for cycle 19 (55).

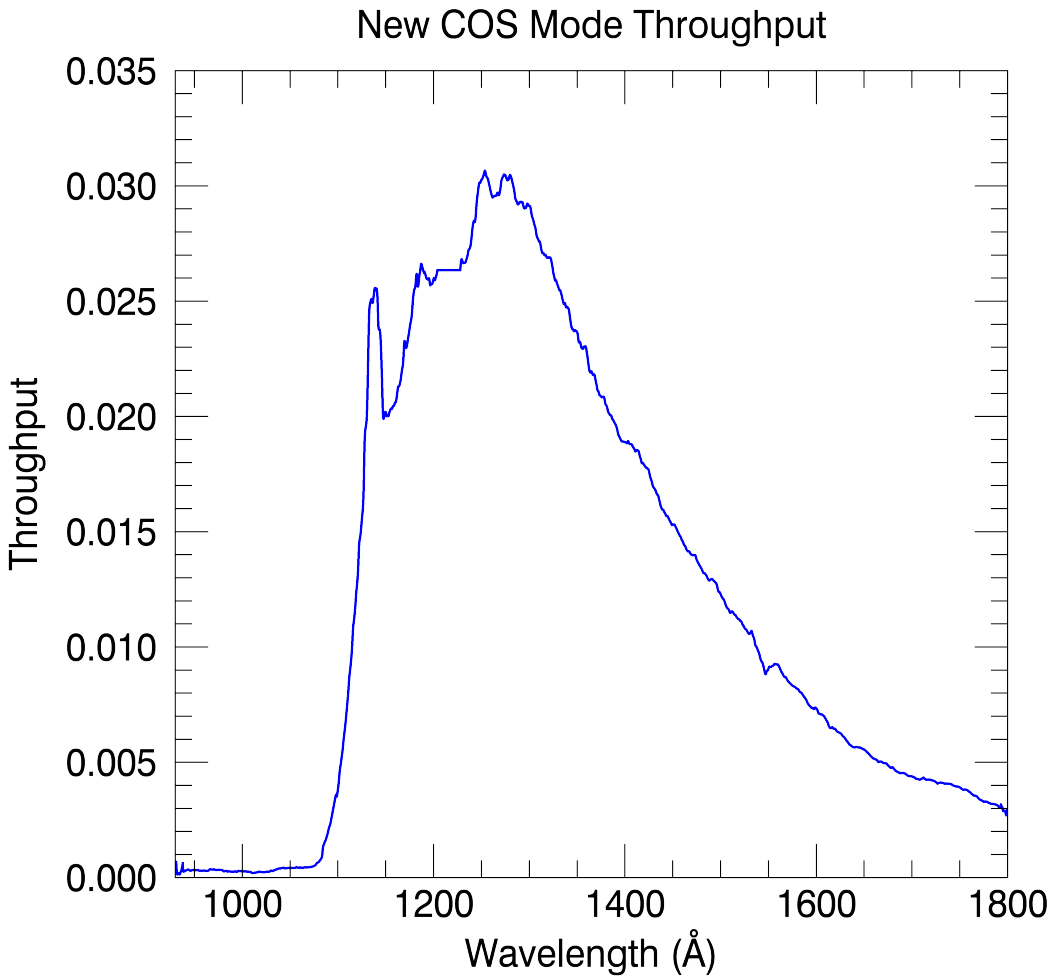

Figure 3.7: Throughput plot of the new COS mode, based on a reference spectrum of AV243 by FUSE and FOS.

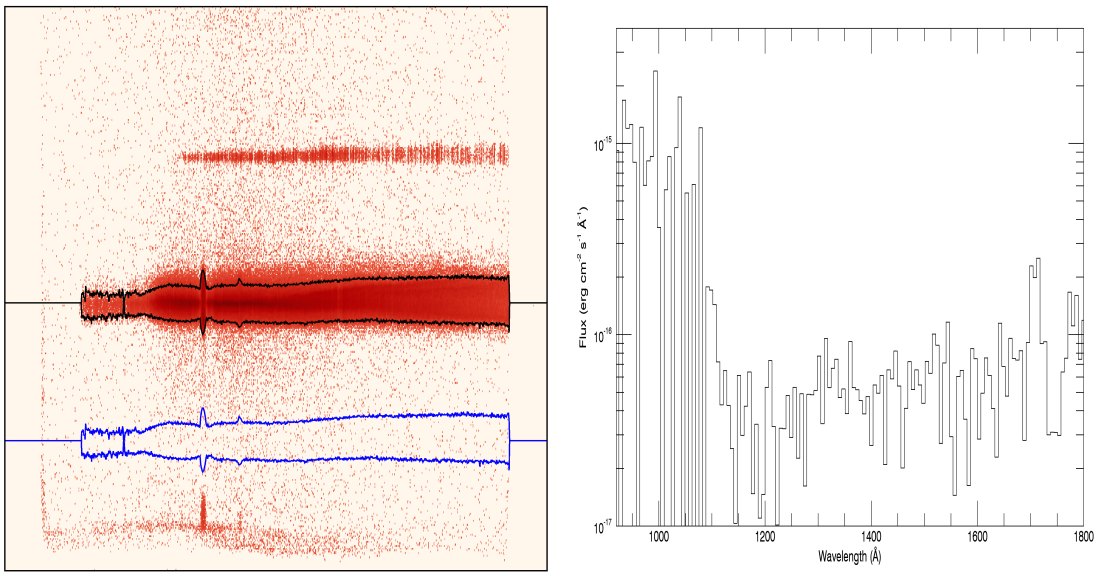

Figure 3.8: **Left:** Geometric corrected COS image with extraction window drawn in black around the target flux. This same extraction window is moved to an off-target region of the image, drawn in blue, to define the background flux for the measurement. **Right:** The one-dimensional background equivalent flux.

trum. The extraction region is moved to an off-target region of the image, and a new spectrum is calculated from the background counts alone. Our observations have successfully shifted the minimal astigmatism from 1550 Å to 1250 Å, suggesting that pushing further into the far-UV is possible, and a CENWAVE=650 mode could be a worthwhile project in the future. In Figure 3.9 the relative focus position of this potential mode is calculated by extrapolating a curve of focus positions for existing CENWAVE modes.

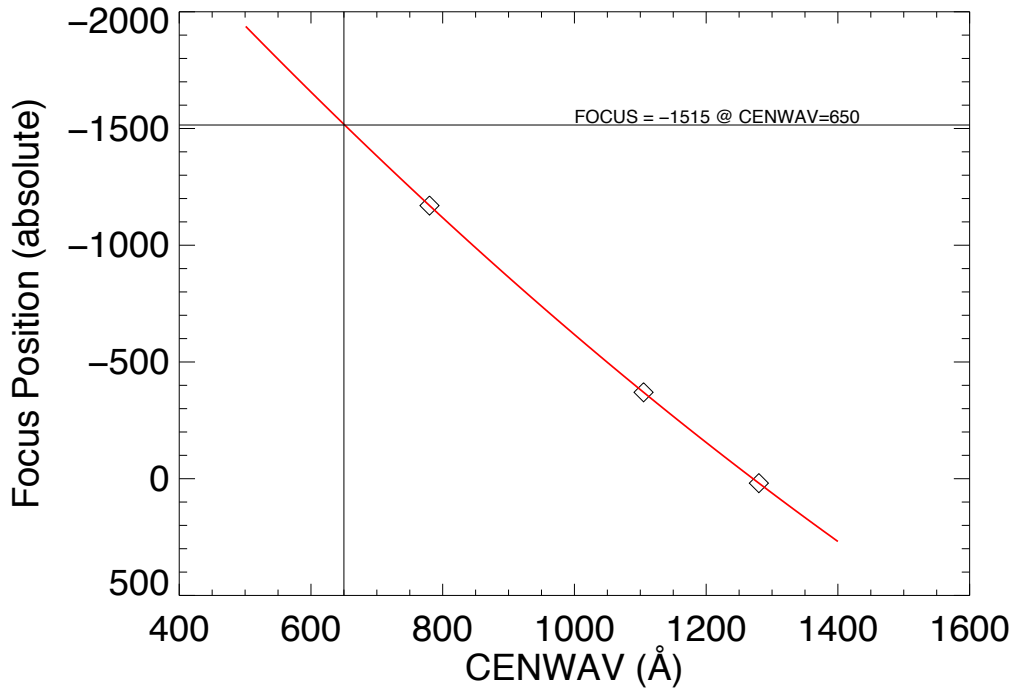

Figure 3.9: Points showing the relative focus position for CENWAVE=1280, 1105, and 800, with an extrapolated curve estimating the focus positon for a potential CENWAVE=650 setting.

3.5 Discussion

This new mode offers significant improvements over the existing modes used to observe spectra in the far-ultraviolet range. Currently there are two observing modes for the COS G140L covering wavelength ranges from 100 Å to 2400 Å, but the ability to observe this range is spread across two observing modes and detector segments, making it difficult to obtain science data without allowing for extra observation time and decreased data quality (55). The new mode enables observation between the two segments, allowing for easier and faster calibrations of flux and wavelength. By centering this mode so that the low-astigmatism portion of the bandpass is in the 900-1100 Å region, the sensitivity at these wavelengths is increased by lowering the background limit. Additionally, looking at a complete range from 900-1850 Å will no longer require a grating change, increasing potential science time and thus the total sensitivity of measurements.

There are several immediate applications for this new mode that will explore new physics. The dynamics of young star-forming galaxies are still being explored, and Lyman-α photons from these sources would fall directly into the range of the new mode at a sensitivity unseen beforehand with the G140L grating. Low redshift observations of these galaxies would greatly help in understanding how the re-ionization of H I occurs at $z \sim 6$, as it is postulated that the Lyman continuum is responsible for this ionization. The Lyman alpha radiation could be a proxy for the Lyman continuum (42), and observation by COS into this wavelength range will significantly aid

our understanding of this phenomenon.

This new mode could also be useful in exploring the the He II Lyα forest. FUSE observations of He II in the intergalactic medium (IGM) on quasar lines-of-sight (HS 1700+6416 and HE 2347-4342) showed that source hardness is related to small fluctuations in large-scale ionizing background (100; 101; 102; 103), and similar studies were done with G130M and G140L gratings on COS (104; 105; 106). The new gapless COS mode opens up possibilities to put constraints on the variance of this effect in different regions of the IGM and at the redshift associated with He II re-ionization. Opening up this new mode in COS could bring background levels down to a level where He II absorptions could be measured at redshifts of $\sim$2.

As of early 2018, the COS team at *Space Telescope Science Institute* is working to implement the CENWAVE=800 mode as a standard option for HST proposals, including full support with the exposure time calculator. We hope this new mode will be operational for Cycle 26 proposals.

Support for this work was provided by NASA through grant number 12501 from the Space Telescope Science Institute, which is operated by AURA, Inc., under NASA contract NAS 5-26555.

Chapter 4

Hydrogen Cells as Narrow-Band Geo-Coronal Lyman-Alpha Rejection Filters for Astrophysical Photometry

4.1 Goals of Hydrogen Cell Development

Space-based imaging observations of astrophysical sources in the far-UV has long been hampered by the bright geocoronal Lyα emission in the exosphere of the Earth. Attempts to image the sky below $\sim$1200 Å down to the lithium-fluoride edge at $\sim$1040 Å are complicated by the extremely intense Lyα emission line at 1216 Å, which has

a brightness between 2-20 kilorayleighs (107). A Lyα rejection filter in combination with a solar blind imager would enable relatively broadband photometric imaging in the hitherto unexplored bandpass below Lyα. A far-UV photometric system can be constructed by subtracting images acquired through sharp absorption-edge cutoff LiF, MgF_2, and CaF_2 windows. This would produce synthetic bandpasses from ~1040-1150 Å and ~1150-1280 Å, where 1150 Å and 1280 Å are the edge filter cutoffs of MgF_2 and CaF_2, respectively. By filling an evacuated cavity with a small amount of hydrogen gas and subsequently dissociating the molecules with a hot tungsten filament, we create a strong absorbing column of neutral atomic hydrogen atoms. With far-UV transparent windows mounted on this cell, incoming light is attenuated only at Lyα as it passes through, while the column remaining transparent to all other wavelengths.

This technique of absorption cell narrow-band filters has been used to measure the deuterium to hydrogen (D/H) ratio in planetary atmospheres, notably with the *Hydrogen Deuterium Absorption Cell* (HDAC) (108), part of the *Ultraviolet Imaging Spectrograph* (UVIS) instrument on Cassini, currently orbiting Saturn, and on the PLANET-B mission to Mars. On UVIS, two individual absorption cells are mounted in front of a channel electron multiplier detector and provide varied optical depths (τ = 0 - 13) of neutral hydrogen and deuterium in the respective cells, resulting in two tuned narrow band filter with a high resolution full-width-half-maximum on the order of 0.001 nm. Doppler shifts due to the proper motion of Cassini spacecraft

allow for wavelength scanning in a narrow range around Lyα. The Cassini HDAC is capable of measuring D/H Lyα ratios on Titan to within $\sim$10% (108). Unofrtunately, calibration of HDAC in flight experienced anomalies and no results on the D/H ratio were acquired (109). This same strategy, with hydrogen and deuterium absorption cells, was also used on the PLANET-B mission to measure the same D/H ratio in the upper atmosphere of Mars (110). It was not tested in flight however, as the PLANET-B mission failed prior to reaching Mars orbit.

This filter functionality, heretofore applied to measure planetary D/H ratios, can be adapted to imaging telescopes, and we aim to design a practical, efficient hydrogen cell filter to be mounted on a solar blind microchannel plate detector. In fact, the Cassini HDAC did take geocoronal Lyα observations to measure the decrease of the exosphere hydrogen density as a function of the distance from Earth (111), demonstrating the effectiveness of the absorptions cell to the bright geocoronal Lyα. Such a filter will be of great use to far-UV missions in low earth orbit. We will estimate the effective area of an absorption hydrogen cell on a Schmidt-like camera instrument.

4.2 Hydrogen Absorption Cells and Test Equipment

As a proof of concept we assembled an absorption cell and tested it in the rocket group's vacuum calibration and testing equipment. The hydrogen cell, shown in

Figure 4.1: **Left:** Photograph of the experimental hydrogen absorption cell used for testing and calibration. **Right:** Photograph of the external pump manifold with hydrogen leak system.

Figure 4.1 (Left), consists of two MgF_2 windows mounted on 7 cm aluminum flanges, and sealed on either end of a 15.6 cm cavity. This cavity also contains a tungsten filament and two gas leak-in valves. A small vacuum gauge for measurement in the 0.001-10 torr range is included to accurately leak the appropriate pressure of hydrogen into the cell and monitor the pressure over the duration of operation of the cell. Various specifications for these components are listed in Table 4.1.

The cell was placed in a vacuum chamber and is illuminated with a windowless vacuum monochrometer, shown in Figure 5.14. Vacuum feedthroughs for the pumpout of the interior of the hydrogen cell and for the hydrogen leak are connected, as well as a power line for the tungsten filament. A G tube photomultiplier with a CsI photocathode sensitive to UV light is installed in line with the lamp and the two

Parameter	**Value**
Length of cell	15.6 cm
Diameter of cell	7.0 cm
Volume of gas column	31.4 cm^3
Cell Material	304 Stainless Steel
MgF_2 Window Thickness	0.16cm
MgF_2 Window Diameter	1.6 cm
Individual MgF_2 Window Transmission at 1216 Å	0.33
Tungsten Filament	0.06 cm x 0.005 cm

Table 4.1: Characteristics of the experimental hydrogen absorption cell.

MgF_2 windows of the cell to measure the total flux through the cell. Importantly, this phototube is not sensitive to visible wavelengths and is solar blind, eliminating the contribution of the filament. The chamber is pumped down to 10^{-6} - 10^{-5} torr to allow for UV measurements. Once the pressure inside the vacuum chamber is suitably low, we use an additional external pump manifold with a small valved hydrogen tank to evacuate the hydrogen cell through the vacuum feedthroughs to a 10^{-4} - 10^{-3} torr scale. Following the attainment of a sub 10^{-3} torr pressure in the cell, we backfill with H_2 to the desired pressure and seal it in preparation for tests. This pump manifold is shown in Figure 4.1 (Right).

Operation of the cell is straightforward. Lyα photons from the monochrometer enter the cell and are detected by the phototube. A DC power supply is used to provide a current that increases the temperature of the tungsten filament, which dissociates the molecular hydrogen in the cell. The signal from the phototube is recorded by a precision electrometer, and is analyzed as a function of power through

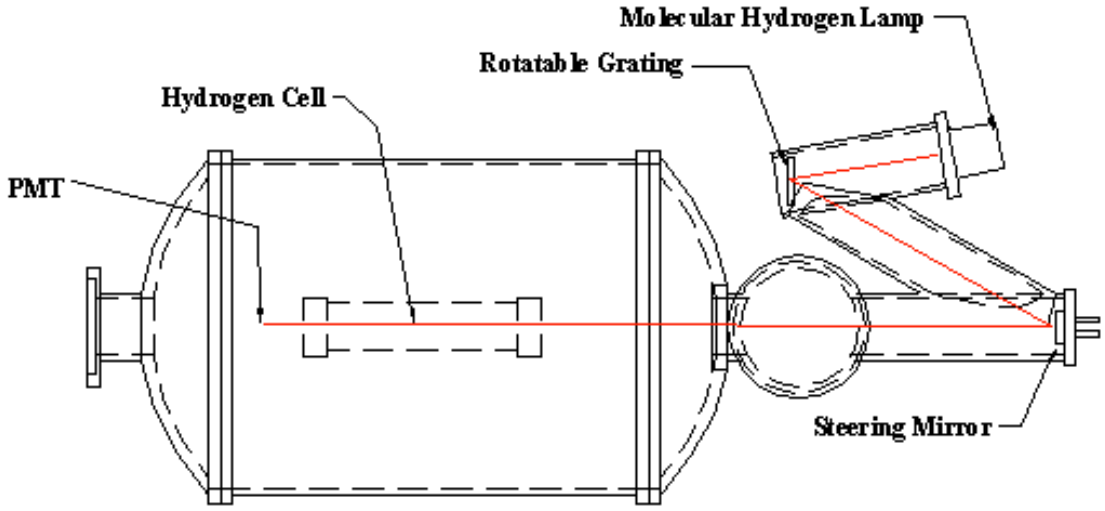

Figure 4.2: The vacuum monochrometer used in testing with the hydrogen cell in the test chamber. The light path is drawn in red, passing through the cell and into the photomultiplier tube (PMT).

the filament and the initial cell pressure. The attenuation is a simple ratio of the total flux of the light through the cell with filament on to that with the filament off.

4.3 Results

In Figure 4.3 we show our result. We measured the transmission of Lyα as a function of pressure in the cell and current through the filament. At one torr, the transmission efficiency reached a minimum of 0.7. In this instance, the current through the filament was high enough to dissociate the molecular hydrogen at $\sim$ 10 volts, but there just wasn't enough of a column density of atomic hydrogen to fully absorb all of the light. Upon increasing the hydrogen pressure up to three torr, the column

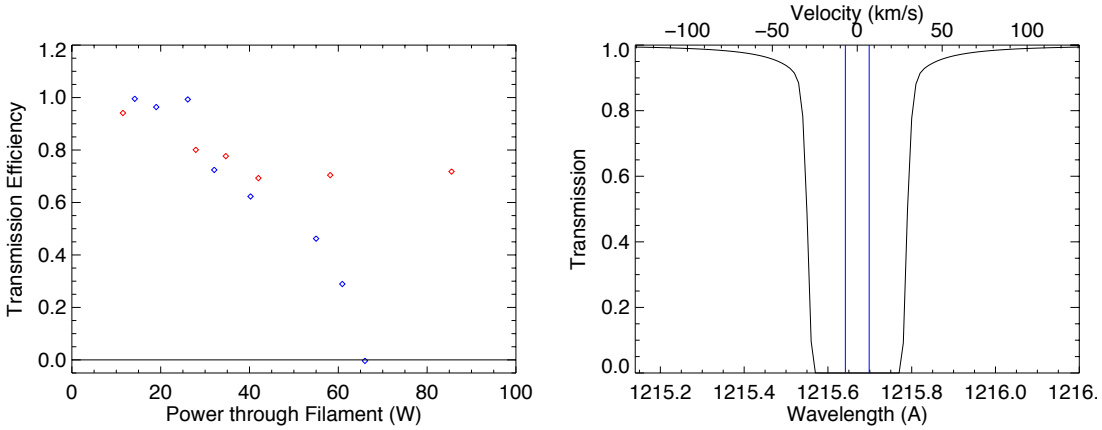

Figure 4.3: **Left:** Transmission efficiency of the hydrogen cell at 1 torr (red) and 3 torr (blue) of hydrogen. All incident light is Lyα at 1216 Å. **Right:** Hydrogen cell absorption profile in low earth orbit. Vertical lines correspond to ± 7 km s^{-1} Doppler shifts of the Lyα line.

was sufficiently high enough to completely absorb the incoming Lyα at $\sim$ 66 watts of filament power.

The absorption profile of a 3 torr hydrogen cell in low earth orbit (ie an orbital velocity of 7 km s^{-1} is shown in Figure 4.3 (Right), plotted against both wavelength and the corresponding Doppler velocity. Notably, much of the interplanetary Lyα, which has a brightness maximum of 700 rayleighs (112) and a Doppler velocity of $\sim$ 23 km s^{-}1 (113), will fall within the high absorption range of the cell.

4.4 Future Applications

Our simple proof-of-concept experiment verifies our ability to produce a hydrogen absorption cell using readily available laboratory equipment. Our challenge will be to produce a design simple enough and robust enough to withstand the rigors of the space flight environment where-in light weight and a low power consumption are highly desireable.

The hydrogen cell filter could be well-suited to a Schmidt-like camera type of telescope. This would allow a wide-field imaging observation of the sky while eliminating geocoronal Lyα saturation of the detectors. With the minimal number of reflections offered by a Schmidt camera, a high effective area would be possible when adding the additional MgF_2 or LiF windows on either end of the hydrogen cell; properties of these windows are shown in Figure 4.4 .

The manufacture of a hydrogen cell of this type would be relatively simple, with two separated windows mounted onto an aluminum support structure. It would only require a pump out vacuum feedthrough that could also be used for the hydrogen leak-in, a simple filament and its power inputs, and a small pressure gauge to monitor the amount of hydrogen gas inside. For a 50 cm diameter optic with a 25 cm central obscuration, an estimate for the structure of the Schmidt camera, a rough calculation of the effective area is possible, and shown in Figure 4.5.

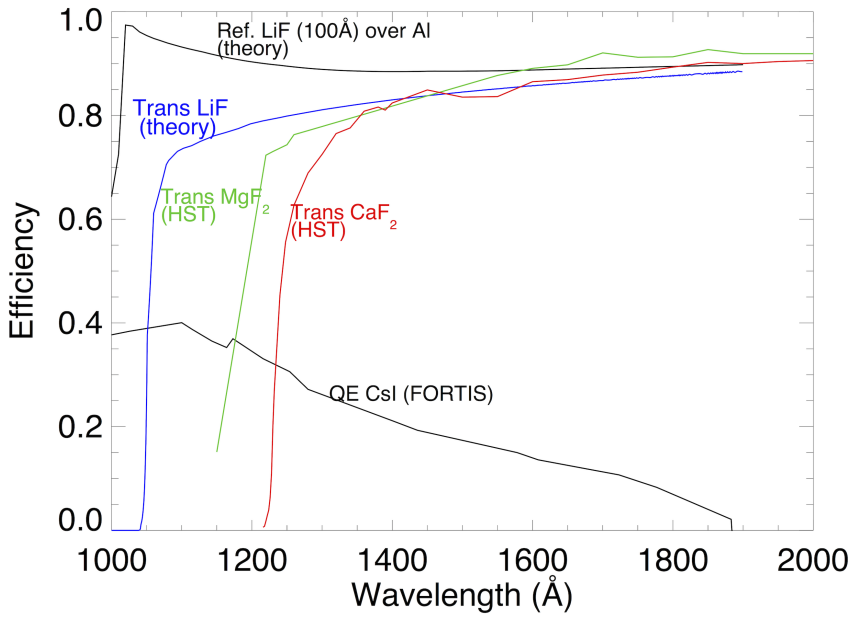

Figure 4.4: Transmission efficiencies of LiF (114), MgF_2, and CaF_2 windows, reflectance efficiency for LiF over Al mirror, and the quantum efficiency of a CsI photocathode detector.

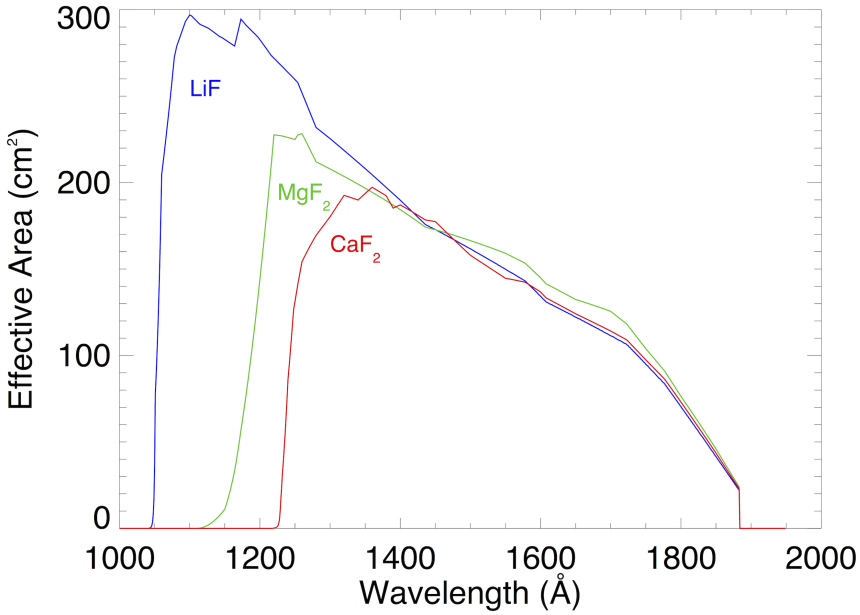

Figure 4.5: Effective area calculations for a theoretical imaging instrument with a 50 cm diameter mirror and a 25 cm central obscuration.

Chapter 5

FORTIS

The Far-Ultraviolet Off-Rowland Circle Telescope for Imaging and Spectroscopy (FORTIS) is a sounding rocket-borne ultraviolet imager and spectrograph developed and built in-house by the sounding rocket group at Johns Hopkins University (115; 116). It is a Gregorian telescope with an f/10 focal ratio at the secondary focus. As shown in Figure 5.1, the optical elements consist of an f/2 primary mirror, a microshutter array (MSA) at the prime focus, an f/5 triaxial elliptical secondary mirror with a diffraction grating holographically ruled on its service, an achromat lens in the zero-order imaging channel, and three microchannel plate detector channels. Due to low mirror reflectivities in the ultraviolet ($\sim$40%), the spectrometer design includes only two "bounces" in the optical path; minimizing the optical element count compared to more complicated optical designs allows for greatly increased sensitivity due to the limited efficiencies of these optical elements in the far-ultraviolet. The

grating ruled on the secondary mirror splits the beam into three distinct data channels, a zero-order imaging channel and two first-order (+1 and -1) spectral channels, which correspond to the three independent detectors at the final focus of the telescope. The focus of the telescope is tuned to minimize the astigmatism (resulting from the tri-axial ellipse secondary) in the spectral channels in order to maximize the signal-to-noise in the observed spectra. Because of the difference in path length between the zero-order reflection and the two diffracted spectral gratings, an extra lens is added for the imaging channel to account for the resulting astigmatism. This lens, a cylindrical CaF_2 and MgF_2 doublet, also serves as a wavelength filter to cut off flux at $\lambda \leq 1250$ Å. The two spectral data channels (termed -1 and +1) allow for redundant spectral coverage, as well as extending the (non-redundant part) wavelength range beyond that of what is provided by a single channel of the instrument by mapping wavelengths from a given spot in the sky to different areas on the microchannel plate (MCP) detectors. Finally, the microshutter array at the prime focus enables multi-object spectroscopy and on-the-fly optimization of the mask pattern on the sky. Table 5.1 shows an overview of the optical properties of the FORTIS telescope. The design of FORTIS gives it an effective area of about twice that of the *Hopkins Ultraviolet Telescope* (117) (HUT) with half the primary mirror diameter.

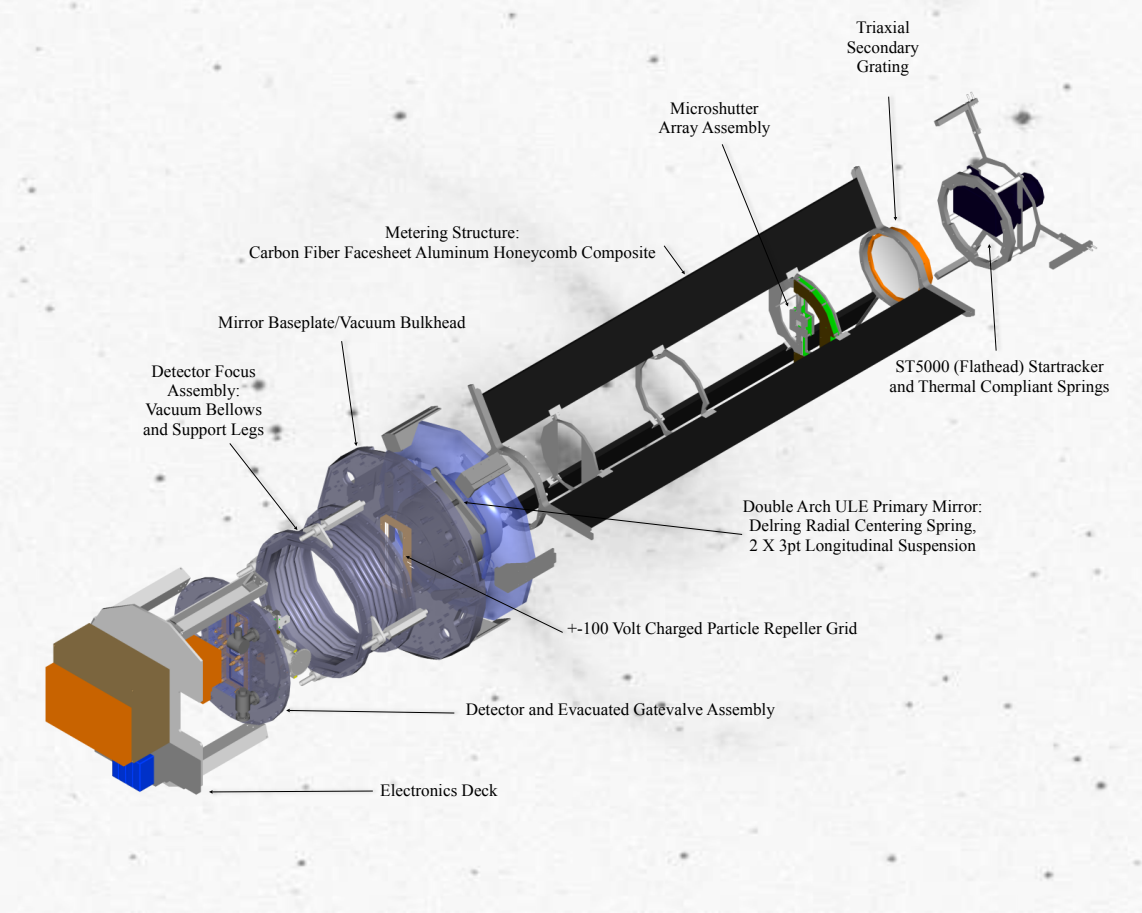

Figure 5.1: Exploded rendering of the FORTIS telescope.

Table 5.1: FORTIS Telescope Summary

Parameter	**Value**	**Parameter**	**Value**
Prime Focus Platescale	$206\farcs3$ mm^{-1}	Inverse Dispersion	20 Å mm^{-1}
Primary Diameter	500 mm	Field of View	$1800'' \times 1800''$
Primary Radius	2000 mm	Microshutters in FOV	43×86
Central Obscuration	219 mm	Single Shutter Area	$15\farcs9 \times 36\farcs9$
Secondary Diameter	165 mm	Telescope Clear Area	1600 cm^2
Secondary Radii xz, yz	520.83, 520.68 mm	Spectral Bandpass	900 – 1700 Å
Eccentricity xz, yz	2/3, 0.66679	Spectral Resolution	1500
Secondary Image Distance	1562.50 mm	Spatial Resolution	$1 - 4''$out to $\pm$ $450''$
Zero-order Platescale	$41\farcs25$ mm^{-1}	Detector Pixel	0.011 mm
System Focal Ratio	f/10	Detector Area	45 mm $\times$ 170mm
		Peak Effective Area	$\sim$ 45 cm^2

5.1 Primary Science Goals

The primary science goal of FORTIS is to observe bright UV emission in nearby galaxies in order to directly measure Lyα emission and quantify the relationship of Lyα escape (f_{esc} from UV-bright young stars to the local properties of the emitting area. The absorption and emission properties of the atomic hydrogen gas and dust in galactic environments around bright stars is not well-understood, and is an important parameter in star formation feedback and potentially a proxy for Lyman Continuum (LyC) emission. f_{esc} has important implications for galaxy formation processes and could inform investigations into important parameters in reionization by ionizing photons from bright star formation at high redshift. Far-UV emission from bright stars is generally scattered or absorbed by dust and neutral gas in the host galaxy before escaping into the intergalactic medium, making direct measurements of these spectra difficult. This is especially true of LyC photons, which have a very high

scattering cross-section off of neutral H I atoms. Lyα photons, on the other hand, are much more efficient at escaping the host galaxy due to resonant scattering off of the same H I, resulting in an flux of last scatter in Lyα off the galaxy. The Lyα cross-section drops sharply in the red line-wings as the photons Doppler shift (or in IGM, redshift) away from the rest-frame gas, and by this mechanism we observe Lyα escape. This process is strongly dependent on the local H I gas properties and dust presence, and the FORTIS instrument is uniquely suited to exploring this physics.

The multi-object capability of FORTIS enabled by the MSA allows for individual spectra of different regions of galaxies spanning the $200'' \times 100''$ pitch of each shutter, with the short edges of the shutters along the dispersion direction. The shutter arrays provide a unique flexible routine for an arbitrary pattern of apertures on a target, so each observation can be tailored to maximize scientific output for a given target. We require targets to be far-UV bright, redshifted just high enough to resolve their Lyα signals from the bright geocoronal Lyα emission; the FORTIS spectral resolution of $\frac{\lambda}{\Delta\lambda} \approx 377$ requires a redshift of at least $z \approx 0.003$. Finally, the target search is optimized for galaxies that have a large span across the sky to maximize the number of rows of the MSA that can be deployed to open in flight.

The flexibility of FORTIS enables secondary science applications, and the program is not limited by potential targets. Sounding-rocket borne observations of comets at JHU have a long history, and FORTIS is prepared for a target of opportunity, should a particular interesting comet appears in the sky, as happened for the second flight

of FORTIS in November 2013. Multi-object UV spectra are also of interest in the Magellanic Bridge, the Cygnus Loop, a nearby supernova remnant, and in globular clusters where the MSA could pick out individual stars. More discussion of these secondary science goals for the future is found in Section 5.6.4.

5.2 Optical Design

5.2.1 Primary Mirror

FORTIS has a 20cm diameter parabolic f/10 primary mirror with a 10cm diameter central hole. It was manufactured by *D.A. Loomis Custom Optics* for FORTIS in 2007, and has since been reshaped by *Rayleigh Optical* immediately preceding the third flight of the telescope (36.312 UG). The primary mirror was coated with SiC at NASA Goddard Space Flight Center (GSFC) in March 2012 for the first two flights of FORTIS, and following the reshape of the mirror was again coated with SiC at GSFC in September 2015. The SiC coating is fairly robust, and the lifetime (including the recoat) of the reflectivity of the primary mirror as a function of wavelength is shown in Figure 5.2.

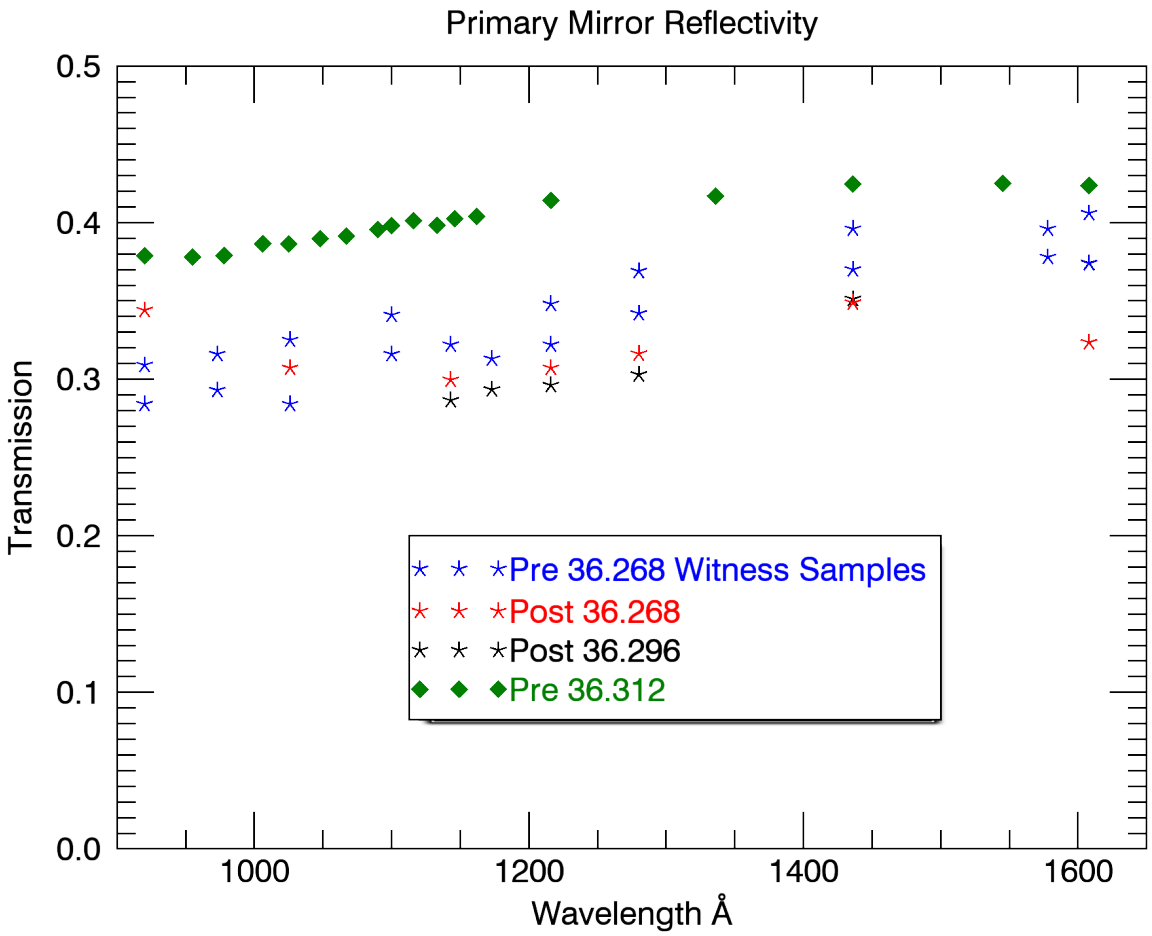

Figure 5.2: Primary mirror reflectivity (SiC coating), from before the maiden flight in mission 36.268 UG through measurements after a recoat preceding mission 36.312 UG.

5.2.2 Secondary Mirror and Grating

The tri-axial ellipse secondary mirror serves as both a focusing and diffractive element in the optical design. The tri-axial shape results in an inherent astigmatism at the focal plane, and we introduce a cylindrical CaF_2/MgF_2 doublet lens to account for this astigmatism in the zero-order channel, allowing for there to be a focus in all three data channels. This lens is also designed to absorb incoming photons at

$\lambda < 1250$ Å, so that the very strong geocoronal Lyα emission from ambient H I recombinations is rejected from the image of the target.

Two secondary mirror substrates were fabricated in 2010 and one was flown for the first two FORTIS missions; three more were manufactured in late 2014 for the third flight. The substrate of the 165 mm diameter f/5 mirror is a tri-axial ellipse, manufactured by *Precision Asphere*. Following shipment of the secondary and our own verification of focus quality (see Figures 5.3- 5.8), the gratings are holographically ruled with a grating by *Horiba Scientific*, with a square-edged ruling of varying depths determined by the desired peak wavelength efficiency in the first spectral order. and finally coated with platinum. The gratings were then brought to GSFC for coating with SiC to impart the ultraviolet reflectivity across the whole face of the grating. Combining the grating and mirror is especially suitable to the ultraviolet where reflective efficiency is low, so limiting the total number of "bounces" of each incident photon significantly increases the effective area of the instrument.

Ruling the grating on a focusing element demands extra care at the secondary focus, as the optical path length will be different for the zero order beam and for the first order diffracted beams, which will necessarily result in different focal planes for the zero order and the first order diffractive beams. Additionally, the tri-axial nature of the elliptical grating substrate introduces a fundamental astigmatism into the image in each order. The position of the detectors in the focal plane is carefully tuned such that the astigmatism in the cross-dispersion direction is minimized in the spectral-

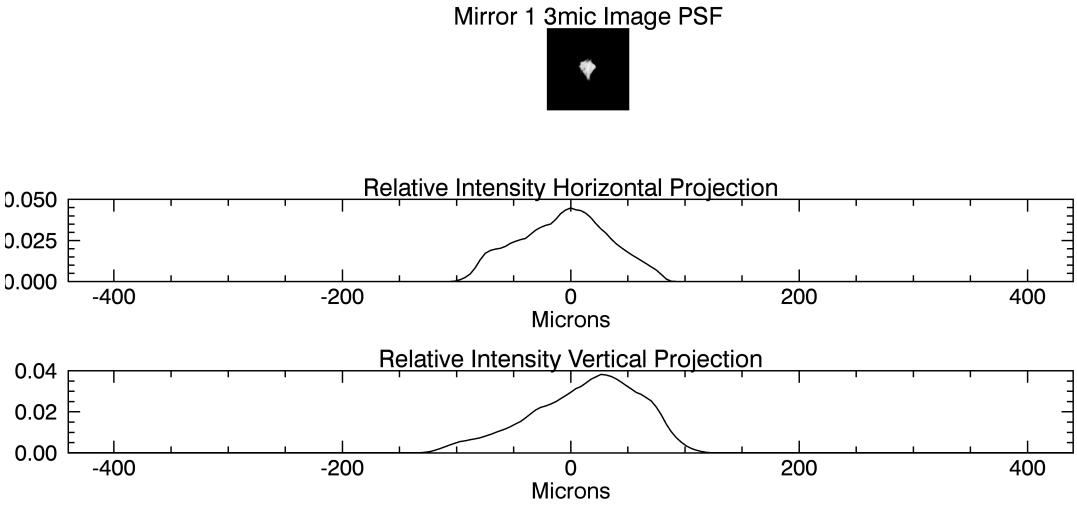

Figure 5.3: First secondary mirror substrate at focus, with a 3 micron pinhole source.

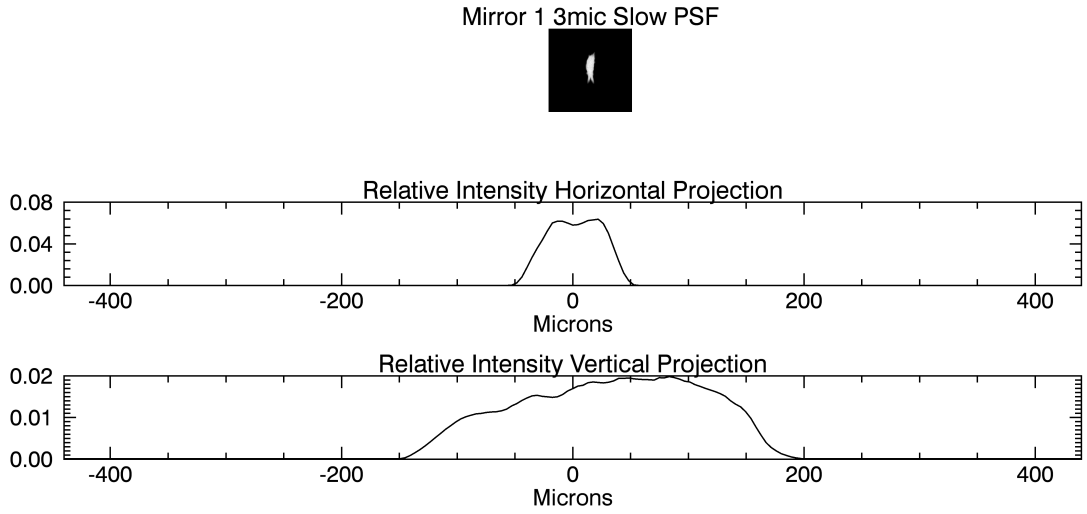

Figure 5.4: First secondary mirror substrate slightly slow of focus, with a 3 micron pinhole source.

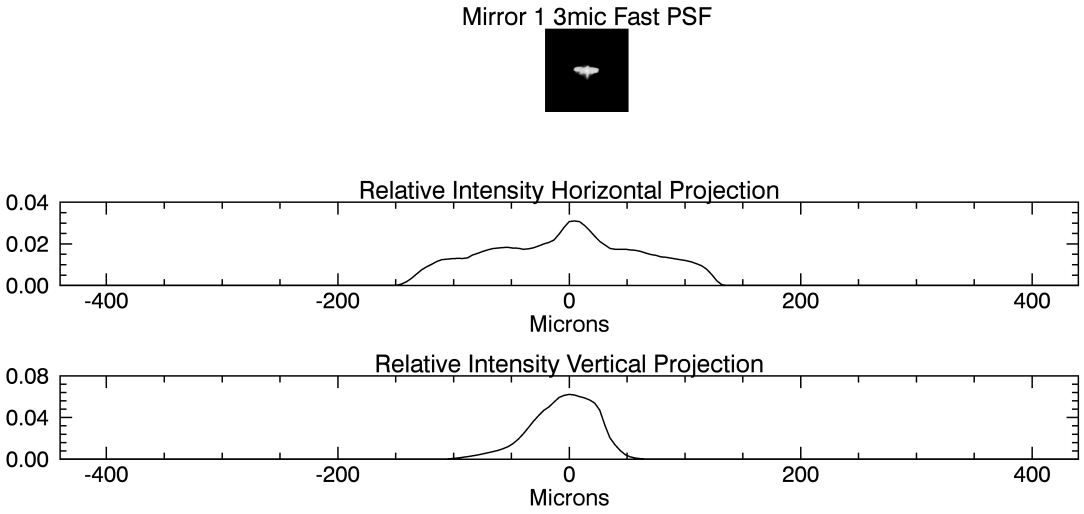

Figure 5.5: First secondary mirror substrate slightly fast of focus, with a 3 micron pinhole source.

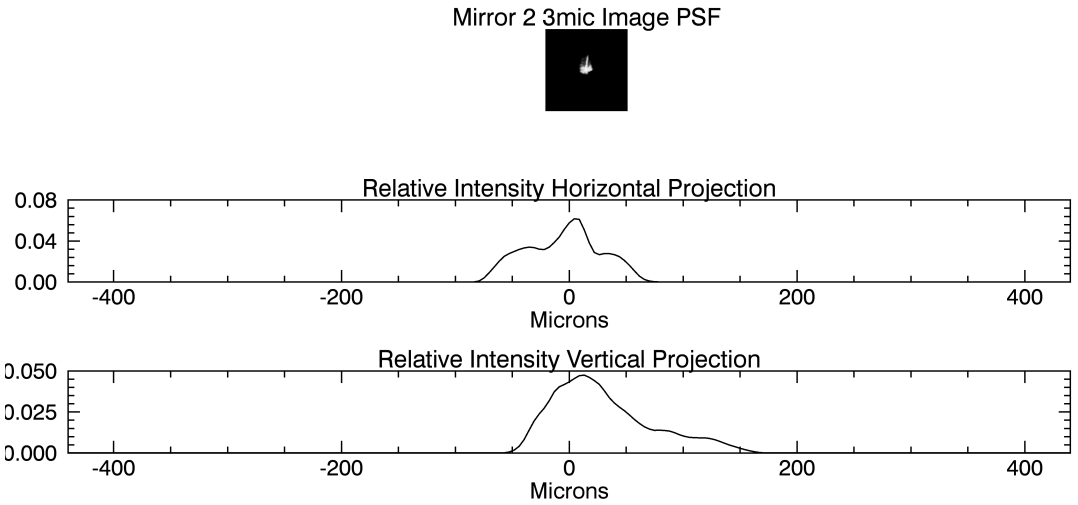

Figure 5.6: Second secondary mirror substrate at focus, with a 3 micron pinhole source.

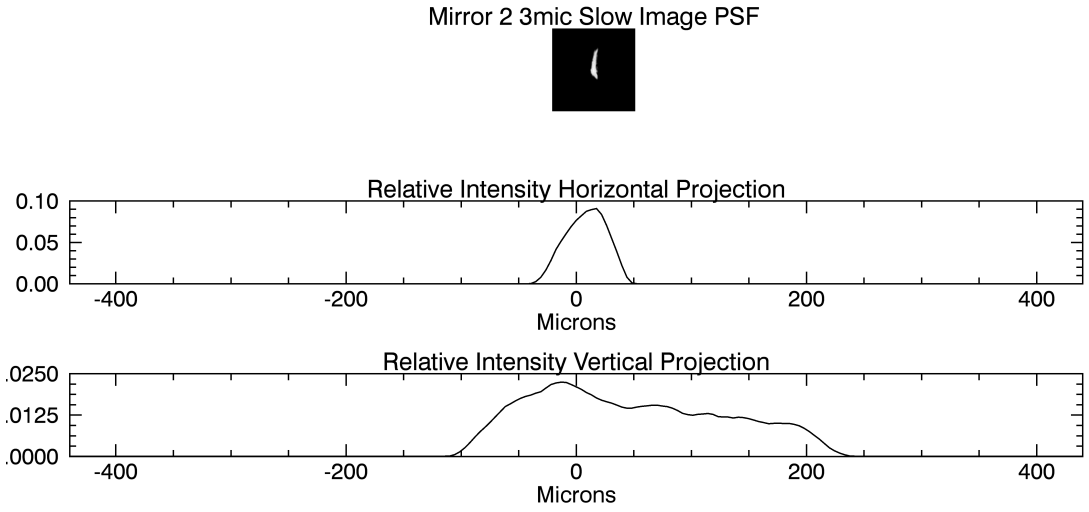

Figure 5.7: Second secondary mirror substrate slightly slow of focus, with a 3 micron pinhole source.

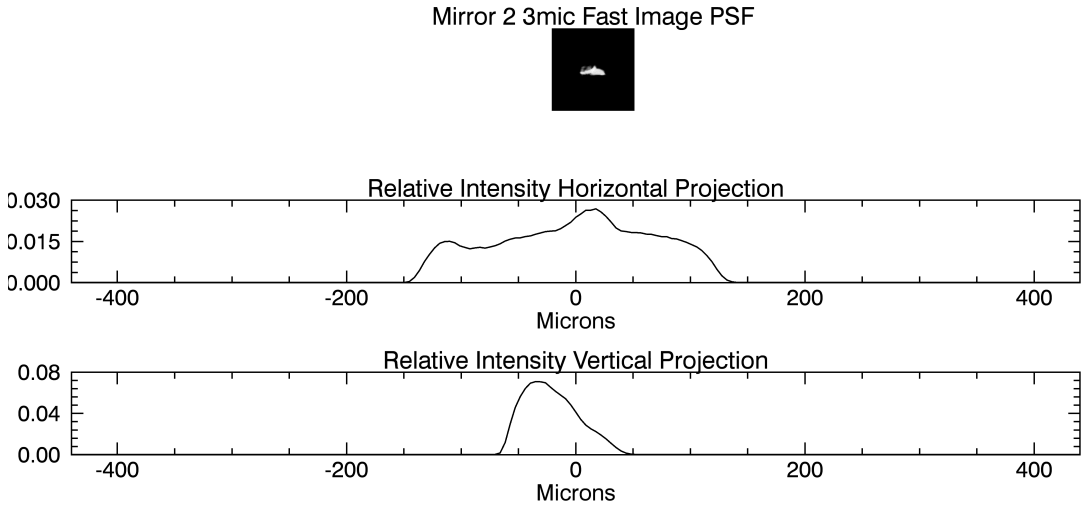

Figure 5.8: Second secondary mirror substrate slightly fast of focus, with a 3 micron pinhole source.

order channels, but this results in a relatively large cross-dispersion astigmatism in the zero-order imaging channel. To compensate for this effect, a cylindrical doublet lens (CaF_2 and MgF_2), shown in Figure 5.9, is mounted immediately in front of the zero-order MCP to focus the incoming beams down to a point and clean up the image of the sky. The effect of this lens on the secondary mirror image is shown in Figure 5.10. Importantly, the lens doubles as a filter to transmission of photons below $\sim$1220 Å in order to block geocoronal Lyα from illuminating the imaging detector. This geocoronal Lyα foreground is extremely bright (2-20 kilorayleighs (107)) and will drastically decrease the signal-to-noise of the image of the target, which is especially problematic for FORTIS given the automatic target acquisition on-the-fly. Because this achromat lens is only in place over the zero-order channel, allowing this geocoronal Lyα through to the spectral channels is acceptable if the rest-frame Lyα emission from the target is sufficiently redshifted away, so that the two emission lines can be resolved in the data. The throughput efficiency of the grating in the spectral orders is lower than that of just the SiC coating, as photons are distributed across all the possible diffraction orders, which further emphasizes the importance of the double-sided spectrograph in maximizing spectral data output. A sample of the measured efficiencies of the -1, 0, and +1 orders of the grating are shown in Figure 5.11.

Given nominal flight performance and recovery the reflectivities of the primary and secondary mirrors, as well as the transmission of the achromat lens, do not signifi-

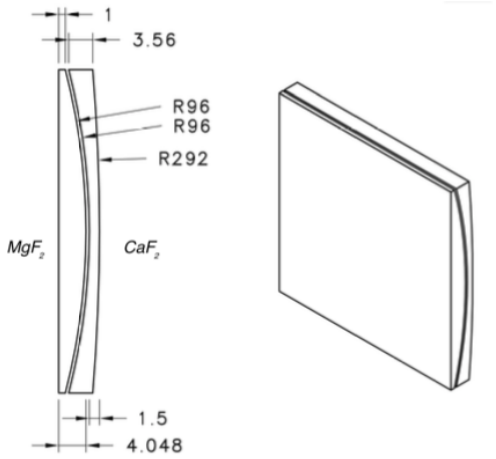

Figure 5.9: Achromat doublet lens that is placed immediately in front of the zero-order imaging detector. Measurements are listed in millimeters.

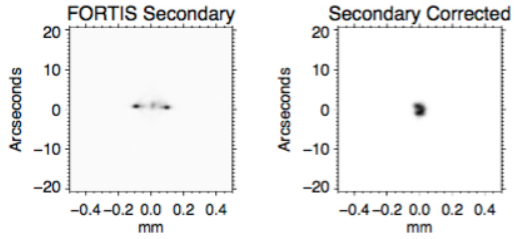

Figure 5.10: **Left:** Illumination of the FORTIS secondary mirror with a 5 μm pinhole. **Right:** The same pinhole and mirror, with the doublet lens to correct the astigmatism (118).

cantly degrade and do not generally require re-coats. The MCP detectors' photocathode, alternatively, is greatly affected by exposure to atmosphere (especially water), and does lose quantum efficiency over time, especially as testing and installation of the MCPs often demand short atmosphere exposure on the plates. These efficiencies will determine the effective area of the instrument, and depending on requirements of the mission the MCPs will be sent back to *Sensor Sciences* for reapplication of the

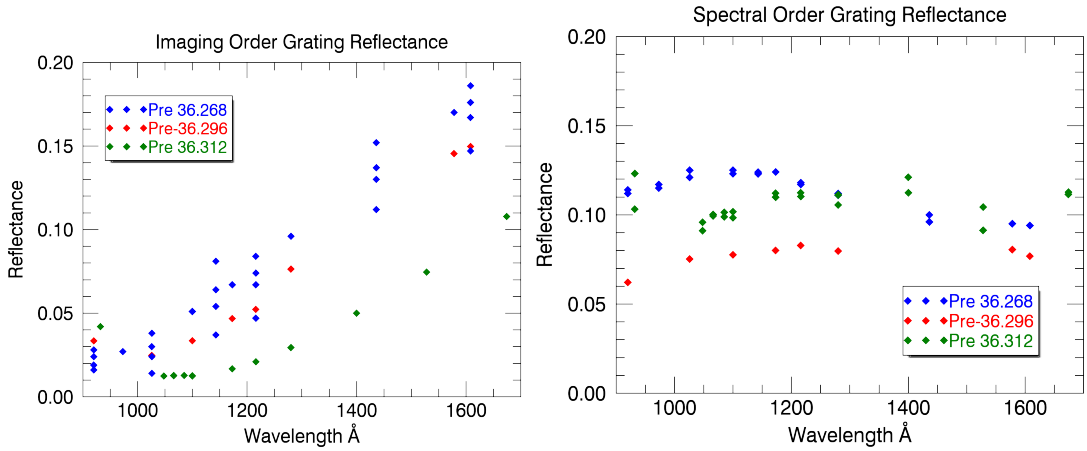

Figure 5.11: Efficiencies of each order of the FORTIS flight grating. Note that for the 36.312 UG mission a new grating was installed with deeper grooves, moving the peak first order efficiency to a longer wavelength.

photocathode.

5.3 Microchannel Plate Detectors

5.3.1 Detector Design and Operation

At the focal plane FORTIS has three cross delay line microchannel plate (MCP) detectors custom-designed and manufactured by Sensor Sciences LLC (119). The plates are coated in CsI photocathodes, which emits a small burst of electrons when an ultraviolet photon strikes them. These electron bursts are accelerated away from the front of the MCP and into the microchannel tubes by a negative voltage (∼-600 volts), and attracted toward the back of the detector by a high positive voltage (∼+3000 volts) at the rear. When the accelerated electrons strike the sides of the

channels, the burst is amplified and the total charge of the photon response increases down the channels. After emerging from the back of the channels, this electron burst collides with the grounded grid of cross delay lines. The resulting electronic pulse travels down each side of the delay line grid, and the time delay between the arrivals of that signal at each end of the plate is dependent on the x- and y-position of the electron burst incident on the grid. The total charge of the pulse is also measured, which we refer to as the pulse height of the photon count. This pulse height is a useful diagnostic for tuning detector parameters like the high voltage setting of each MCP. If the count rate of incident electron bursts on the grid is too fast, the timing data between events will be confused and data will be lost, but the readout rate of the timing signal is very fast, and rates of $\sim 10^6$ counts s^{-1} are manageable. This is significantly faster than expected count rates in operation, and well above the data processing speed further down the data pipeline. The physical characteristics of each of the three FORTIS MCP detectors is shown in Table 5.2.

Table 5.2: FORTIS MCP Characteristics

	-1 Order	**0 Order**	**+1 Order**
Size (mm)	62.5 × 42	42 × 42	62.5 × 42
x Pixel Size (μm)	10.85	13.07	10.39
y Pixel Size (μm)	7.55	13.93	7.55
x-Position Bits	13	12	13
y-Position Bits	13	12	13
Pulse Height Bits	4	6	4
High Voltage[a] (V)	4050	4100	4000

Once the signal from the electron bursts in read into the amplifiers and time-to-

amplitude converter at each side of the respective cross delay line grids, the signal from each detector is output in 30-bit digital signals to a custom multiplexor (MUX) developed by the Instrument Development Group (IDG) at JHU. The MUX restructures this data word into two separate 16-bit data words; one word for the y-position and another word immediately following it for the x-position. Since the spectral order has a larger active field of pixels, more bits are dedicated to describing the x- and y-positions in those two channels, sacrificing bits in the pulse height information. Each 16-bit word out put from the MUX dedicates 13 bits (12 bits in the imaging channel) to either the x- or y-position, and 2 bits (3 bits in the imaging channel) to the pulse height. The remaining bit is denoted as the control bit, and will alternate as the MUX outputs alternating x- and y-bits. This control bit is used to latch onto the data stream and consolidate the x- and y-words of a single count together, as well as serving as a useful diagnostic for the health of the data stream. These 16-bit words are fed into a FIFO for immediate readout.

In laboratory testing, the ground support equipment (GSE) supplies a clock signal to the FIFO, and reads out the data word by word. In flight, the telemetry subsystem sends the clock signal to the three data FIFOs and packages the data into a binary matrix to be sent via uplink to the ground in real time, allowing the payload team to monitor the incoming science data as it comes in. For the first launch of FORTIS (36.268 UG), the clock rate from telemetry was set to 125 kHz for each independent channel, which allows for a readout rate of 62.5k counts s^{-1}, as each count requires a

separate x and y data word. Following higher than expected count rates in all three channels but especially the spectral channels, the telemetry clock rate for subsequent flights was set to 250 kHz in the spectral channels. This required the addition of dedicated 10 Mbps links for each spectral data channel, and an additional 10 Mbps link for the zero-order imaging data as well as the rest of the payload's housekeeping and monitor data. This sets the maximum readable count rate out of the FIFOs to 125k counts s^{-1} of real-time data streaming in. At the ground, we read the three data streams into three independent National Instruments PCIe-6536 Digital I/O cards, and save the x- and y-positions of each photon, along with the time-tag and pulse height. The data is plotted into a real-time GUI showing the images from each detector along with plots of the pulse height distribution, collapsed x- and y-profiles, and displays of various statistics like the average and instantaneous count rates.

The data acquisition system will not have a linear response to the incoming count rate. This was measured (118) in a vacuum chamber by illuminating both the detectors and a reference EMR 542G photomultiplier tube, and tracking the relative change in the responses as a function of the intensity of the beam. Figure 5.12 demonstrates this relationship; there is a loss of $\sim$7% of the incoming counts at the maximum count rate (62,500 counts s^{-1}) allowed from telemetry. Following the second flight of FORTIS, 36.296 UG, a similar measurement was made using the flight telemetry system and tracking the resulting observed count rate as that saved onto telemetry's recorder, omitting the GSE that was a significant bottleneck in processing and displaying the

data. For this measurement a lamp mounted within the rocket skin emitted a beam through a pinhole into the detector assembly and photomultiplier tube. In order to cover the full dynamic range of count rates, three pinholes were used with overlapping effective count rate ranges that could be combined into a coherent view of the detector response over the whole range, shown in Figure 5.13. This is consistent with the nonlinearity found in the laboratory response, and is extended to show a dead-time correction of ∼17% loss at the maximum telemetry clock rate of 250 kHz (and thus 125,000 counts s^{-}1) in the spectral order detectors and FIFO readouts. The GSE on which the data is displayed is not capable of processing this maximum rate, and to account for the loss in GSE functionality at high count rates telemetry can clock the data FIFOs as fast as it can, but simply drop half of the counts before passing them on to the ground equipment at the bottom of the uplink. This allows for full diagnostic functionality in real-time data acquisition, and a subsequent recovery of the full set of science data after the flight from the telemetry system's data recorders, which automatically copy and save every digital word acquired from each independent FIFO.

5.4 Telescope Calibration

Calibration and evaluation of optical performance is carried out in the FORTIS lab at JHU. The use of a vacuum ultraviolet monochrometer with an active wavelength

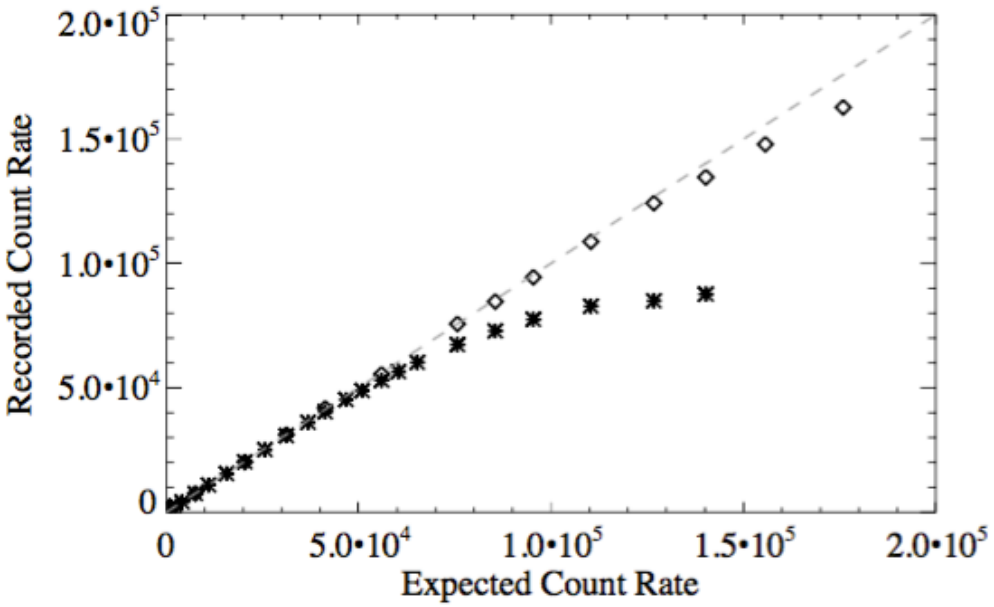

Figure 5.12: Real response of the detector and ground equipment as a function of incoming count rate, with the real-time data display is activated (stars) and when counts are just read and saved to disk without the corresponding GUI display (diamonds). The dashed line represents an ideal system with no counts lost due to down-time in the apparatus (118).

range from ∼1000 Å to ∼2500 Å is crucial for this testing, and the reflectivity, transmission, and quantum efficiency of the various optical elements is tested in the test chamber in Figure 5.14.

Before and after each launch of FORTIS a full calibration check of each optical element is performed in this test chamber, and the resulting reflection and transmission efficiencies for the pre-flight 36.312 UG mission can be seen in Figure 5.15. These can be combined into an effective area calculation, which is the fundamental unit that describes the sensitivity and expected photon flux from science targets; the pre-flight 36.312 UG effective area plot for the three data channels is shown in Figure 5.16.

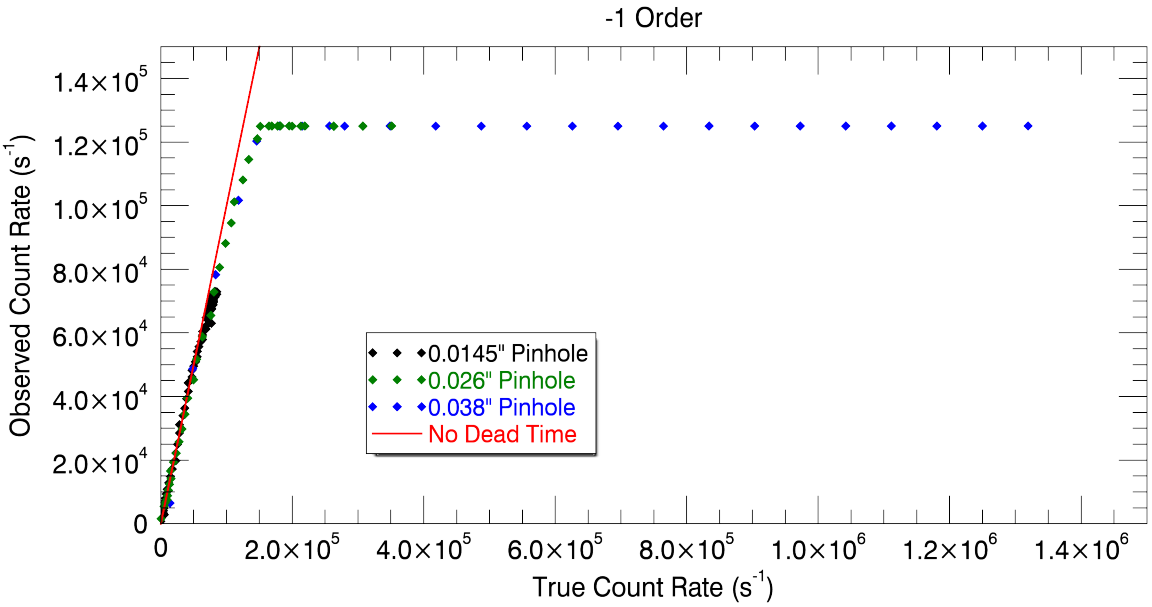

Figure 5.13: Detector readout and telemetry data word count (so double the incoming photon count rate) as a function of expected incident counts. Note that three separate pinholes on the emitting UV lamp were required to cover the full dynamic range of the system, with enough overlap to create a cohesive picture of the detector and telemetry response.

5.4.1 Detector Calibration

One of the critical calibrations necessary for FORTIS operation and data analysis is the quantum efficiency (QE) of the detectors. The QE is wavelength-dependent, and is given by the ratio of the observed photon count and the incident photon count:

$$QE(\lambda) = R_O \frac{(\lambda)}{R_I(\lambda)} \tag{5.1}$$

Measuring the MCP QEs requires the use of the Calibration and Test Equipment (CTE) at JHU, vacuum monochrometer with a large chamber in which optical elements can be mounted and tested against a reference photomultiplier tube, seen in

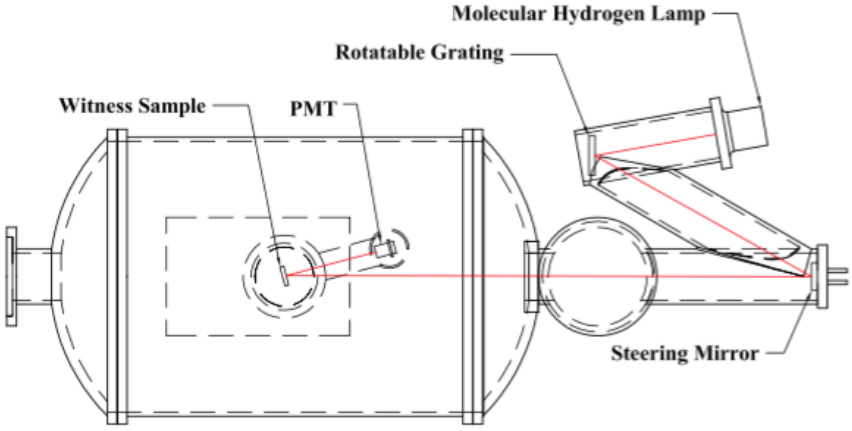

Figure 5.14: Schematic of the ultraviolet monochrometer and vacuum chamber for light sensitivity calibration and testing, in this example case a mirror witness sample. Hydrogen is leaked into the lamp chamber and excited to produce line emission, and the rotatable grating coupled with a small slit allowing entry into the rest of the assembly serves to isolate individual wavelengths for exposure on the sample. The labeled photomultiplier tube (PMT) is mounted on a moveable stage to intercept both the incident and reflected beam.

Figure 5.14. For the MCP QEs, the three MCPs are mounted on a flange at the rear of the CTE chamber, and a photomultiplier tube (generally a EMR 542G tube, which is active to wavelengths above ∼1050 Å) is placed on a swivel that can be externally moved in and out of the beam path. The photomultiplier outputs a current to a Keithley 6514 System Electrometer, and this current is calibrated to a NIST MgF_2-windowed Cs_2Te photodiode (Serial Number 682-3) for wavelengths longer than 1100 Å and to a NIST windowless Al_2O_3 photodiode (Serial Number 239) for wavelengths shorter than 1216 Å. The CsI photocathode on the detector faces have been found to significantly degrade over time and exposure to atmosphere, requiring periodic re-coats of the photocathode and careful handling of the detectors to keep them in

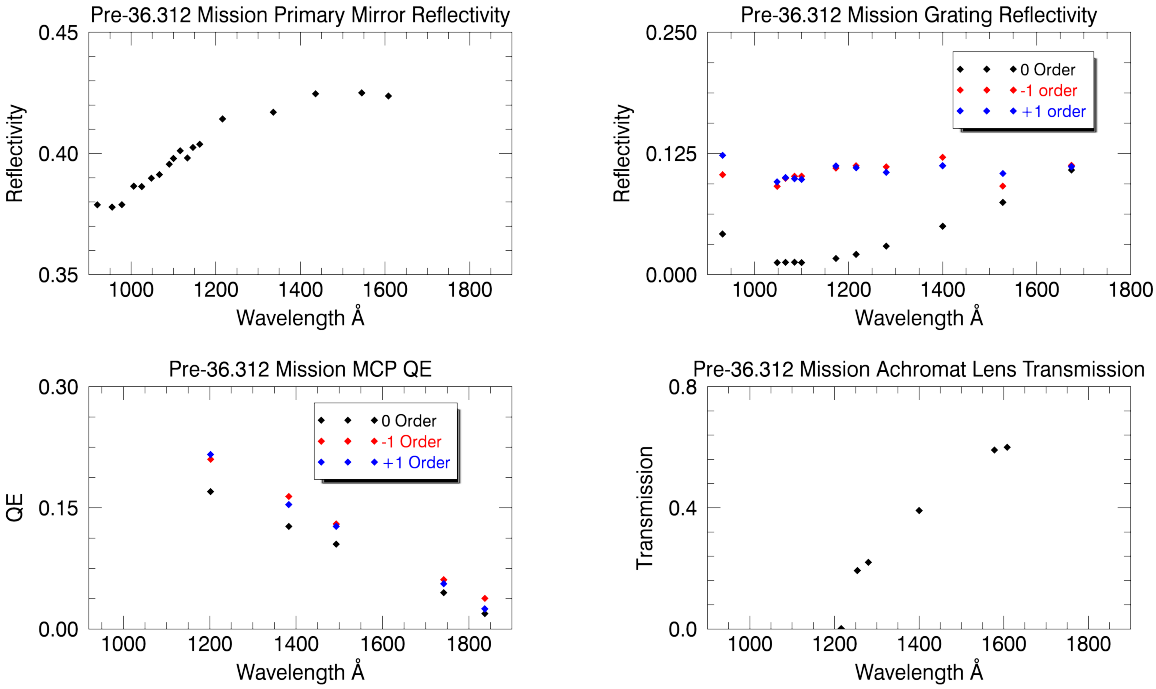

Figure 5.15: Sample of efficiency measurements of the FORTIS optical elements prior to its 36.312 UG mission.

vacuum as much as possible. Figure 5.17 shows the progression of MCP QE measurements over the detectors' lifetimes, with a new photocathode before the third FORTIS flight, 36.312 UG.

5.5 Microshutter Array

5.5.1 First Generation MSA

The microshutter arrays (MSAs) that enable the multi-object spectroscopy are cutting-edge technology developed by GSFC for use on the *Near-Infrared Spectrograph* (NIRSpec) aboard the *James Webb Space Telescope* (120; 121; 122). The MSA is new

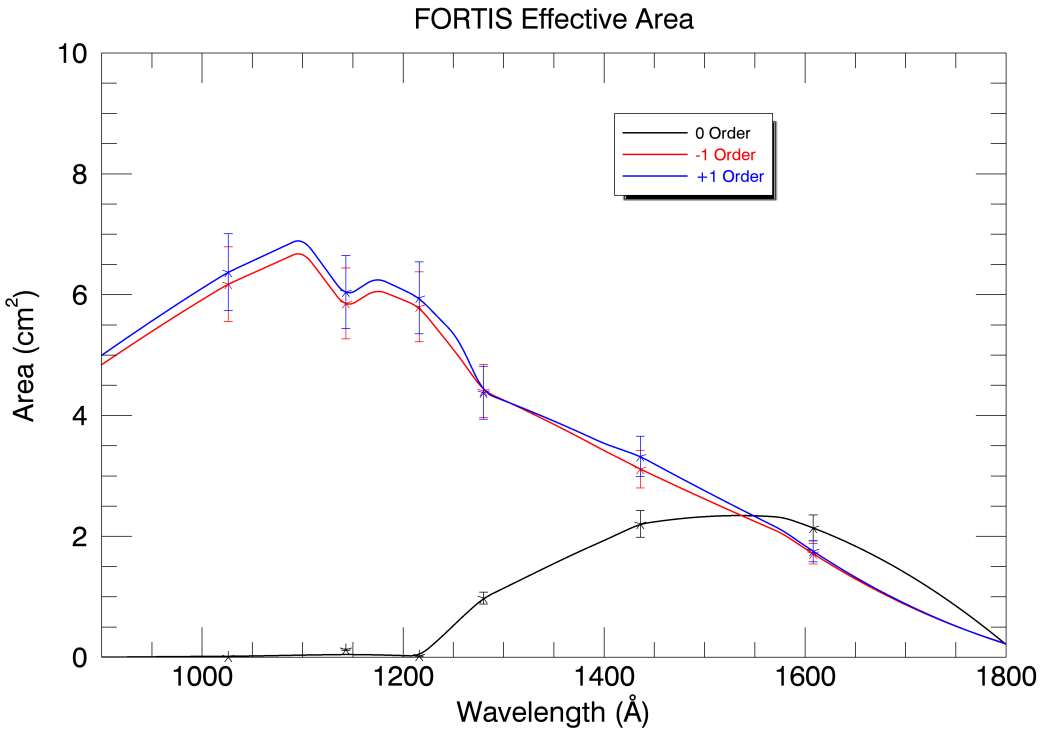

Figure 5.16: Sample of efficiency measurements of the FORTIS optical elements prior to its 36.312 UG mission.

technology; FORTIS is the first mission on which MSAs have flown and been used to observe scientific targets outside the laboratory. The array is a square with sides of roughly 1 cm, and is populated with 128 by 64 individual shutters to be externally opened and closed by the FORTIS flight computer. Each shutter, when opened, provides an aperture 100 μm by 200 μm. When closed, a silicon nitride shutter 0.5 μm thick attached to a torsion bar blocks this aperture, which is framed from the eggshell shutter carrier by a light shield. An open shutter fills a $15\farcs9 \times 36\farcs9$ rectangle in solid angle, with an open area ratio of 0.73. The first-generation MSA design has a thin coating of magnetic material on each shutter, in order to allow the shutters

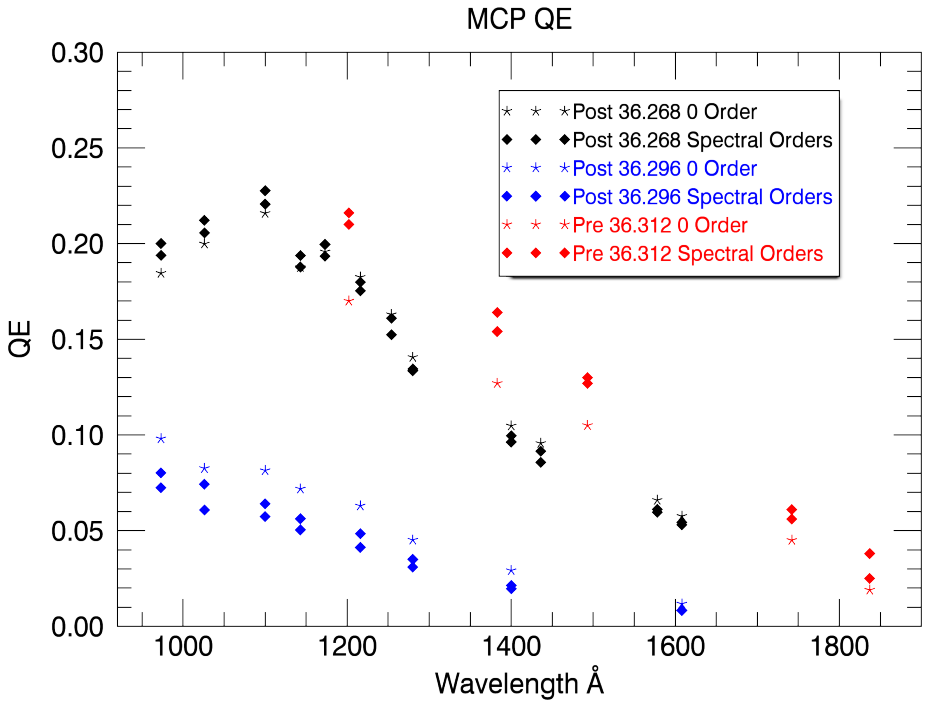

Figure 5.17: MCP detector QE measurements. The decrease in MCP response in the post-36.296 reflects degradation over time and exposure to atmosphere, demonstrating the need for regular photocathode reapplications.

to be partially opened or closed by a magnet scanning over them. Each shutter has electrodes deposited on its surface to allow for electrostatic latching when an opposite voltage is applied to the support structure of the array. As the magnet scans across the front face of the MSA, Supertex HV584 level shifters switch the voltage polarity on the grid in sync with the magnet motion according to whether a particular shutter is requested open or closed.

The MSA itself is mounted on a circuit board denoted the "Big-D" due to its shape as it fits into the prime-focus Θ-shaped structure, shown in Figure 5.18. Operation of the MSA is controlled by the flight computer, a *National Instruments* cRIO 9076

module, with an FPGA and four inserted cards for signal monitoring and control lines. Two of these cards are NI-9403 32 channel 7μs digital I/O cards, and two are NI-9401 8 channel 100ns TTL digital I/O cards.

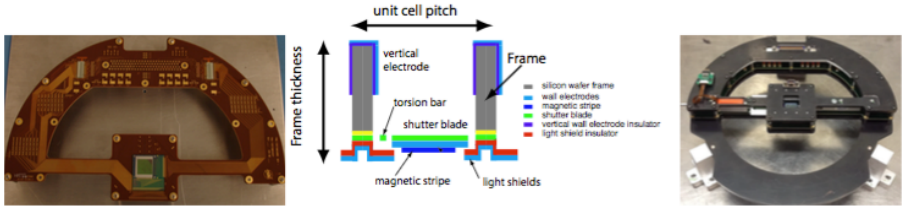

Figure 5.18: **Left:** Big-D circuit board with the microshutter array mounted near the bottom of the image. **Center:** Schematic of the unit cell of a microshutter. **Right:** The Big-D, MSA, and magnet mounted inside blackened aluminum support structure, ready to be placed at the prime focus of the FORTIS telescope.

The magnet motor assembly is unique to the FORTIS system, and was designed and assembled at JHU. A Faulhaber LM-0830 linear motor is mounted onto the "Big-Θ", with the MSA magnet mounted on a yoke on the drive rod. In the first iteration of the magnet assembly, utilized on the first two FORTIS flights, the location of the magnet was determined by two optical limit switches at either end of the linear drive. The MSA driver code monitored these limit switches to ensure that the magnet started and ended a given motor activation at the right locations, but otherwise did not take magnet position into account when addressing the area (more discussion of the drawbacks of this in section 5.5.5). The motor runs autonomously, responding to activation signals from the flight computer to start and stop, but is otherwise not externally controllable. Details of MSA operation are described in section 5.5.2.

The total MSA comprising 128 by 64 shutters overfills the sky image at the prime

focus, and the active science data area is given by roughly 88 by 43 shutters. The rows and columns outside this active area are "masked" out of any addressing pattern by never applying a latching voltage to them, and are hard-written into the flight software and not adjustable without recompiling and deploying the flight software. Occasionally (depending on the MSA used), the fine wire bonding of rows and columns to the Big-D can short each other or to ground, which drags down the voltage to the rest of the array enough to make addressing impossible. If this occurs, the same masking procedure of the shorted row or column will preserve the effectiveness of the MSA as a whole, at the expense of an always-closed row or column. Shutters themselves are also somewhat susceptible to damage from any foreign objects on the array, and a few stuck-open or stuck-closed shutters can be found on the flight arrays. Stuck-open shutters are more of a problem to science data due to the potential for spectral confusion of multiple open shutters in a given row (i.e. along the dispersion direction). The arrays selected for flight are those with minimal (≤ 2) stuck-open shutters. Manually plugging a small block of stuck-open shutters is possible, but not ideal. The fragility of the wire-bonding and of the shutters themselves demand very careful handling, and great care is taken to keep the MSA and Big-D as clean as possible at all times.

5.5.2 MSA Operation

The operation procedures for the MSA addressing was based on the NIRSpec system, but a significant amount of customization was required for functioning FORTIS arrays. The MSA and "Big-D" is sensitive to small changes in voltage settings, so it is necessary to do careful testing and adjust voltage and timing parameters for a given MSA in the payload.

The MSA generally functions in one of two states, "Latched" or "Addressed," with the corresponding magnet position on either side of the array. A latched array is entirely open (excepting the masked rows and columns), while an addressed array has a designed pattern of open and closed shutters (again with the same mask of closed rows and columns). When transitioning from addressed to latched, the magnet is first given the signal to move across the array, while the row (back electrodes) and column (front electrodes on the shutters) rails are set to a low holding voltage ($V_L \approx 24$ V). The magnet serves to partially open the shutters as it passes over, and electrostatic attraction from the bias voltage between the shutter and the side of the frame snaps the shutters fully open. After the magnet reaches the other side ("Latched"), the column rail is set to a high latching voltage ($V_H \approx 30$ V) and the row rail is set to 0 V. This hold voltage is high enough to keep the open shutters open for as long as required, but the shutters will quickly revert to closed if the voltage on the row rail is dropped to zero. When addressing a pattern, this row voltage is first removed in order to allow charge to bleed off the MSA before the synchronized addressing. The

signal for motion is sent to the magnet motor and it will begin to travel across the face of the array, parallel with the rows. The cascading voltage signal therefore is synchronized to follow the magnet column by column from one side to the other. For each active column in the cascade, individual shutters are selected to be opened by activating the latching voltage ($\pm V_H$) in the appropriate row. When the addressing cascade has finished traversing all columns of the array, the lower holding voltage is applied to the column and row electrodes to hold the array constant.

Prior to the third FORTIS launch on mission 36.312 UG, steps were taken to account for environmental effects causing timing errors in the sync between the motion of the magnet and the address cascade on the array itself. The success of an address was very susceptible to timing errors (see Figures 5.19- 5.20, and required a significant rewrite of the flight software in both the real-time and FPGA operation of the cRIO. In the first iteration of MSA operation, the magnet motor was given the move command, and timing parameters for the synchronous address (time per column address, offset from magnet initialization command) were set in the lab prior to launch. With the encoder, the FPGA could track the position of the magnet in real-time and verify that the MSA was performing the per-column address procedure in sync with the magnet. The motor operation was sometimes inconsistent in lab conditions, and ensuring a successful sync was a significant improvement in MSA operation. The limit switches on the magnet slide were replaced by a motor encoder tracking the position of the magnet as it moves across the extent of its dynamic range. The

encoder has a resolution of 5 μm, which is more than suitable for tracking its position relative to shutters that are 100 μm wide. The encoder functions by reading a linear glass slide with fringes etched into its surface, and outputting three TTL data signals as it traverses. There are two sensors (A and B) that both read the fringes, but are out-of-phase by half a fringe ($\frac{\pi}{2}$). This creates a four-state system, with a unique sequence between the four states for travel in each direction over the fringes, and $\Delta x = \pm 5 \mu m$ for each complete sequence. The new system resulted in an addressing procedure more resilient to environmental effects on the motor operation.

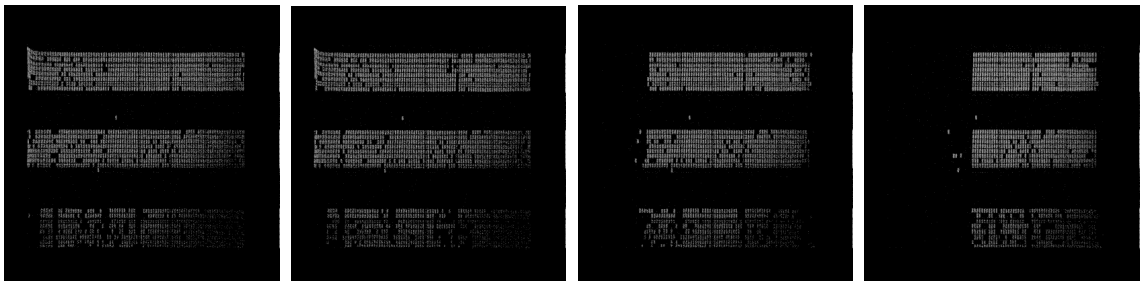

Figure 5.19: Attempted MSA addresses of three horizontal bars, while progressively delaying the magnet scanning from its ideal start time. As the magnet is delayed by 200, 400, and 600 ms the address pattern is wiped out and fewer desired open shutters are actuated.

5.5.3 MSA Address Strategy

This free operation of the MSA, in principle (before accounting for individual failed open and failed closed shutters) allows an arbitrary pattern of open shutters in the primary focus. This is what enables FORTIS's multi-object spectroscopy, as the array overlays multiple small apertures on the sky. In practice, FORTIS primarily

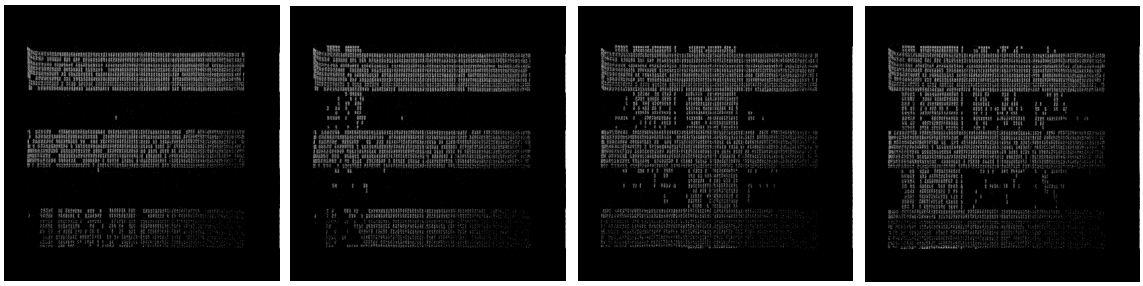

Figure 5.20: Attempted MSA addresses of three horizontal bars, while progressively advancing the magnet scanning earlier from its ideal start time. As the magnet is started early by 200, 640, and 1040 ms the address pattern is wiped out and fewer desired open shutters are actuated.

uses the Zero Order Microshutter Interface (ZOMI) for acquiring individual objects in the 0.5° field of view. Generally, the first step in the FORTIS science observation procedure is to open all the shutters of the array and acquire a zero order image of the sky. During this initial imaging of the sky, the spectral detectors will not be powered, as the geocoronal Lyα flux is high enough to swamp the count reading software and fill the FIFOs. The achromat lens that cuts off ¿99% of the incoming flux below ∼1200 Å prevents this geocoronal Lyα from overwhelming the imaging channel in a fully open MSA configuration. The imaging order counts are recorded in the flight computer (as well as transmitted to ground via TM). Once an image of the sky through the open array has been compiled, the ZOMI command is sent to the payload through command uplink. This command instructs the flight computer to map each recorded photon count to the shutter in the array that covers the portion of the sky it covers, and build a histogram counting photons in each shutter. From this histogram, the brightest shutter in each row (along the spectral dispersion direction)

is selected. Once this image is complete, similar to the example shown in Figure 5.21, the magnet scans across the MSA and addresses the resulting one-open-shutter-per-row pattern. Following a completed address, the spectral order detectors are powered on and begin collecting science data. The geocoronal Lyα background will still be very bright in the spectral orders, but as almost all of the shutters (all but 64 at most) are closed, the count rate is low enough to prevent the software from locking up.

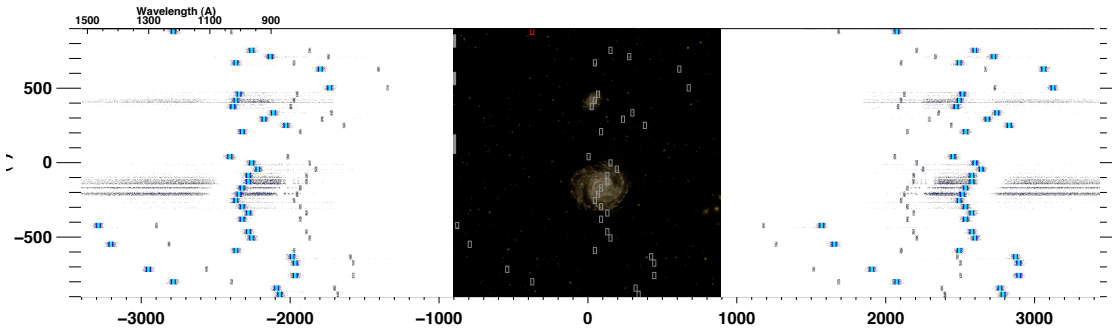

Figure 5.21: Simulated science data of MSA address pattern on the nearby galaxy M61 using the ZOMI routine.

This MSA target acquisition routine provides a flexible, reliable way to achieve multi-object spectroscopy on an arbitrary distribution of targets in the 0.5° field of view. It eliminates the need for fine ACS targeting, as the MSA address pattern can move to accommodate small errors (order of arcminutes, well above the precision achievable by the ACS system) in the expected targeting. Furthermore, the ZOMI routine can be modified to better suit the expected science data depending on the source. For the second launch of FORTIS on mission 36.296 UG to observe the comet

ISON, the ZOMI would capture the bright center of the comet in the correct shutter, but the rest of the rows would be non-optimally free to open on whichever shutter was brightest. With the comet in the field of view there would only be a single point source for the MSA to center up on (the center of the comet), and the rest of the target field would be the continuous cloud of emission around it. Since the ZOMI is intended to pick out individual point sources in a larger object it would not be ideal for this target. For this reason, the K system was developed. The K system preserves the first half of the ZOMI, searching for the brightest shutter in the active field (required to be near the center, assuming minimal errors in ACS pointing), and sets that shutter as the center of the comet. The rest of the MSA is addressed to a K pattern centered on that brightest shutter. A column of shutters opens intersecting that central shutter with alternating open and closed rows. In rows with a closed shutter in that central column, a shutter opens to the side along two diagonal rays upward and downward from that central shutter. This can be seen in practice in Figure 5.22. This pattern is designed to acquire a spectrum of the bright center of the comet, as well as sample the spectral signature of the comet in a range of angular distances from its center both parallel and not parallel to the direction of the tail.

If the individual emission lines targeted for observation can be identified, the MSA can even utilized in a configuration with multiple open shutters per row. The proposed Cygnus Loop observation would make use of this, as the emission line spectrum is expected to be dominated by a few bright lines, and with proper spacing of open

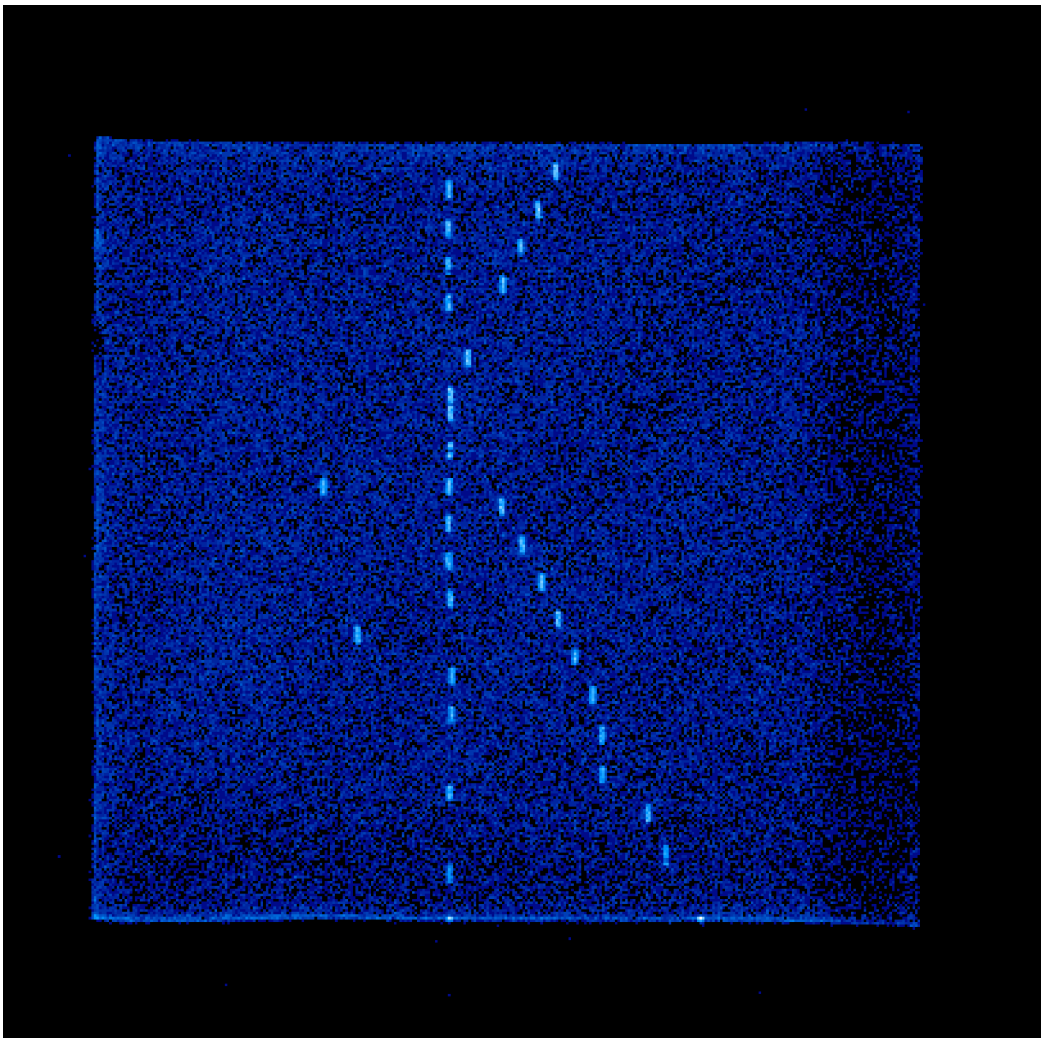

Figure 5.22: Sample of a K pattern addressed on the MSA. The red circle indicates the "center" of the comet, found automatically by the flight computer by selecting the shutter with the most counts during the image acquisition phase of the observation, and the rest of the K pattern is built on top of that. Note that in order to accommodate the masked columns in this array, described here by the red rectangle, the shutters in the lines of the K pattern that intersect the masked area are brought in toward the center. This is to maximize science counts, as shutters called to be opened in a masked column will necessarily never actuate, and moving the call to an active area of the array allows for an open shutter in that row. This array has a few stuck open shutters on the left half, as well as a few failed closed shutters in the address.

individual shutters confusion between shutters on the same row can be avoided. The observation would center on the edge of the Cygnus Loop, a ∼600 pc middle-age supernova remnant. FORTIS is sensitive in the spectral range where expected high-ionization emission will occur, especially at O VIλ1034, Lyα, and C IV λ1549. A simulated example of such an MSA configuration and the resulting spectra (scaled from *Hopkins Ultraviolet Spectrograph* (HUT) Cygnus Loop spectra) is shown in Figure 5.23. This observation is planned for the Next-Generation FORTIS instrument in a future launch.

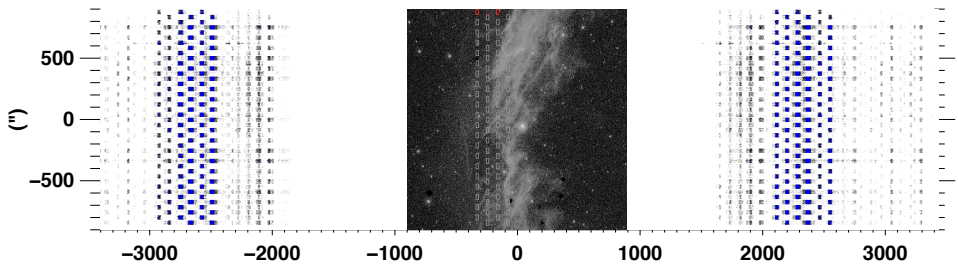

Figure 5.23: Simulated science data of MSA address pattern on the Cygnus Loop edge using a predetermined MSA configuration to maximize spectral counts, to open as many shutters as possible without confusing emission line features from two shutters on the same row. The spectrum for each open shutter is an archival HUT spectrum of the Cygnus Loop scaled to the GALEX NUV flux of a given pixel.

5.5.4 MSA Performance

The MSA shutters and the corresponding wire-bonded Big-D board are difficult to manufacture and vulnerable to environmental damage. The total functionality of different MSAs can vary between ∼65%-90%, as shorts in the bonding between the

substrate, and the Big-D must be masked out of operation and remain closed. A latched (given the "all-open" command) MSA is shown in Figure 5.24, with several masked columns remaining closed. A corresponding address pattern of two open columns in the middle of the MSA is also shown in Figure 5.24. Voltage parameters are set to minimize the number of stuck-open shutters rather than stuck-closed shutters, as spectral confusion from two open shutters in a row is more damaging to the FORTIS science goals than a small percentage (<10%) of missing sky coverage is.

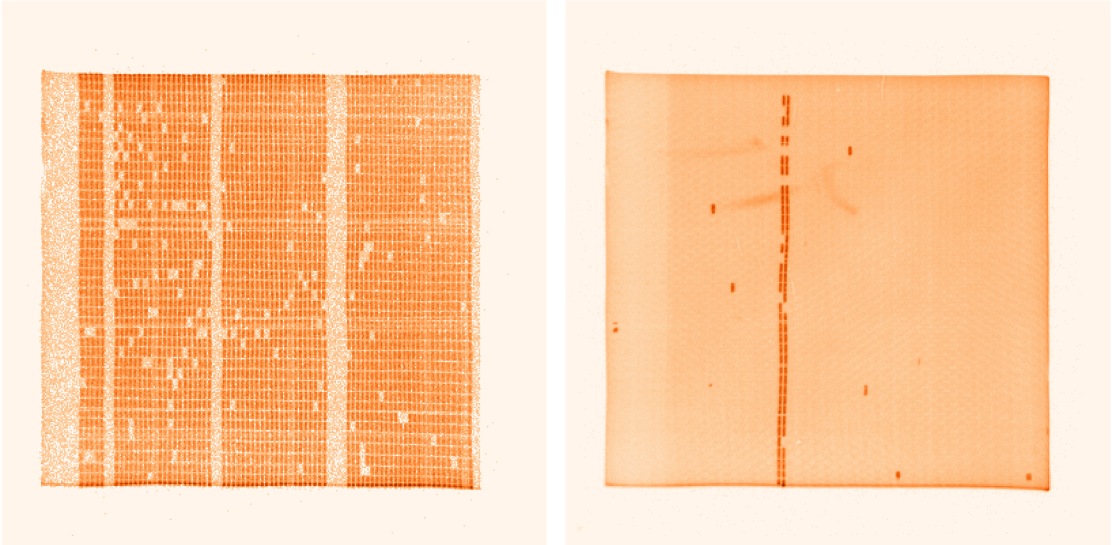

Figure 5.24: **Left:** Example of an MSA latch (all-open) prior to the 36.296 UG launch. The masked columns are given no latching voltage due to current leaks that drag down the whole array if enabled. Not all of the remaining shutters are open, but ¿90% of the non-masked array is sufficient for science purposes. **Right:** A corresponding address of two open columns near the center of the array. The few open shutters are clear, but the vast majority of the rest array is closed.

5.5.5 Next Generation MSA

In testing and flight, the scanning magnet used to actuate the shutters first generation MSAs proved to be a significant source of risk. This biggest issue outside of considerable required maintenance of the motor assembly was the vulnerability of the MSA addressing effectiveness to slight variations on input parameters (see Figures 5.19- 5.20). The array addressing routine needs to be carefully synched with the scanning of the magnet. Extreme environmental conditions like vibration and lack of gravity - effects that are unavoidable in a suborbital space flight - can throw off the smooth and timely movement of the magnet, and damage array addressing by a large margin. In 2015 GSFC began development of the Next Generation Microshutter Array (NGMSA), which eliminates the scanning magnet from the whole assembly, and actuates microshutters by charging the front electrode of the array with a fast, high voltage pulse, which will open the shutter enough to be electrostatically held open by a steady voltage on the back electrode. This was enabled by technological innovations in the torsion bar thickness and in the atomic layer aluminum deposition, which greatly reduced the necessary electrostatic forces needed to pulse open the array. The NGMSA holds several advantages over the first-generation model, most importantly in eliminating the requirement of the scanning magnet. The new system should also result in much faster address speed, with more reliable addressing in extreme environment. Additionally, the pulsed actuation regime does not open every shutter with every address attempt, unlike with the scanning magnet where a

full actuation was required for each shutter (even the closed ones) for a given address pattern. This greatly increases the working lifetime of the array as a whole, as even though the shutters have proven to be very robust to repeated actuation, they do have a finite expected lifetime of successful actuations.

Initial development of NGMSA samples, including operation of a laboratory testbed with functioning pulsed actuation arrays, is currently underway at GSFC. The FORTIS team works very closely with the GSFC NGMSA engineers, and a complementary lab testbed is under production at JHU. Work has been done to adapt the Big-D circuit board concept to the mostly-new driver and chip requirements for the NGMSA, and GSFC has begun production of a Big-Θ board that fits cleanly in the FORTIS telescope structure. The next flight of the FORTIS instrument will make use of the NGMSA following integration of the required hardware and development of the necessary software changes in the flight computer and ground equipment.

5.6 FORTIS Mission Targets

FORTIS galaxy targets are selected for bright UV emission in nearby galaxies, mainly using archival near-UV and far-UV images from the *Galaxy Evolution Explorer* (GalEx). We demand that target galaxies have a high enough redshift to shift rest-frame spectral emission lines sufficiently so that they are not confused with geocoronal lines, most importantly hydrogen Lyman-α. There is a very bright Lyman-α envelope

around the Earth, even at night, due to resonant scattering of photons off hydrogen atoms. This foreground easily washes out any Lyman-α of interest from the target unless it is redshifted sufficiently longward to resolve that particular emission. The FORTIS spectral resolution of $\frac{\lambda}{\Delta\lambda} \approx 377$ demands a minimum redshift of $z \approx 0.003$.

Potential targets for flight mission observation were selected from the NGC galaxy catalog. The selection criterion of at least an angular size of $\geq$ 4' along one axis was demanded in order to maximize the number of available microshutters and thus individual spectra accessible to observation at one time. Due to the relatively low redshift, high brightness, and large angular size on the sky, the target search is not limited by selection effects. Finally, it was required that any potential target would be observable from White Sands Missile Range (WSMR), which functionally limited the search to the northern sky. Given alternative launch locations (such as a proposed plan to collaborate with the Australian government for launch sites), the southern sky holds a number of galaxy targets suitable for this program. Once target candidates are found, FUV GALEX images of them are examined for UV-bright sub-regions suitable for MSA selection, which will generally be individual bright star-forming regions within the spiral structure, as well as occasionally galactic companions within the FORTIS field of view. Objects with more bright sub-regions are preferentially selected for FORTIS missions to maximize the multi-object utility of the MSA.

Using the GALEX NUV and FUV images of the selected targets, an estimated power-law spectral index β can be estimated and used to construct FORTIS spectra

models for each pixel in the GALEX images. Thus simulated science data in all three FORTIS channels can be constructed for a given target, sampled to the FORTIS resolution and expected effective area. One example of this simulation is shown for the first flight target M61 in Figure 5.25.

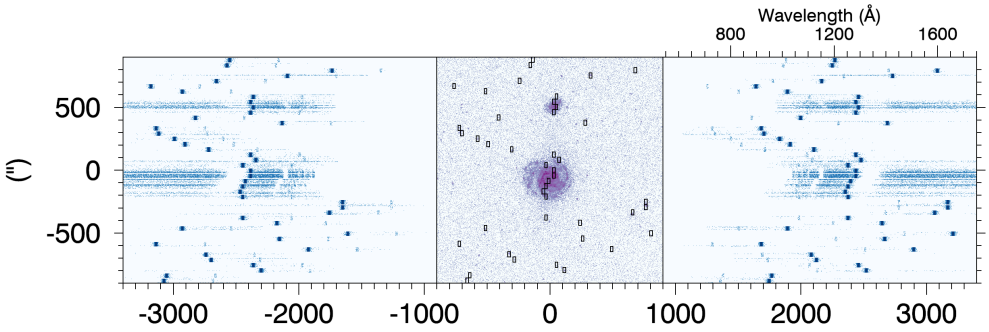

Figure 5.25: Simulated science data of ZOMI address pattern on the galaxy M61. The synthetic spectra are created assuming a raw power law fit to GALEX FUV/NUV fluxes per pixel, along with a Lyα brightness scaled to flux at $\sim$1500 Å (47). This emission is then attenuated by theoretical H I and H_2 absorption from column densities given by the Bohlin (77) gas-to-dust approximation, assuming an intrinsic stellar spectrum power-law index of $\beta = -2.5$ to calculate the dust content.

5.6.1 Mission 36.268 UG

FORTIS was first flown at 22:15 MDT on May 8, 2013, observing the star-forming galaxy M61, a barred spiral galaxy in the Virgo cluster. The vehicle was a Terrier first-stage booster and a Bristol Aerospace Black Brant IX second-stage sustainer. This mission was the maiden flight of FORTIS, and M61 was the first target selected in the program to measure Lyα escape from UV-bright star-forming galaxies as it relates to the local gas and dust properties at emission.

M61 was selected because of its large size on the sky (roughly 6' by 7') and its orientation with respect to Earth, allowing for observation on its face rather than on the edge. It has multiple smaller knots of evident star-formation within its greater structure (123; 124; 125), which is ideal for the MSA's acquisition routine. The redshift of this galaxy is 0.005224, enough to shift the Lyα emission by $\sim$6 Å, which is well outside the minimum resolving separation of a filled FORTIS microshutter. It also has a blue companion, NGC 4301, a smaller but still UV-bright spiral galaxy about 9' from M61 in the sky, within the half-degree FORTIS field of view. The recent history of supernovae in M61 (seven in the past 100 years (126)) indicates a population of young hot stars, which are very bright emitters of Lyα and LyC photons. The relatively high density of neutral H I in galaxies similar to M61 will prevent direct observation of Lyα emission from the bright stars, but resonant scattering of Lyα photons can serve as an escape mechanism into the empty IGM, which FORTIS will be able to directly measure.

The galaxy companion NGC 4301 also provides a unique opportunity for maximal science data on this mission. The roll angle of the telescope during flight is set such that M61 and NGC 4301 are aligned vertically in the MSA, and the ZOMI targeting routine can address open shutters across the face of both objects. Given the MSA configuration in the FORTIS data simulation in Figure 5.25, the GALEX FUV flux in the brightest shutter on M61 is 1.6×10^{-13} erg cm^{-2} s^{-1}. The estimated resulting count rate in that shutter is 13.31 s^{-1} in the zero-order image, significantly higher

than the dark rate of 0.003 s^{-1}.

5.6.1.1 Launch Preparation

Prior to the first launch of FORTIS, the instrument was tested to numerous environmental and systems requirements to confirm launch readiness. The majority of this testing took place at *Wallops Flight Facility* (WFF), where the rest of the NASA and *Orbital Sciences* team operates. The scientific payload constructed at JHU interfaces directly with the telemetry (TM) section of the rest of the payload, and ensuring that the two systems were operating smoothly together is crucial for functional operation of the mission. Once the data and monitoring interface is complete, mechanical testing begins.

Prior to buildup of the whole payload, the FORTIS team did vibrational testing on the telescope containing a dummy primary mirror mass model, as well as separately on the MSA assembly Each of these individual components survived the vibration, with one mounting screw on the MSA mounting plate in the telescope section shaking loose during a z-axis vibe (along the thrust axis). The fragile nature of the MSA as well as its lack of space-flight heritage made it especially important to verify that vibrational requirements could be met by the instrument design. The MSA assembly, including the Big-D board with wire bonding and the motor magnet, passed this initial vibrational test with no resulting problems.

Full integration of FORTIS with the rest of the payload systems took place in

August 2012 with no major concerns. Prior to launch, however, additional vibration test of the fully assembled payload is required, especially for an instrument's first flight. The FORTIS team checks the functionality of the detectors after each individual vibration run, and detector voltage monitors were outside nominal range in the middle of the test. This required a teardown of the payload, and a loose screw within the detector resulted in a short circuit from the anode to chassis, increasing the high voltage to the plates 600V above intended. The detector needed to be sent back to the manufacturer to be repaired, and insulation was added to prevent the short from occurring in the future.

Upon return of the detector and verification that FORTIS was once again functional, the environmental testing at WFF continued. On the second attempt of vibrational testing, vacuum in the detector housing was lost mid-vibration. It was determined that a seal broke on a pump-out port, and additional mechanical supports were added to lessen the load during acceleration. This repair was completed at WFF and FORTIS was once again prepared to move forward with flight certification. Following the z-axis vibration, anomalies in the MSA monitor signals were measured from the payload, and upon deconstruction of the instrument for inspection it was found that the MSA assembly had been significantly damaged. The connection between the magnet motor drive shaft and the magnet yoke was severed, and the drive shaft was freely moving. As this occurred during vibration, this shaft bounced rapidly around the area immediately above the MSA itself and the wire bonding, resulting

in near-total destruction of the MSA (see Figure 5.26). There was a backup MSA (with a slightly smaller active area of shutters) ready for installation, and following a parameters optimization and recalibration of optical alignment of the MSA with the rest of telescope, FORTIS was ready to proceed. Following another buildup, the fourth set of vibration tests were passed in January 2013. After finalizing the moment of inertia measurements, bending properties, and mass balancing, the FORTIS payload was ready for shipment to the launch facility.

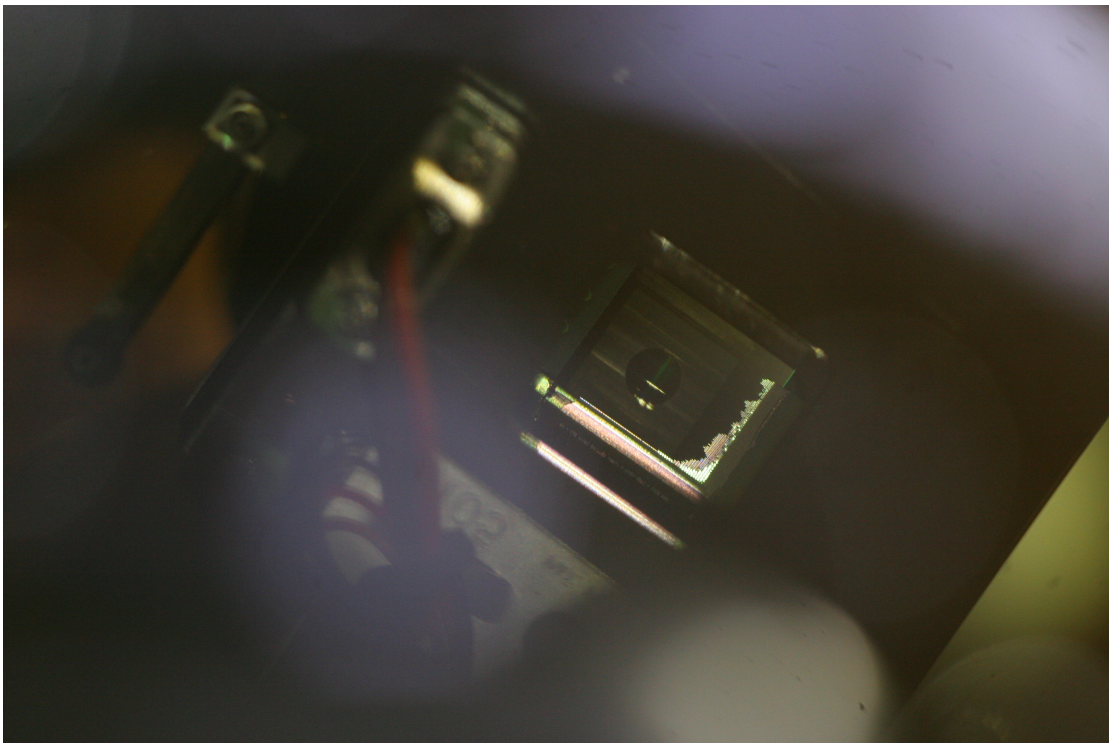

Figure 5.26: Remnants of the first flight microshutter array for mission 36.268 UG. All of the MSA that remains is the jagged edge of metallic shutters around the bottom edge of the square array, with the rest of the substrate and shutters themselves distributed throughout the telescope section.

5.6.1.2 Mission Flight

The FORTIS team started flight preparation at WSMR on April 21, 2013 and stayed through recovery of the payload on May 11, 2013. Once the NASA and JHU teams are together at WSMR, final integration and testing takes place over the few weeks before the scheduled launch. Sequence tests are performed, where all mission timers and uplinks for each flight system are executed in time with a simulated countdown, both when the payload is evacuated and at atmosphere. Sequence tests are required before and after final vibration testing and co-alignment of the telescope with the ACS pointing system. Following all passed tests and final mass property measurement, the FORTIS payload was integrated with launch motors on May 5 2013. Final tests verify signaling between the launchpad and groundstation, including actuation of all commands possible in the launch configuration. As the telescope section of the payload is not passively evacuated on flight, a vacuum pump assembly specially designed to fit within the launcher structure was designed at JHU, and actively pumping on the payload until roughly an hour before launch.

System performance of the flight on May 10 was nominal. When the ground uplink system was enabled to send commands, the MSA was given the signal to be addressed with a two-shutter wide slit in the middle of the array, denoted as the "Plan B'.' Once the instrument was aimed on the target by the ACS pointing, the high voltage in all three detector channels was activated. The zero-order imaging detector measured $\sim$11,000 counts s^{-1}, and the spectral order channels were immediately swamped with

an incident count rate well exceeding the internal limits of 62,500 counts s^{-1} per channel, shown in Figure 5.27.

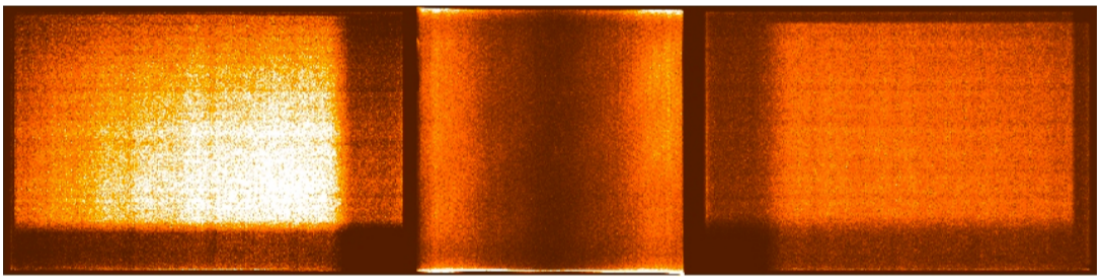

Figure 5.27: Raw flight data of all three channels of FORTIS from the 36.268 UG mission. There is no discernable structure in any channel, as any sky image is overwhelmed by background. The zero-order image shows a clear profile along the dispersion direction, with the count rate increasing away from the center of the detector plate. The spectral order images show confusion between x- and y-positions, resulting in two rectangles of data overlapping in a symmetric pattern. This x-y confusion is due to control-bit flipping, which occurs when counts come in too fast for the avionics to read out of the buffer in time.

The MSA was actuated to all-open with no apparent change to the data, and the background overwhelmed any possible signal over the course of the flight. A 3' pitch movement command was sent with two minutes of science time remaining in order to verify the existence of any acquired sky objects in post-flight data analysis.

5.6.1.3 Mission Recovery

The FORTIS payload including all subsystems landed roughly 80km downrange of launch, and recovery began at daylight following the descent, about 6:00 AM May 11 2013. The payload descended on parachute and touched down on a porous aluminum crush bumper, designed to absorb the energy of the impact by crumpling under the

weight of the payload on its initial landing. This crush bumper is affixed to the shutter door on the end of the telescope. The shutter door, provided by NASA, is a vacuum-sealed door on the aft end of the payload, and opens once the motors have finished burning and separated from the rest of the vehicle. The door stays open through the flight until an altitude of ∼100 km, then closes as reentry procedures begin, leaving the telescope under vacuum as it touches down. When FORTIS landed on the crush bumper in May 10, the shutter door shattered on impact, precipitating an implosion into the payload. This sucked about 300 pounds of desert sand into the telescope and caused significant damage to some of the optical elements (Figure 5.28).

Upon visual inspection of the MSA, which lies at the prime focus and so ∼3 feet from the shutter door, it appeared to have survived the implosion. However it is likely with all the debris in the previously evacuated section that a significant amount of the individual shutters or wire bonding were damaged. Regardless, by the time the payload was transported back to the Vehicle Assembly Building and cleared of most of the debris, the array was visually destroyed beyond repair (Figure 5.29).

After a comprehensive review of the landing, it was determined by a NASA Anomaly Investigation Board that the shutter array was manufactured from a more brittle type of aluminum than was specified in its design. Tests to the hardness and toughness of the shutter door pieces were significantly lower than that of 6061 aluminum, the material specified to be used in the shutter door construction. The source of the error in manufacture was not determined, but outside of two other shutter doors

Figure 5.28: Photos from recovery the morning following the launch of FORTIS on mission 36.268 UG. The shutter door with the crush bumper attached is collapsed inward into the telescope, and the mounting of the ST5000 startracker and FORTIS secondary mirror/grating near the door is destroyed. The grating is shown fully removed from its mount in the bottom-left image, with sand fully covering its face.

made at the same time as the 36.268 UG broken one, all existing shutter doors were re-tested and verified to be compliant with the hardness requirements of flight.

5.6.1.4 Mission Data

The images in the three science detectors were dominated by a scattered light background. The telemetry (TM) recorded counts at the maximum count rate possible for the spectral channels (62.5 kHz), with the ground science equipment receiving and recording about 58 kHz of those data. This is expected, as the ground equipment

Figure 5.29: Photo of the 36.268 UG flight MSA after recovery.

drops ∼10% of the datastream from TM when fully saturated. The zero-order channel was not fully saturated, but did read at a much higher-than-expected rate of up to ∼14 kHz. This indicates a very strong background of Lyα in all three detectors; the achromat lens (¡1% transmission to Lyα) in the Optical path of the imaging channel was enough to attenuate the signal below the saturation rate. Comparing the pulse height measurements of the data taken in the spectral orders with those in optimal observation conditions in the lab, the estimated maximum count rate in each spectral detector was 1.4-3.6 counts^{-1} s^{-1} pixel^{-1} (Figure 5.30), which corresponds to a total count rate of ∼7.3 million counts s^{-1} in each order (118). Assuming that the source of this scatter is geocoronal Lyα light finding a path into the detector plates, the low transmission of the achromat on the zero-order channel indicates a count rate of

2.2 million counts s^{-1} there. This is drastically higher than can be handled by the avionics, and completely overwhelmed any science data. A re-design of the telescope to reject off-axis geocoronal Lyα was necessary.

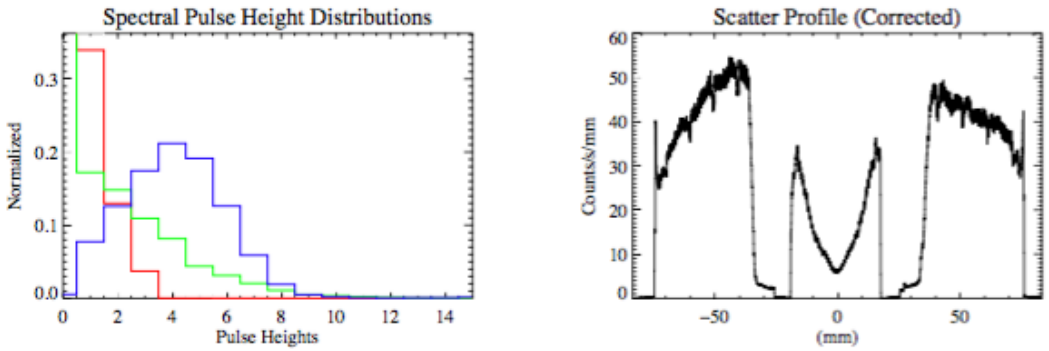

Figure 5.30: **Left:** Pulse height distributions of the -1 channel on 36.268 UG (green), a lab source at 1.4 counts s^{-1} $pixel^{-1}$ (red), and a lab source nominal below-saturation rates (blue). **Right:** Estimated incident photons on the three channels on the 36.268 UG mission as a function of distance from the center of the plates on the dispersion direction. Note that the active area for each channel is 42mm long across the dispersion direction (118).

5.6.2 Mission 36.296 UG

While FORTIS was specifically designed to search for Lyα emission from nearby galaxies, a multi-object far-UV spectrometer has applications beyond that narrow focus. The JHU sounding rocket program has a long heritage of UV comet observations (127; 128; 129; 130; 131) by sounding rocket-borne instruments at lower solar elongation than possible by orbital instruments like HST. The Oort Cloud comet C/2012 S1 (denoted as C/ISON), appeared on a sun-grazing orbit in 2012. This comet was dynamically new, meaning that it had not ever traveled to the inner solar

system before, much less barely scraped by the edge of the sun. This makes it especially interesting as a target for spectroscopy, as volatile elements and compounds would be very active as the comet got warmer and warmer, having not been burned off in previous orbital passes near the sun. The FORTIS far-UV bandpass between 800 and 2000 Åis well suited to measuring productions rates of CO, H, C, C^+, O, and S, as well as finding traces of previously undetected species like Ar, N, N^+, N_2, and O^{5+}. These chemical signatures are will trace the origins of Oort cloud comets, especially with respect to their composition relative to the proto-planetary source of gas a dust that formed the solar system.

FORTIS is uniquely suited to far-UV observation of comet spectra due to it tolerance with respect to pointing relative to the sun. HST, the only other current far-UV observatory, is limited to targets greater than 50° away from the sun on the sky, while FORTIS can observe targets down to 25° solar elongation. As the comet approaches the sun the brightness monotonically increases and more volatile species are produced, so the ideal observation would occur as close to the sun as possible. C/ISON crossed the 50° barrier on November 1 2013, but only reached 25° elongation on November 21, 2013, during which time it has proceeded from 1 AU to 0.421 AU away from the sun. This approach to the sun significantly increased water and other chemical production on the comet, demonstrating the value in observation by FORTIS near November 21, 2013.

5.6.2.1 Flight Preparation

After recovery of FORTIS after mission 36.268 UG there was significant work to be done on the components. The grating had been buried under desert sand, and had two large chips carved out of its surface in the implosion. The flight MSA was destroyed, but the Big-D mount and motor assembly was undamaged. The ST5000 Startracker can be replaced by NASA, but its mounting was destroyed and would need to be rebuilt. Following cleaning the primary mirror was found to have lost <10% reflectivity (Figure 5.2), qualifying it for launch. The mounting design for the ST5000 was left unchanged, and the JHU machine shop manufactured the replacement parts. GSFC replaced the MSA and Big-D board, and the activeness evaluation and optical alignment was completed in the summer of 2013. The grating was carefully cleaned, taking care to try to clear out the grooves of any leftover debris from the implosion. After reflectivity measurements, it was found to have only lost a third to a half of its spectral efficiency, still preferable to the backup grating in storage. While this did result in a fairly significant drop in effective area, the expected brightness of the comet target made this less of a concern than it would be for a galaxy observation. The expected count rate was high enough to require an upgrade to telemetry systems, setting aside dedicated 10 Mbps TM modules for each spectral data channel at 250 kHz sampling rate. The payload monitor and command lines were consolidated with the zero-order imaging channel data, which has room due to the much lower expected count rate through the Lyα achromat filter. After these changes, the maximum

theoretical count rate in the spectral orders in 125 kHz.

To address the dominant scattered light background seen in the 36.268 UG observation, new light baffles to replace the heat shield lining the rocket skin were designed and manufactured. These baffles prevent low-angle reflection by slightly off-axis light striking the inner surface of the skin and bouncing directly into the detectors. Thin blades of low-UV reflectivity delrin (roughened to further prevent reflections) are layered at a $\sim$1 cm spacing, such that any UV photons will be forced into multiple bounces and be scattered away. The new baffle system, repair of the secondary/ST5000 mount, new MSA functionality, optics calibration, and general certification for launch was completed between recovery of the first FORTIS flight in May 2013 and shipment to WSMR for 36.296 UG in October 2013. Environmental testing and coalignment with ACS was completed with no complications.

5.6.2.2 Launch Windows and Strategy

Following mission 36.268 UG FORTIS required improvements and repairs, with a short turnaround after the previous launch. Unlike most astronomical sources, C/ISON had a window for interesting measurement, and the launch date was set for November 19 2013, with backup dates on November 20 and November 21. The close proximity of the sun on the sky to the target is of special concern to UV instruments, as the H I envelope around the Earth lights up extremely brightly (up to $\sim$20 kraylegh) is resonantly scatter Lyα emission when fueled by solar photons. To combat this, the

flight plan used the Earth to occult the sunlight. This was achieved by launching ∼20 minutes before the sun rose in the morning, and catching comet C/ISON as it rose in the East just before dawn, shown in Figure 5.31. This flight plan requires careful planning, as the delays of five minutes to a few hours that are generally allowed on launch countdowns would not be possible. The roll angle of the telescope pointing was also set such that the open shutter door would occult any remaining sunlight or geocoronal Lyα from the horizon.

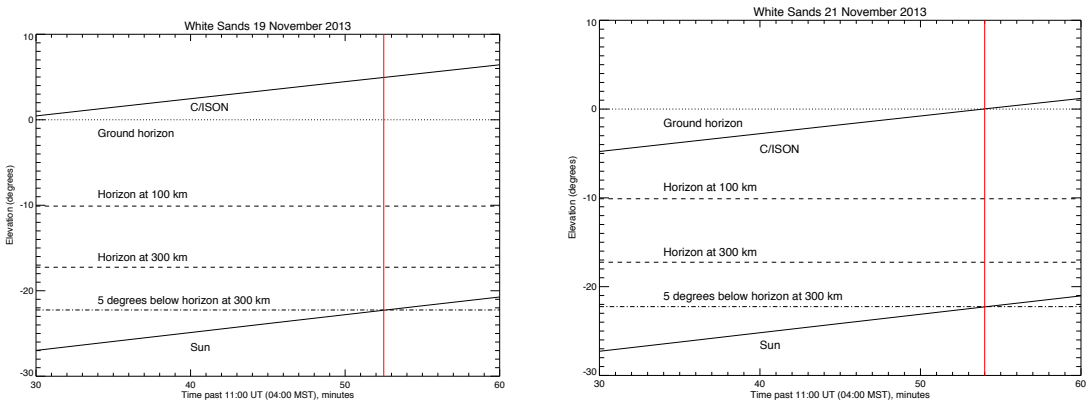

Figure 5.31: Launch window data for November 19 and November 21, 2013 to observe comet ISON. November 21 was at the end of the window, as only about six minutes separated the C/ISON rise above ground horizon from the sunrise at apogee horizon. As the altitude of the payload increases in flight the level of the horizon lowers on the sky, which is shown by the three horizontal lines. The expected maximum altitude in flight was near 300 km (and ultimately was 270 km).

As briefly described in section 5.5.3, the MSA addressing strategy is different for the comet target than for galaxies. Comets will generally appear as a single bright spot in the center, with a diffuse cloud and tail around it, decreasing in brightness with distance from the comet itself. This does not suit itself well to the ZOMI routine,

which is intended to select multiple bright pointlike sources within an extended target. Thus for observing comet C/ISON the maximization routine was preserved to find the brightest single shutter and center a pre-designated pattern around that spot. The sky around the comet's launch night location was examined for bright sources, and it was verified that the comet would be significantly brighter than any background object. Further, due to the proper motion of the comet on the sky ($\sim$48$''$ in RA, 21$''$ in Dec over the 360 second observation), an object tracking plan was put into place with the ACS system, where the telescope would successively target six different locations on the sky. As the movement of the comet would span slightly more than one shutter if pointing were constant, this was necessary to keep the comet center spectrum from moving across the detectors and smearing itself out.

The pattern selected for the MSA is designated as the K. It consists of a central shutter determined by the placement of the comet center, then a vertical column of every other shutter rising up and down from there. For each row without an open shutter in that column, a shutter to one side is opened, following a design similar to a letter K. A simulation of this is shown in Figure 5.32. This pattern was designed to ensure the MSA selects the bright center of the comet, and also collects a sample of spectra of the comet's halo and tail.

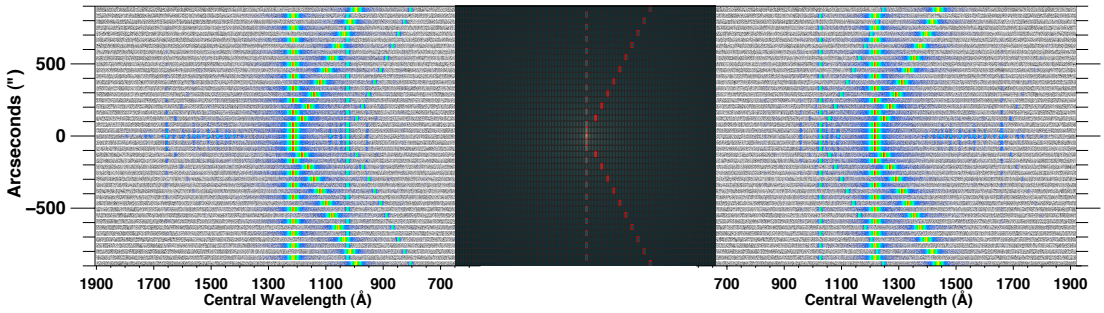

Figure 5.32: Simulation of ISON science data with the K pattern of the MSA overlaid.

5.6.2.3 Mission Flight

FORTIS was launched at 4:40 AM on November 20, 2013. The payload reached an apogee of 270 km and had high-voltage time of 395 seconds before reaching 100 km altitude and closing up for reentry. Unfortunately the MSA addressing was not functional during flight, and no K pattern of open shutters was ever completed. The MSA was mostly open for the whole flight, resulting in no usable spectra due to massive spectral confusion between multiple apertures along the dispersion. This also resulted in a much higher count rate through open shutters, swamping the spectral order avionics above the maximum possible count rate. Over the course of the flight however, the MSA was repeatedly actuated, and on one attempt to address a narrow slit on the MSA enough shutters were closed for ∼60 seconds such that the -1 detector counted effectively, below the maximum where count data would be lost. This allowed for a determination of the absolute magnitude of Lyα brightness, to which later observations (when data is lost due to full FIFOs) can be scaled. The block of open shutters around the center of the comet precludes spectral data, but does

provide images in each of the three orders, with different wavelength bandpass ranges between the imaging channel and the spectral channels (due to the achromat lens, see Figure 5.16). The spectral order images are dominated by Lyα, both geocoronal and cometary. Following the flight, the recovery for 36.296 UG proceeded smoothly, and the FORTIS instrument was shipped home in good shape.

5.6.2.4 Mission Data

While the science data did not include individual spectra due to the MSA failure, enough light from the comet was captured to make use of the three images in the detector channels. The spectral order channels were counting very quickly due to the mostly-open array, above the hardware-limited 125 kHz $\sim$55 seconds during the flight, maintaining all count information in that interval. The flight data in this interval is shown in Figure 5.33 (132). The -1 channel image is a snapshot in Lyα of C/ISON just before its full disintegration as it approached its perihelion on November 28, 2013 (133). In this configuration some fraction of the incoming counts are lost by the onboard avionics as they cannot be read to disk when the data FIFOs are full, but by using the absolute brightness of the center of the comet in the partially-closed MSA configuration (when FIFOs were not filling) as a normalization factor the count rates that made it to telemetry can be scaled to correct the measured brightness.

Water is the most abundant volatile in comets, and is the dominant source of hydrogen in the coma of comets. The production rate of water off the comet is calcu-

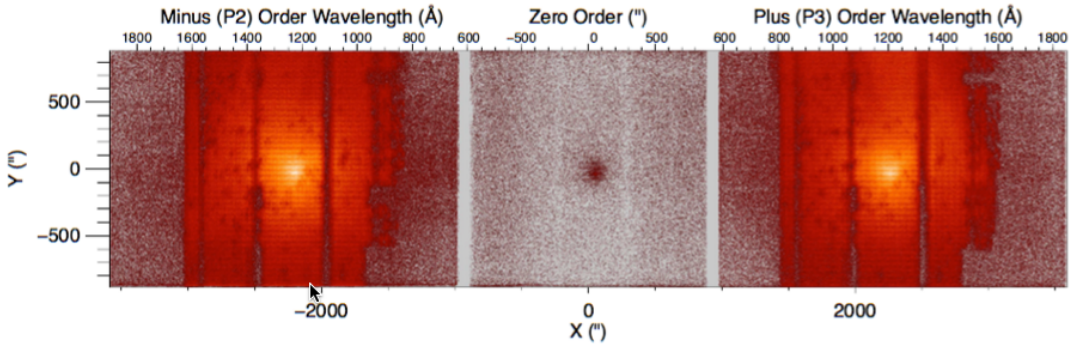

Figure 5.33: Raw flight data images in all three channels over the interval where the incident count rate was low enough in the -1 spectral channel to count effectively (132). The zero order channel shows the comet image with the MSA pattern superimposed, which in this case is a nearly fully open array. Note that two wide columns in the pattern are masked out of functionality due to electrical shorts between these columns and the rest of the array. Units are given in X and Y as arcseconds, with the corresponding wavelength scale along the top axis for an object located within the middle column of the MSA. Due to the fully-open MSA the wavelength scale is not demonstrative for this data, and the spectral order images here are dominated by cometary and geocoronal Lyα emission.

lated using the steady-state Haser model (134) assuming that all Lyα emission results from cometary water dissociation, as discussed in Budzein et al (135). According to the Haser model the number density of a volatile, n, as a function of the distance from the comet r, is given by;

$$n = \frac{Q}{4\pi v r^2} e^{-\frac{r}{v\tau}}, \tag{5.2}$$

where Q is the production rate at the comet, v is the velocity of the outflowing material, and τ is the species lifetime. This provides a method for calculating a water production rate given an observed column density along the line of sight, which can be generalized into a spherically symmetric number density. Lyα emission from comets

is driven by resonant scattering by incident solar photons, which depends strongly on the distance from the comet to the sun. The scattering efficiency ("g-factor") in photons s^{-1} for a general scattering transition in the optically thin case is given by:

$$g_i(v_s) = \lambda_i^2 f_i F_\odot(v_s) \frac{\pi e^2}{m_e c^2} \frac{A_i}{\Sigma_i A_j}, \tag{5.3}$$

where λ_i is the line wavelength, f_i is the oscillator strength, $\frac{A_i}{\Sigma_i A_j}$ is the branching ratio for the given transition (= 1 for Lyα since there is no other path for a de-excitation from the first excited state to get to the ground state), and $F_\odot(v_s)$ is the incident solar flux at 1 AU. The incident flux is also redshifted by the heliocentric radial velocity v_s, resulting in the dependence on v_s. The g-factor for Lyα at 1 AU and $v_s = -62.7$ km s^{-1} (heliocentric radial velocity of C/ISON at launch) is given by interpolation from Table 1 of Combi et al (136), $g_i = 2.2 \times 10^{-3}$ photons s^{-1}. The resonant scattering emission is isotropic, so the brightness in rayleighs (1 rayleigh = $\frac{10^6}{4\pi}$ photons cm^{-2} s^{-1} $steradian^{-1}$) of the scattering object as a whole is described by:

$$B_i = \frac{\bar{N} g_i}{10^6 r_s^2}, \tag{5.4}$$

with $\bar{N}$ representing the mean H I column density. This mean column density from the observed Lyα brightness corresponds to a water production rate in the steady-state Haser model in equation 5.2. The observed Lyα brightness as function

of distance from the center of the comet is shown in Figure 5.34 (132), for both the "Partially Open" and rescaled "Full Open" images. This profile extracted from a region 20 pixels wide extending outward from the center of the comet in the direction away from the sun on the sky. Overlaid on this plot is the corresponding Lyα brightness for two given steady-state water production rates in the Haser model. The data suggest that the observed Lyα signal away from the comet indicate a lower water production rate. This is consistent with a rapidly increasing volatile production as the comet approaches the sun, as volatiles further away from the comet represent the state of the comet surface at earlier times than the volatiles that are nearer.

Unlike the spectral order channels dominated by Lyα, the source of the flux in the imaging channel was more unclear. The transmission of the achromat is functionally zero below $\sim$1250 Å , so Lyα does not contribute. In order to determine the dominant wavelength, the transmission of the Earth's outer atmosphere can be used. The flight plan of the C/ISON observation, as described in Section 5.6.2.2, required the comet to be very low on the horizon. This introduces a significant contribution of atmospheric absorption to the data, which is dependent on the altitude of the telescope on its flight. This is readily evident in zero-order channel images of the comet over different segments of the flight, shown in Figure 5.35.

The transmission drop-off as the payload descended is wavelength dependent, and this dependence can be utilized to determine the line emission. The brightest expected lines (137) in the FORTIS bandpass are O I λ1302, S I λ1475, CO λ1280-

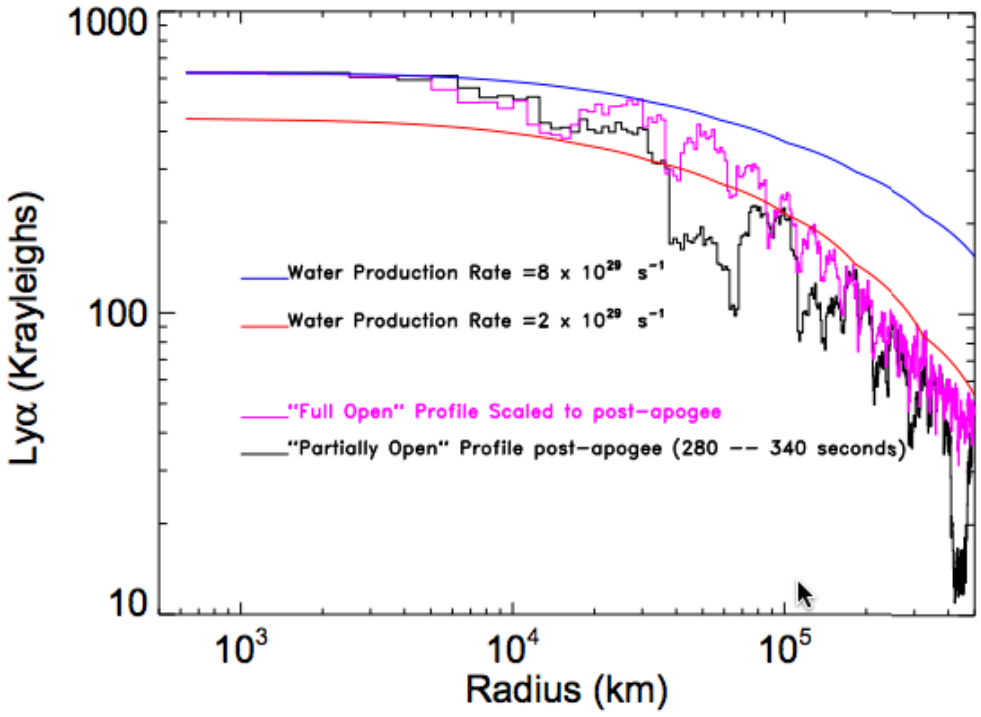

Figure 5.34: Lyα brightness as a function of distance from the center of the comet (132). The green and red lines represent expected radial brightness for the listed water production rates in the steady-state Haser model. The shift from the lower to high water production closer to the comet suggests rapidly increasing volatile production as the comet nears the sun.

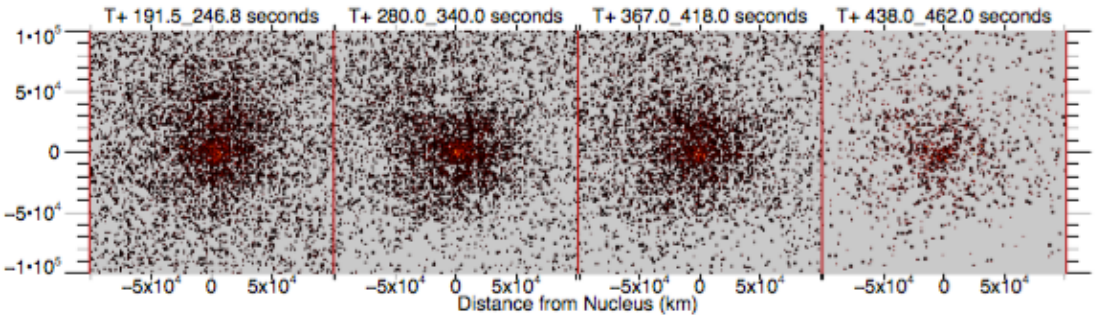

Figure 5.35: Background-subtracted zero-order images of C/ISON over different segments of the flight, starting as FORTIS approaches apogee into the downleg before turnoff (132).

1800 (solar pumped CO bands (138)), and C I λ1657 (132). While HST (using COS) observations of C/ISON on November 1, 2013 (139) showed a strong S I λ1425 presence, the g-factor for this scattering is strongly dependent on heliocentric radial velocity, dropping sharply as the velocity increases (well below S I λ1475 at v_s=-62.7 km s^{-1}). Furthermore, the COS aperture is 2.5″, significantly smaller than FORTIS's field of view. The angular extent of sulfur contributions is expected to be much lower than that of CO, and much of the extended CO emission is therefor ignored by the COS observation. In the FORTIS field, the sulfur is not expected to be nearly as prevalent as CO or volatile material containing CO, and should be negligible. The O I signal is expected to be quite bright due to the high abundance of emitting O from water dissociation, but the low radial geocentric velocity ($\sim$4.5 km s^{-1}) of C/ISON predicts a high absorption of this signal by atomic oxygen in the Earth's atmosphere envelope, where the column density of O is $\sim 10^{16}$ even at the flight's apogee.

The absorption of the UV light by atmospheric O_2 and atomic oxygen, which is strongly dependent on wavelength, is given in Figure 5.36 as a function of flight time for three relevant line species. Before roughly 420 seconds into the flight the CO, C I, and O I signals are impossible to distinguish as they all make it into the telescope through the atmospheric oxygen. However, when the falling edge of the measured emission on the downleg manifests itself will depend on the wavelength of the incoming light. Matching the measured count rate drop-off as FORTIS falls into the atmosphere to the expected for the various lines, shown in Figure 5.37,

demonstrates that the light incident on the zero-order channel is dominated by C 1 λ1657 (132).

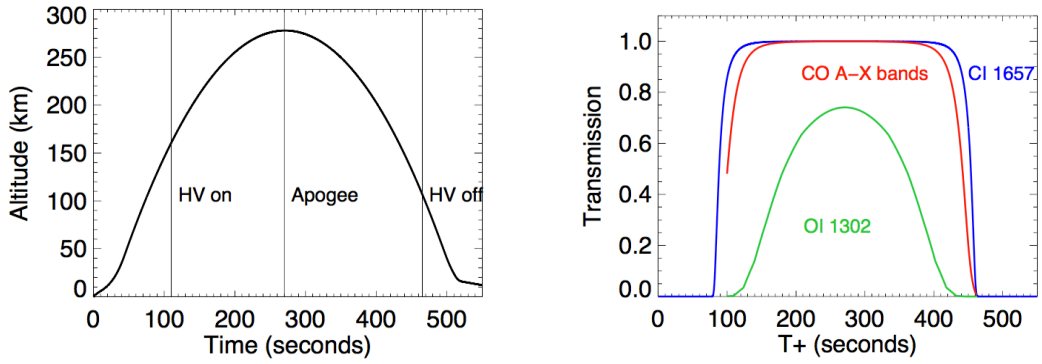

Figure 5.36: **Left:** Altitude of the FORTIS flight over time from launch, with the apogee and bounds of observation time marked. **Right:** Resulting transmission through the atmosphere column for the given lines of C I, CO bands, and O I (132).

While FORTIS did not achieve the spectral data desired due to the MSA address failure, the background was sufficiently suppressed from levels measured on the first to provide useful science data. Water production rate evolution calculated from Lyα brightness at different distances from the center of the comet were consistent with measurements taken prior to the FORTIS launch, and FORTIS contributed ultraviolet data points in this analysis before the comet breakup a few days after the launch. The data did not match steady-state Haser model of water production, suggesting a rapid change in cometary water production relative to the time for the produced water to dissipate. The measured water production rates were $Q_{H_2O} = 8 \times 10^{29}$ molecules s^{-1} near the comet center to 2×10^{29} molecules s^{-1} at distances greater than 5×10^4 km. This is consistent with water production rates measured by Combi et al (136), who observed C/ISON with the Solar Wind ANisoltropies (SWAN) Lyα camera on

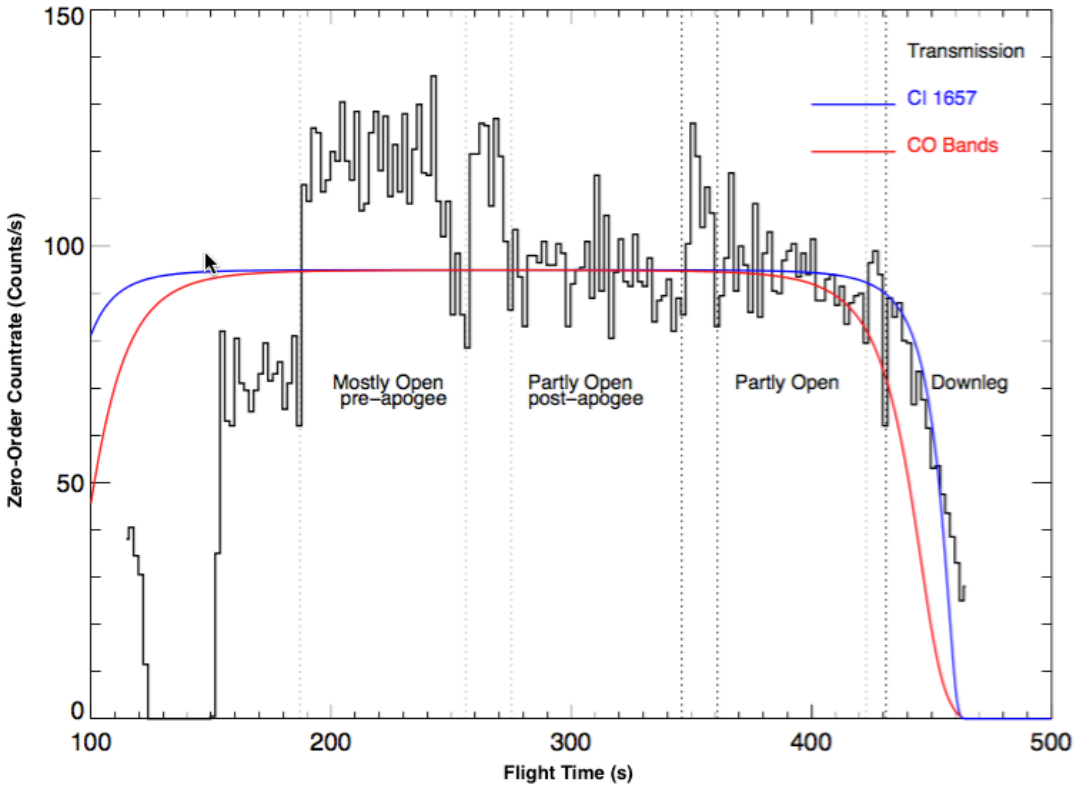

Figure 5.37: Observed count rate in the zero-order channel over the flight (132). Wide variations are due to repeated attempts to address the MSA, denoted by dotted lines. The expected count rates from cometary CO and C I λ1657 are plotted, with a falloff on the edges due to atmospheric oxygen absorption at low altitude. The location of the flux falloff in the time domain suggests that the observed light is dominated by C I.

the *SOlar and Heliospheric Observer* (SOHO), a wide-field Lyα observatory with 1° resolution. The SWAN team calculated a Q_{H_2O} =3.8× 10^{29} s^{-1} on November 19 and Q_{H_2O} = 19.4×10^{29} s^{-1} on November 21, corroborating FORTIS data showing a rapid increase. C/ISON near-infrared spectra was also recorded by the Cryogenic Echelle Spectrometer (CSHELL) at the *NASA InfraRed Telescope Facility* (IRTF), and similar water production rates were calculated over the same period by Della Russo et al (140) and DiSanti et al (141).

Following 36.296 UG, the existing telescope was in good shape and ready for improvements to the background rate suppression and especially the MSA operation. The telescope itself was also improved and updated after the C/ISON mission. More baffling and blackened internal telescope elements were added to suppress background scatter. C/ISON was a very bright source, limiting the required sensitivity of the instrument, but the continuation of the star-forming galaxy project demands the highest signal-to-noise possible to achieve useful data. Three new secondary mirror substrates were ordered (detailed in Section 5.2.2) and ruled, a significant improvement over the existing flight grating that had been damaged in recovery of mission 36.268 UG. The detector was outfitted with a new photocathode, increasing quantum efficiency from the 36.296 UG mission by a factor of $\sim$4. The instrument team was confident in the telescope performance in the next missions to observe star-forming galaxies.

5.6.3 Mission 36.321 UG

The target for this mission was the second in the program to search for Lyα escape from star-forming galaxies, and to investigate the relationship between Lyα emission and the local gas and dust properties. The justification for this target, NGC1365, is similar to that for M61, the galaxy target for mission 36.268 UG. NGC1365 is a barred spiral galaxy at redshift of $z = 0.0055$ ($v = 1636$ km s^{-1}) that spans $\sim 11'$ on the sky across its longest axis. It was selected for far-UV brightness suggesting star formation, as well as a size that suits use by the multi-object spectroscopy enabled by

the MSA. A simulation of FORTIS data from NGC1365 is shown in Figure 5.38, with 17 shutters chosen by the ZOMI targeting routine spanning the galaxy on the sky. The brightest shutter is estimated from the GALEX FUV flux to have an incident flux of 8.01×10^{-14} erg cm^{-2} s^{-1}, resulting in ~ 7 counts s^{-1} in the zero-order image, above the expected $\sim$0.003 counts s^{-1} background.

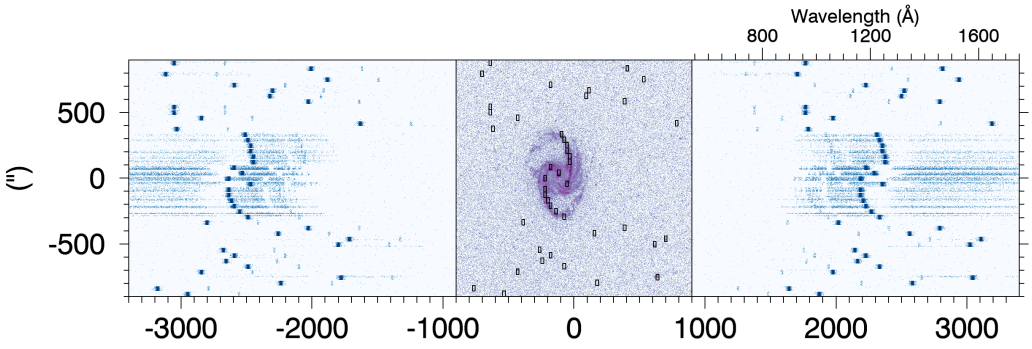

Figure 5.38: Simulated FORTIS science data of the star-forming galaxy NGC1365. The brightest shutters in each row are automatically selected as shown, with the resulting simulated spectra in each side channel. A flat background of 200 counts s^{-1} is added to each channel to approximate scattered light.

5.6.3.1 Flight Preparation

The new baffling to further limit light scattering in the background was manufactured by Stratasys following a study into Lyα bireflectance of candidate materials for reflectance suppression. This study was carried out in the GSE testing vacuum chamber and UV monochrometer at JHU, with results shown in Figure 5.39. ULTEM 9085, a material developed by the *Jet Propulsion Laboratory* (JPL), was found to be an ideal light baffle that could be 3D printed into a useful shape. The resulting baf-

fles, in Figure 5.40 were designed with short blades similar to those installed on the interior of the heat shield prior to the 39.296 mission, replaced curved delrin sheets around the inner telescope structure.

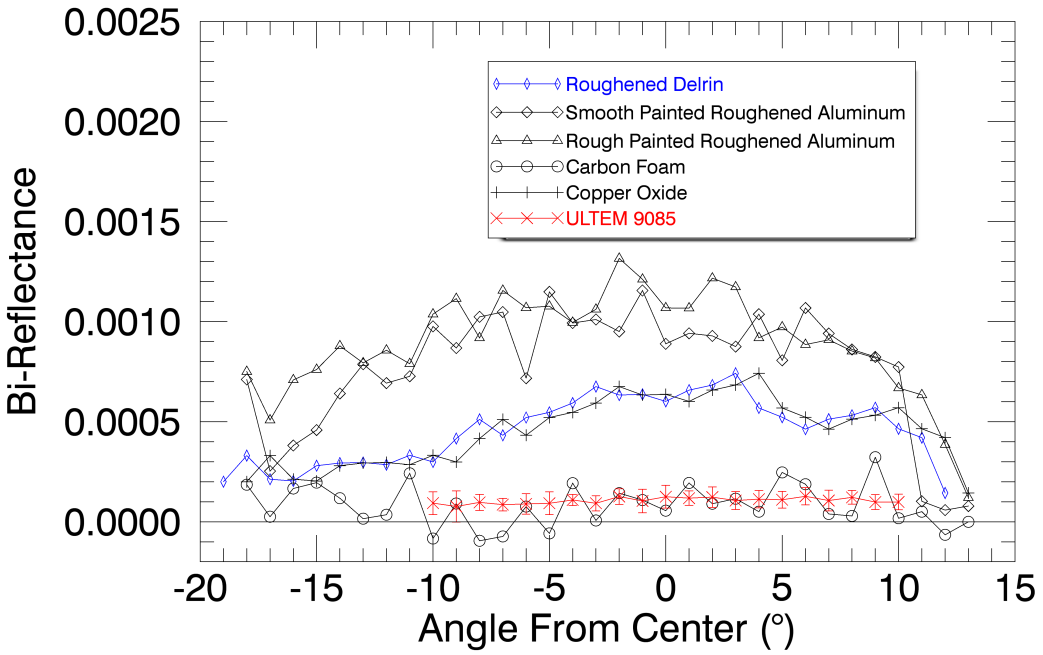

Figure 5.39: Lyα bi-reflectance measurements of several black materials as a function of angle from a direct reflection. Baffles in the FORTIS telescope were previously manufactured from roughened delrin, but the ULTEM 9085 was found to be nearly consistent with no measured scattered light. The carbon foam was similarly effective, but difficult to form into the shapes needed.

As discussed in section 5.5.2, it was suspected that timing errors between the address pattern and the magnet movement across the face of the array were responsible for the failed addressing. An encoder tracking magnet position abandons the need for precise timing in the software, and the flight computer driving the MSA voltages simply waits for the magnet to be in the desired position for each column before continuing the cascading pattern across its face. This required a significant rewrite of

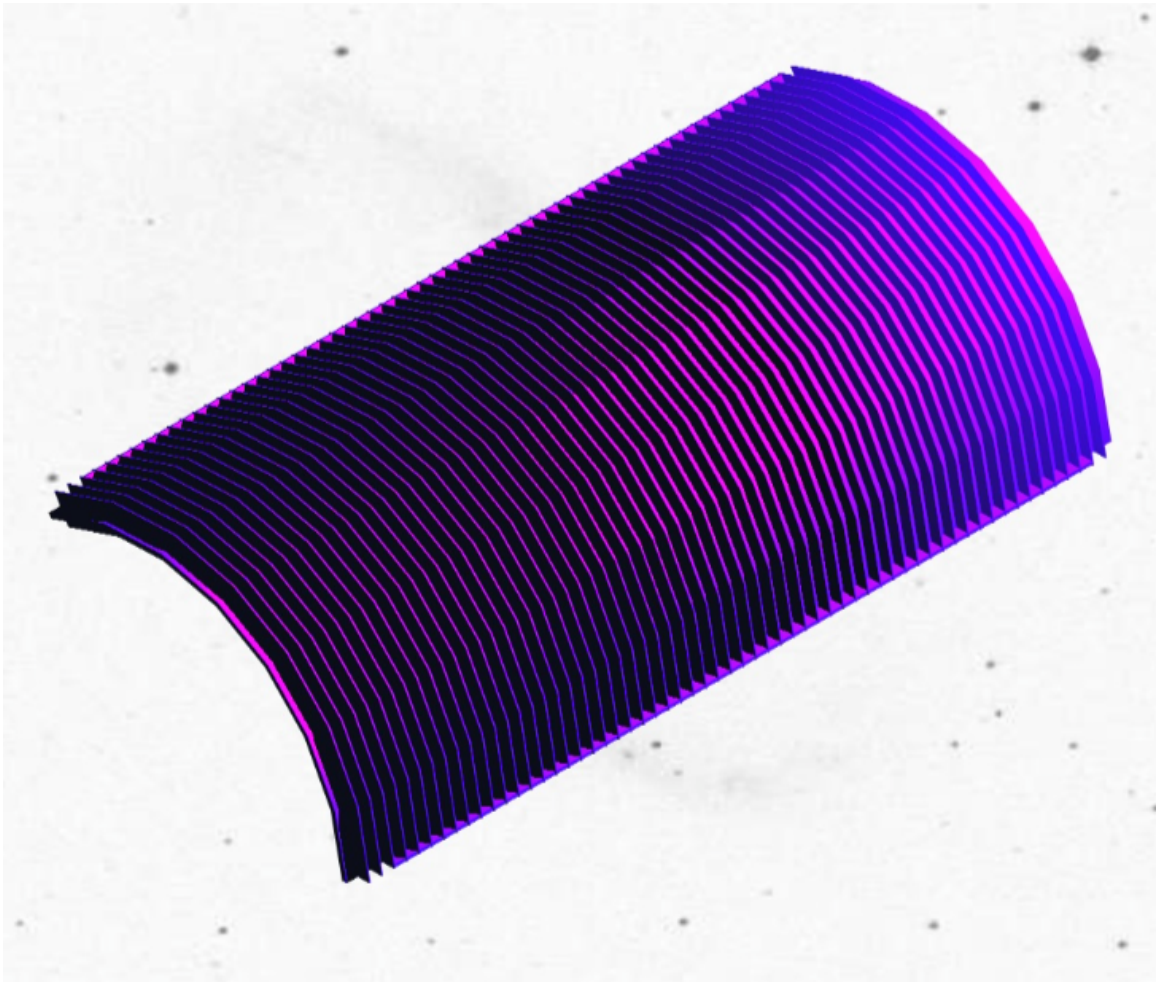

Figure 5.40: Drawing of one of the three baffles 3D printed with ULTEM 9085. These are roughened then affixed to the internal structure of the FORTIS telescope. The blades induce multiple reflections for incoming light, effectively eliminating the photons from scattering into the detectors.

the MSA control code in the cRIO, both in the real-time code and the FPGA code. After extended testing of the new system, it was found to be robust and effective in addressing the MSA, and the magnet position was fully consolidated into the address trigger software. An analog monitor line was built by the IDG added to the FORTIS avionics system, allowing for ground equipment monitoring of the magnet

position through the umbilical cables. A current monitor was also added to the main power bus onboard FORTIS, so that the current could be monitored by the science team while on internal power. This helps diagnose potential problems during MSA operation and high-voltage operation of the three MCP detectors.

The FORTIS team arrived at WSMR in November 2015, and all environmental testing of the FORTIS payload was performed over the following few weeks. This entailed minor adjustments to the MSA flight code, but overall the qualification for flight proceeded smoothly.

5.6.3.2 Mission Flight

FORTIS launched at 11:52 PM MST on December 17, 2015, and all support systems performed nominally on the flight. Unfortunately, almost exactly at T=0 when the first stage engine ignited, the ±100 volt bias in the two wire grids immediately in front of the detector plates were lost. These wire grids are intended to deflect ions incident on the detectors, mostly electrons. This as soon as the high-voltage was activated, there were large signatures of ions in the science data. These ions were bright enough to wash out the galaxy target in the zero-order image, rendering the ZOMI optimization routine unusable. As a backup, the "Plan B" MSA configuration of two open columns across the center of the target was addressed on the array. This should in principle produce spectra in the two spectral detector channels, albeit not necessarily with the slit centered on the brightest knots of emission on NGC1365.

However, the signal from the galaxy was weak enough that it could not be discerned in flight, with a small but still significant O I background in the imaging channel.

As altitude increased and the density of gas fell, the effect of the ions was minimized, allowing for a confirmation that the "Plan B" address was completed. The spectral order channels were nevertheless still bright in scattered background, shown in Figure 5.41. This background was bright enough to obscure the Lyα signal from the target galaxy expected from the "Plan B" MSA address.

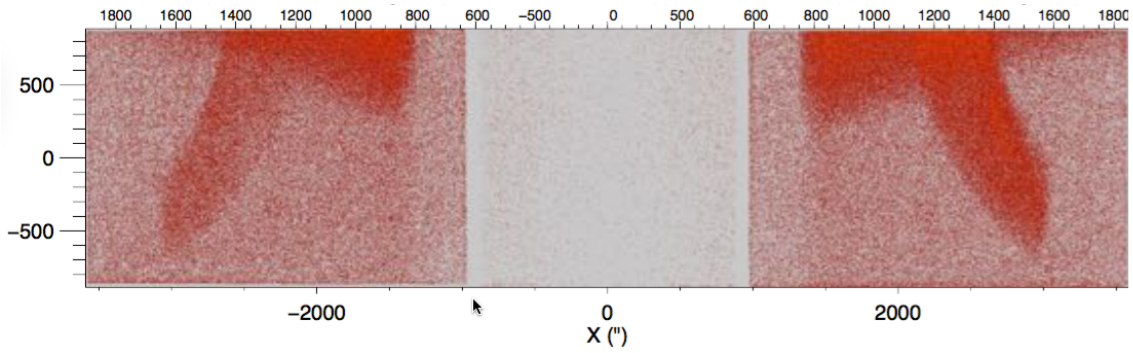

Figure 5.41: All three detector channels while at a high altitude and with the MSA fully closed. The imaging channel is clear of much background, but the spectral channels have a significant amount of Lyα leakage in the clear symmetric pattern, with an average count rate of order 10^2 counts s^{-1} in each.

Recovery of FORTIS following the 36.312 UG launch went smoothly, and the payload was recovered with no issue. Upon return to the lab, debris from the new baffles installed prior to the launch had broken loose and impacted the wire grids, breaking them and creating a short between the two sets of grids that are biased at $\pm$100 V. This was expected from the flux of ions observed in flight. A broken plastic vacuum clamp was also discovered, which split due to the force of acceleration

at launch. This clamp was removed and discarded, and replaced with an aluminum clamp.

5.6.3.3 Mission Data

While the background from the scattered geocoronal Lyα photons washed out spectral data from the target galaxy, the count rate was low enough such that no counts were dropped, and FORTIS was able to recover a complete picture of the scattered profile, specifically the pattern shown in Figure 5.41. This is an important picture to enable the FORTIS team to determine exactly what the path of the extraneous Lyα light is into the detectors, and re-design of the telescope in order to eliminate this background is a major part of the Next-Generation FORTIS project.

5.6.4 Future Work

There are two main improvements that will be made in Next-Generation FORTIS (NG-FORTIS). The first is the installation, testing, and flight preparation of the Next-Generation Microshutter Arrays in development at GSFC (142). The FORTIS team has been working closely with GSFC to acquire arrays that can be electrostatically actuated, forgoing the need for the motor and magnet that caused timing and stability issues in previous launches (see Section 5.5.5). GSFC is near completion of fabrication of new MSAs and wire-bonding to the "Big-Θ" board that fits neatly into the FORTIS telescope structure, replacing the "Big-D." A MSA testbed vacuum chamber with

ultraviolet camera is being assembled at JHU in order to facilitate testing the address procedure development in-situ. The FPGA driver code in the flight computer will be completely replaced to accommodate the new MSA, with a significant re-work to front-panel operation code as well.

The second main thrust of NG-FORTIS is a complete investigation into the scattered geocoronal Lyα (and O I in the imaging order) in the background. The FORTIS team has developed the Wide-Field Lyman-α Geocoronal Simulator (WFLaGS), a vacuum UV collimator with a 10° field of view in order to characterize the effect of off-axis far-UV light in the telescope (143). As the updated telescope design progresses, guided by the light behavior determined by WFLaGS, light capture devices like additional baffles and light traps will be implemented to cover scatter regions of the telescope.

Future NG-FORTIS flights are aimed across a broad spectrum of targets, where wide-field multi-object far-UV spectroscopy can provide interesting science data in ∼3-400 second exposures.

One of the planned future targets is the Magellanic Bridge, a bright region of star-formation formed by tidal interacting between the Large and Small Magellanic Clouds (LMC and SMC). The existence of the young stellar population (144) in the Bridge (145; 146; 147) (∼25 Gyr) indicates the presence of cold gas, which implies H_2 overdensities and metal abundances to facilitate energy radiation as gravitational collapse occurs. Generally, the star formation rate surface density is observed to

track H_2 surface density (148) in star-formation. However, the Magellanic Bridge is a high-ionization region with stellar and gas-phase metallicities lower than the SMC (149; 150), suggesting low dust content. The rate of star-formation on the Magellanic Bridge is surprising given the measurements of environment factors that generally correlate to star-formation. There have been isolated pockets of the Bridge observed to have a much lower gas-to-dust ratio (2-4 times that of the Milky Way) than that of the bridge as a whole (∼10 times Milky Way) (151), suggesting that high-dust localities may shield the H_2 and CO from dissociation by radiation, spurring star-formation. FORTIS is well-suited to select the bright regions of star-formation and measure the dust extinction, and to test whether small-grain dust indicated by steep SMC extinction curves (71; 152) can facilitate H_2 preservation. A FORTIS observation, simulated in Figure 5.42, could acquire individual spectra for up to 50 bright blue stars, each providing a new data point in determining the relation between the local dust content and setting conditions for star-formation.

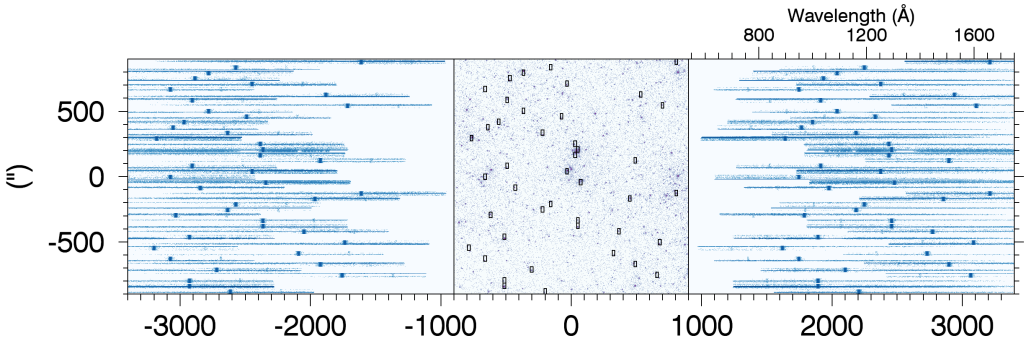

Figure 5.42: Simulated three-channel data for FORTIS acquisition on bright stars in a UV-populated region of the Magellanic Bridge. The spectra are calculated by a power law derived from NUV and FUV GALEX image intensities.

Nearby supernova remnants (SNRs) are bright UV sources along their shockwaves and may span enough of the sky to be good candidates for FORTIS observation. The Cygnus Loop is an example of such an object, a middle-aged SNR only 600 pc from Earth. Its foreground extinction is relatively low ($E(B-V$=0.08), making it an interesting candidate for far-UV observation. The Loop as a whole is 3.5° across, significantly larger than 0.5° FORTIS FOV. Existing elements in the expanding wave interacting with the cold surrounding material have been identified by optical imaging, but there have been no observations of individual lines in the UV. GALEX acquired a NUV image of the Cygnus Loop, but information about individual lines in the image is limited due to multiple emission lines existing in the bandpass. Strong FUV emission has been verified by the *Voyager* Ultraviolet Spectrometer (UVS), the *Ultraviolet Imaging Telescope* (UIT), and *Spectroscopy of Plasma Evolution from Astrophysical Radiation* (SPEAR) but the imaging and spectro-imaging done by these instruments have limited spatial and spectral resolution (153; 154; 155). Bright FUV spectra were confirmed by HUT and FUSE and showed that the lines (O VI $\lambda\lambda$1032,1038 from especially high ionization states were spatially located ahead of the edge of the shockwave in optical emission. The FORTIS MSA enables a unique observation that samples many different regions of the Cygnus Loop, providing snapshots of UV emission in a few bright lines across the shockwave, especially as a function of the corresponding optical emission. In fact, as the emitting species can be fairly confidently predicted from existing archival HUT spectra, a pattern of open shutters

can be addressed that allows for multiple shutters open per row. The lack of a bright continuum spectrum means that cross-contamination of multiple slits along the dispersion direction can be limited as long as the few lines themselves do not overlap. An example of a possible MSA configuration is shown in Figure 5.43 with two open shutters per row, doubling the science data and expanding the spatial range of the measurement across the shockwave.

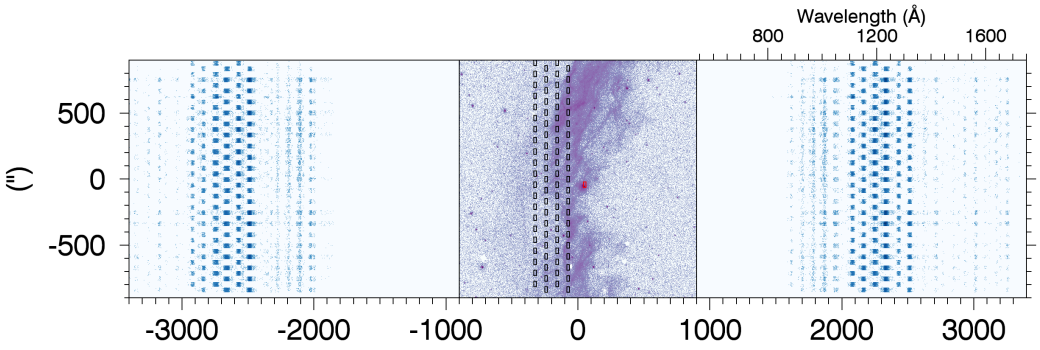

Figure 5.43: Simulated three-channel data of a Cygnus Loop observation. Spectra are derived from an archival HUT spectrum of the Cygnus Loop, scaled per pixel by GALEX NUV flux.

Globular clusters, some of which appear near enough so that individual stars can be selected by the MSA optimization routine, have been known to have a minority set of blue, luminous stars whose existence contradicts the expected main-sequence turnoff edge for a given stellar population (156). Significant mass accretion after star formation, either through a collision with other objects or a slow mass transfer, is thought to be the source of these stars (157; 158). Globular clusters, where the close proximity of stars increases the chances that collisions and interactions between stars will occur, are in ideal environment to observe the dynamical processes that

lead to blue stragglers. Incidence of interaction and mass transfer will depend on the number density of stars, which would result in an expected dependence of blue straggler incidence on position in the cluster, where stars closer to the center are more likely to have exchanged mass or even collided with their neighbors. The distribution of blue stragglers as a function of radius from the center of the cluster has been used as a proxy for the dynamical age of the cluster (159), with remaining questions still exist about whether bright hot stars in the cluster centers traveled in from the exterior or were formed in place (160; 161).

The globular cluster M10 has been identified as a population containing UV-bright stars (162) with a variety of spectral energy distribution power law slopes between 1530 Å and 2270 Å derived from GALEX NUV-FUV channel images (Figure 5.44). A histogram of these measured shows a bimodal distribution (Figure 5.45), suggesting that there are two different populations of stars in this cluster. The dependency of these slopes on distance can provide hints to track the development of the spread of these star populations based on their relative ages. Spectral verification of individual stars may be helpful in resolving the ambiguity in the photometry color bands between white dwarves and blue stragglers (163), for which FORTIS is uniquely suited. The MSA allows individual spectra of up to $\sim$50 of the brightest stars, providing SED power law information down to $\sim$1200 Å and verification of blue straggler identification. A simulation of a potential FORTIS observation is shown in Figure 5.46.

NG-FORTIS is still well-suited and remains primarily equipped to achieve the orig-

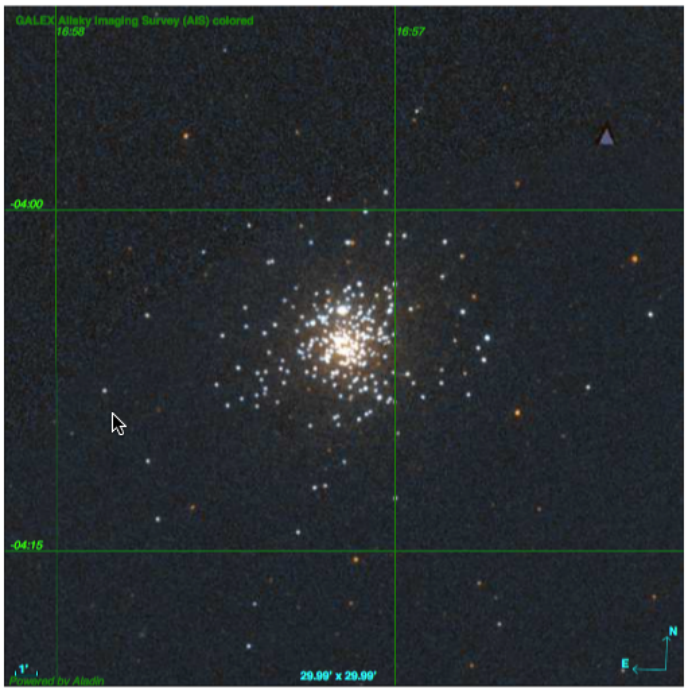

Figure 5.44: GALEX NUV and FUV images overlaid in the FORTIS 30′ × 30′ field of view.

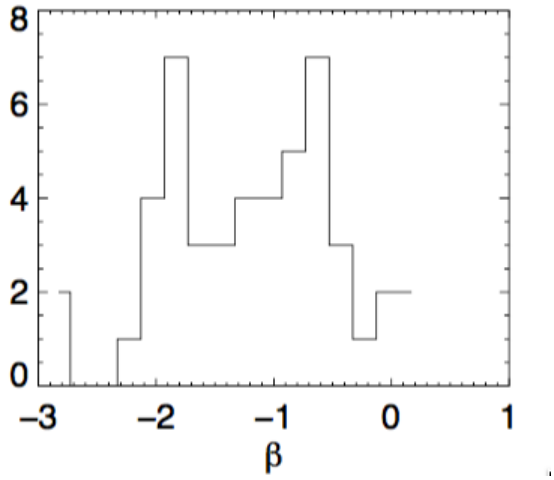

Figure 5.45: Histogram of SED power law indices for the individually resolved stars. Note the bimodality, which suggests that there are two distinct stellar populations in the cluster that formed at different times.

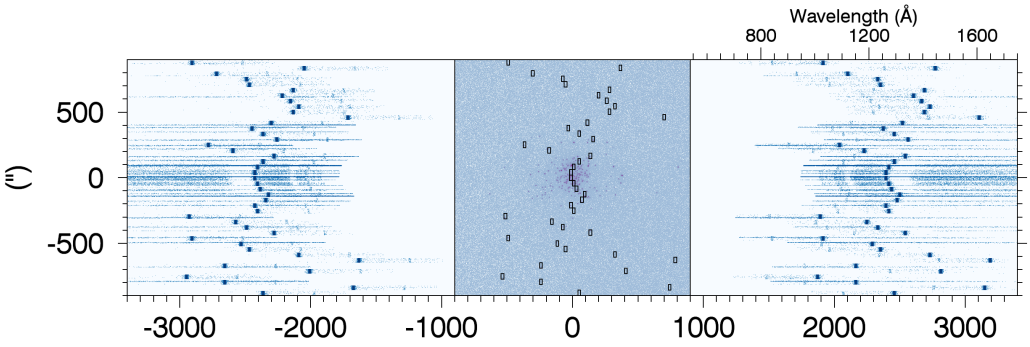

Figure 5.46: FORTIS simulation of one observation of the globular cluster m10. The image and ZOMI MSA selection is based on the GALEX FUV image, with simulated spectra per pixel determined from a power law fit between GALEX NUV and FUV images.

inal primary science goal in investigating Lyα escape from low-redshift star-forming galaxies, as described in Section 5.1. Interesting target objects include the Antennae Galaxies, M83, M33, and NGC55 – all low-redshift UV-bright galaxies that suggest active star-formation and enough spread on the sky for the MSA to acquire individual bright knots of emission. A simulation of the FORTIS observation of M83 is shown in Figure 5.47. Finally as with FORTIS, transient targets of opportunity like bright sungrazing comets are certainly suitable as targets of opportunity, should such a comet appear in the sky.

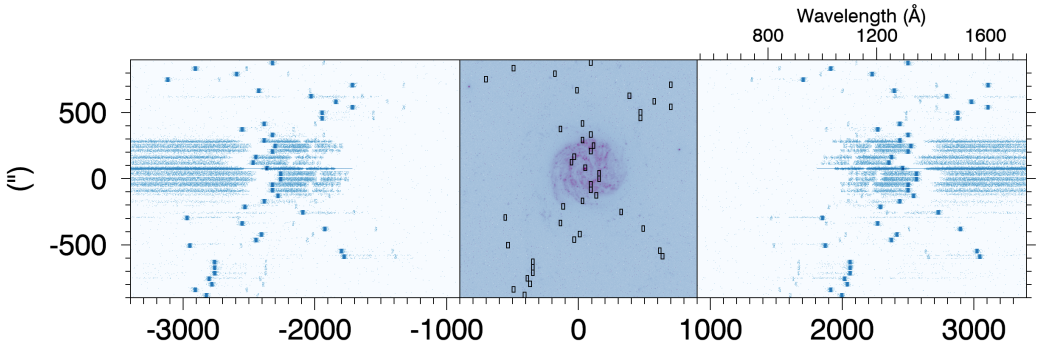

Figure 5.47: FORTIS simulation of one observation of M83, with ∼13 shutters falling on the galaxy . The image and ZOMI MSA selection is based on the GALEX FUV image, with simulated spectra per pixel determined from a power law fit between GALEX NUV and FUV images.

Chapter 6

Conclusion

This thesis describes broad efforts in ultraviolet instrumentation and observation to better understand the ways that high-energy photons escape out of star-forming regions of galaxies. FORTIS is an instrument specifically designed to pick out bright regions of galaxies, isolating them from the the galactic emission as whole in a way that is impossible to do with any existing UV spectrograph. COS has been successfully operating for years, but development of new observation modes that push the boundaries of the telescope sensitivity at shorter and shorter wavelengths is an effective way to keep producing new science in efficent observation programs. Using these instruments we can better target the search for LyC escape, and the SNAP COS program described in Chapter 2 identifies candidates (LY06, LY24, LY52, and LY69 in particular) for LyC leakage at low redshift suitable for deeper observaiton in more expensive far-UV spectroscopic HST programs. In addition to identifying and

describing these targets, we demonstrate that the methods used to find optically thin H I ISM galaxies can be applied to spectra in similar programs that do not require many orbits of the HST time that is always in high demand, streamlining the LyC search.

The new COS mode detailed in Chapter 3 complements the targeted LyC search, as the search for very faint LyC photons are dependent on the most sensitive observing modes possible with existing equipment. While FORTIS, with its short observations, is not well-equipped for a deep LyC search, the multi-object capability provided by the microshutter array means that the relationship between Lyα emission and local propoerties of emitting regions of the galaxies can be teased out of the bulk UV spectrum of the entire galaxy, which may provide valuable insight of how clumpiness of H I in the galaxy, dust content, and other species' relative density relate to Lyα escape. The combination of focused, targeted HST programs and supplementary sounding rocket flights with FORTIS is a promising path for bettering our understanding of Lyα and ionizing photon escape.

Appendix A

COS Spectra and Line Feature Fit

This appendix contains the COS spectrum for each of the observed targets in the SNAP program. The raw data is rebinned by a factor of five for ease of viewing. A two-part piecewise power law continuum fit is normalized to the observed flux at λ = 1530 Å and overlaid on the plot in red. The geocoronal Lyα and O Iλ1302 are fitted to a gaussian curve if present (depending on the sun phase and angle at the time of observation). Finally, a gaussian fit to the intrinsic Lyα emission is performed for emission or absorption depending on the target (occasionally both). For targets with very low signal-to-noise or P Cygni line profile (most evident in LY01), this fit is either left out or not particularly descriptive of the data. Note the vertical lines denoting rest-frame wavelengths (black) and redshifted wavelengthe (blue) for line species of interest in the spectrum. The Lyα line centers are indicated by the bold verticals. Finally, both a SDSS image and acquisition image acquired in 96

seconds by the COS NUV detector before science observation are superimposed in the upper right. In the acquisition image, both the requested aperture location based on SDSS flux centroid (red) and the final science aperture location acquired at the time of observation (black) are shown. These aperture locations vary by an average of $0.33^{\prime}$ and a maximum of $0.96^{\prime}$ over the dataset, well within nominal bounds. The acquisition routine failed for observation of target LY52, thus there is no image shown here for that particular target.

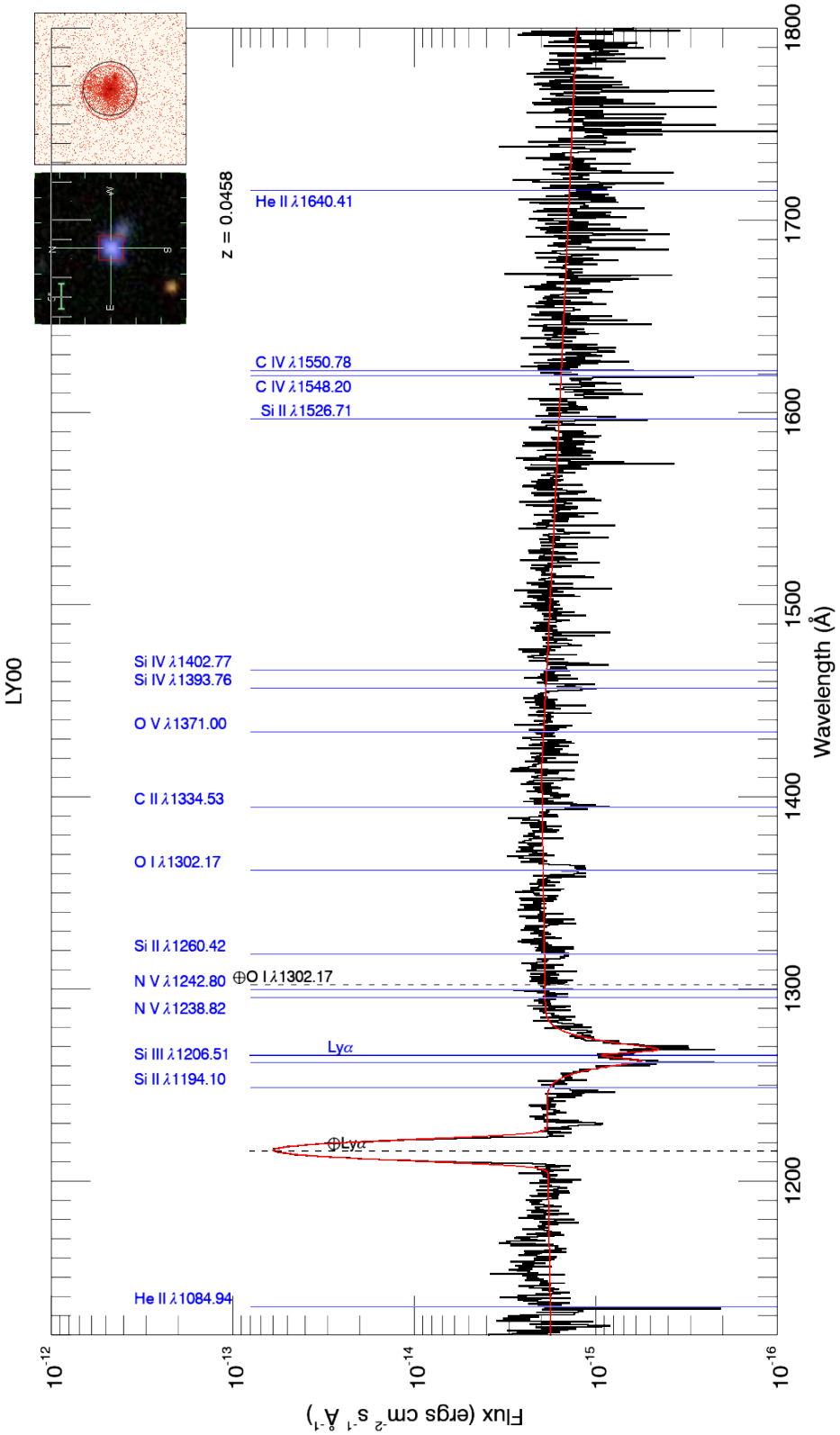

Figure A.1: LY00

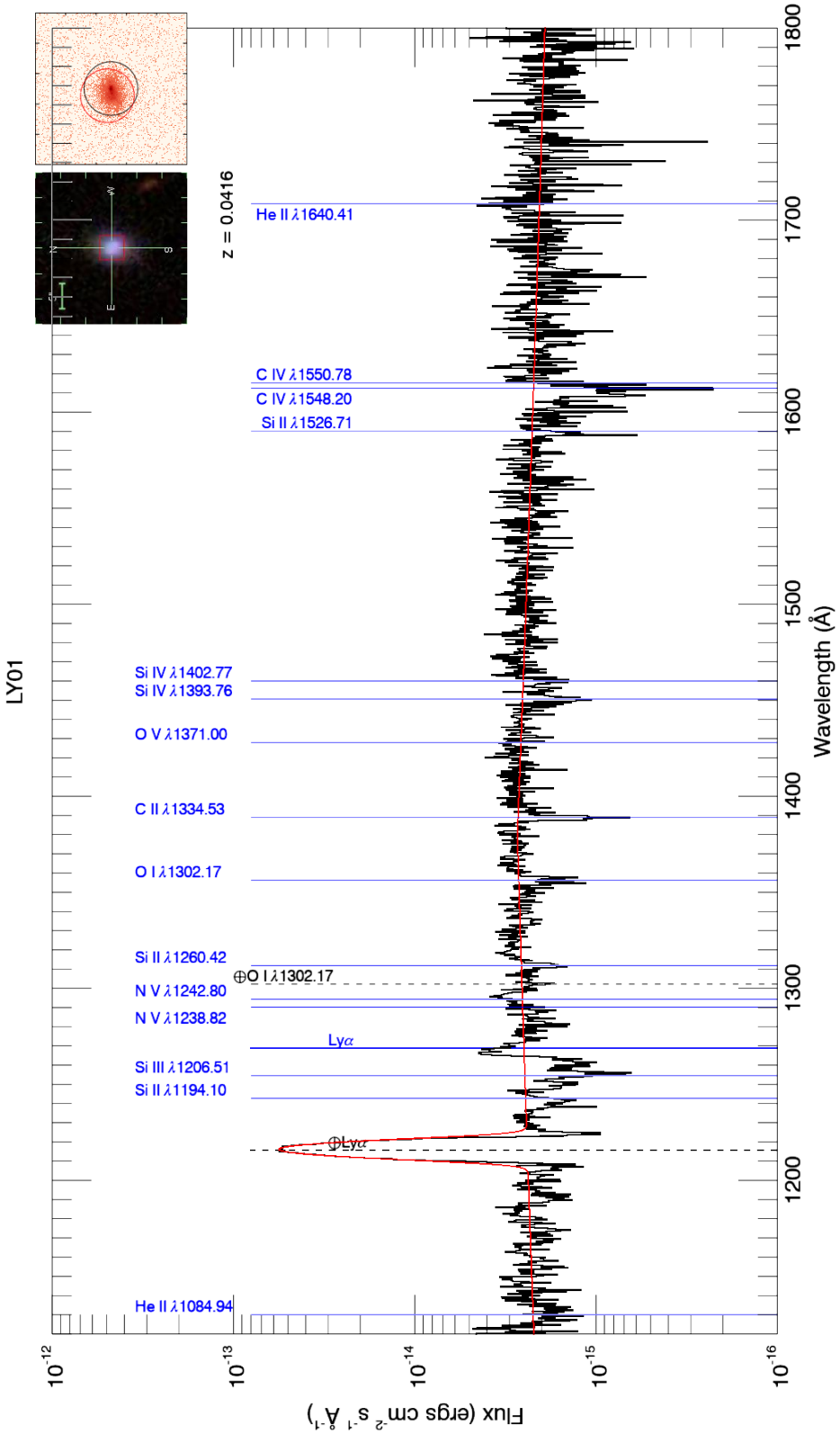

Figure A.2: LY01

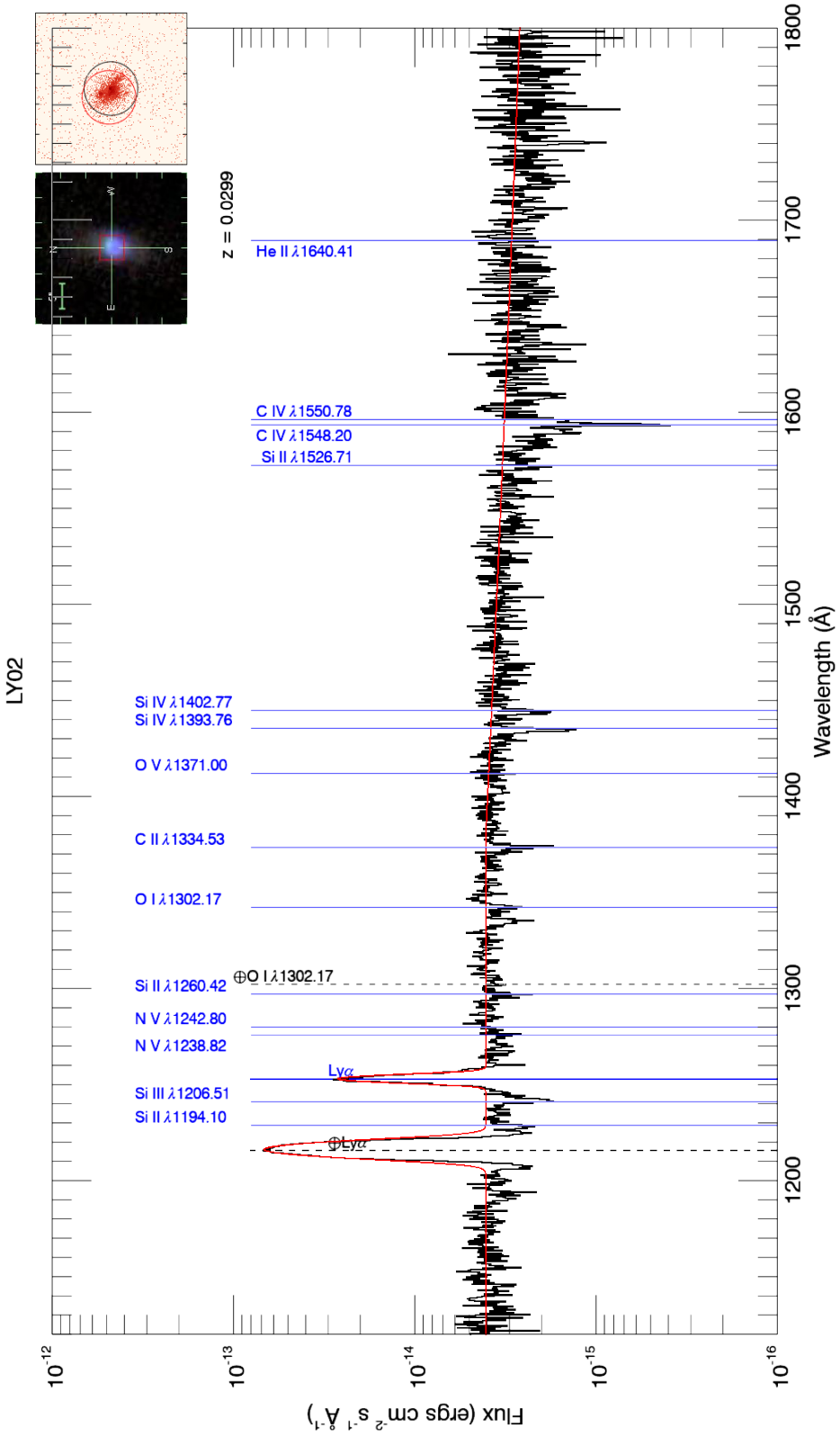

Figure A.3: LY02

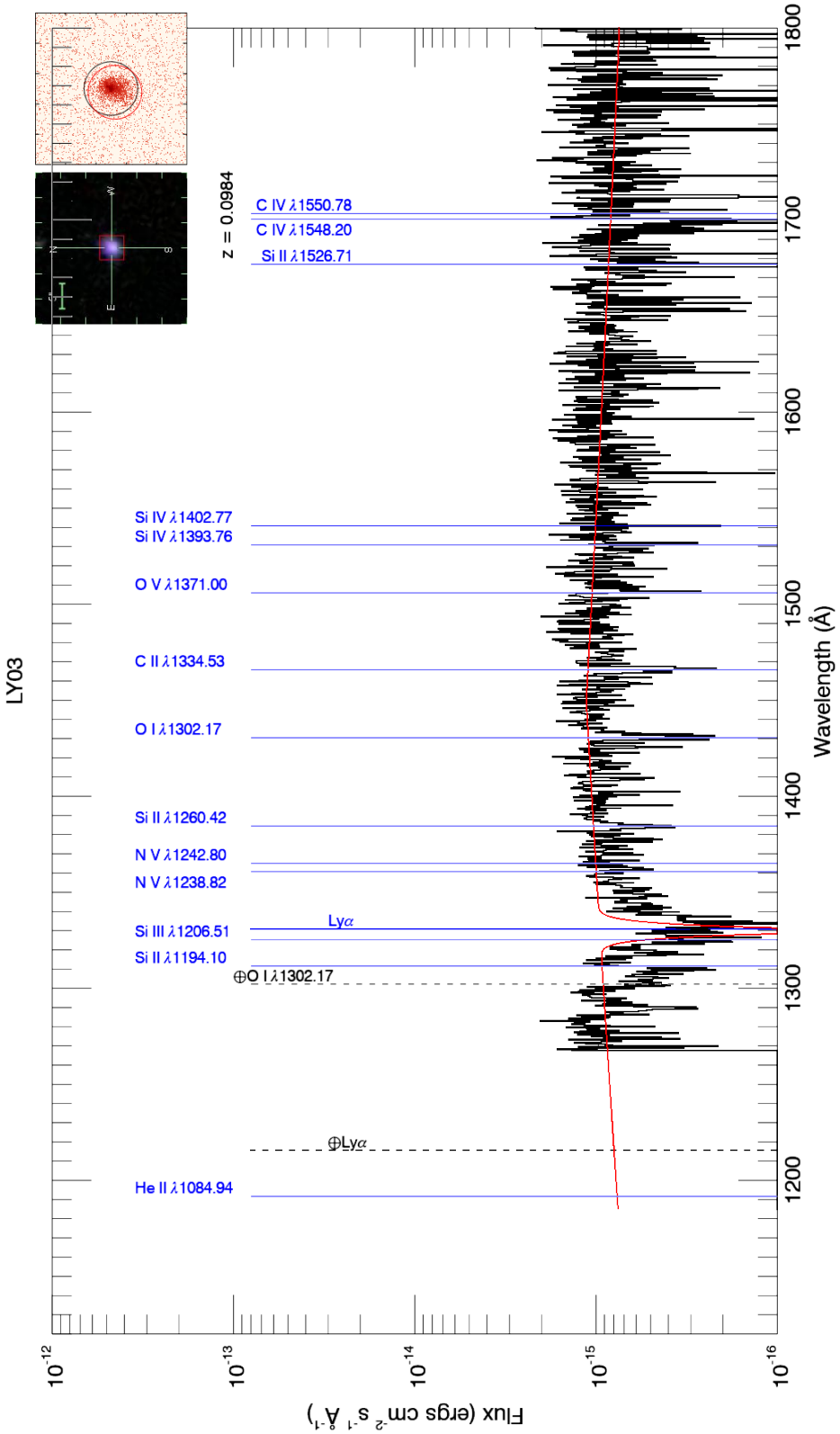

Figure A.4: LY03

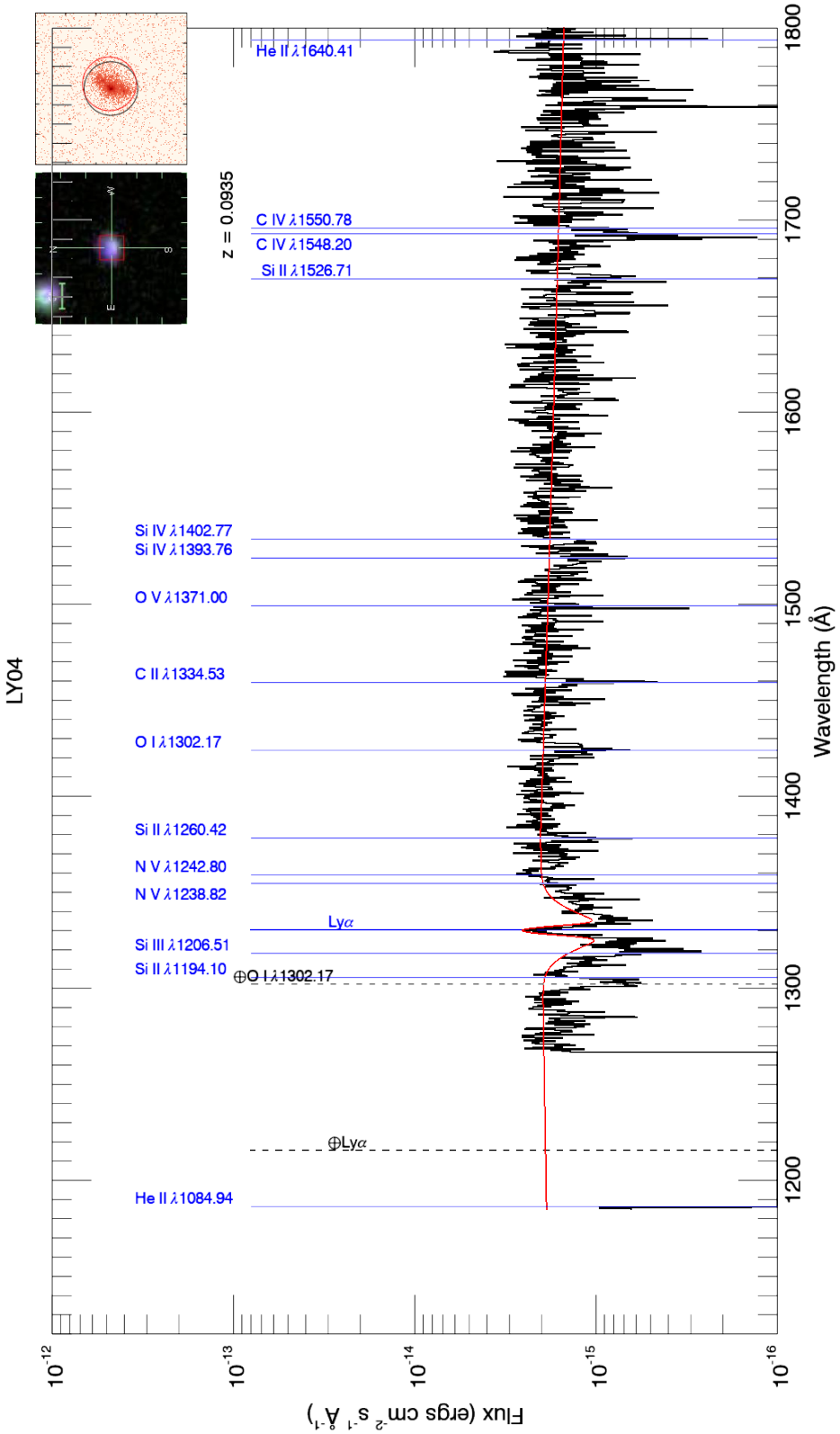

Figure A.5: LY04

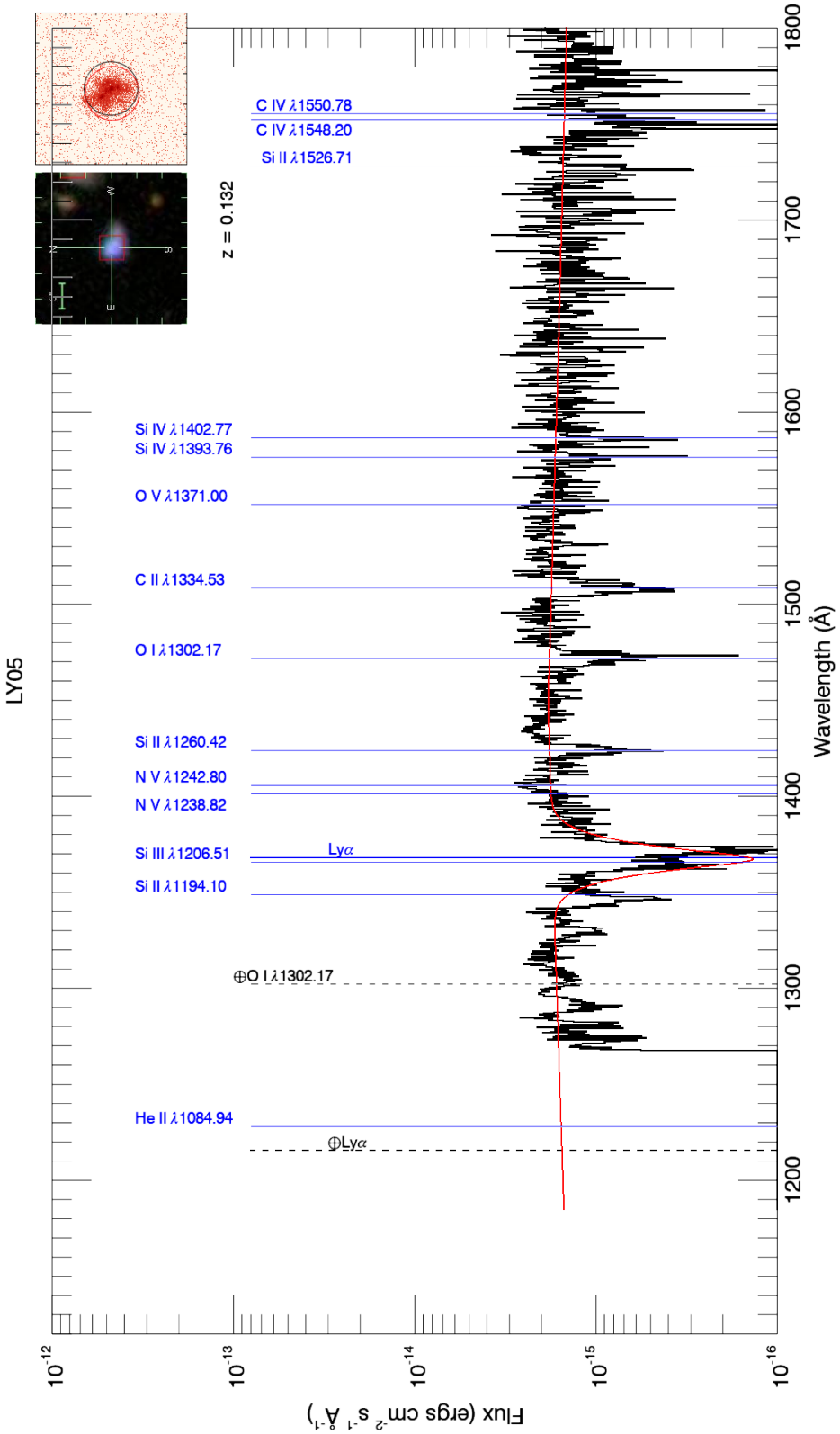

Figure A.6: LY05

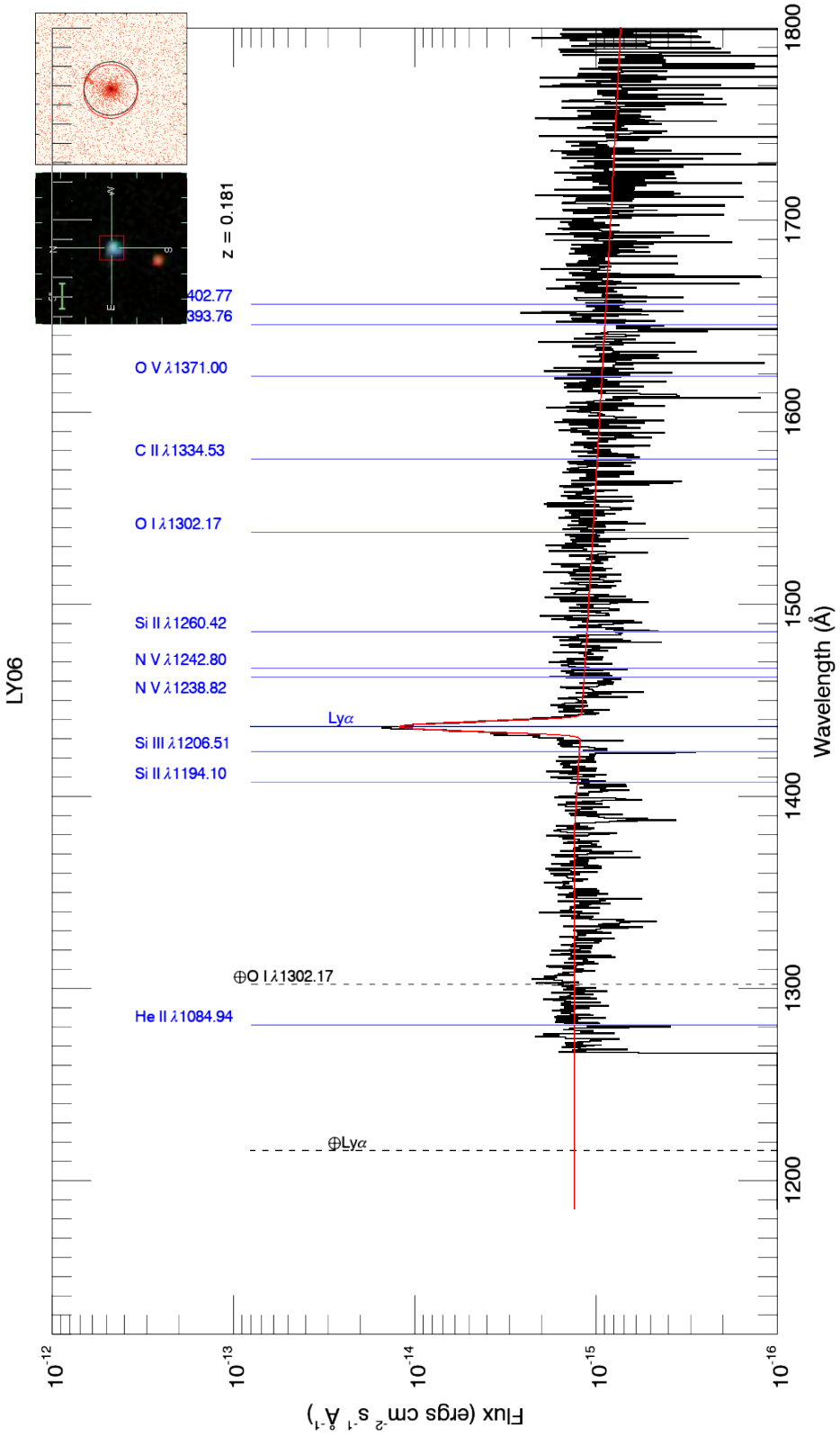

Figure A.7: LY06

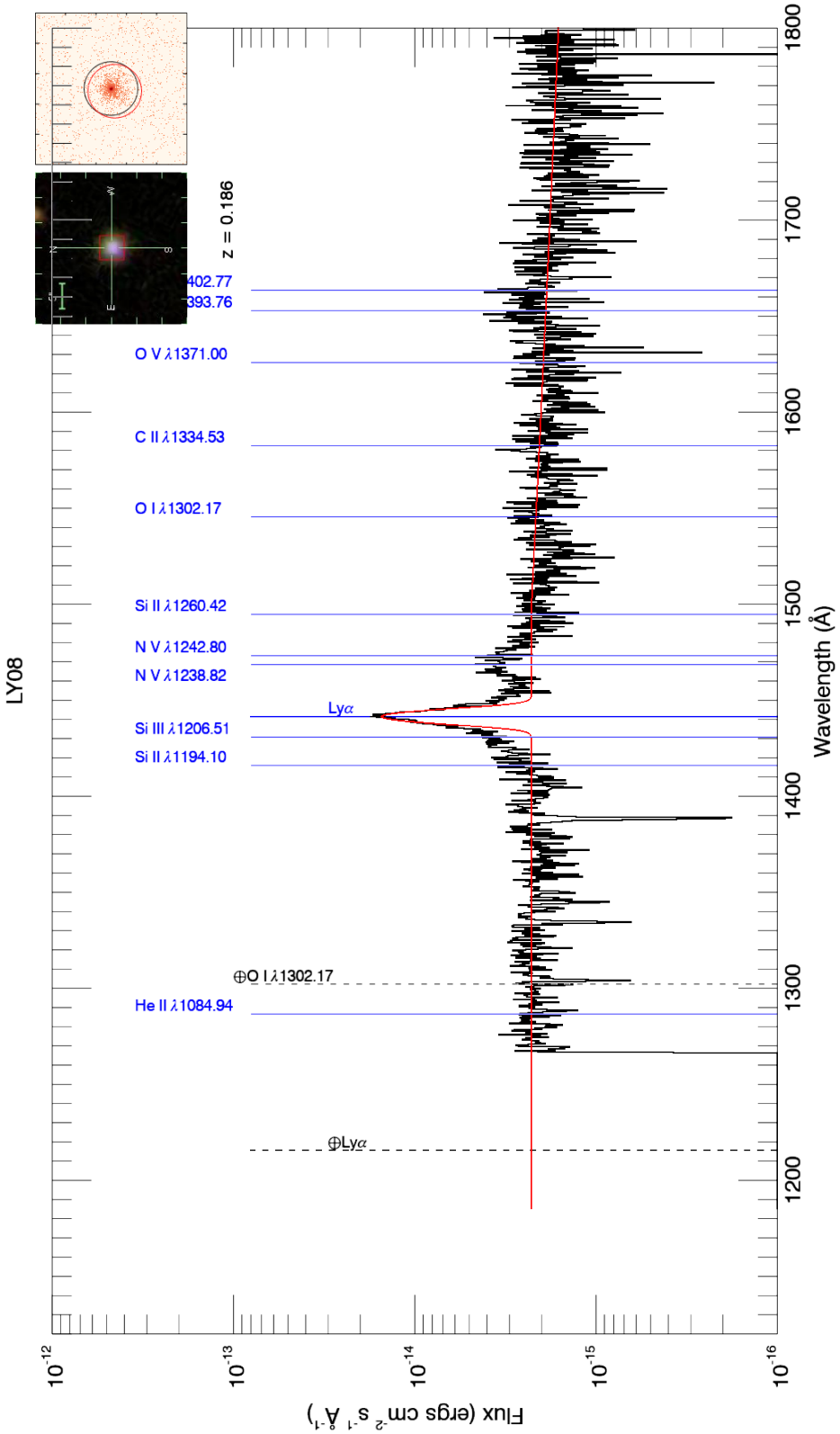

Figure A.8: LY08

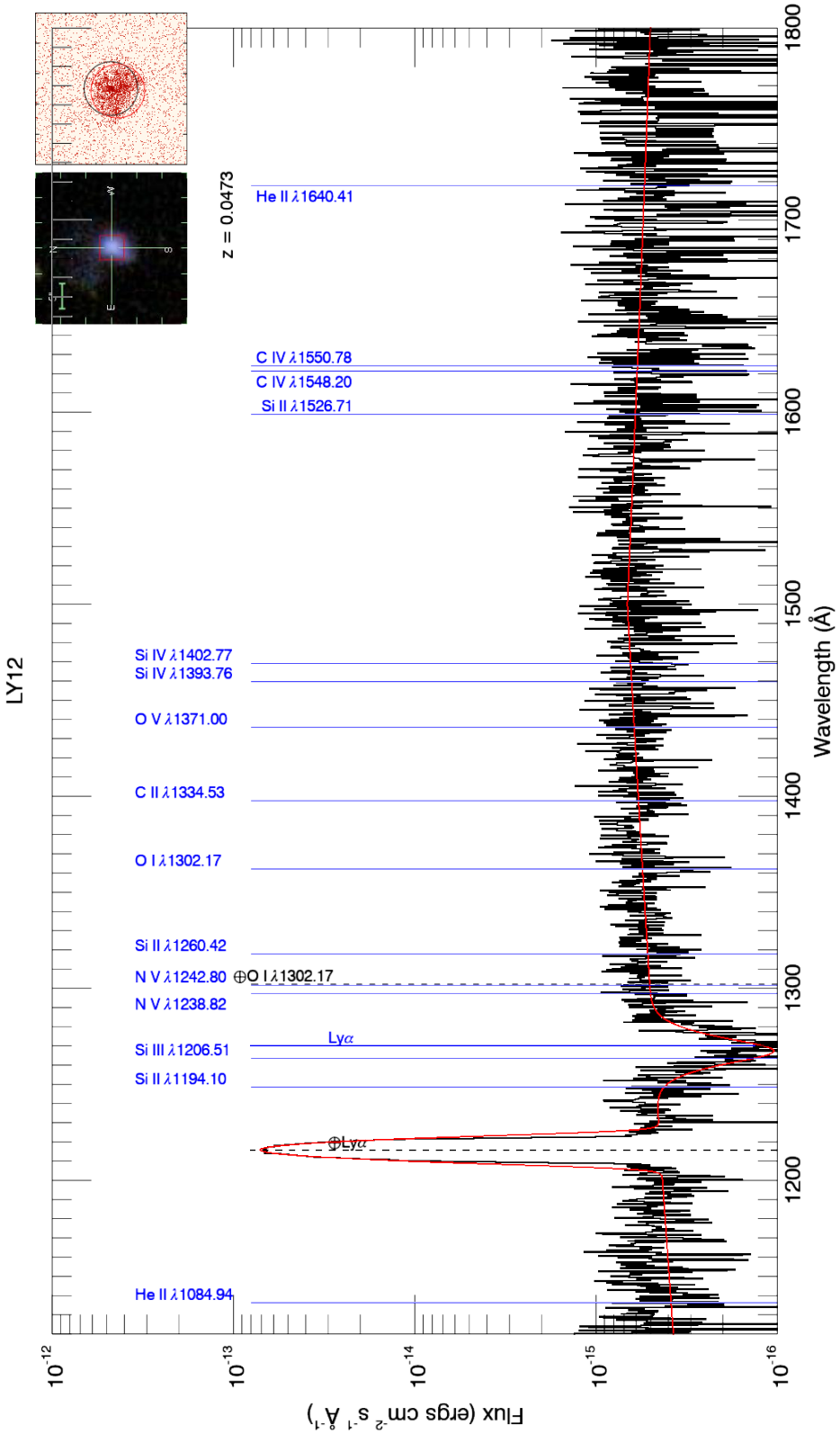

Figure A.9: LY12

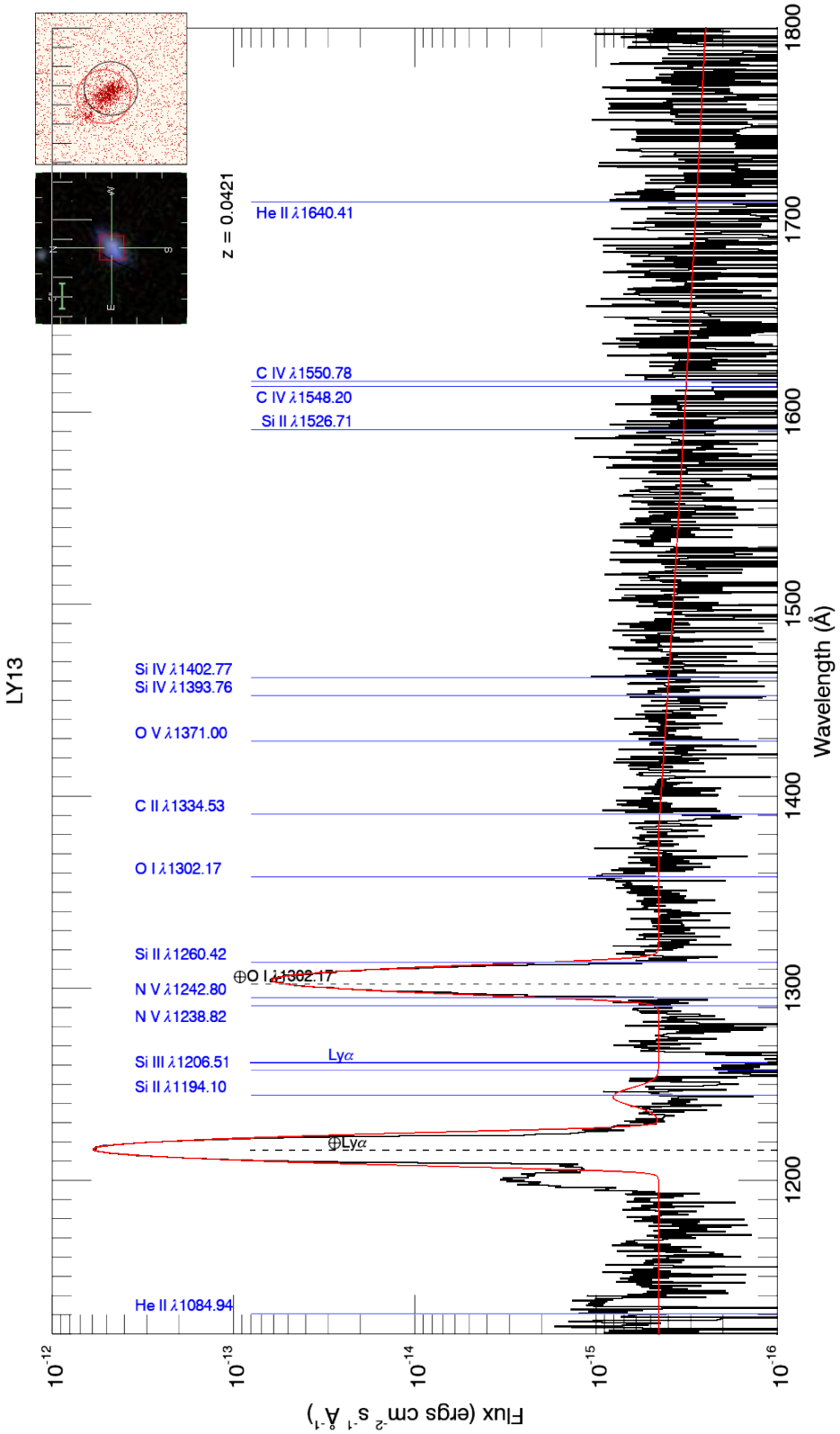

Figure A.10: LY13

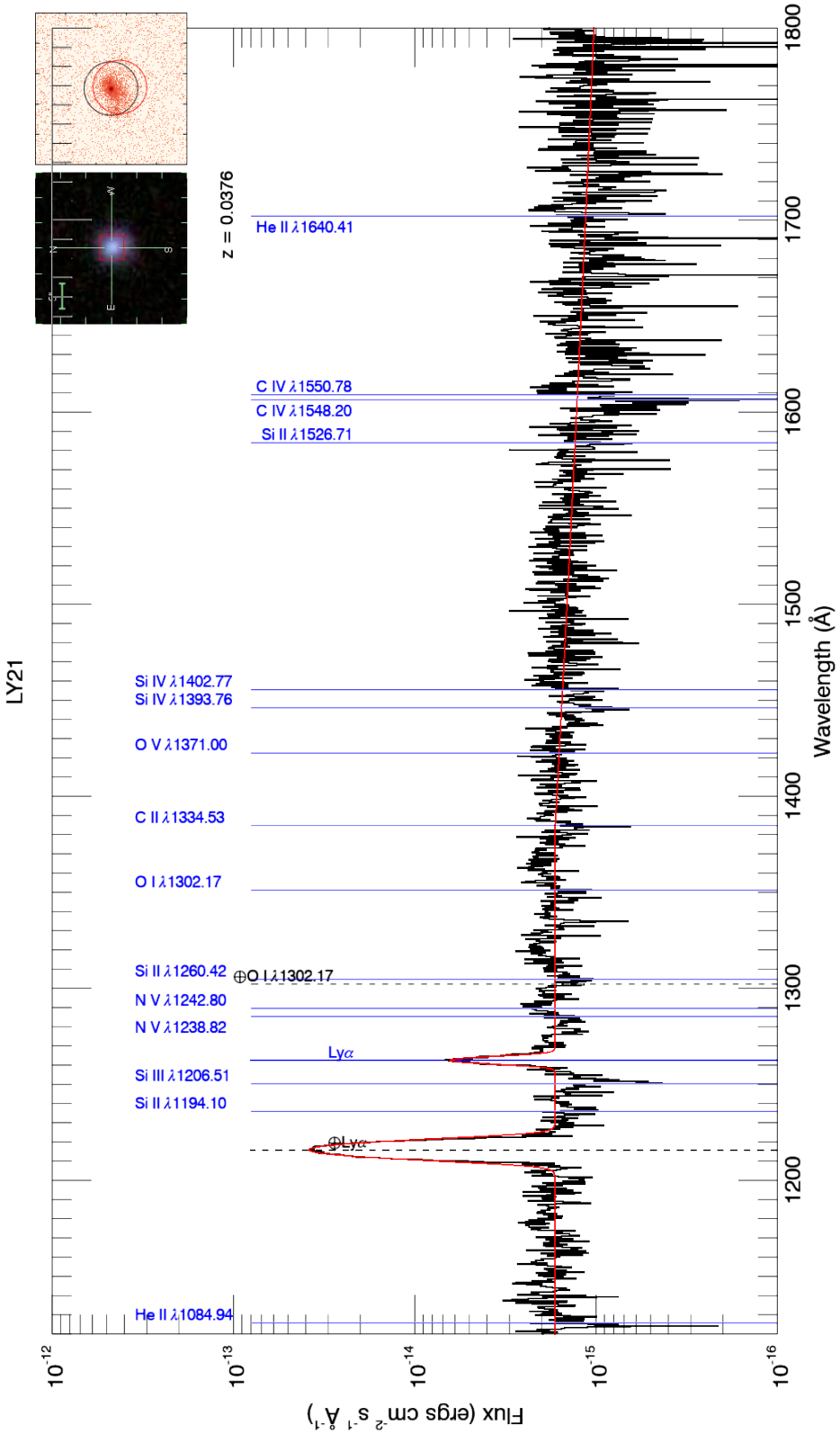

Figure A.11: LY21

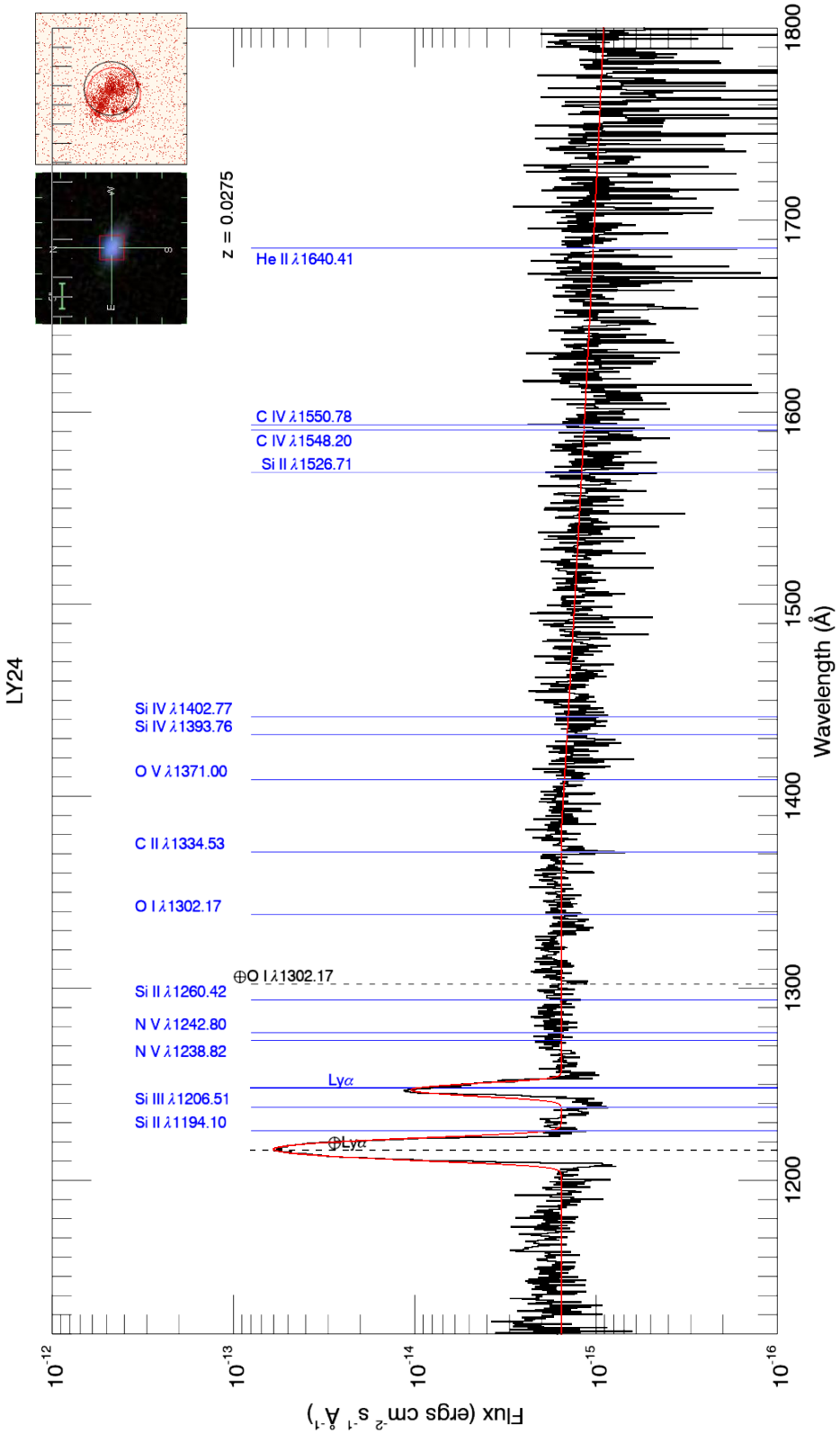

Figure A.12: LY24

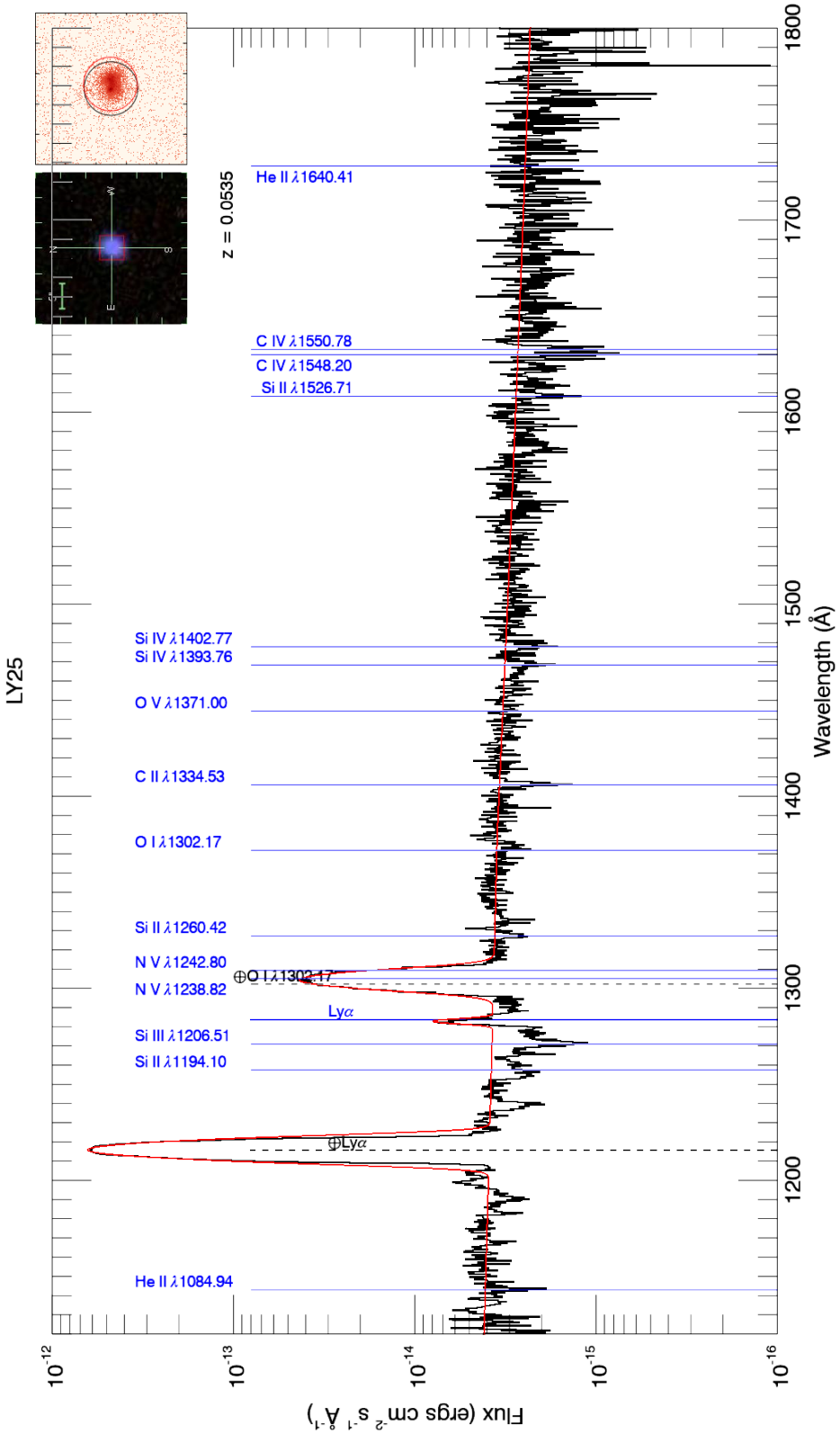

Figure A.13: LY25

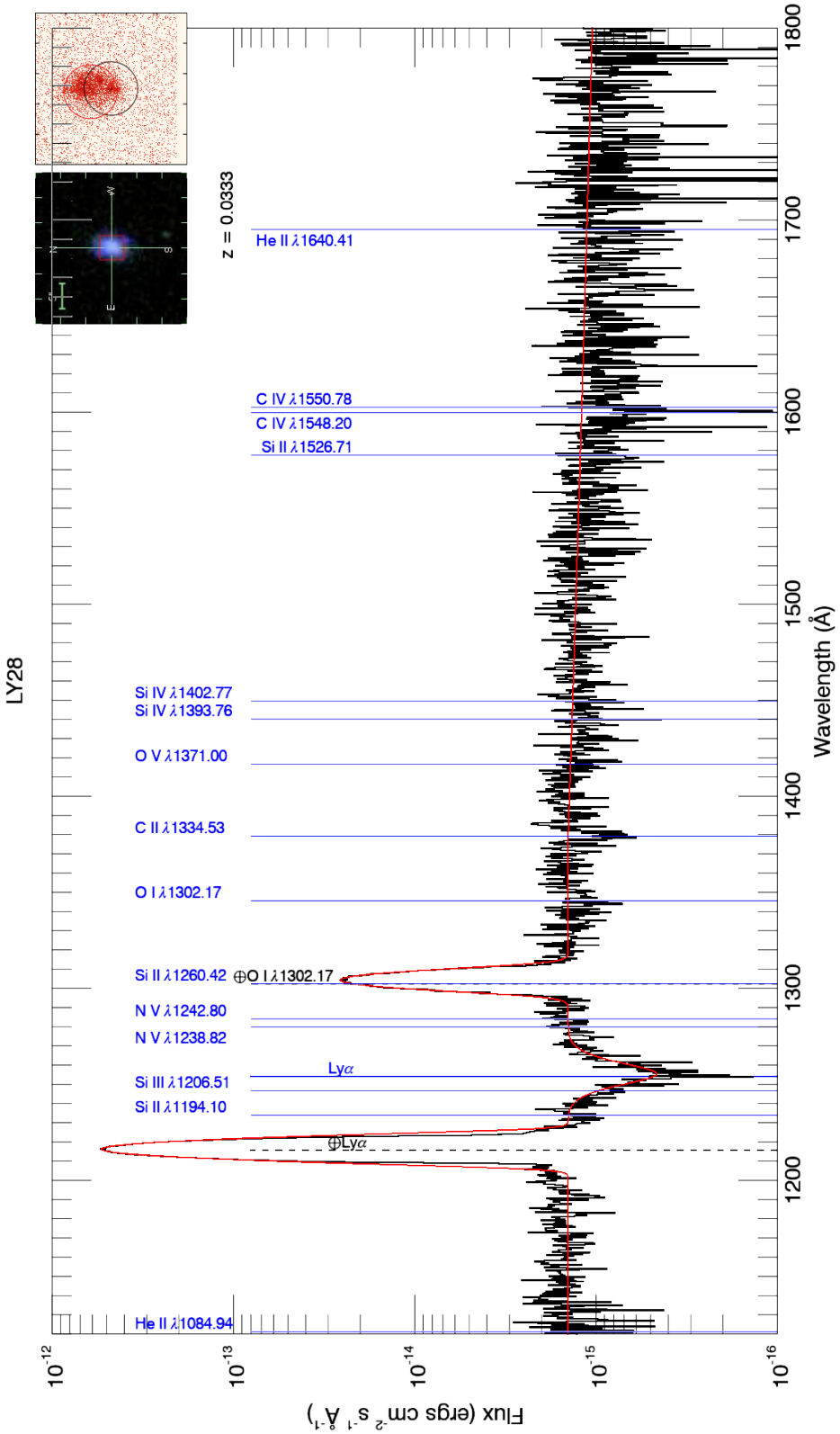

Figure A.14: LY28

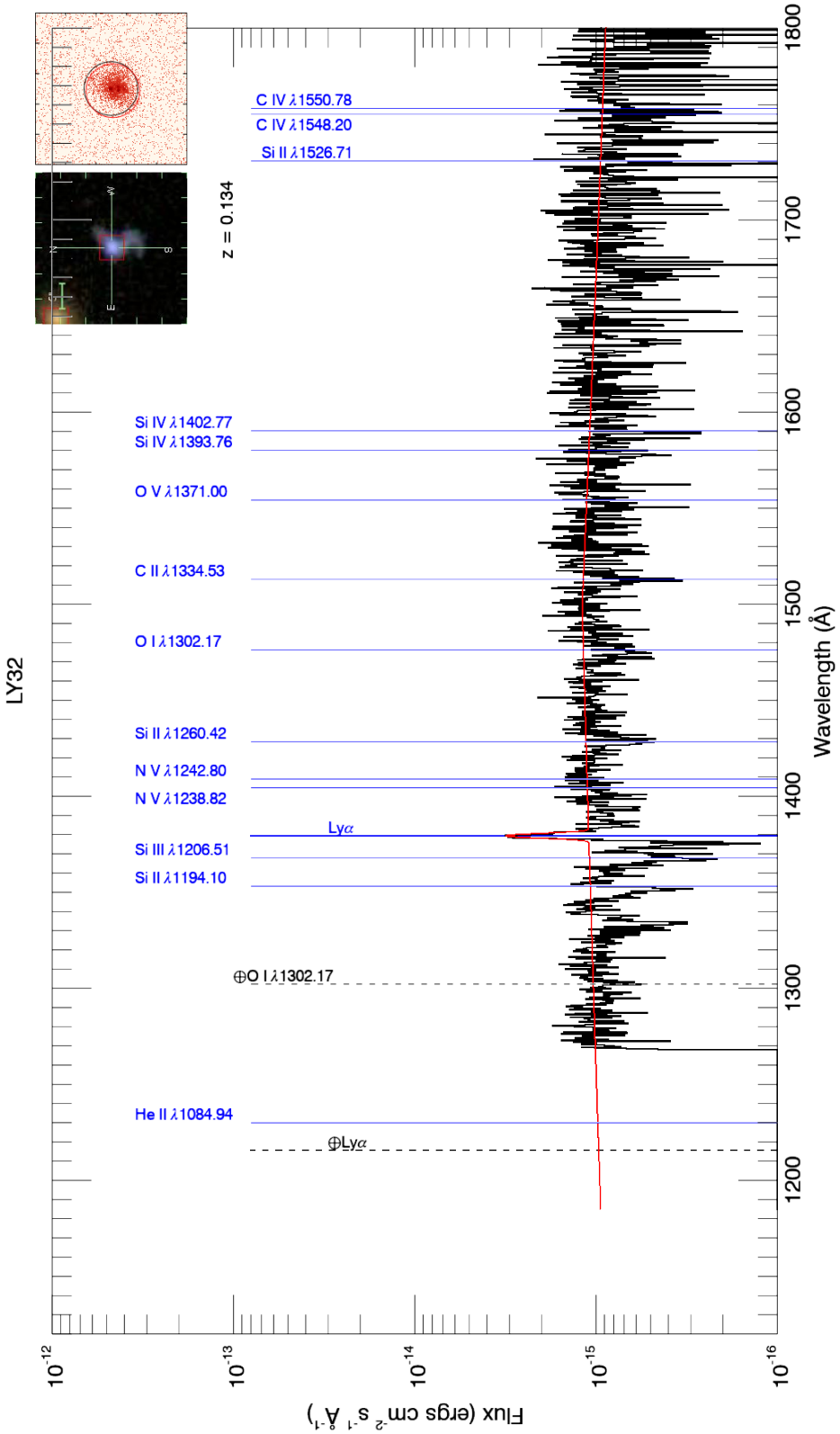

Figure A.15: LY32

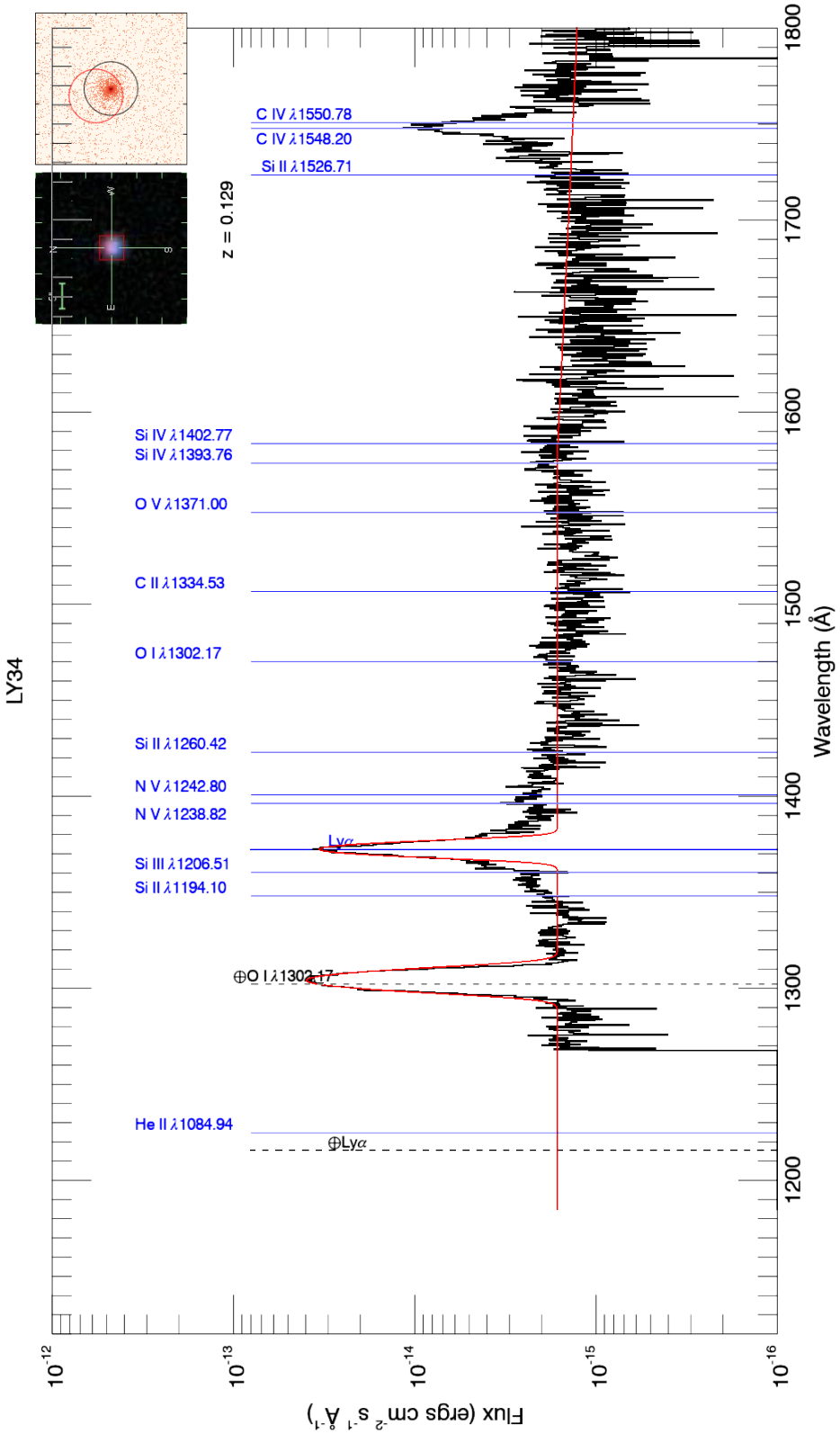

Figure A.16: LY34

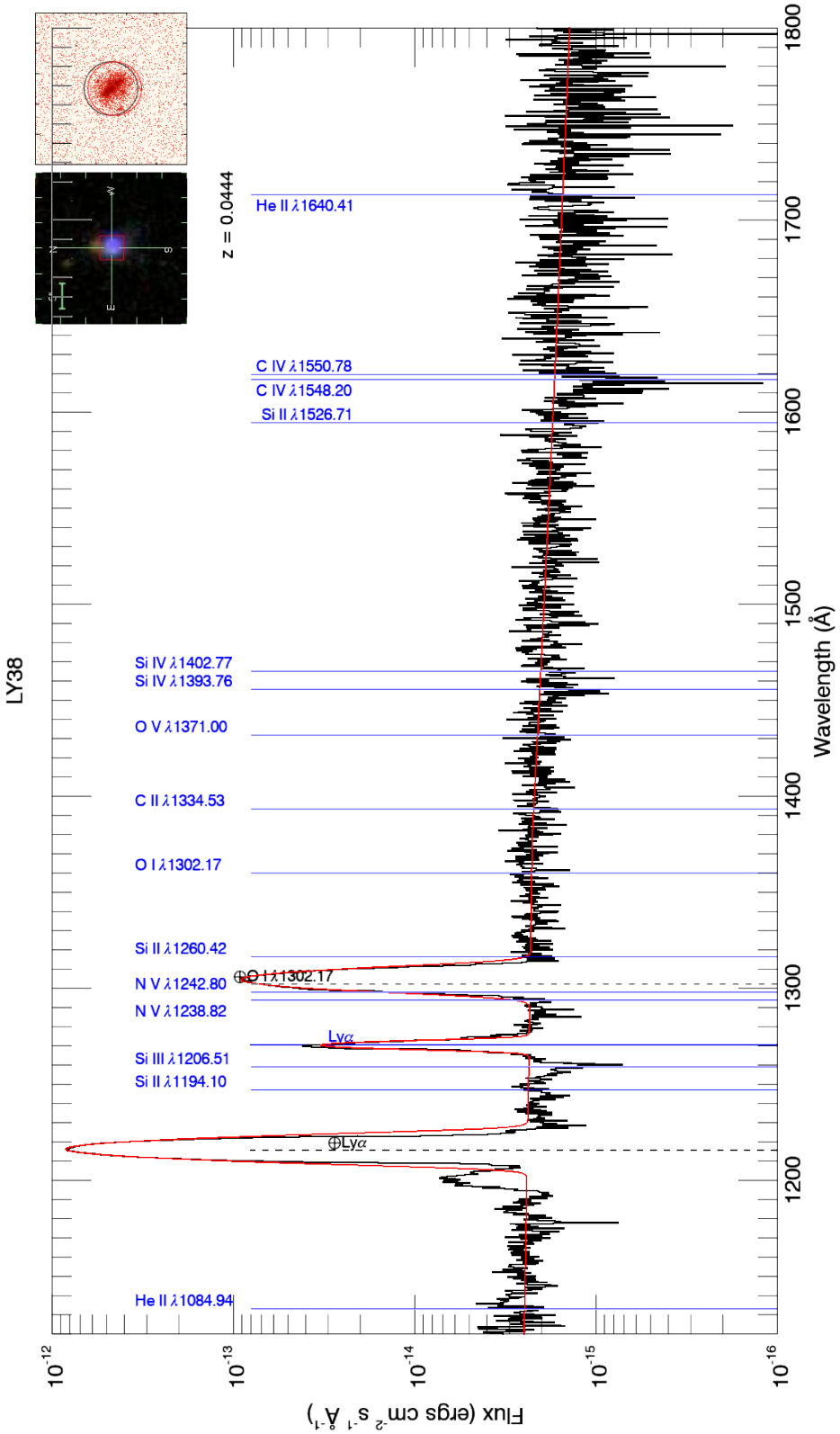

Figure A.17: LY38

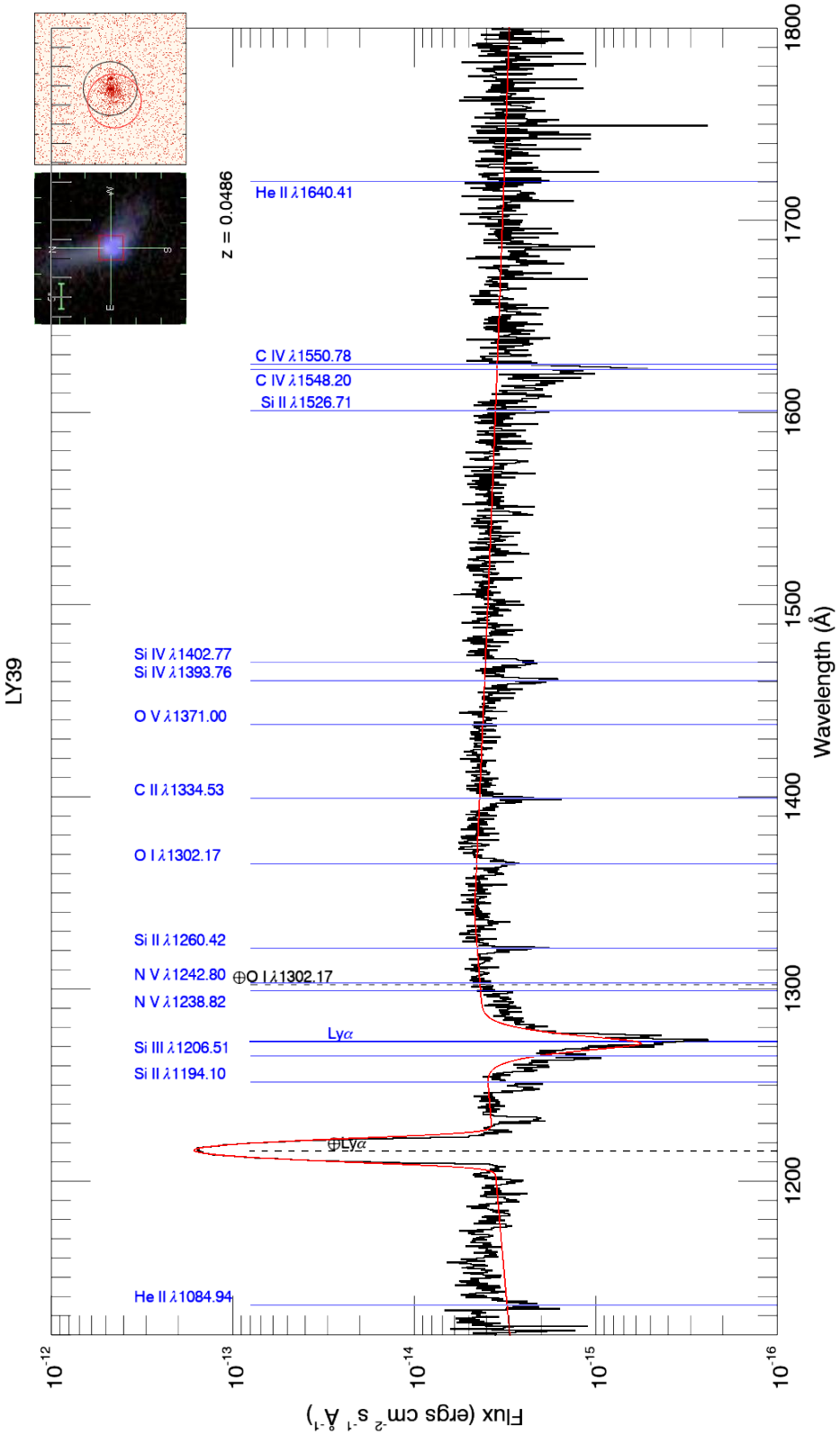

Figure A.18: LY39

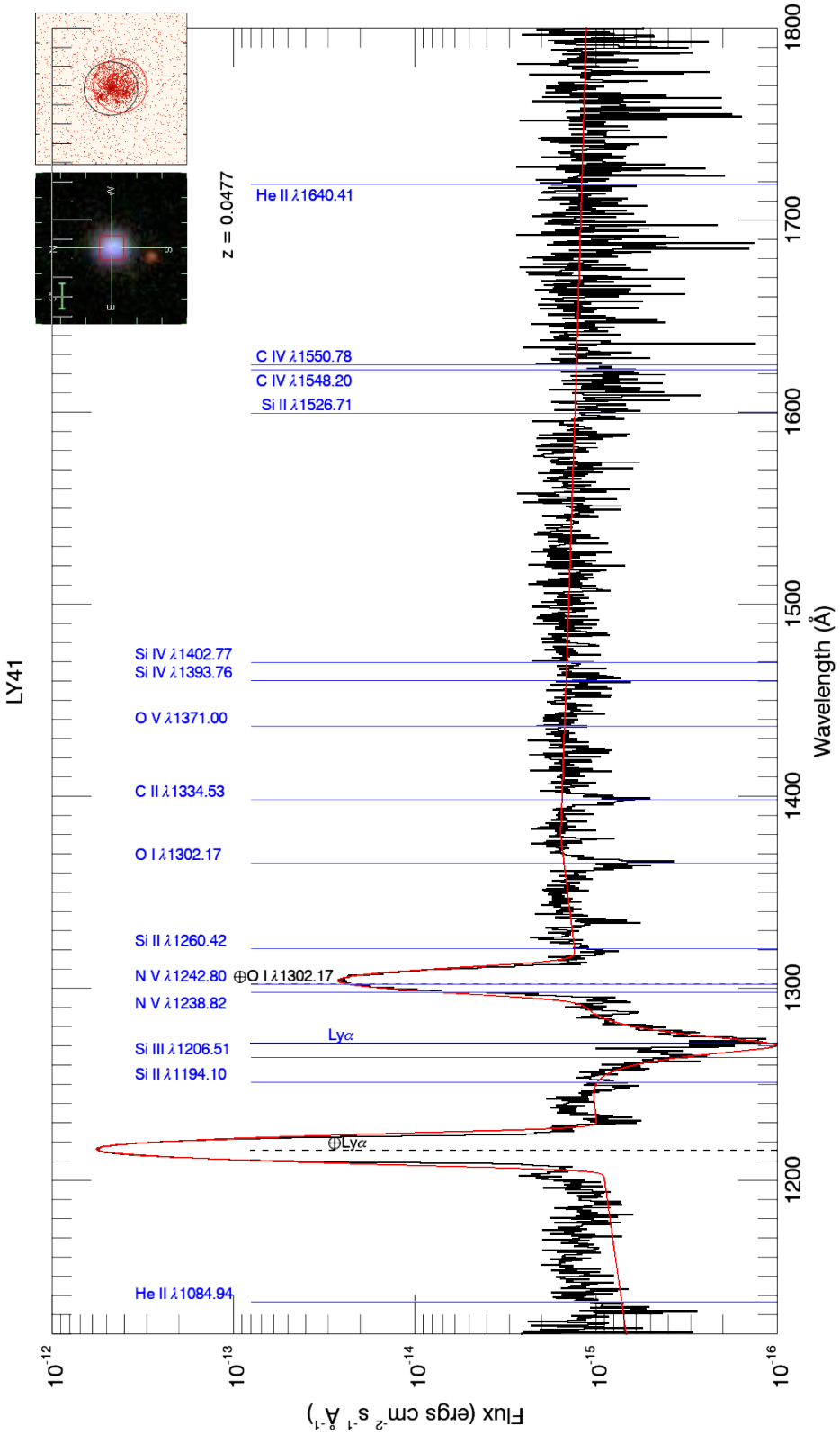

Figure A.19: LY41

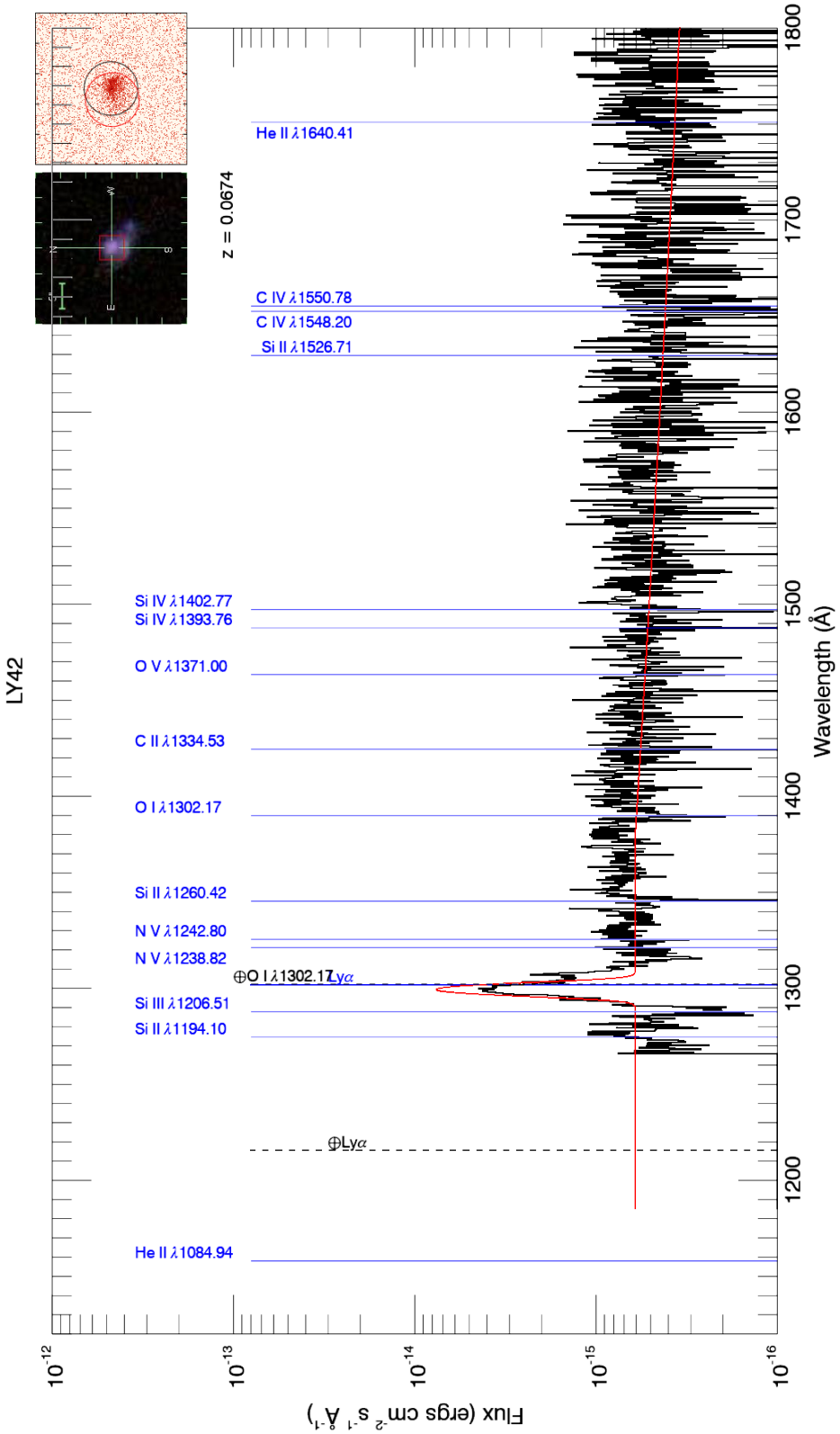

Figure A.20: LY42

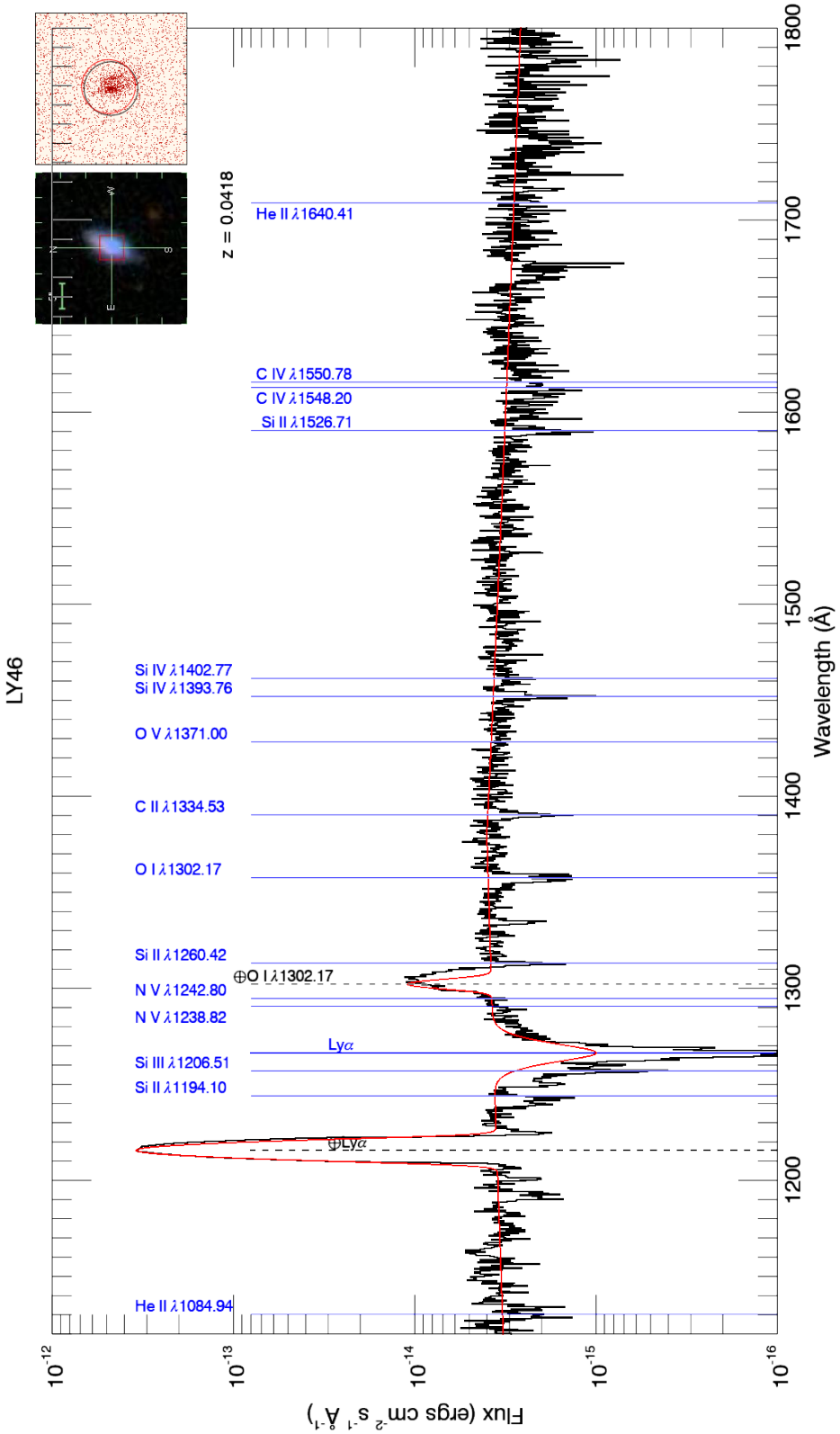

Figure A.21: LY46

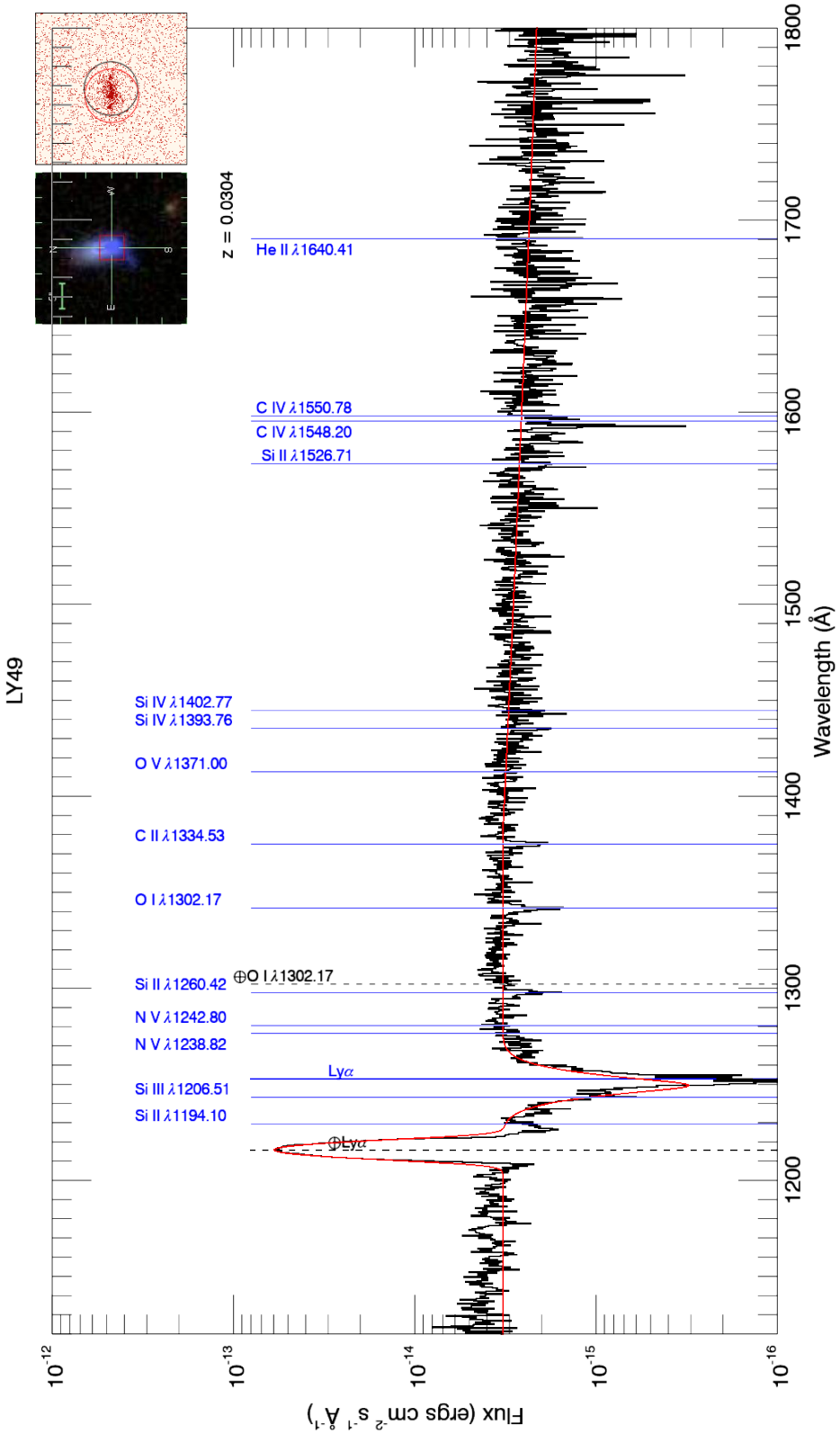

Figure A.22: LY49

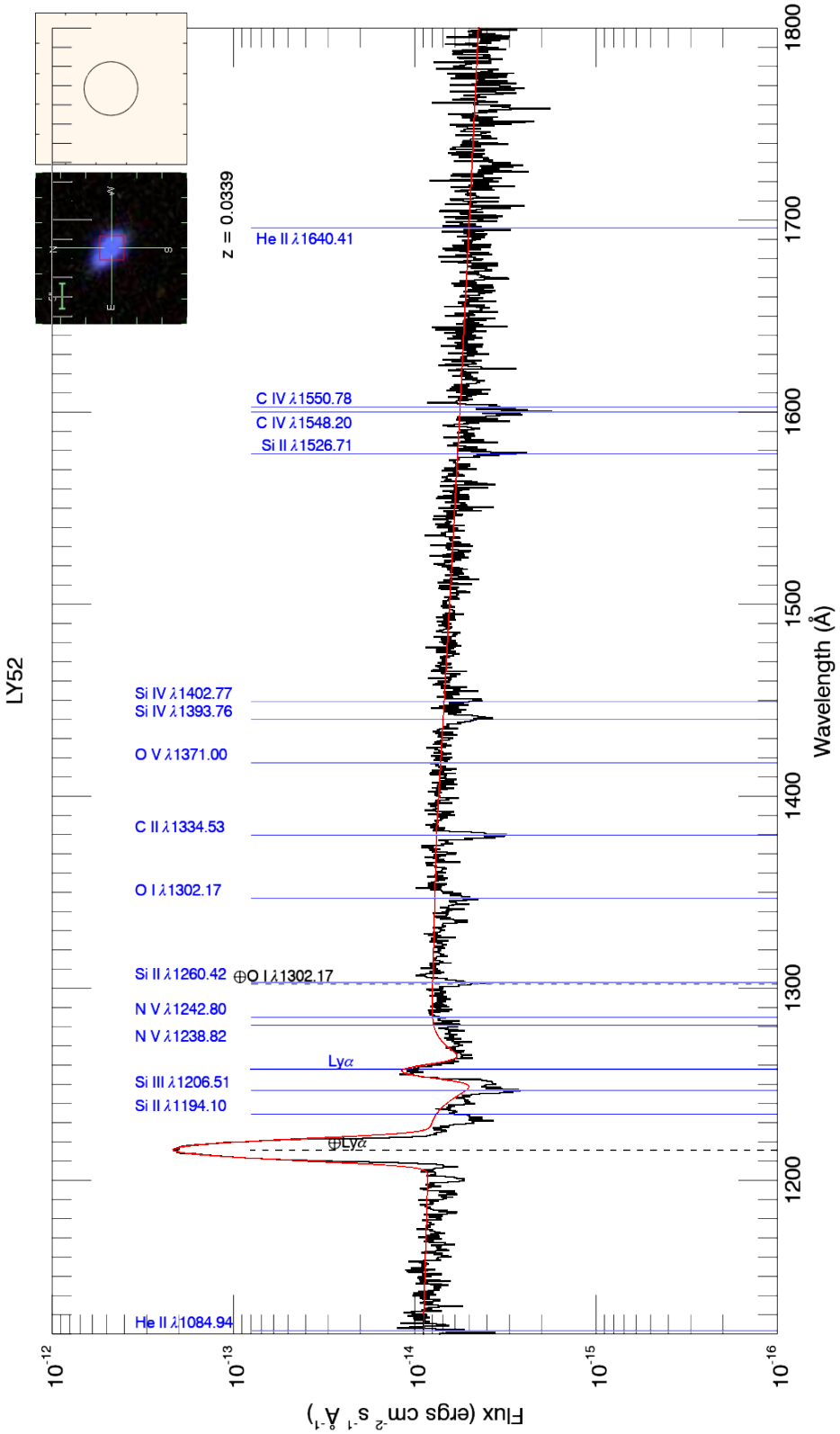

Figure A.23: LY52

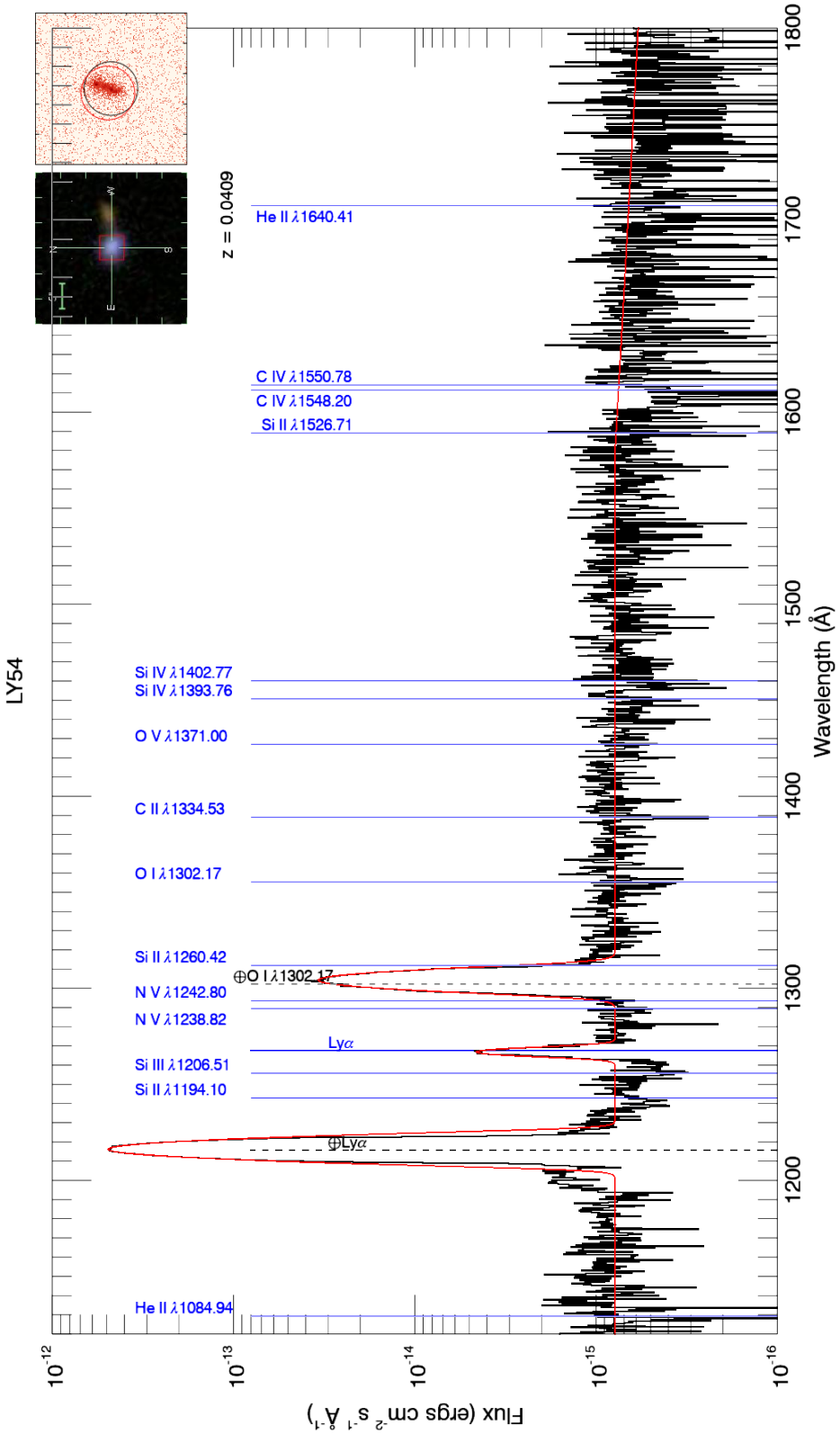

Figure A.24: LY54

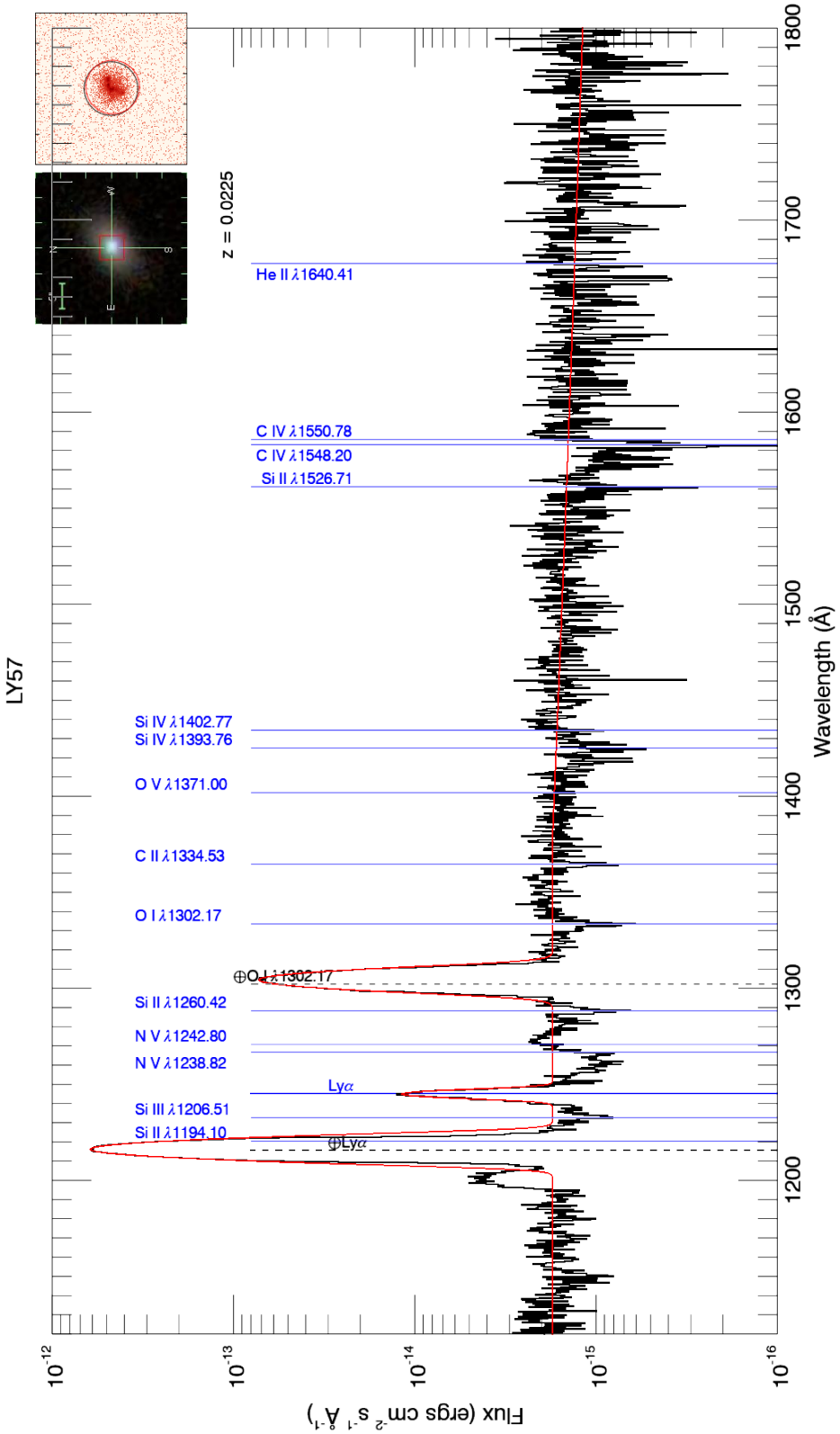

Figure A.25: LY57

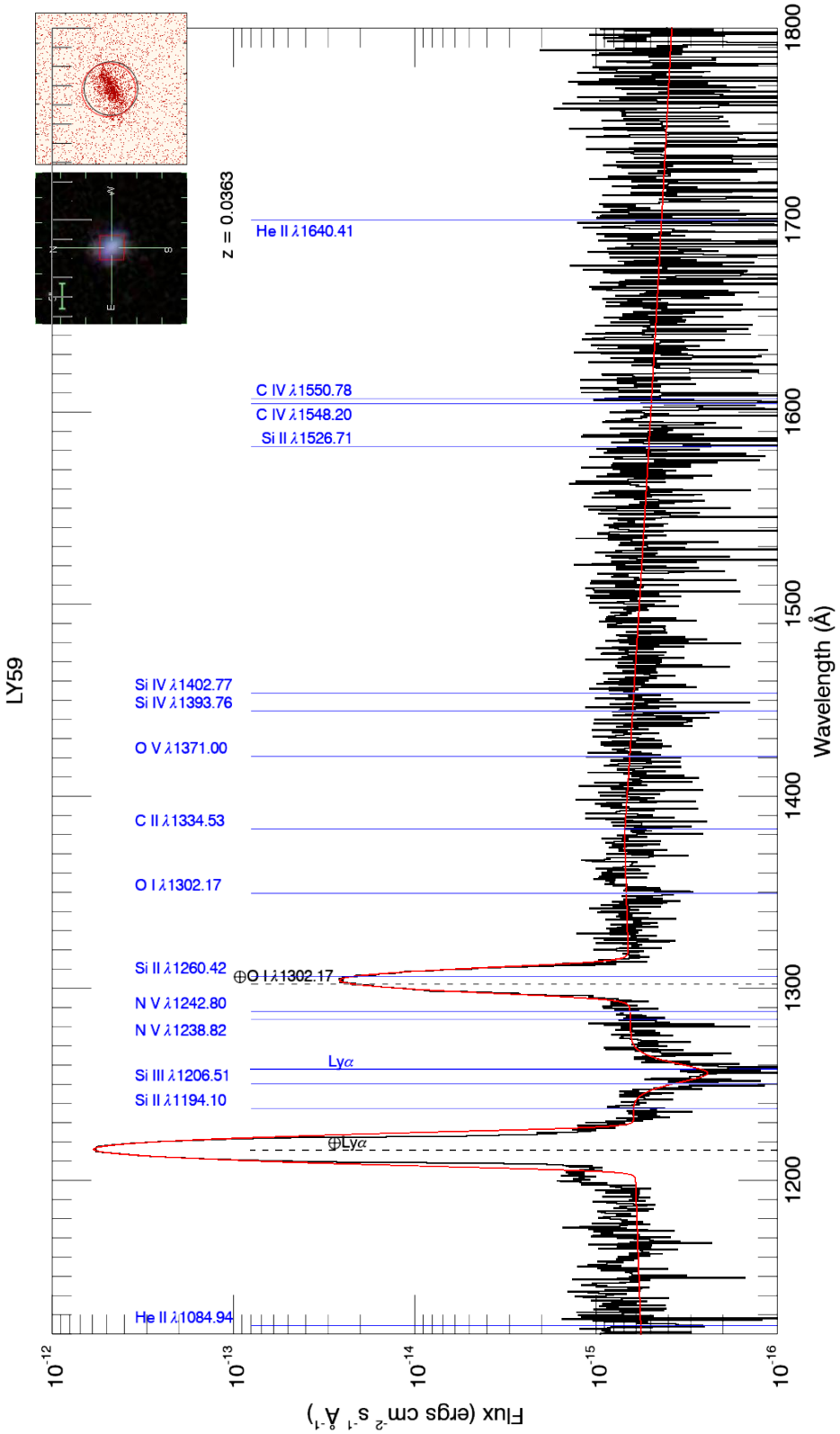

Figure A.26: LY59

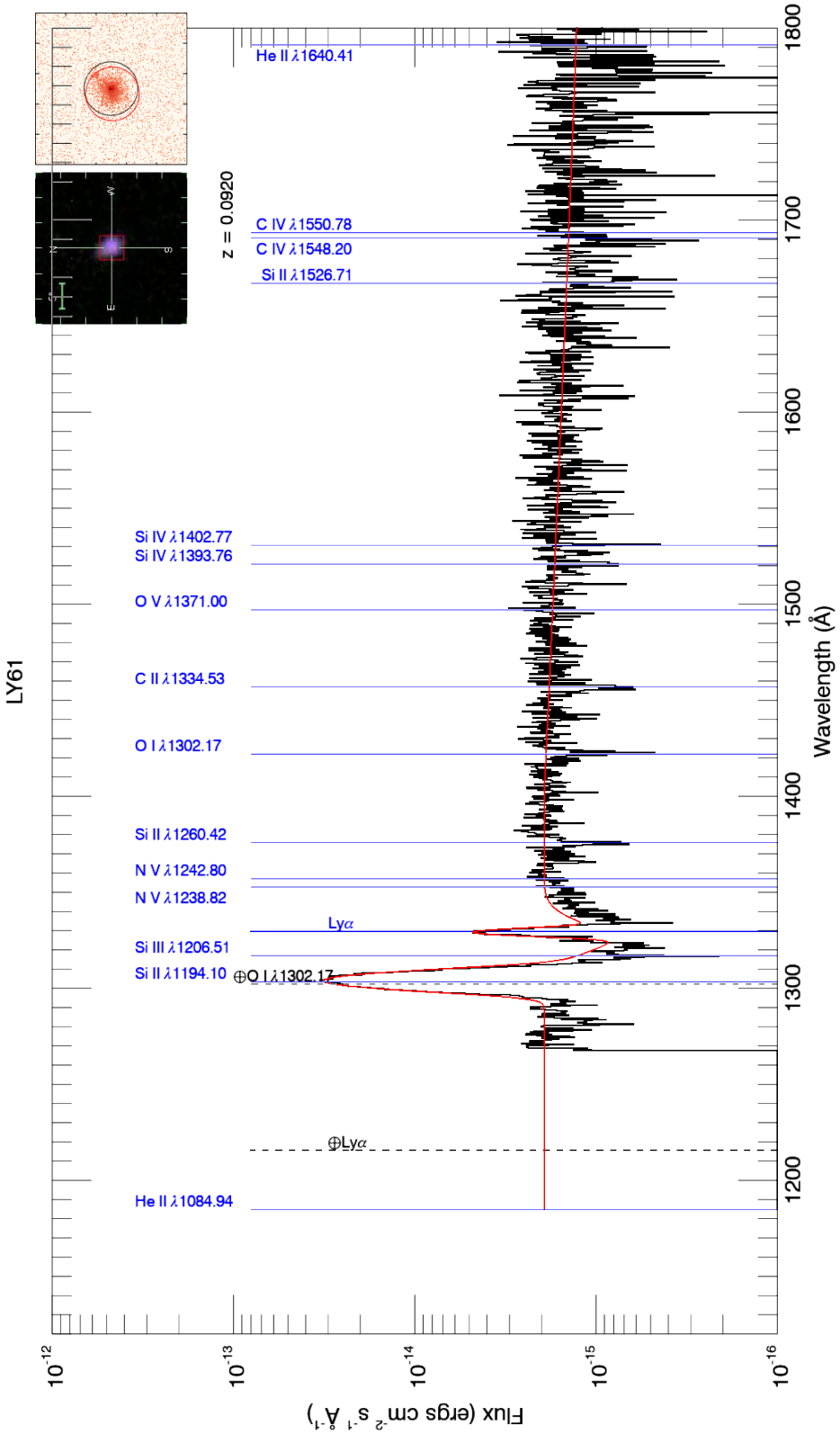

Figure A.27: LY61

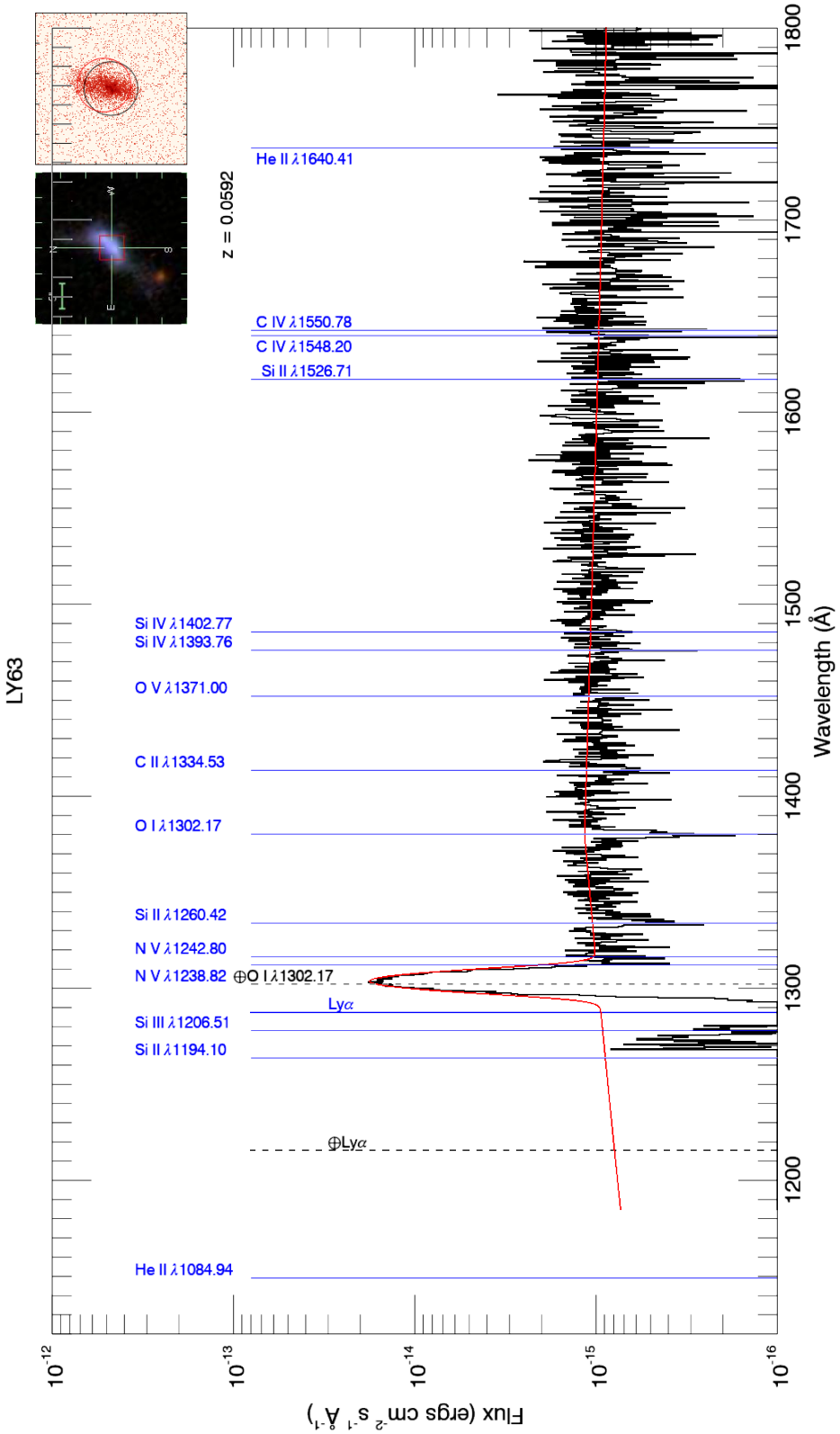

Figure A.28: LY63

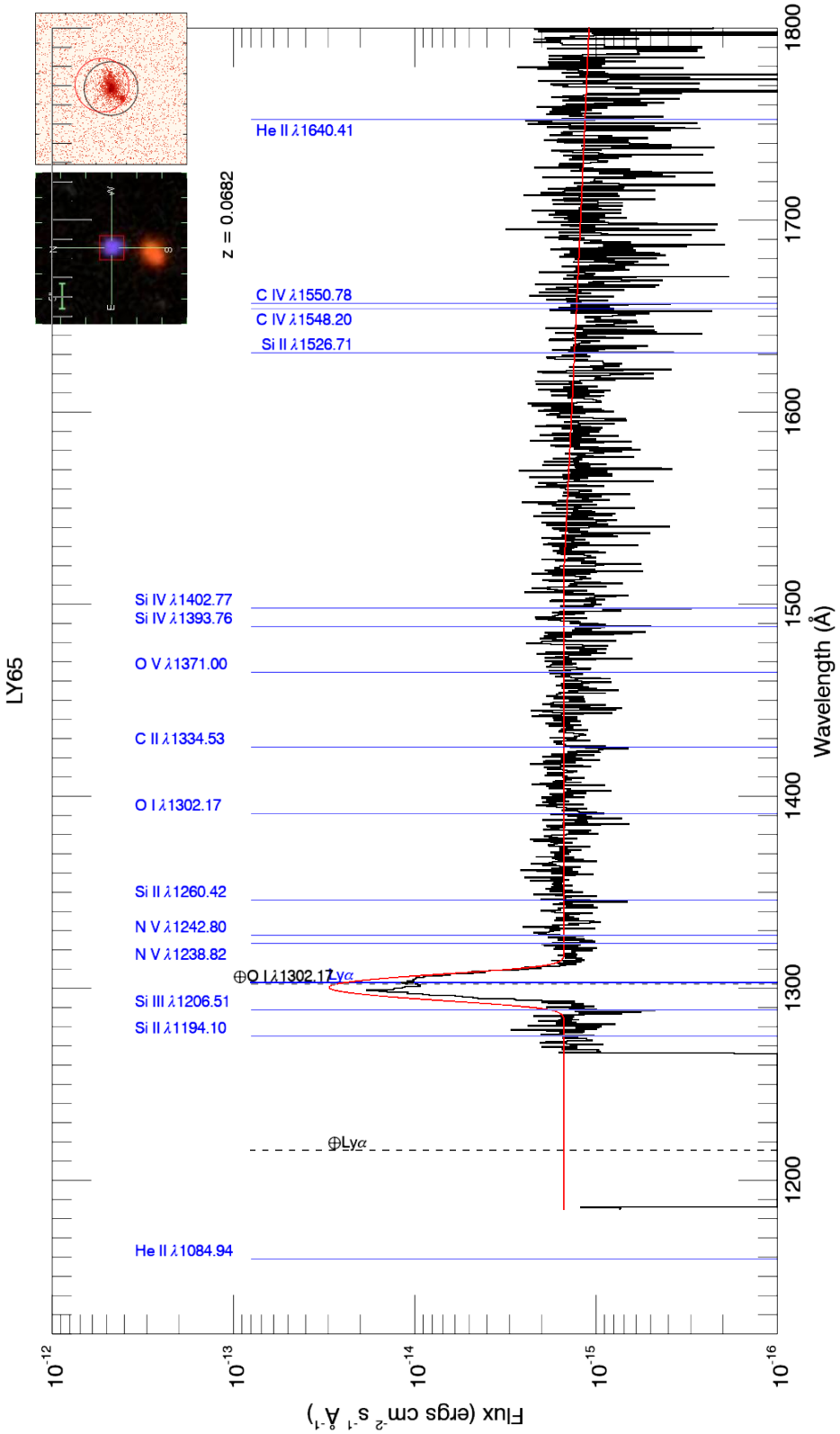

Figure A.29: LY65

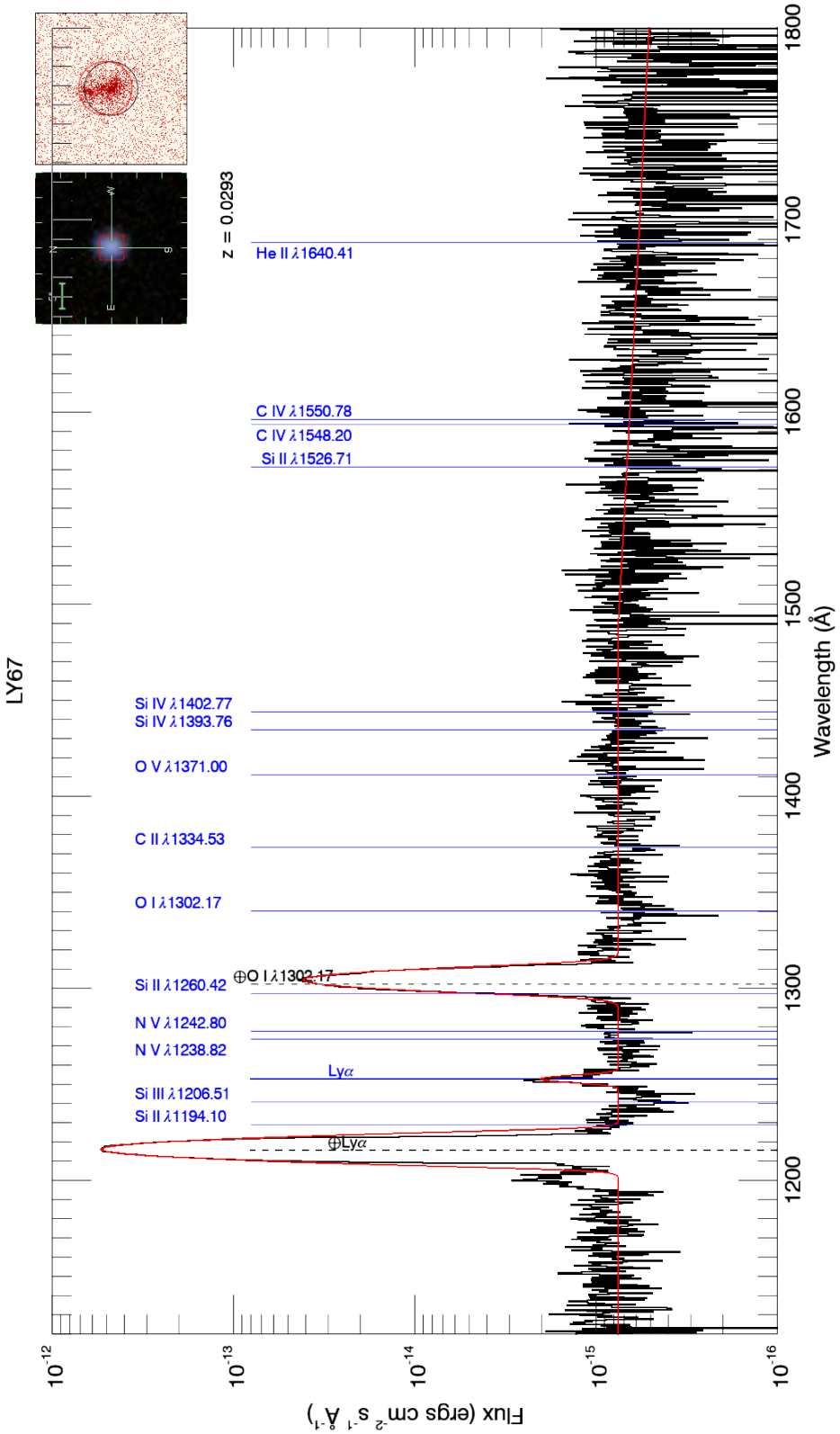

Figure A.30: LY67

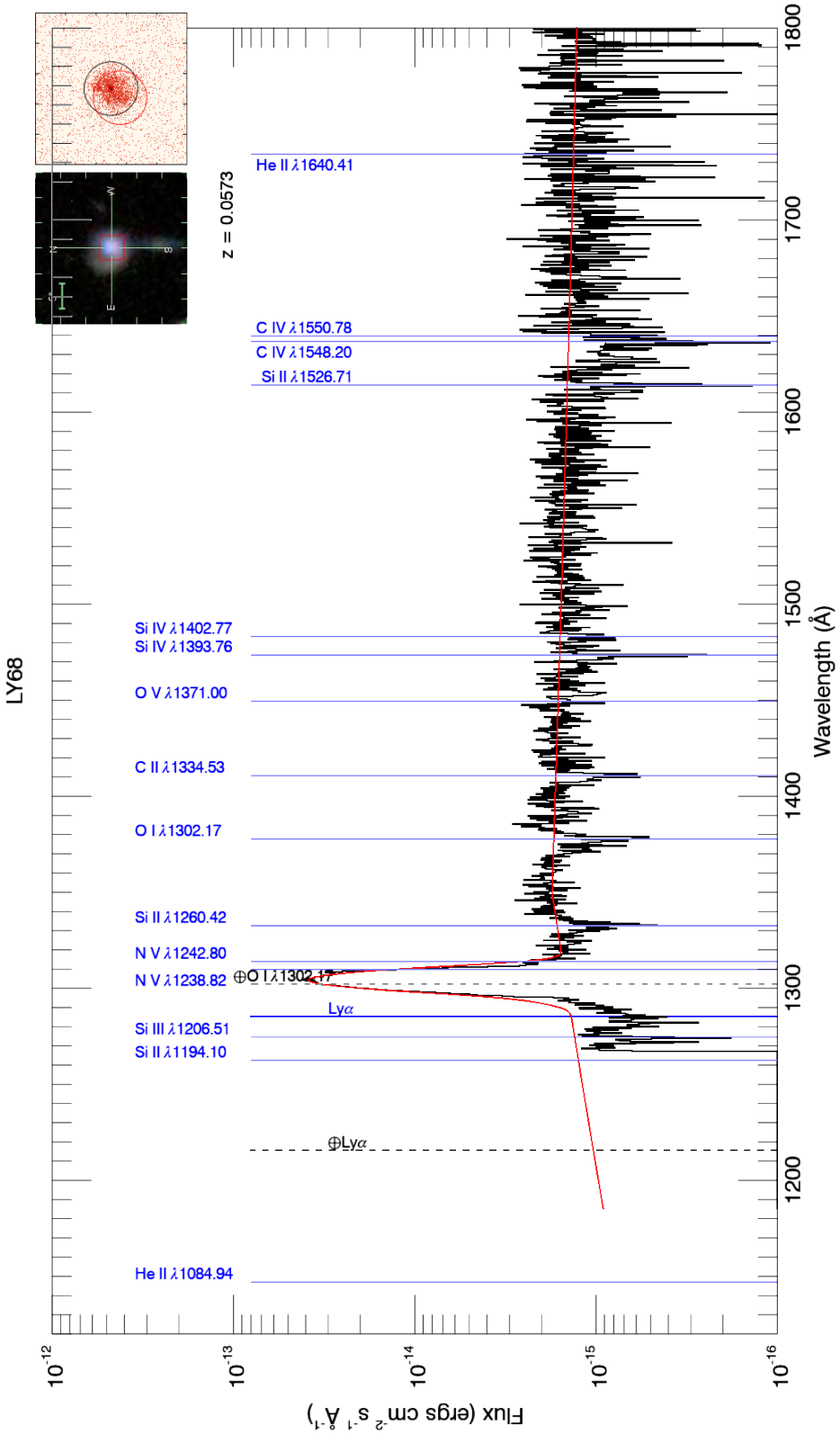

Figure A.31: LY68

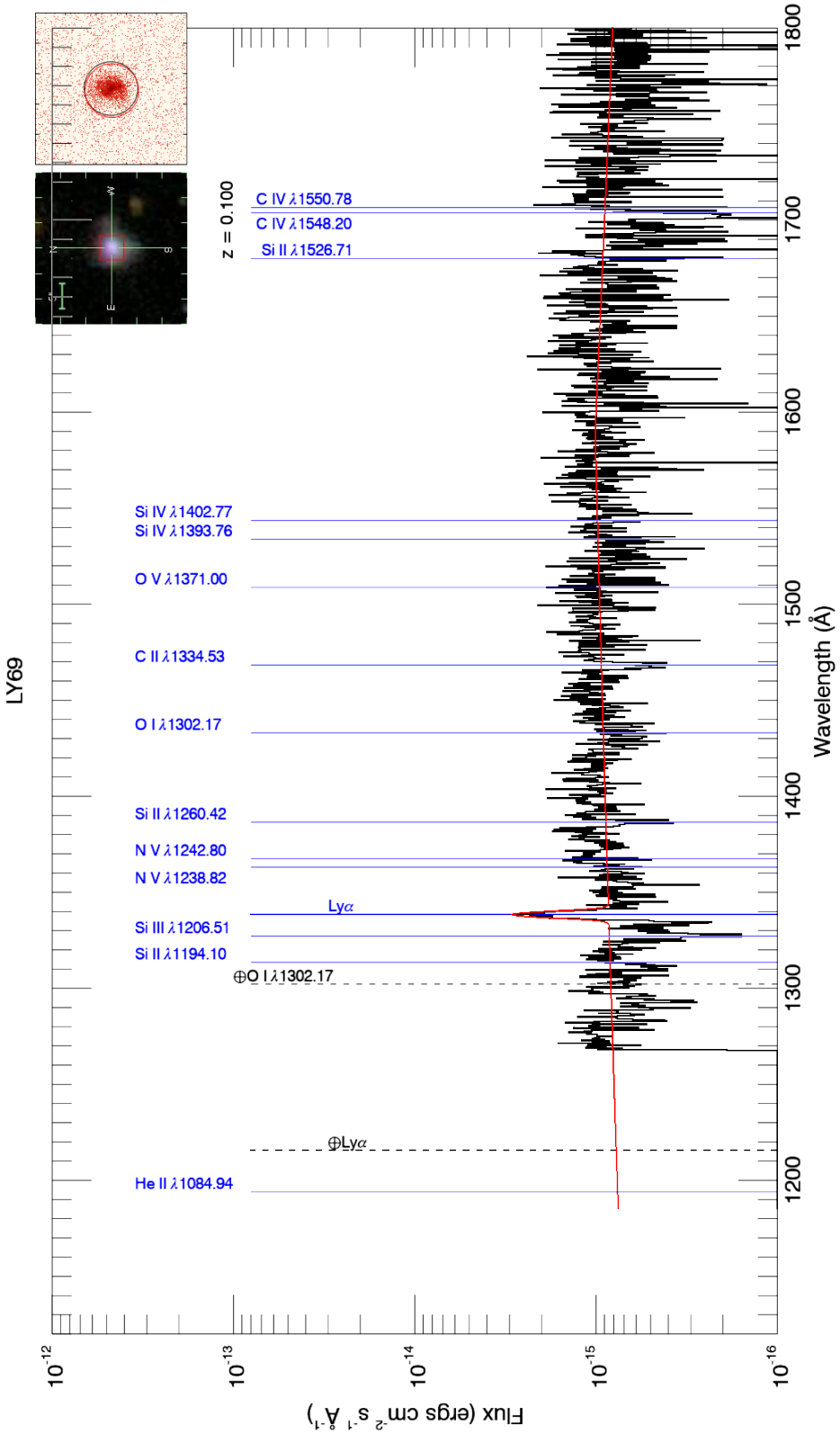

Figure A.32: LY69

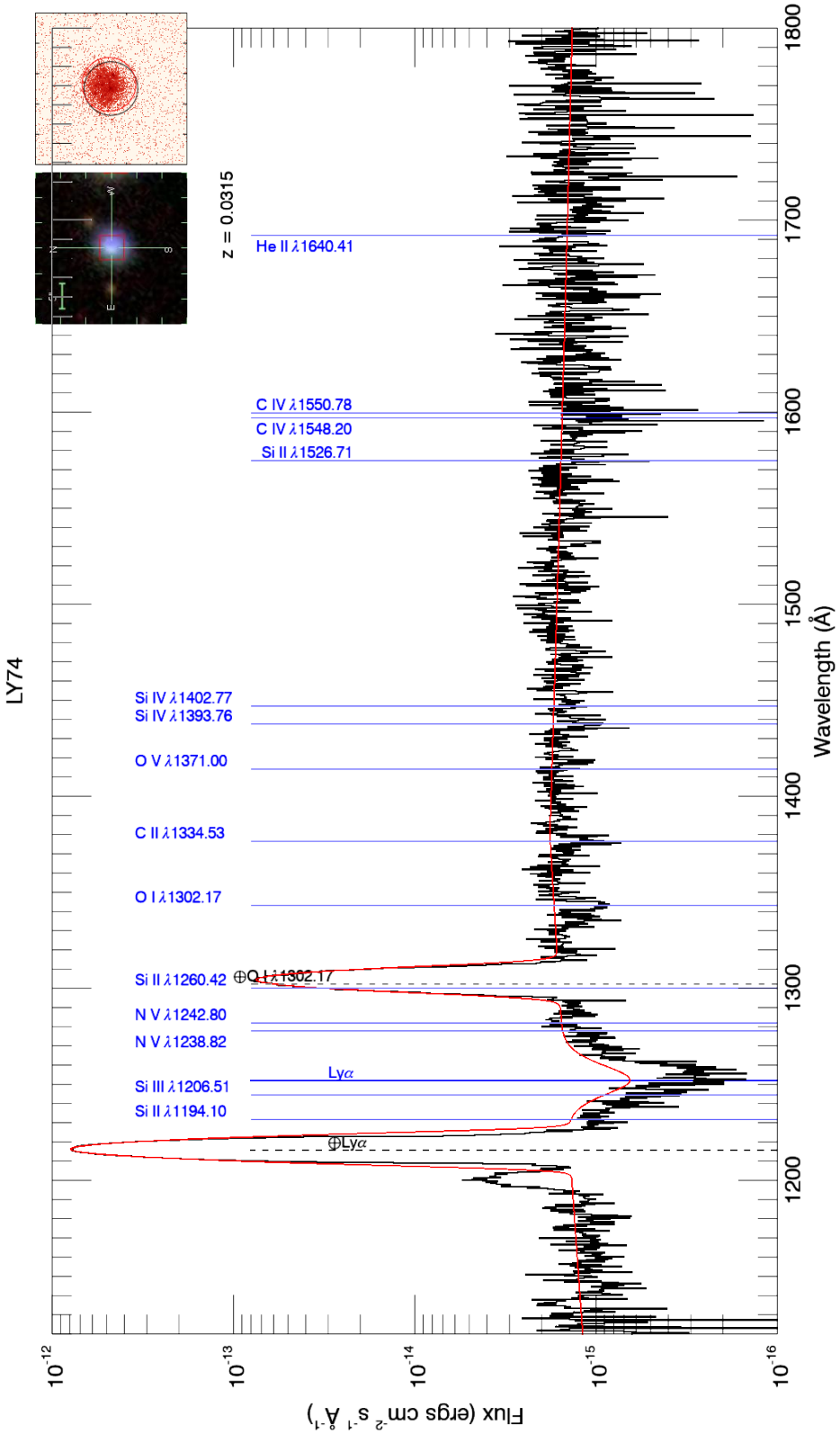

Figure A.33: LY74

Appendix B

COS and SDSS Spectra with SB99 Model

This appendix is a compilation of composite spectra from 900 Å to 10000 Å, showing the full spectrum of each target by COS and SDSS in black, ordered by calculated Lyα escape fraction. Red points describe total fluxes measured by GALEX NUV and FUV images, with bandpass of each GALEX filter spanned by the horizontal bars and the point centered on the mean central wavelength weighted by sensitivity. Each of these different instruments have a different aperture size ($2.5^{'}$ diameter for COS, $3^{'}$ diameter for SDSS, $1.5^{'}$ for GALEX), which risks confusion of the target galaxy with background objects, but none of the galaxies show significant UV emission in the COS acquisition images out to $3.5^{'}$ from the center of the COS aperture. The green line denotes the Starburst99 model fit, normalized to SDSS flux at 4050 Å

(shown by a red dot). The model parameters are written at the top of the plot, and given by instantaneous star formation, metallicity Z=0.040, and a Salpeter IMF. The redshift z, Balmer decrement E(B-V), dust model parametrization R_v, and optimized Fitzpatrick-Massa far-UV extinction parameter c_4 (see Section 2.5) are also printed above. The age of the SB99 model is determined by fit to the SDSS spectrum at the 4000 Å break and this age is listed near that break in green. Finally, the normalization factor determines the initial stellar mass scaled to the SB99 input of 10^6 $M_\odot$, listed in the second line at the top of the window. This SB99 curve will match well the spectra that are dominated by flux by stars in the host galaxy, but will diverge from the data where there is strong AGN activity, especially in targets LY08 and LY34.

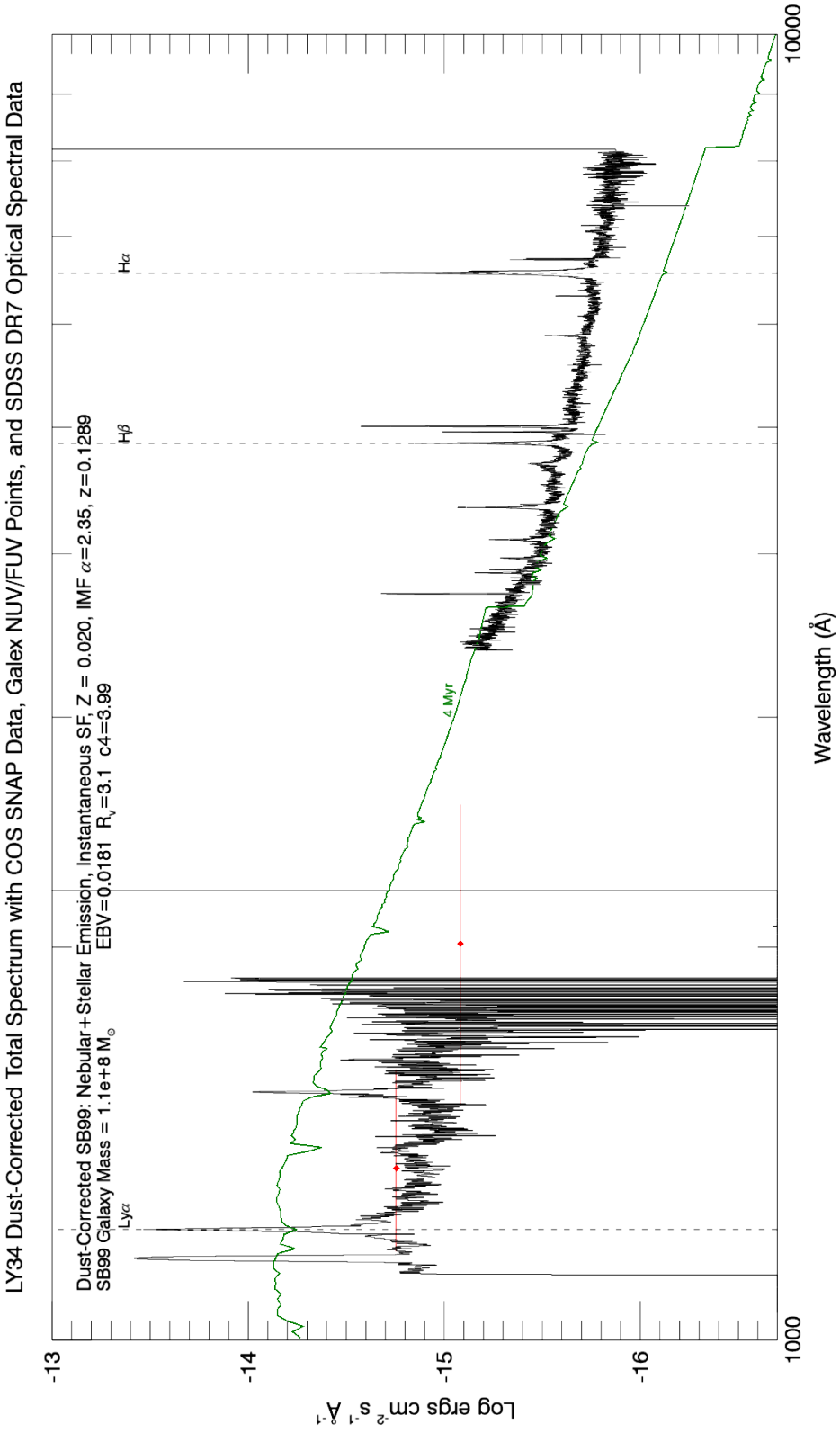

Figure B.1: LY34

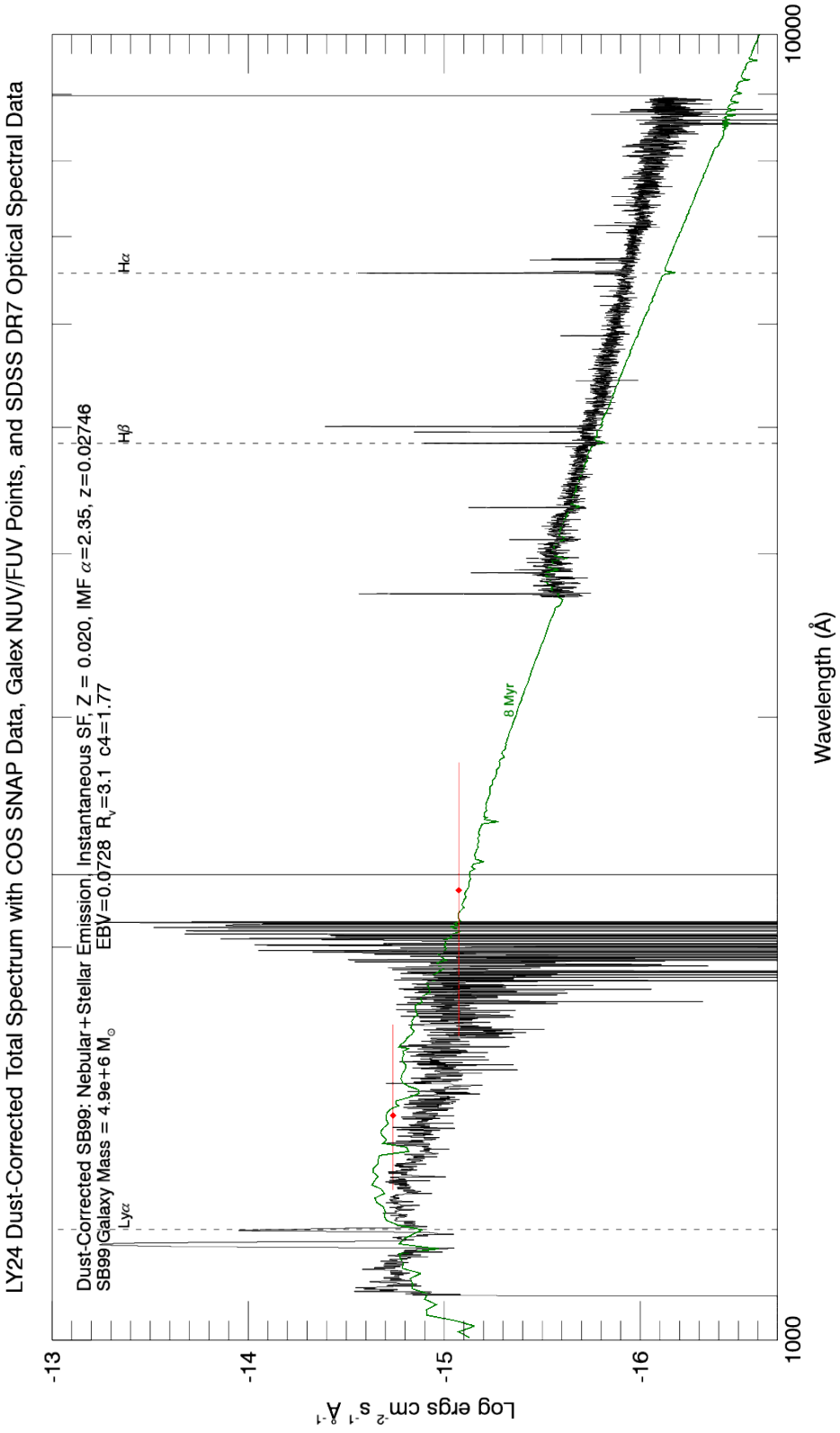

Figure B.2: LY24

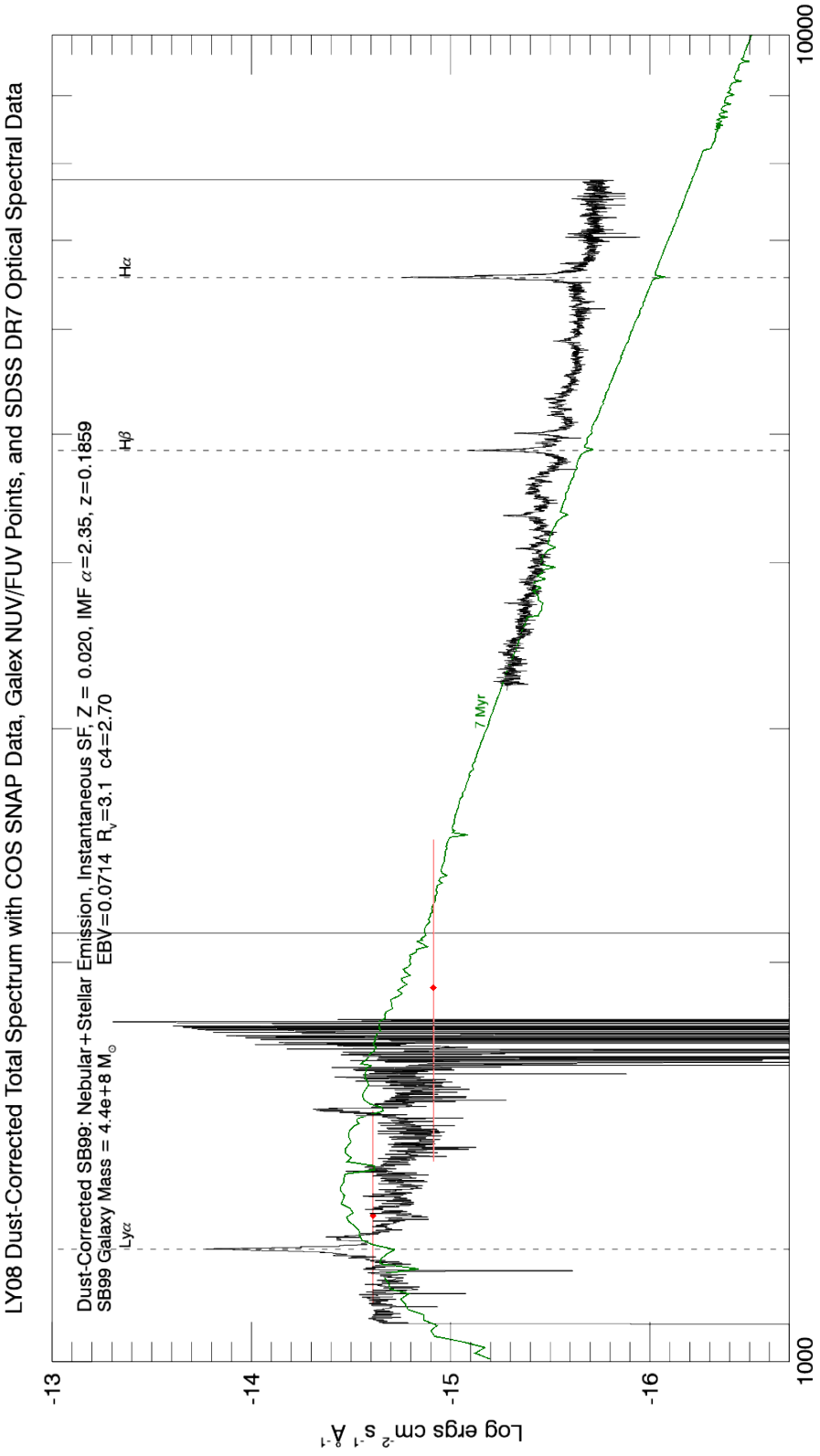

Figure B.3: LY08

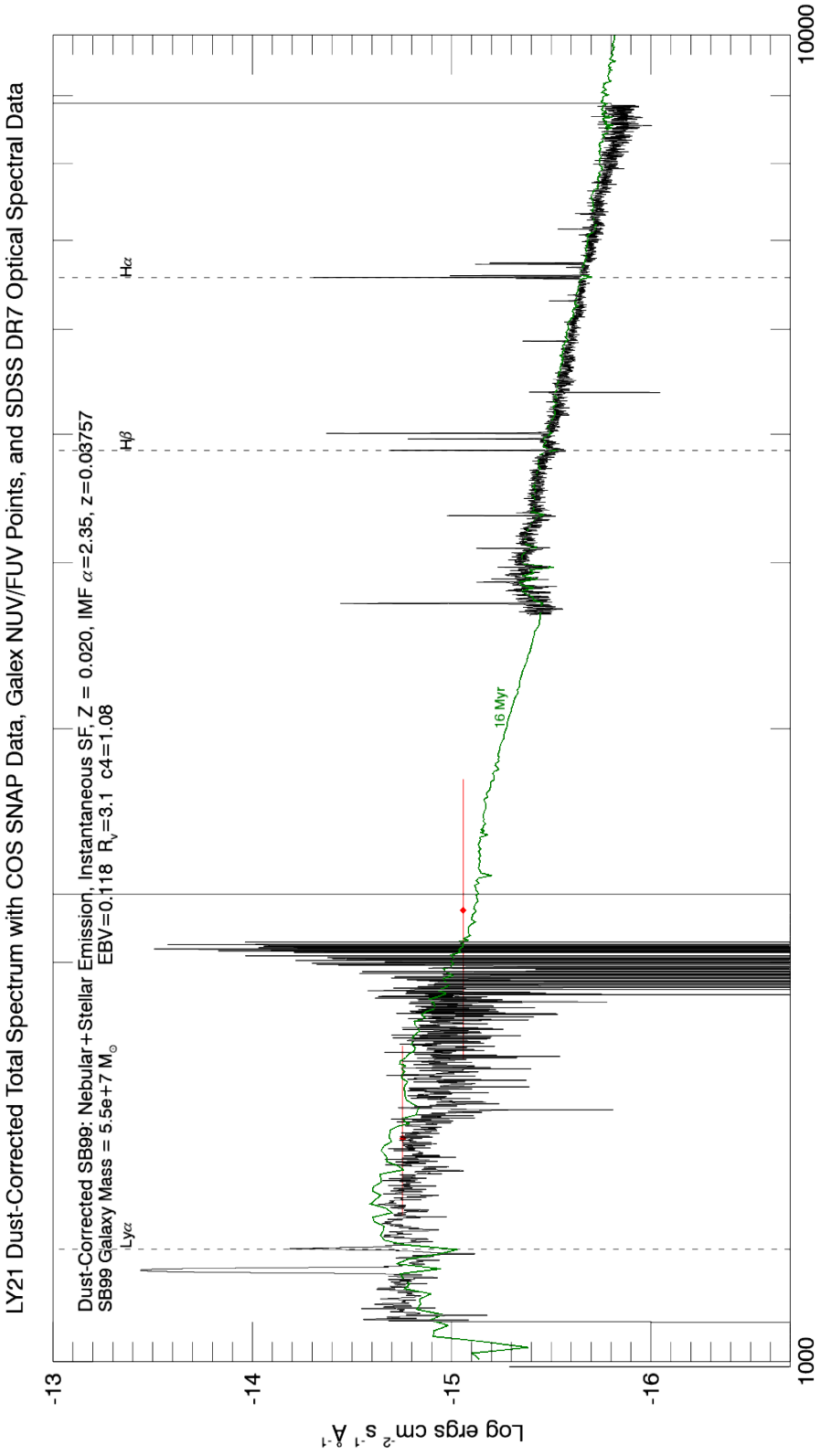

Figure B.4: LY21

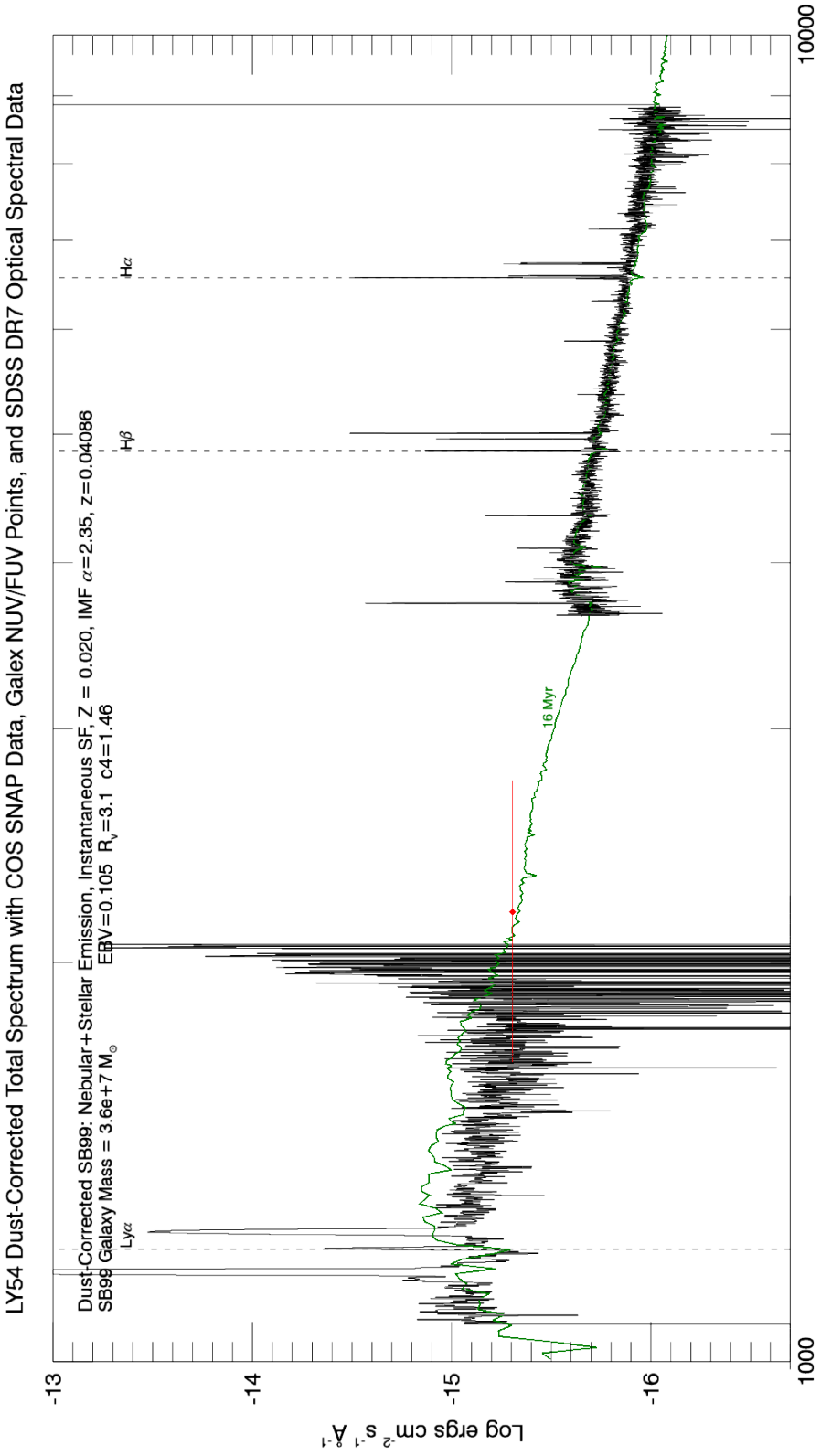

Figure B.5: LY54

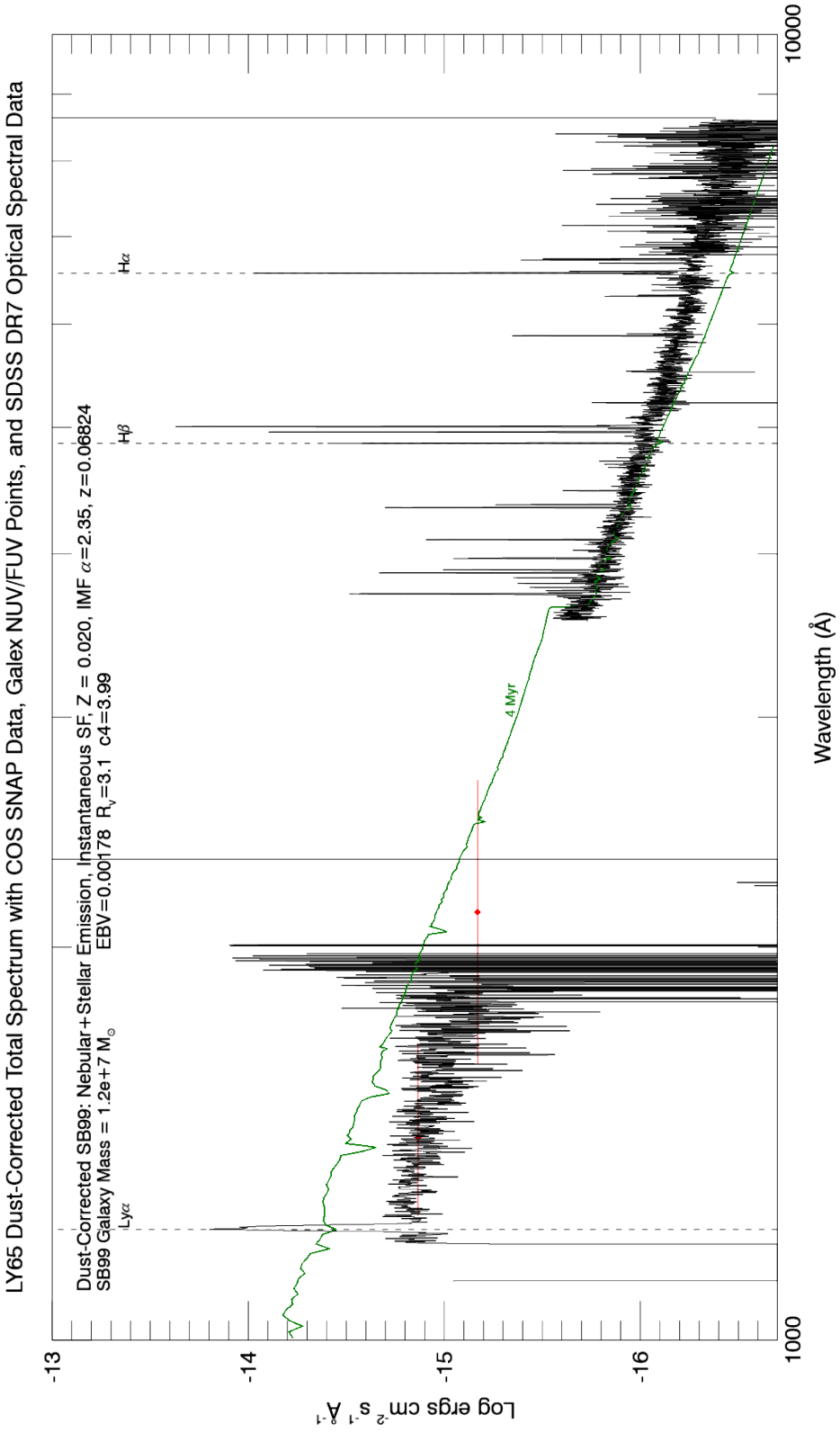

Figure B.6: LY65

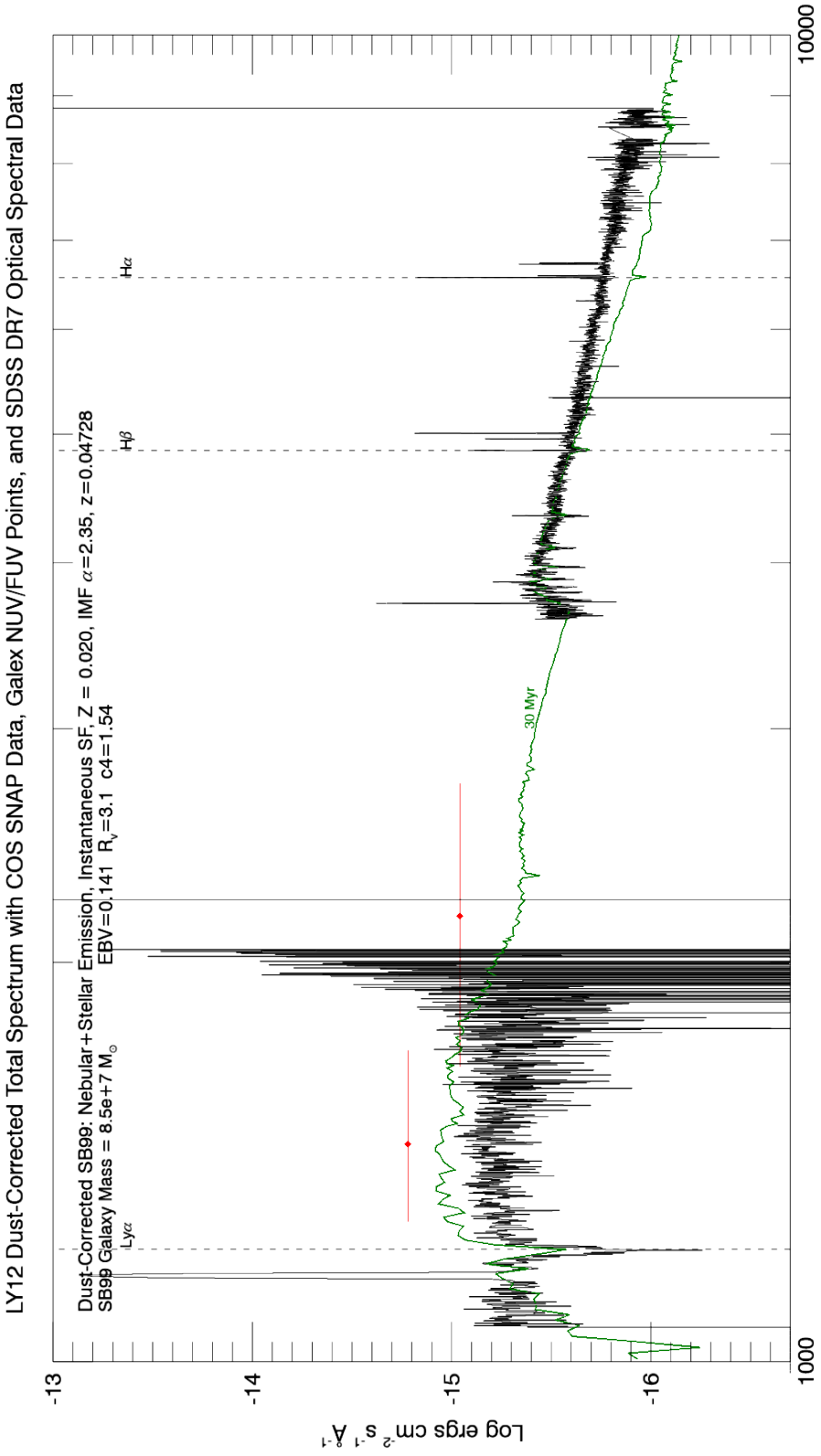

Figure B.7: LY12

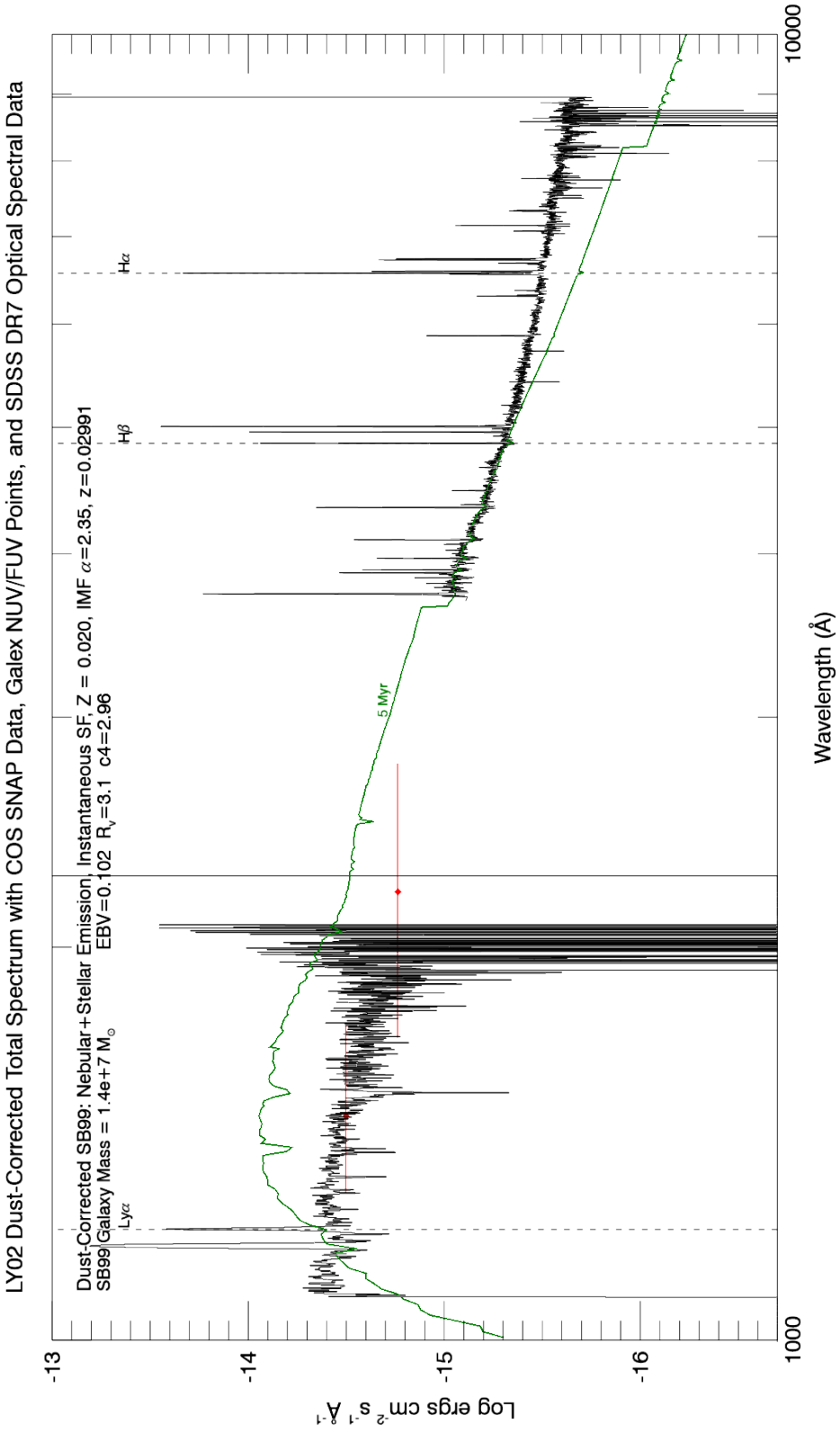

Figure B.8: LY02

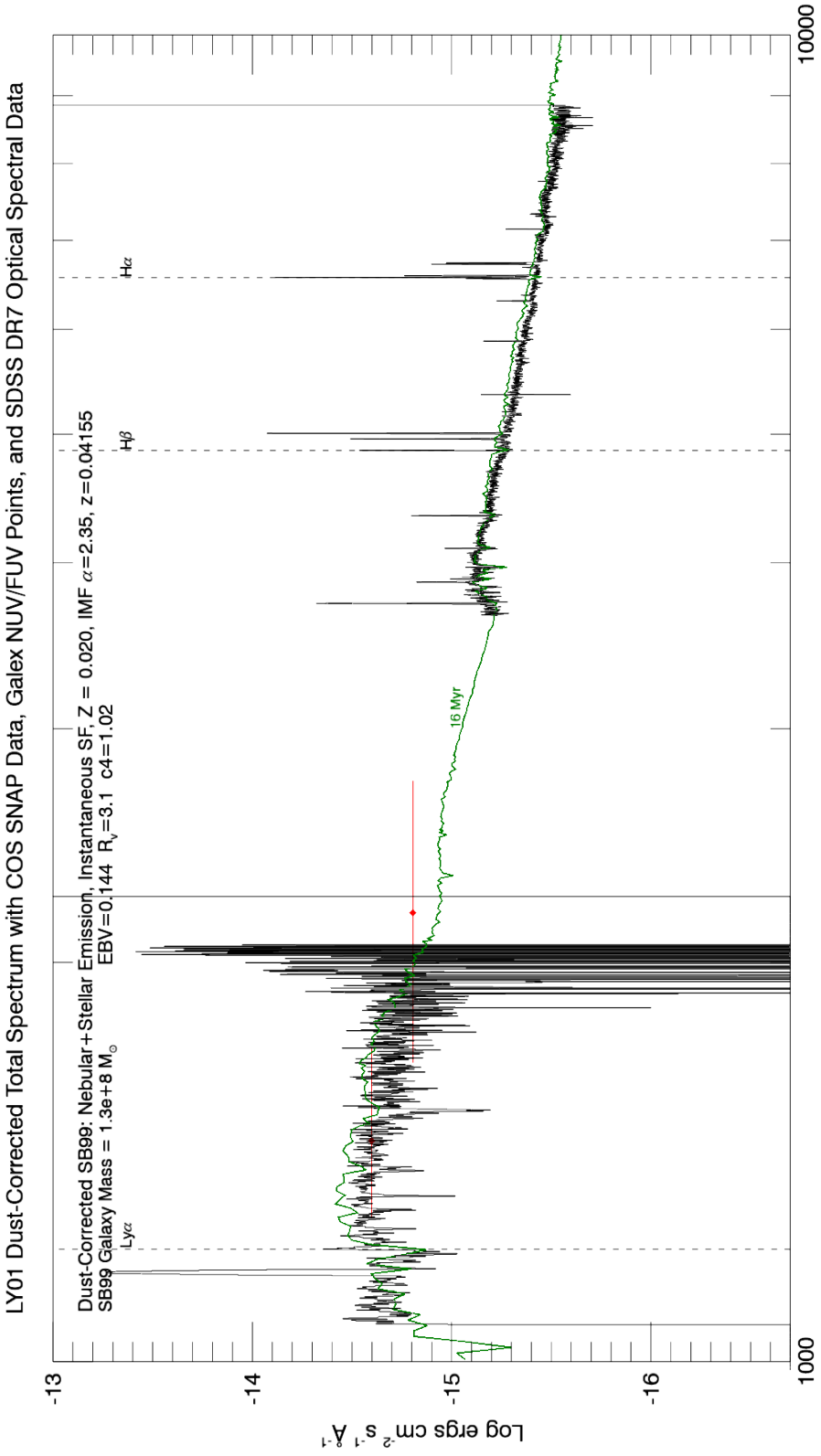

Figure B.9: LY01

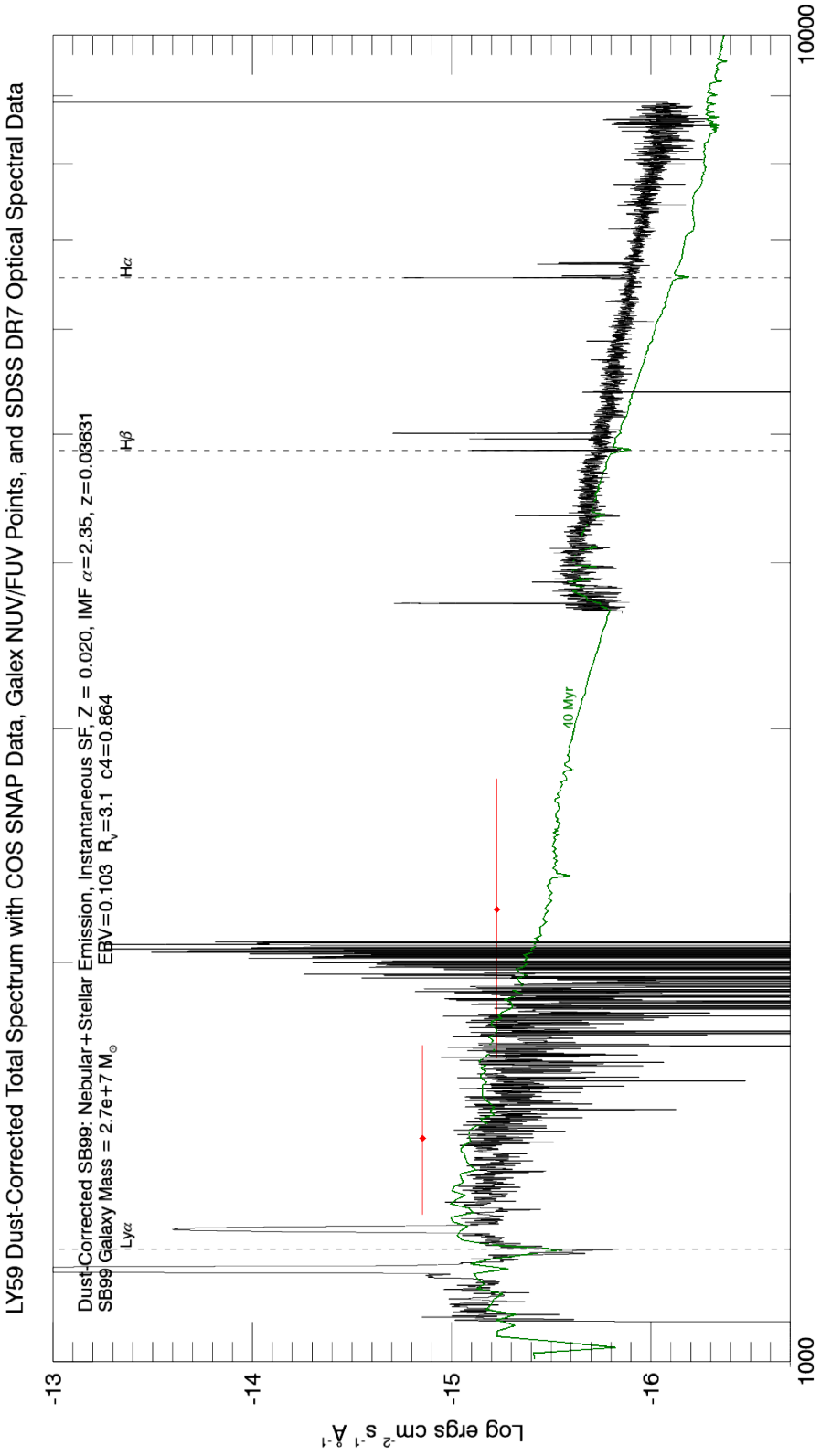

Figure B.10: LY59

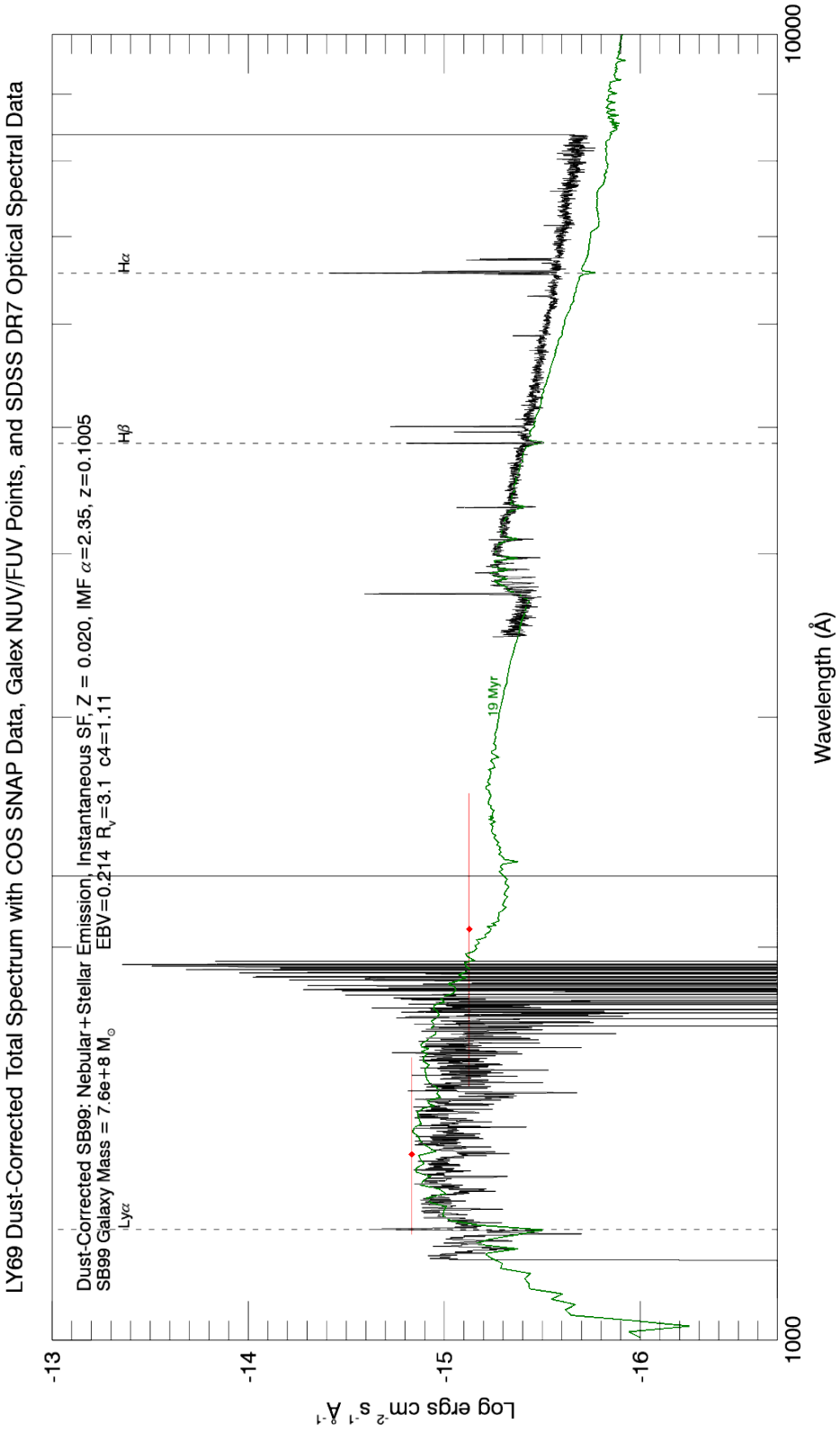

Figure B.11: LY69

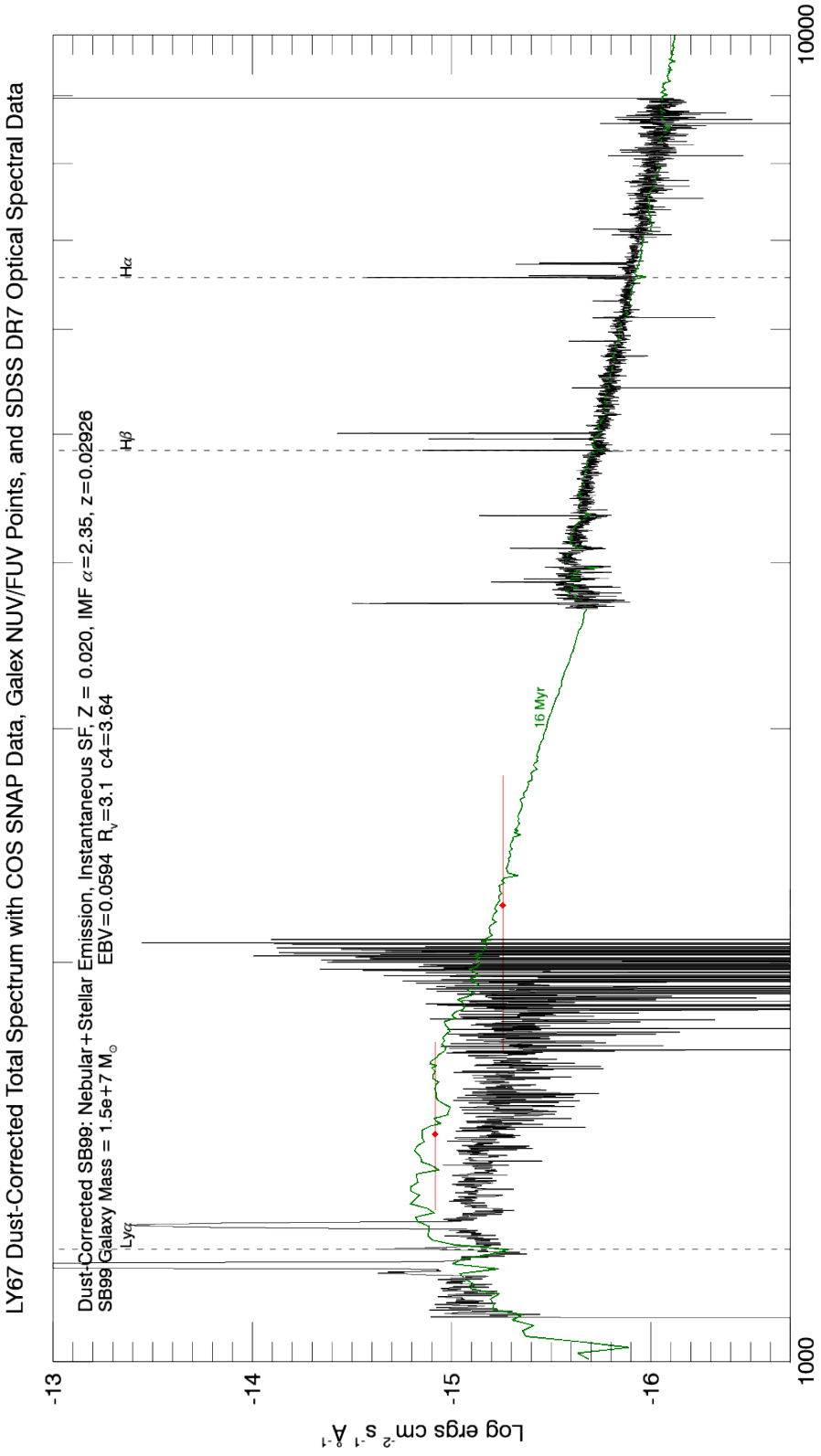

Figure B.12: LY67

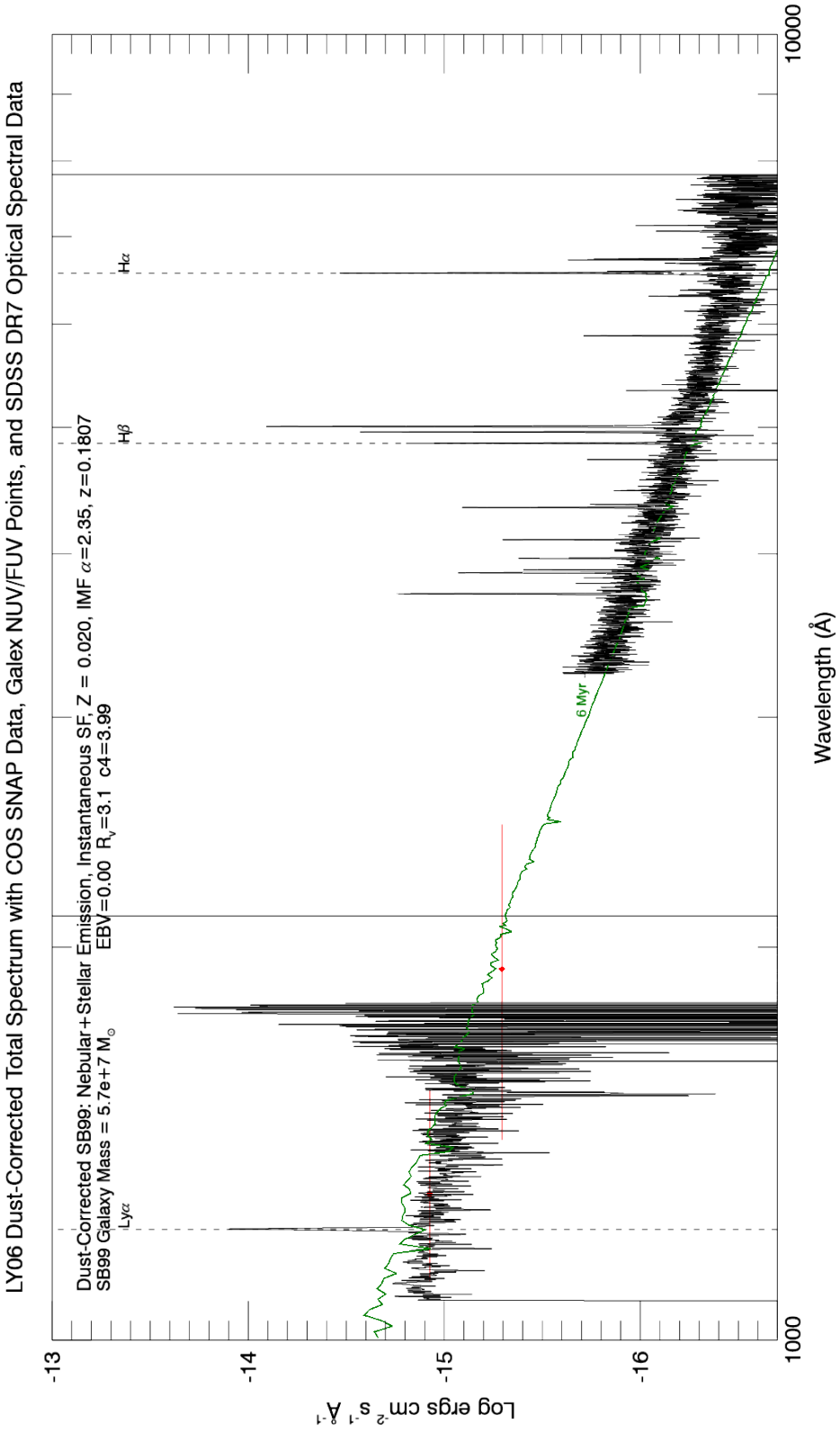

Figure B.13: LY06

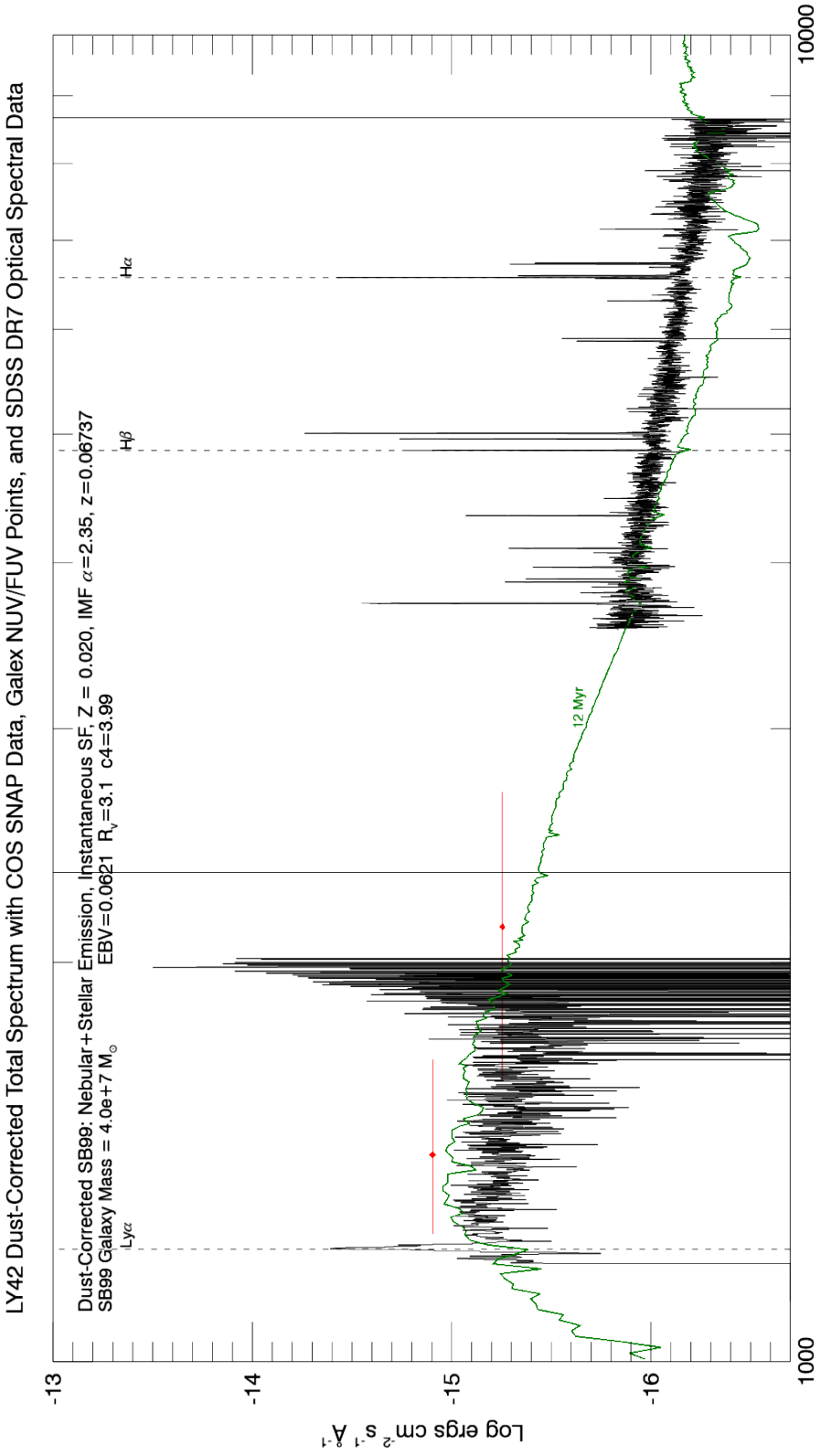

Figure B.14: LY42

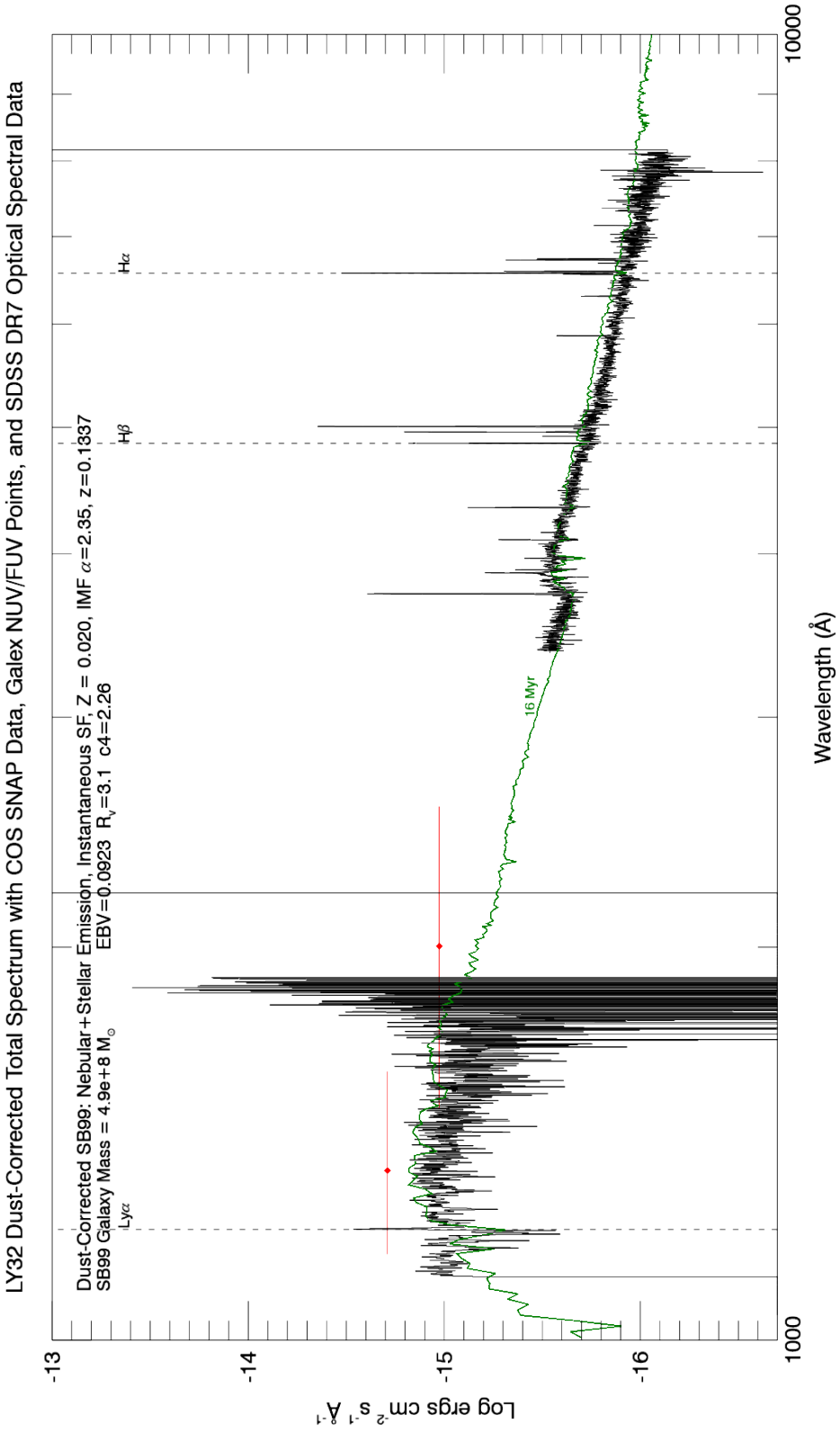

Figure B.15: LY32

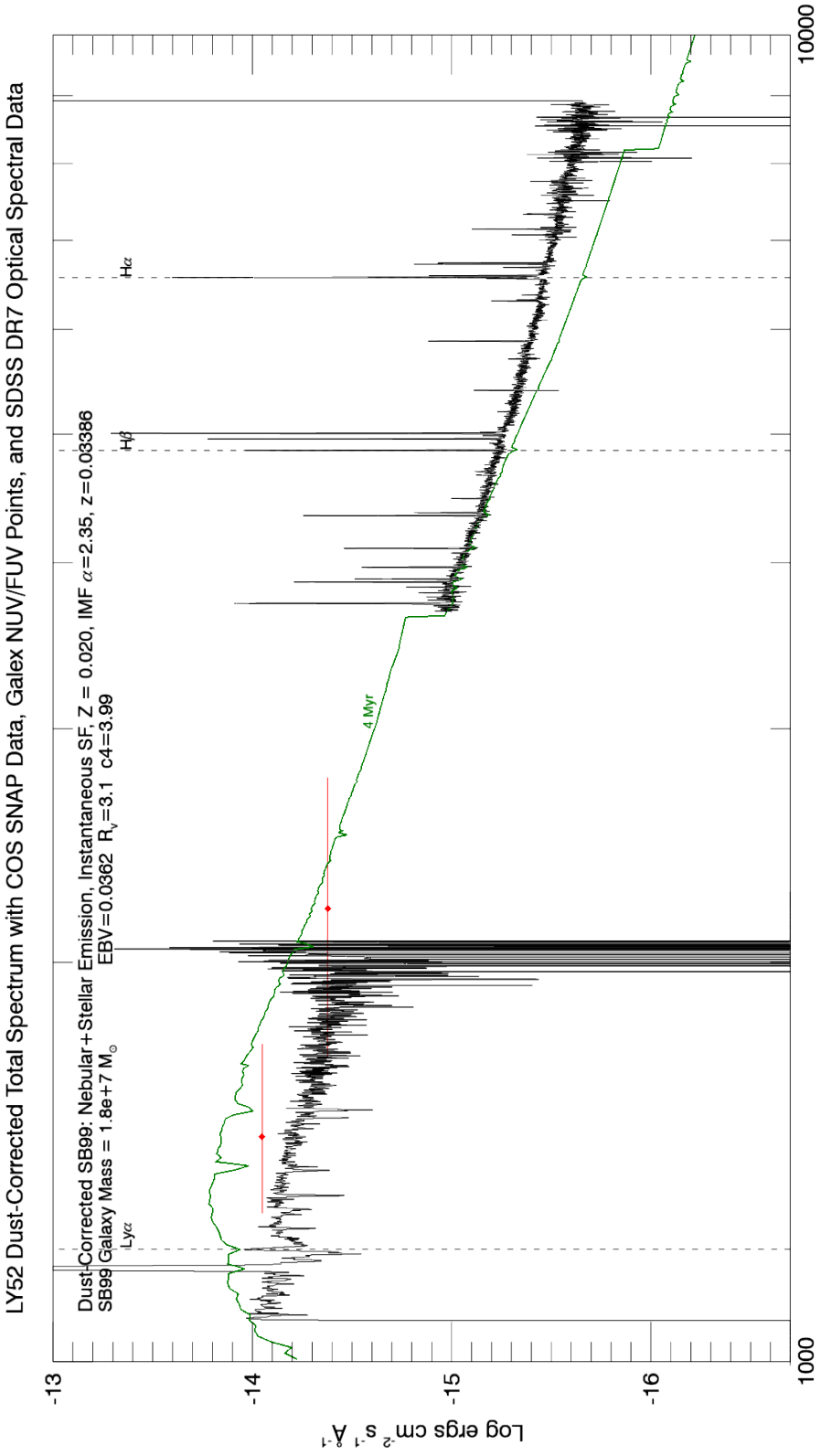

Figure B.16: LY52

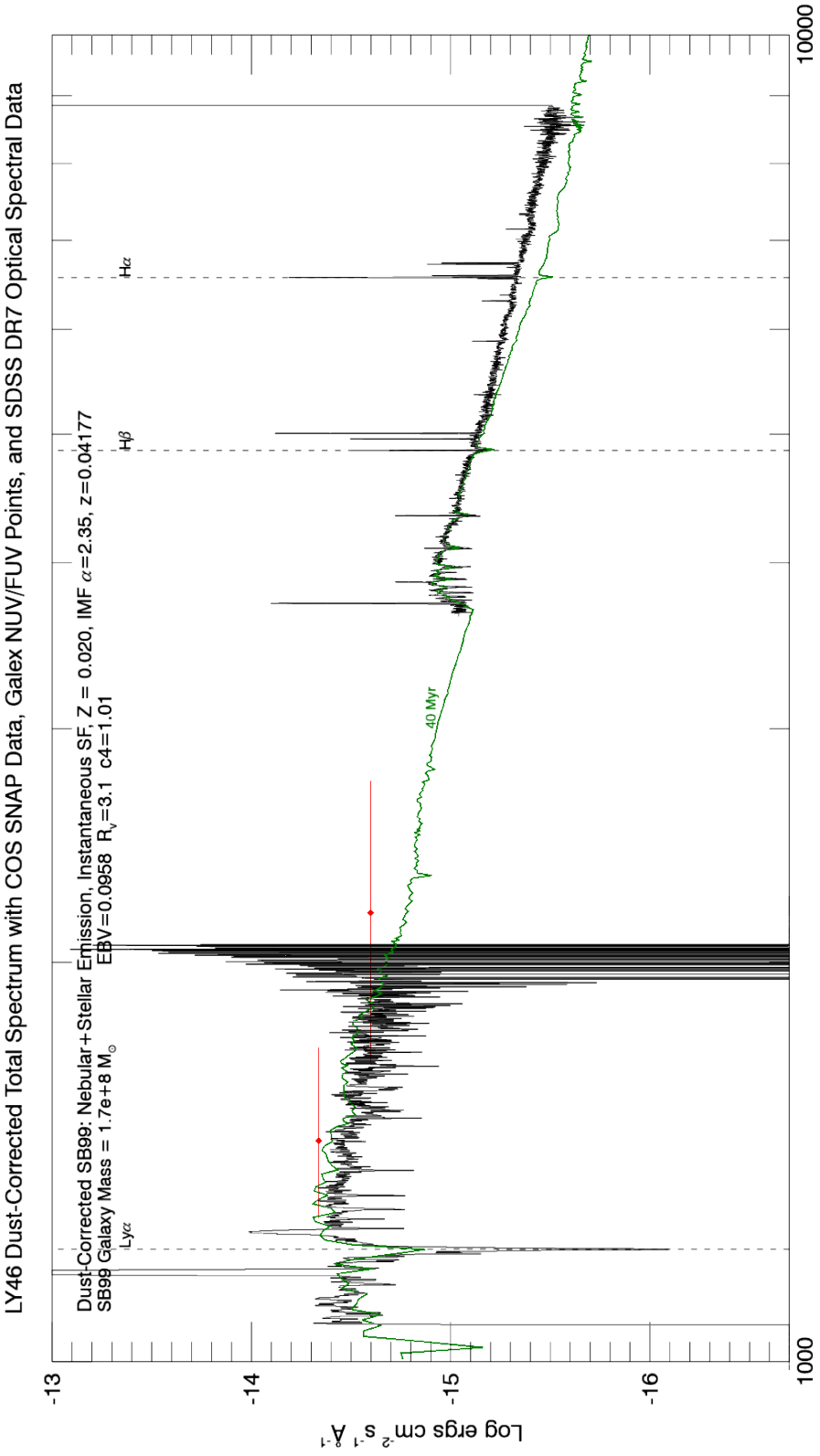

Figure B.17: LY46

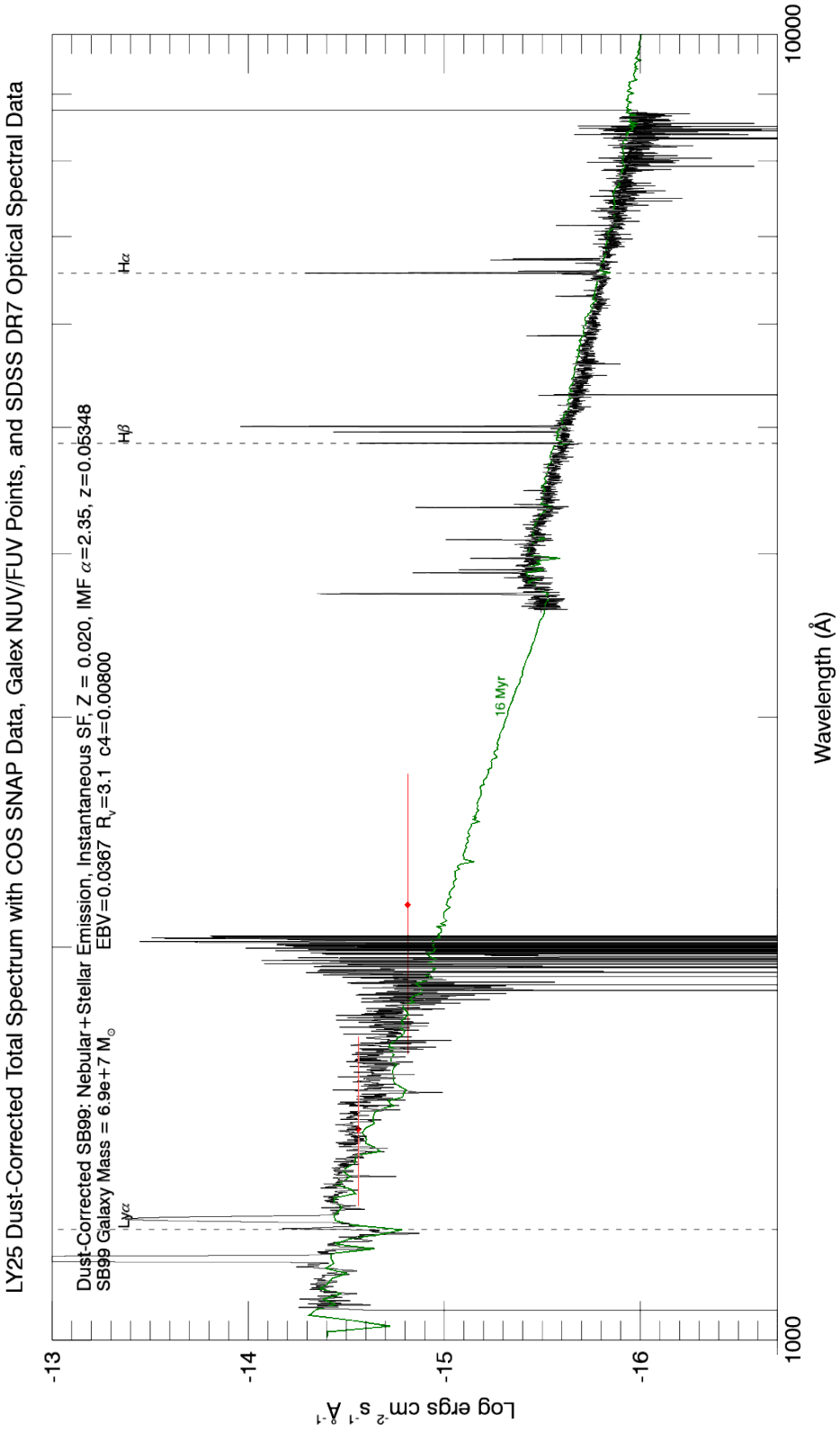

Figure B.18: LY25

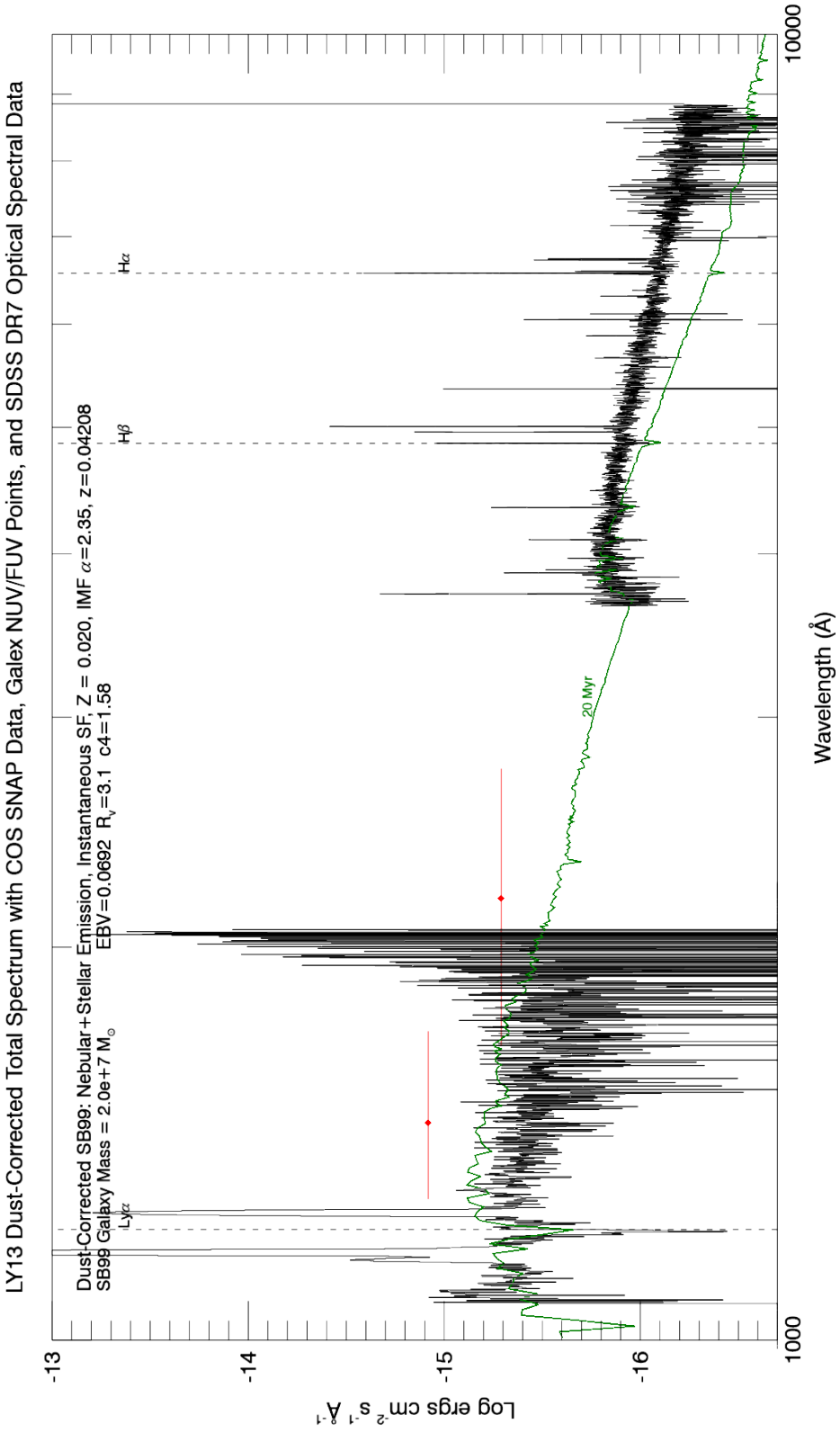

Figure B.19: LY13

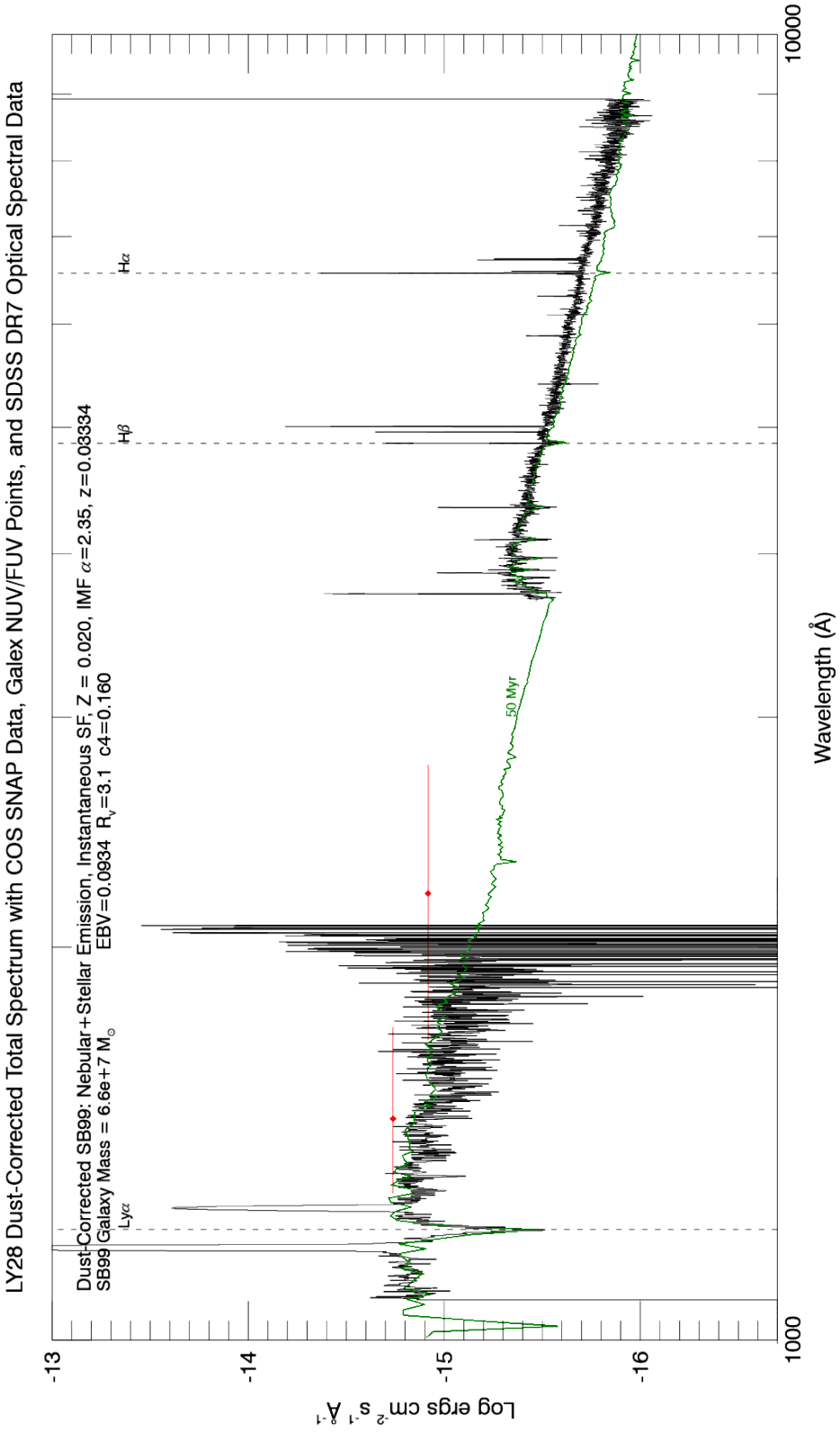

Figure B.20: LY28

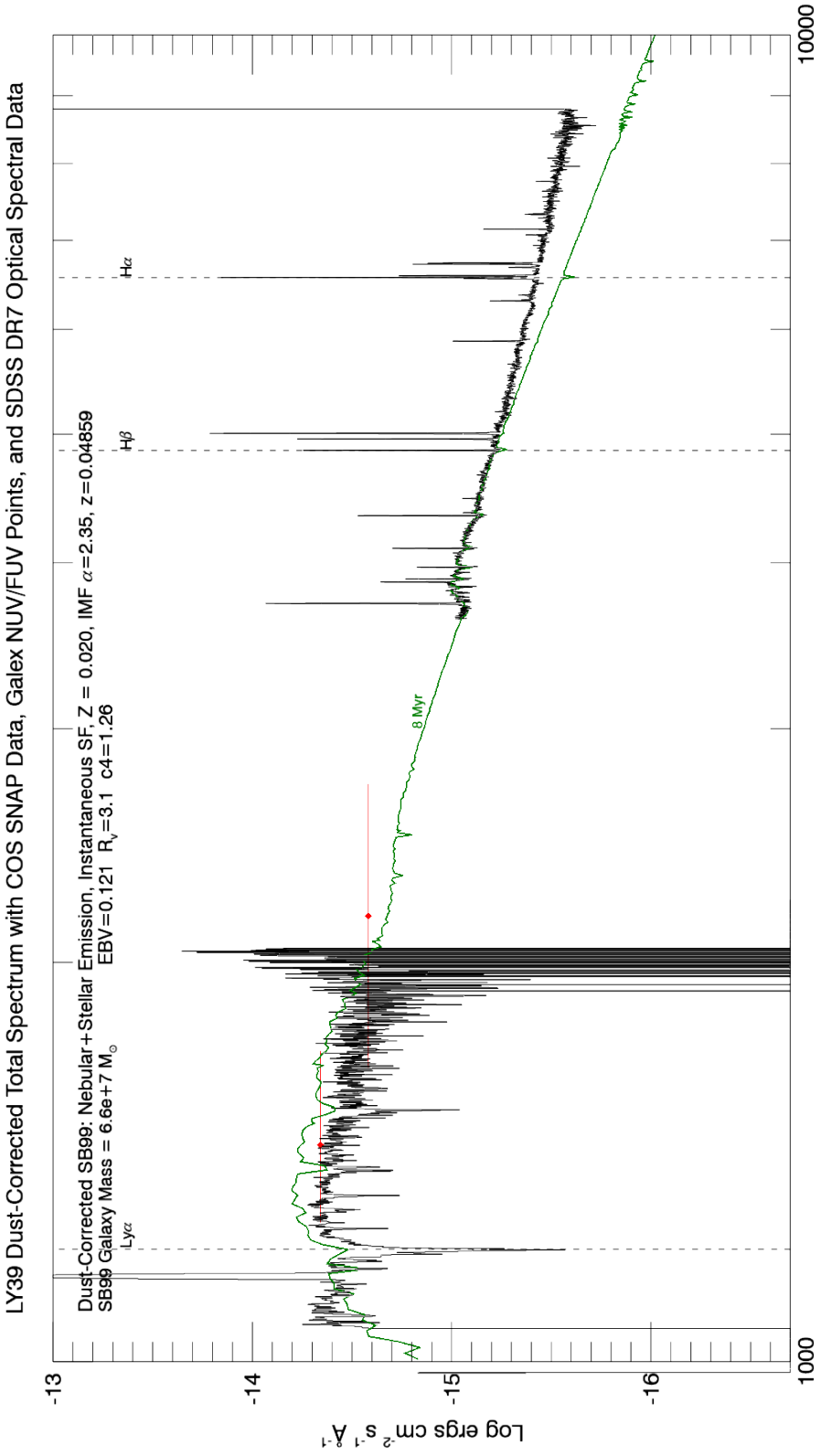

Figure B.21: LY39

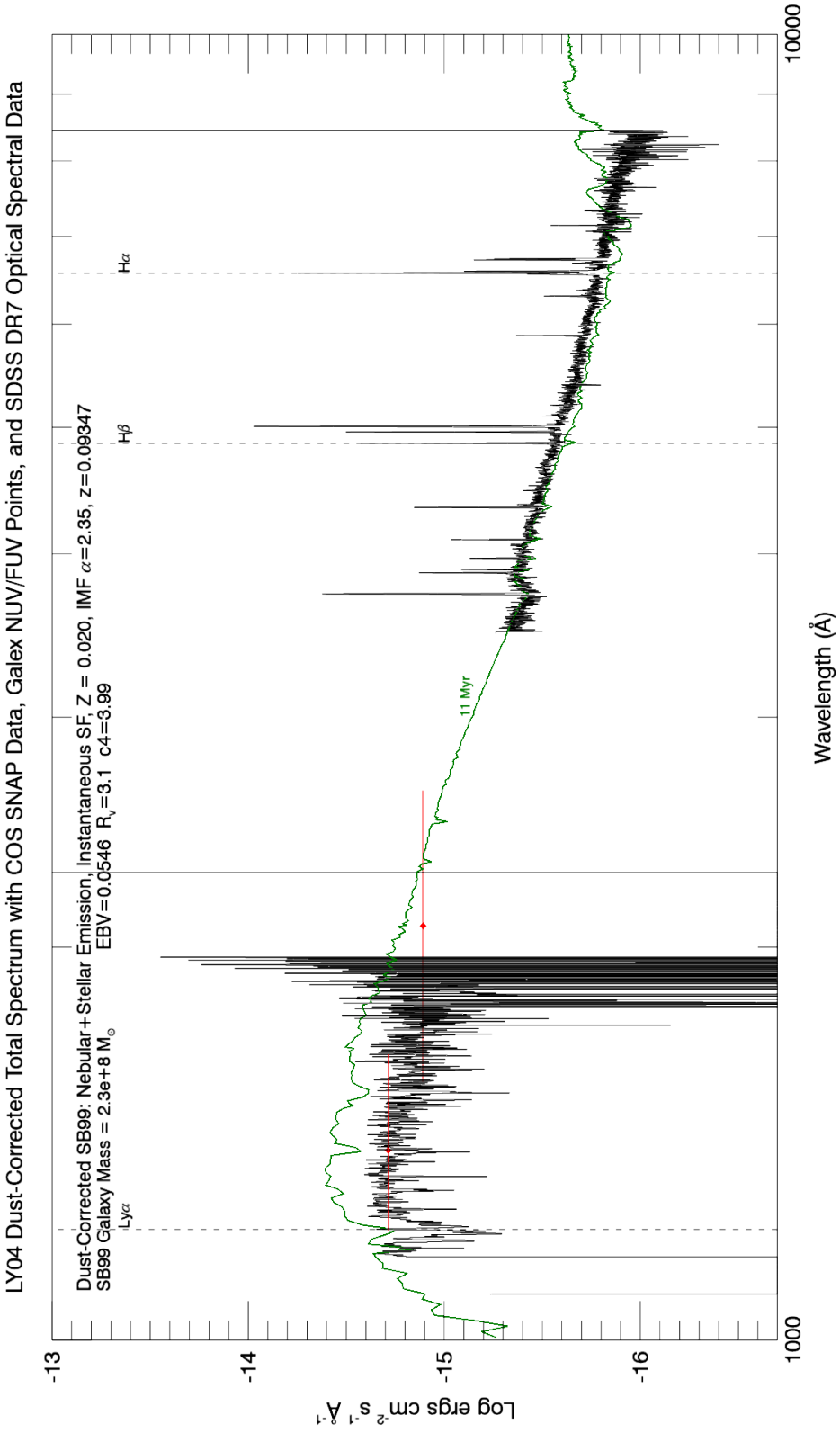

Figure B.22: LY04

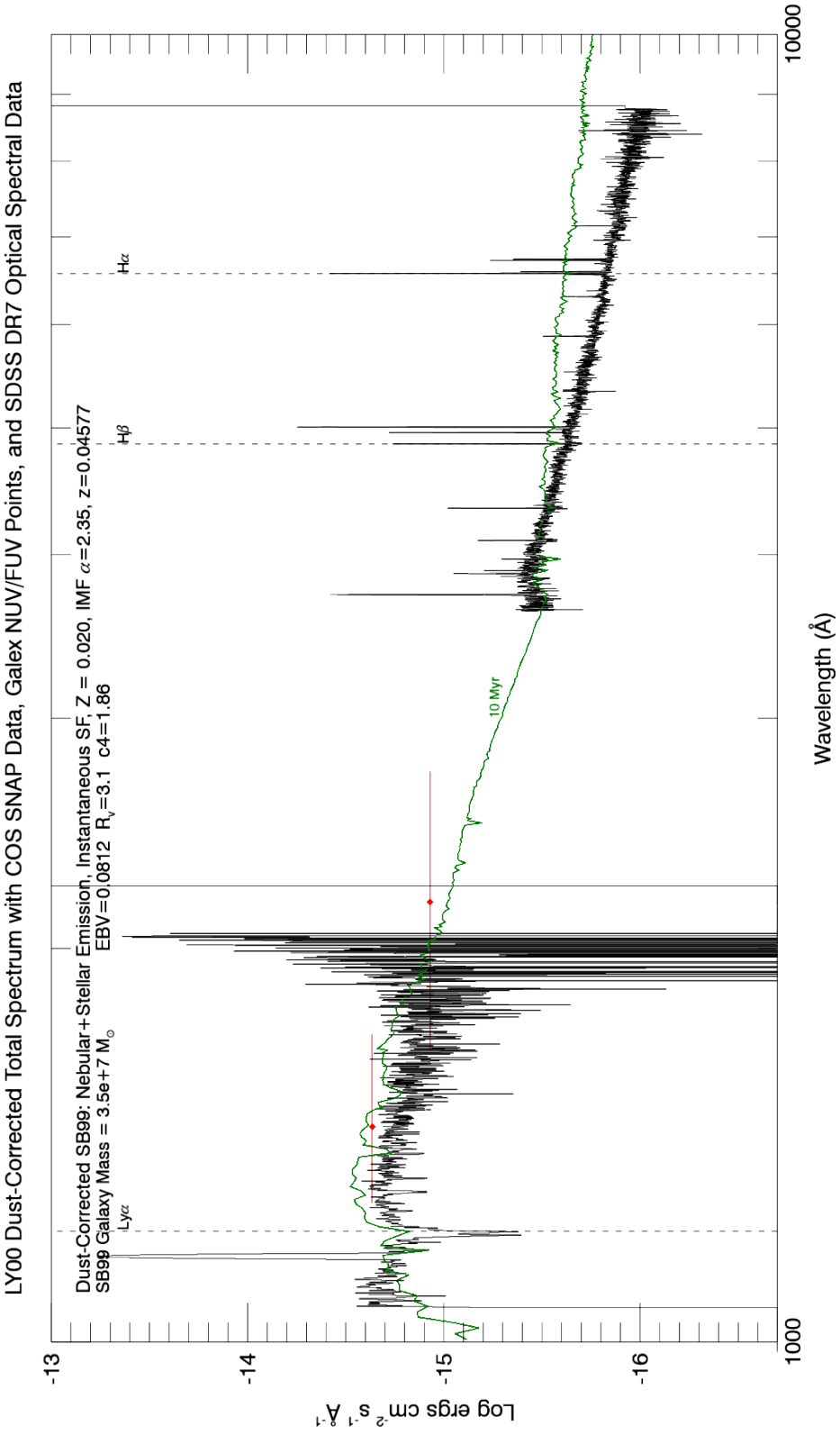

Figure B.23: LY00

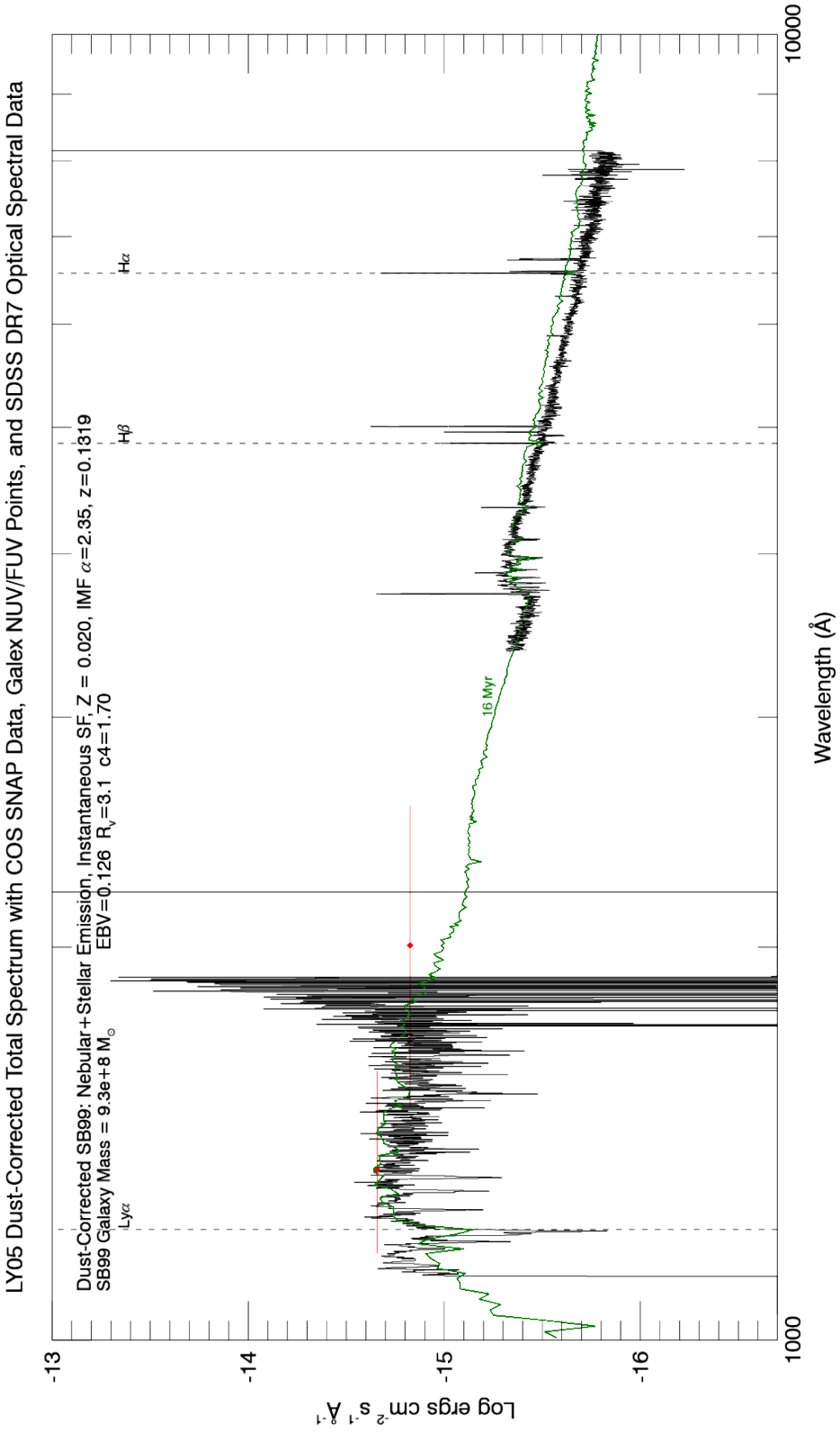

Figure B.24: LY05

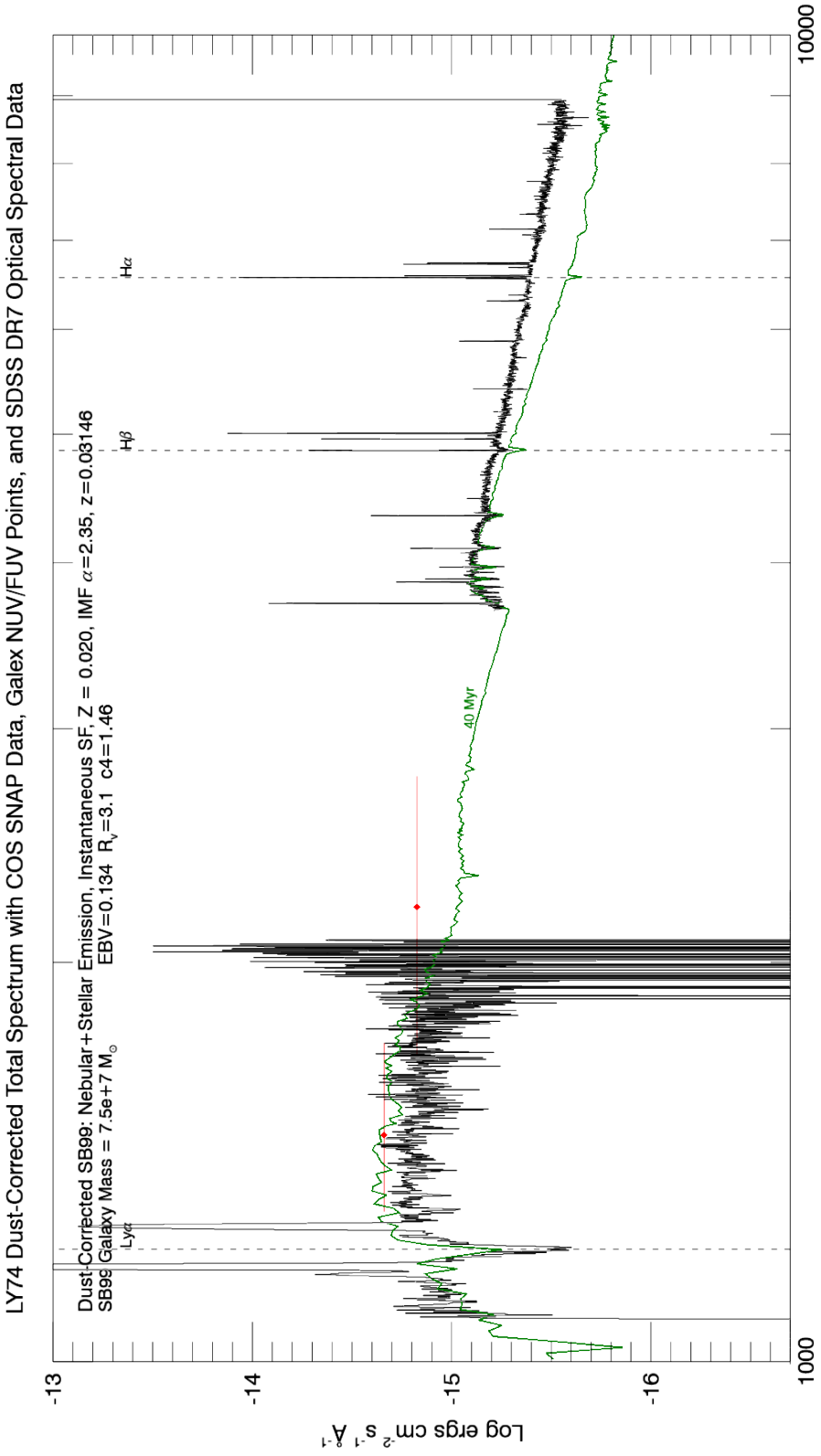

Figure B.25: LY74

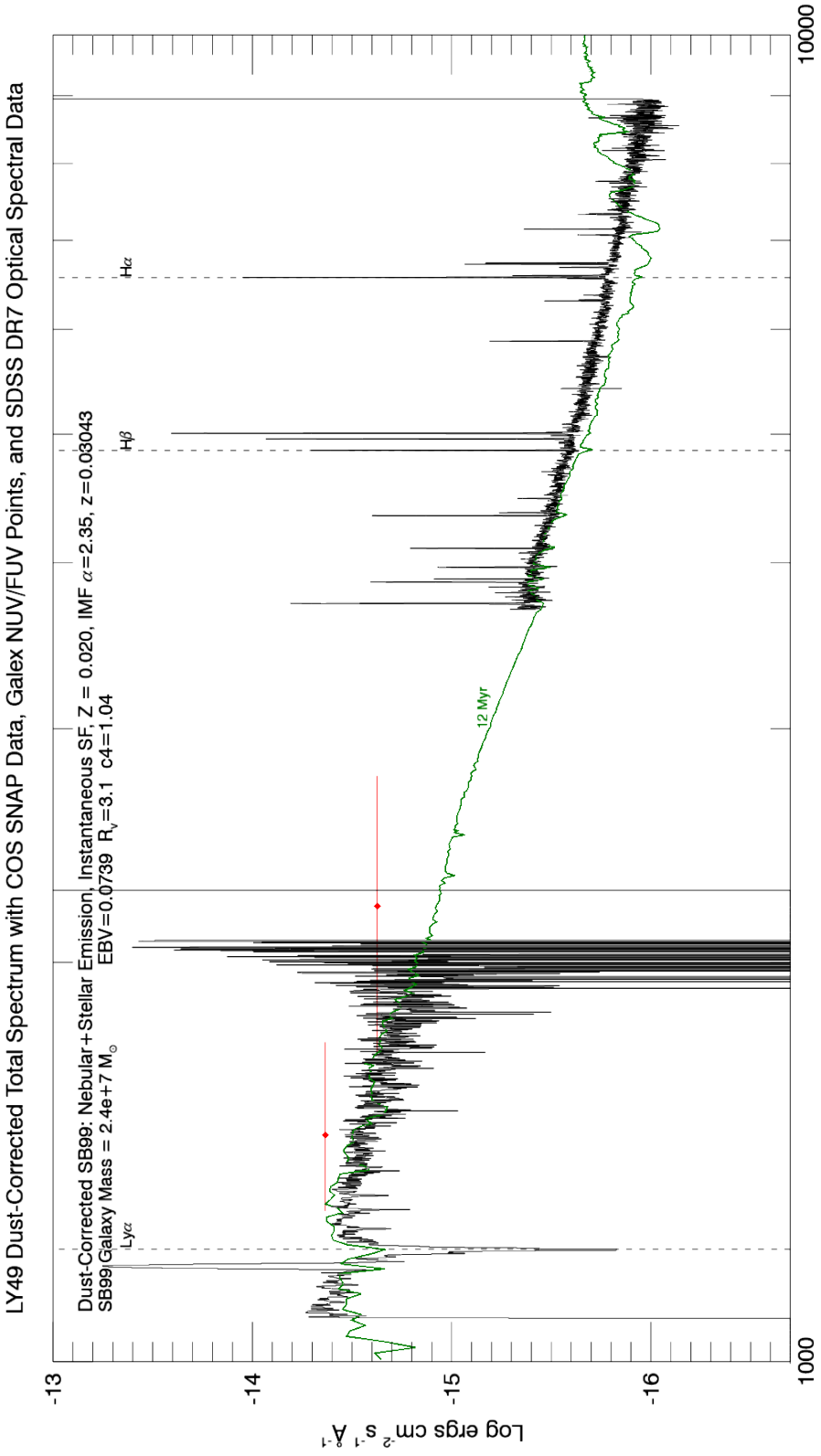

Figure B.26: LY49

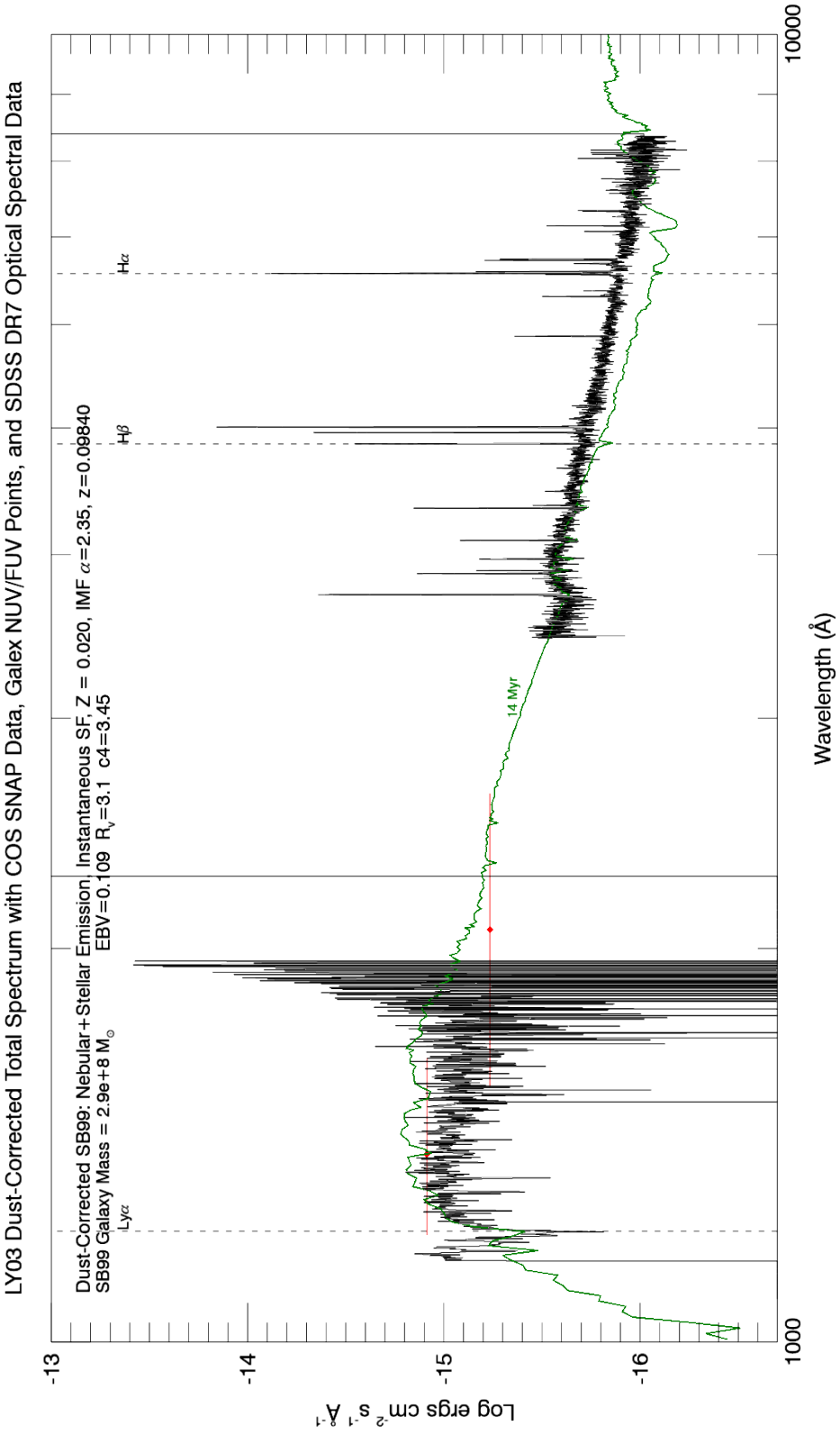

Figure B.27: LY03

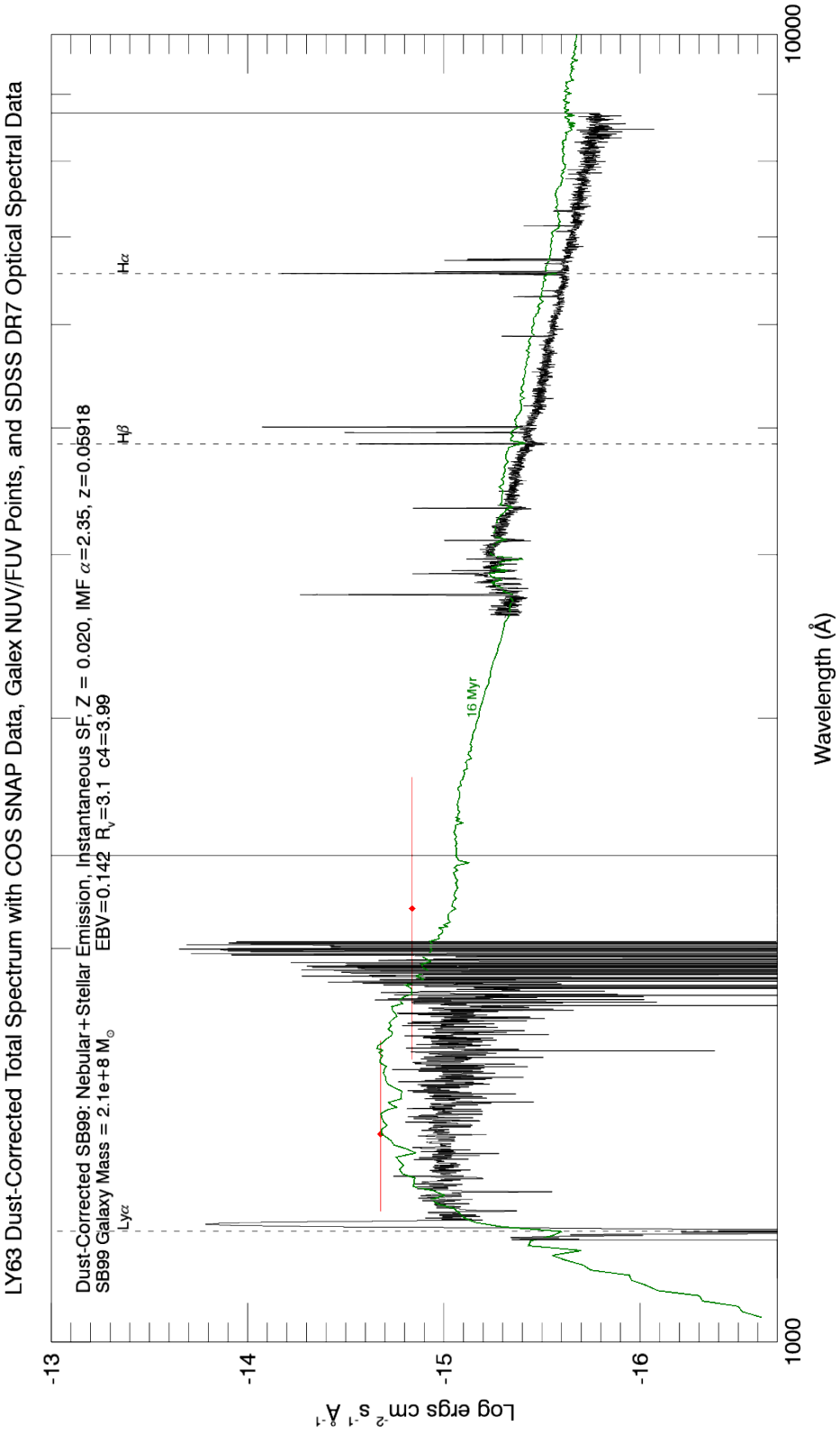

Figure B.28: LY63

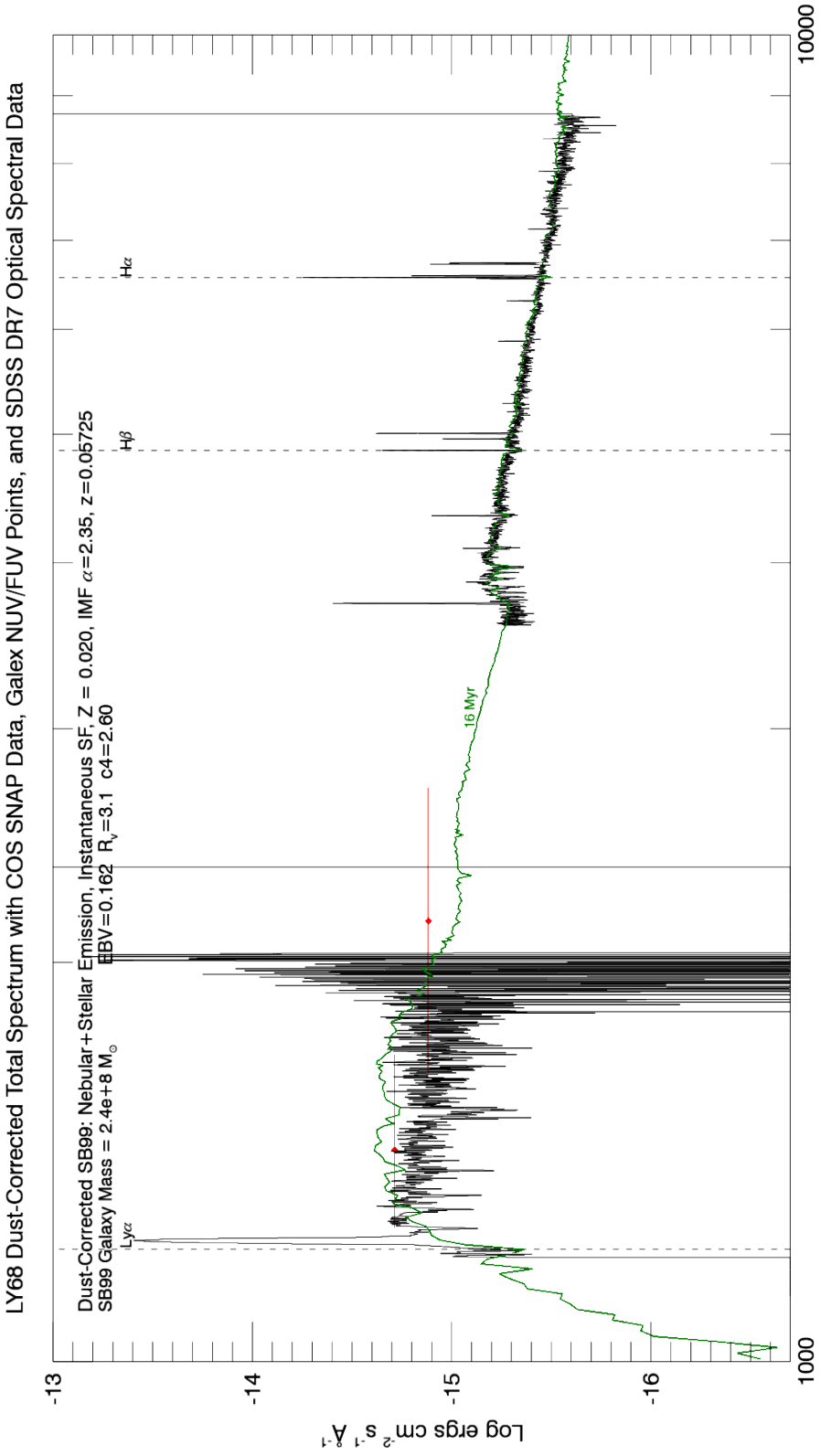

Figure B.29: LY68

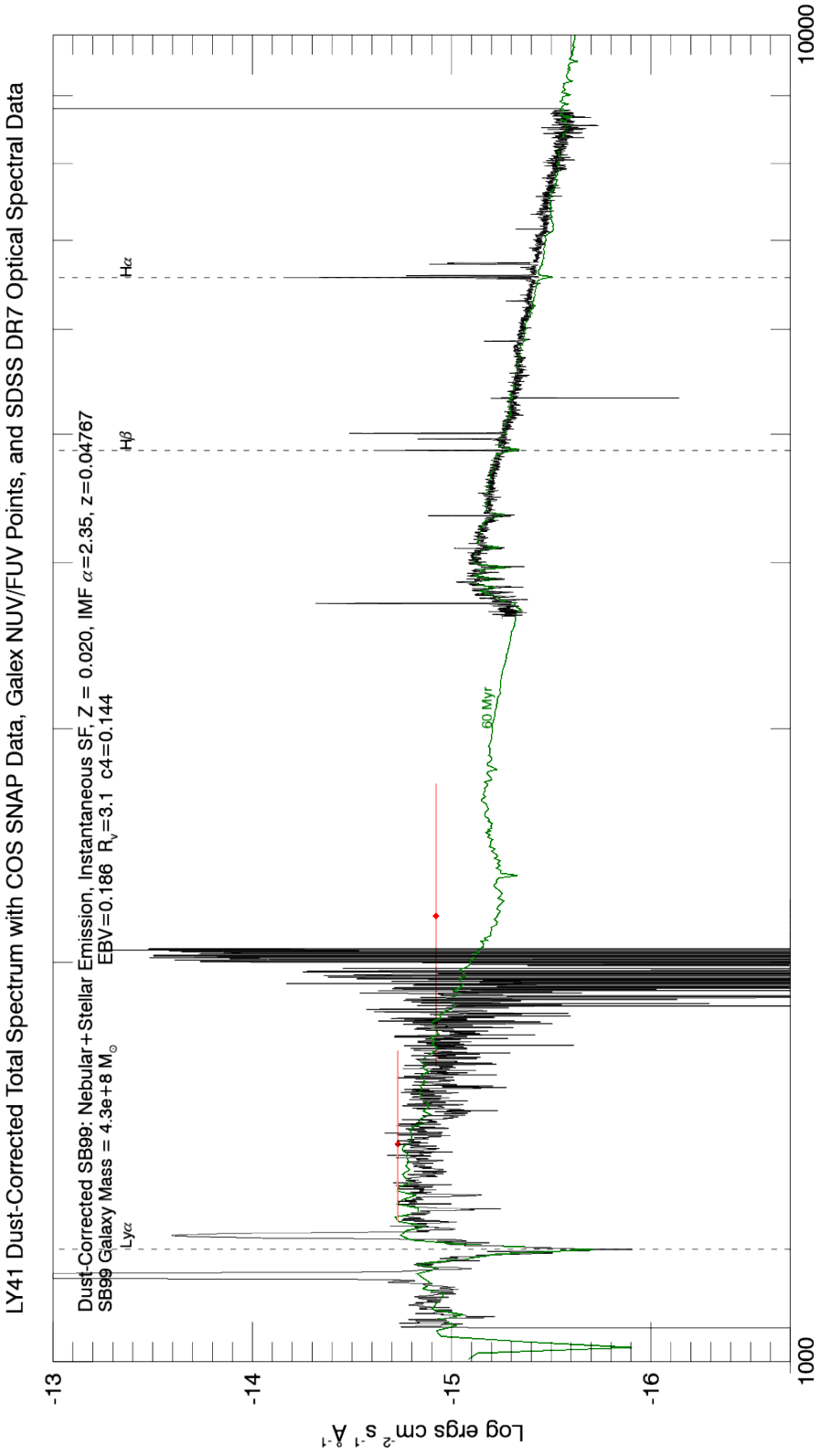

Figure B.30: LY41

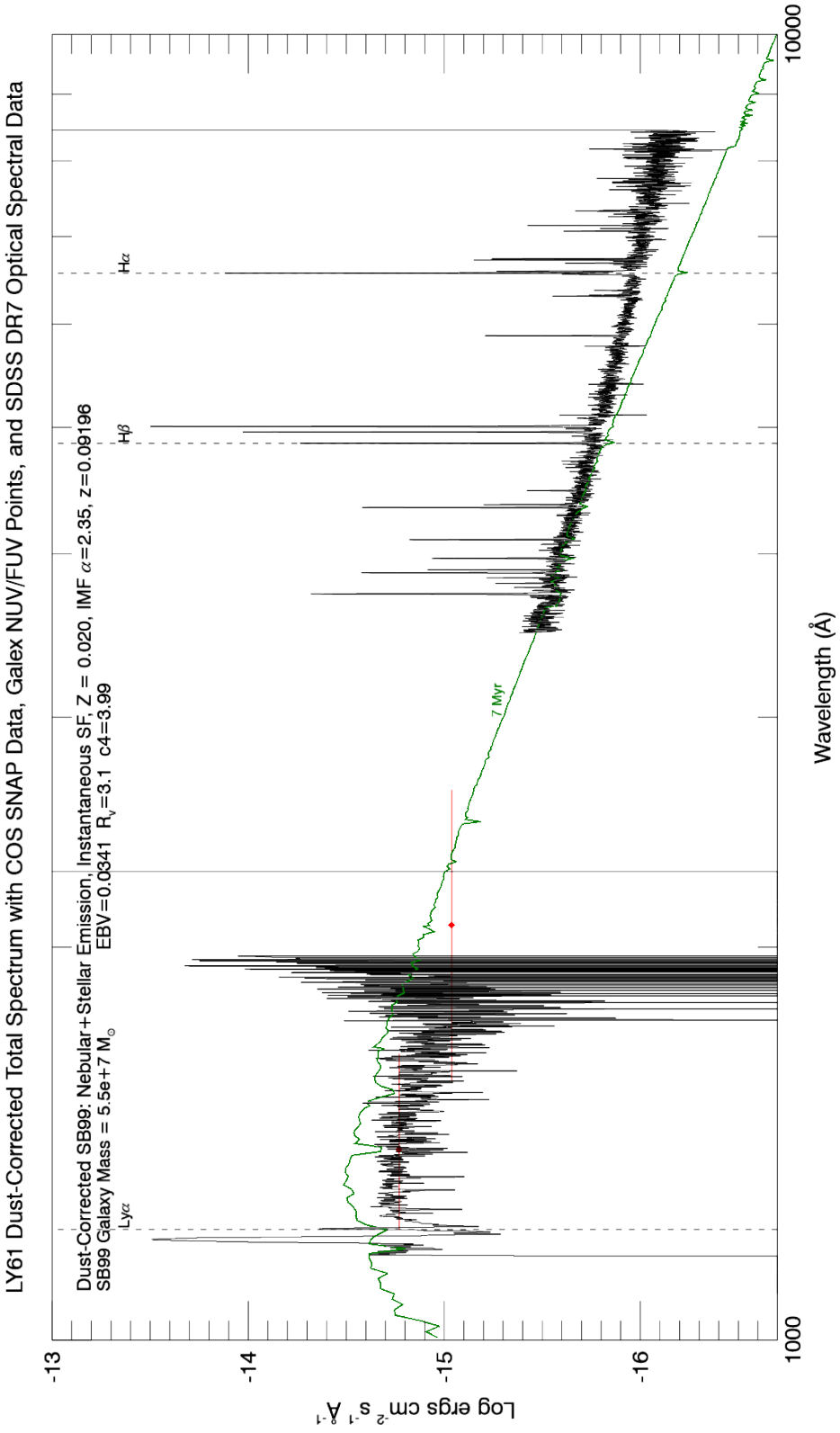

Figure B.31: LY61

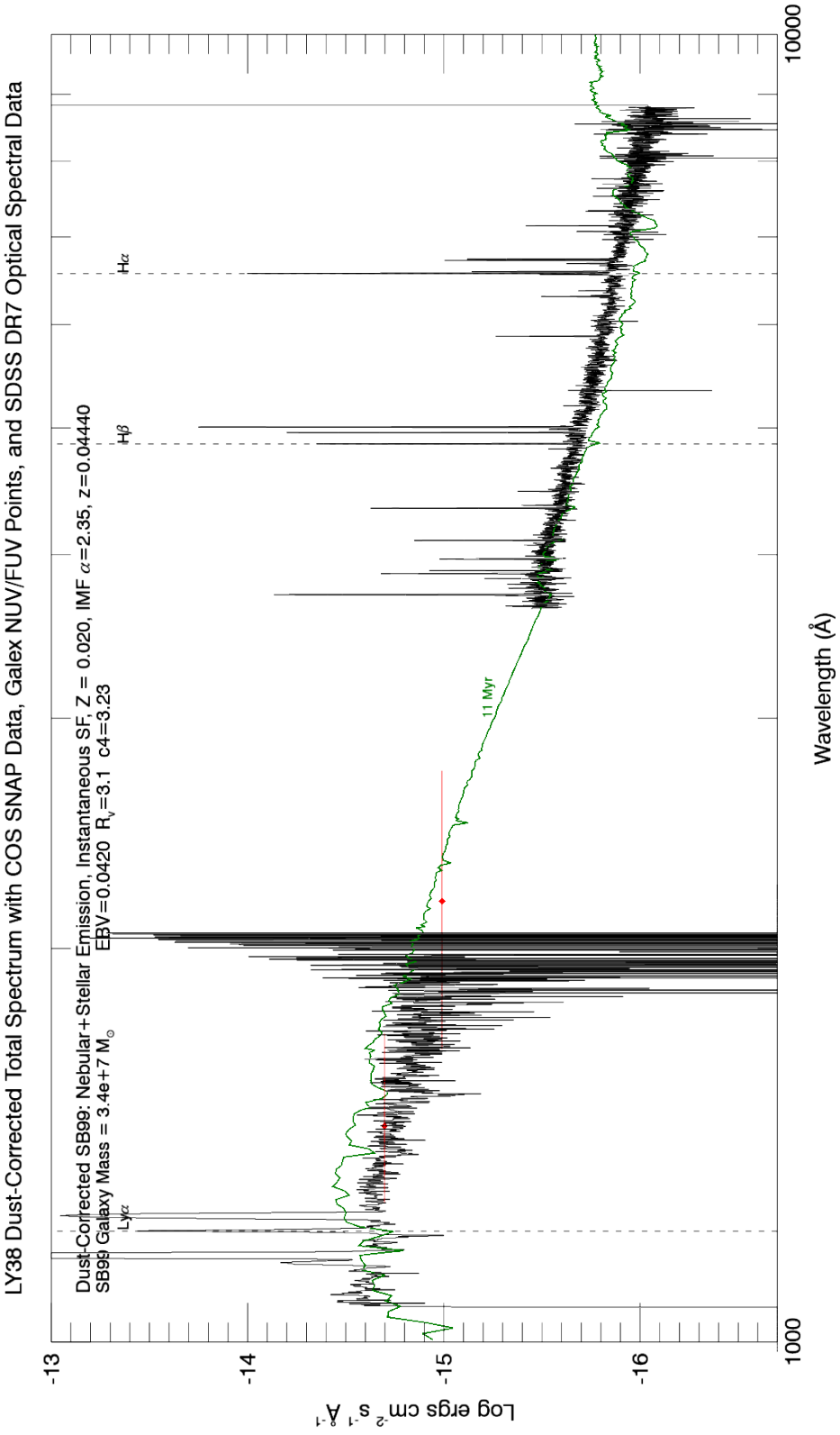

Figure B.32: LY38

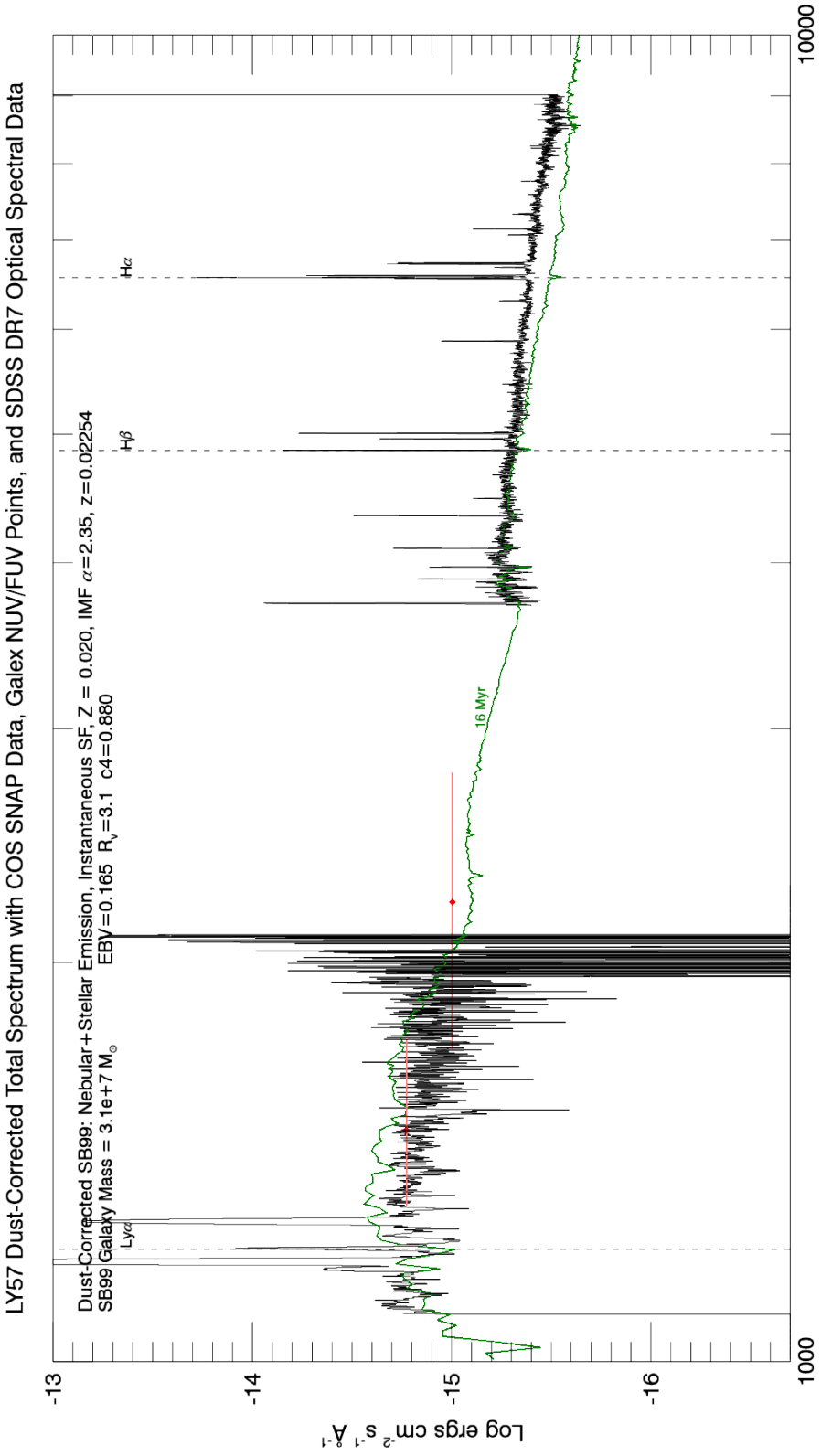

Figure B.33: LY57

Appendix C

COS and SDSS Spectra with SB99 Model

Tiles of the spectra around Lyα (first rows), low-ionization (second, third and fourth rows), and high-ionization (fifth, sixth, and seventh rows) state lines of note across the dataset. These are sorted by Lyα excess flux over the continuum, with the N Vλ1239,1243 Å doublet, Si IVλ1394,1403 Å doublet, and C IVλ1548,1551 Å doublet expanded out for each galaxy. The flux scale is tuned for each plot to best show the fieature of note, but left in absolute unit scale. When the center of geocoronal O I λ1302 Å emission encroaches in the wavelength range (depending on the target redshift), it is labeled with a dotted line and a $\oplus$ symbol, and in a few of the tiles the edge of a large geocoronal O I emission line encroaches into the abscissa space. The vertical grey band denotes redshift error in velocity space.

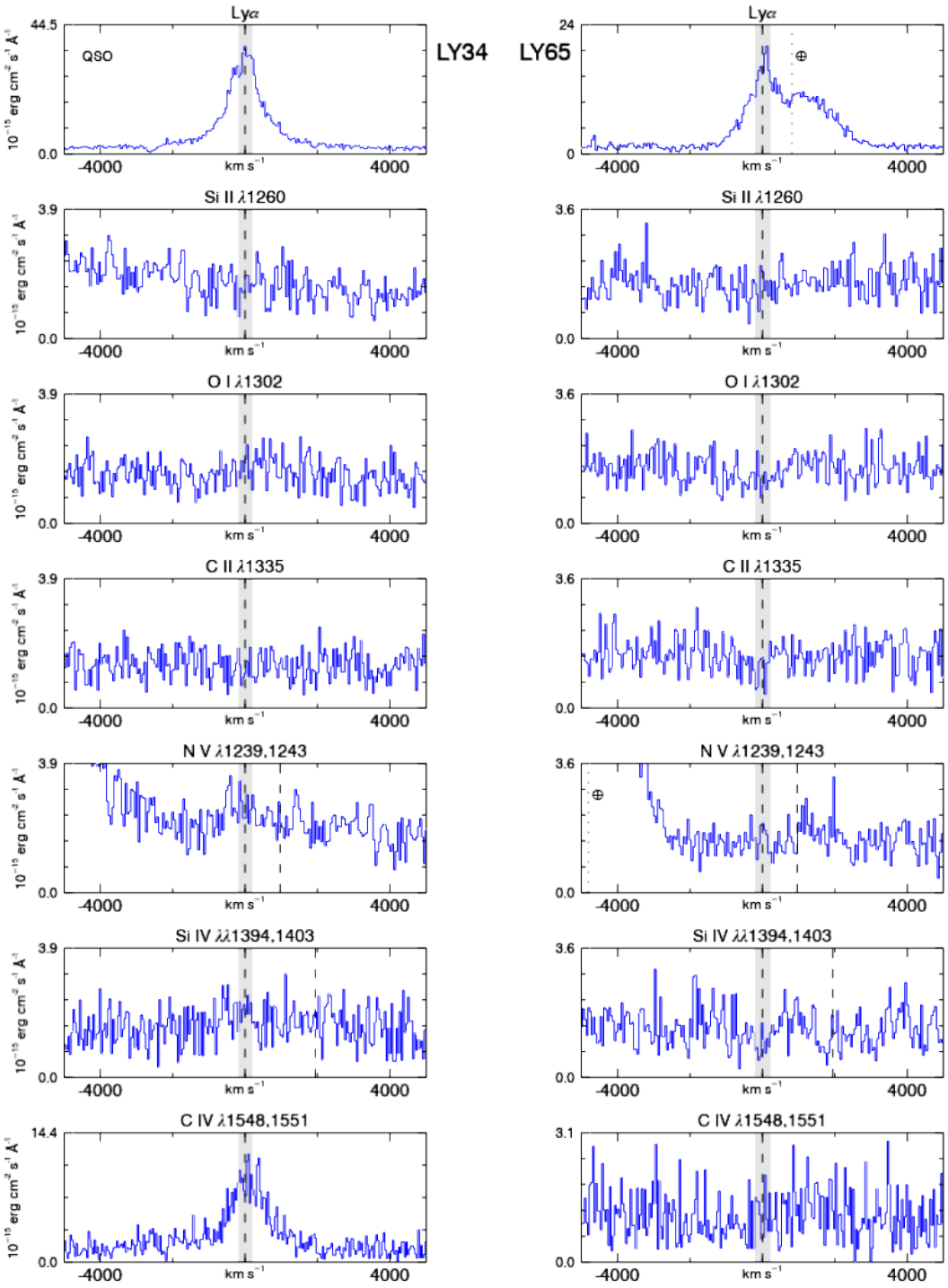
LY34
LY65
Lyα
QSO
Si II λ1260
O I λ1302
C II λ1335
N V λ1239,1243
Si IV λλ1394,1403
C IV λ1548,1551
km s⁻¹
-4000
4000
0.0
44.5
24
3.9
3.6
14.4
3.1

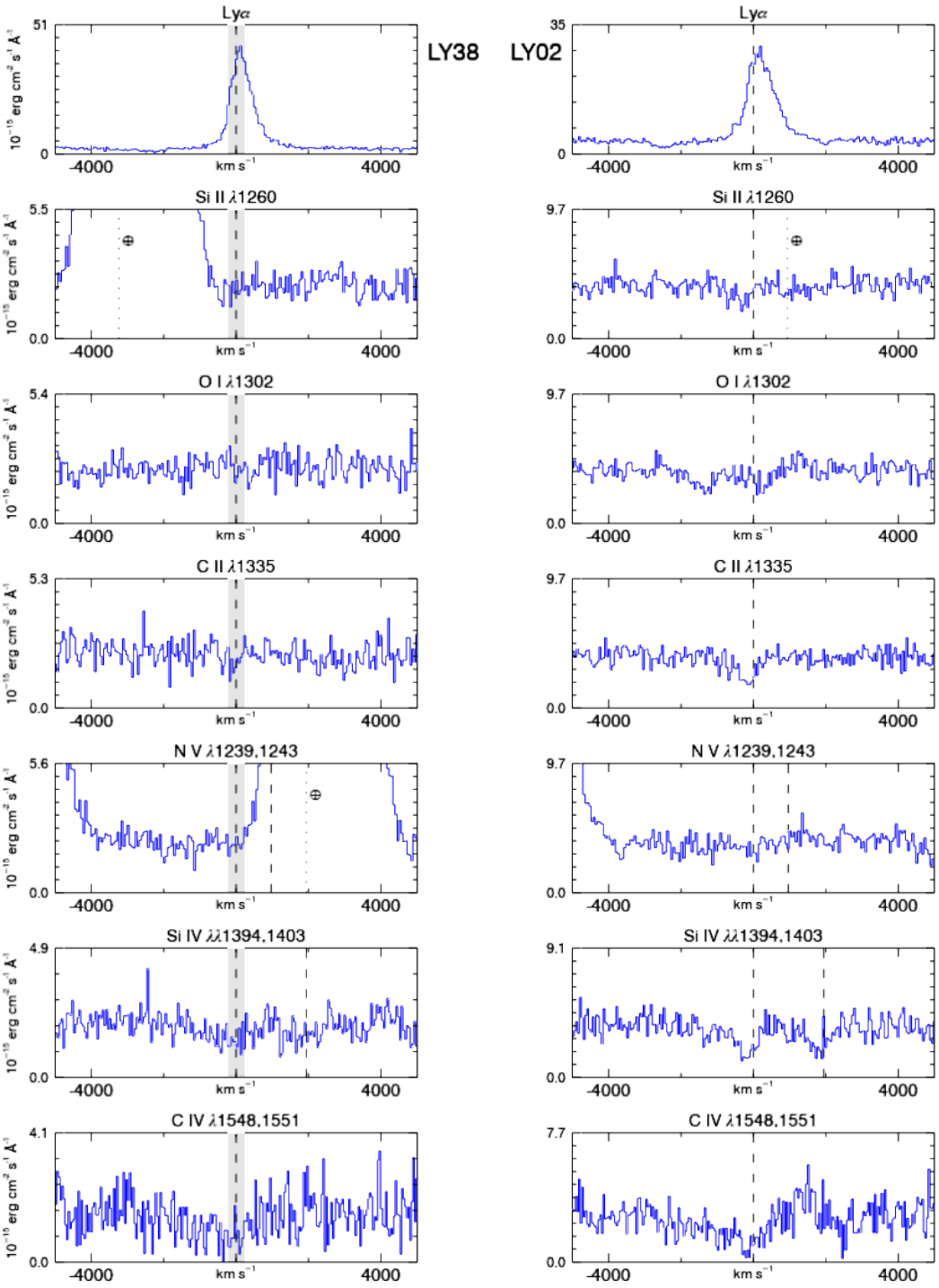
LY38
LY02
Lyα
Si II λ1260
O I λ1302
C II λ1335
N V λ1239,1243
Si IV λλ1394,1403
C IV λ1548,1551
km s⁻¹
-4000
4000
0
51
35
5.5
9.7
5.4
5.3
5.6
4.9
9.1
4.1
7.7

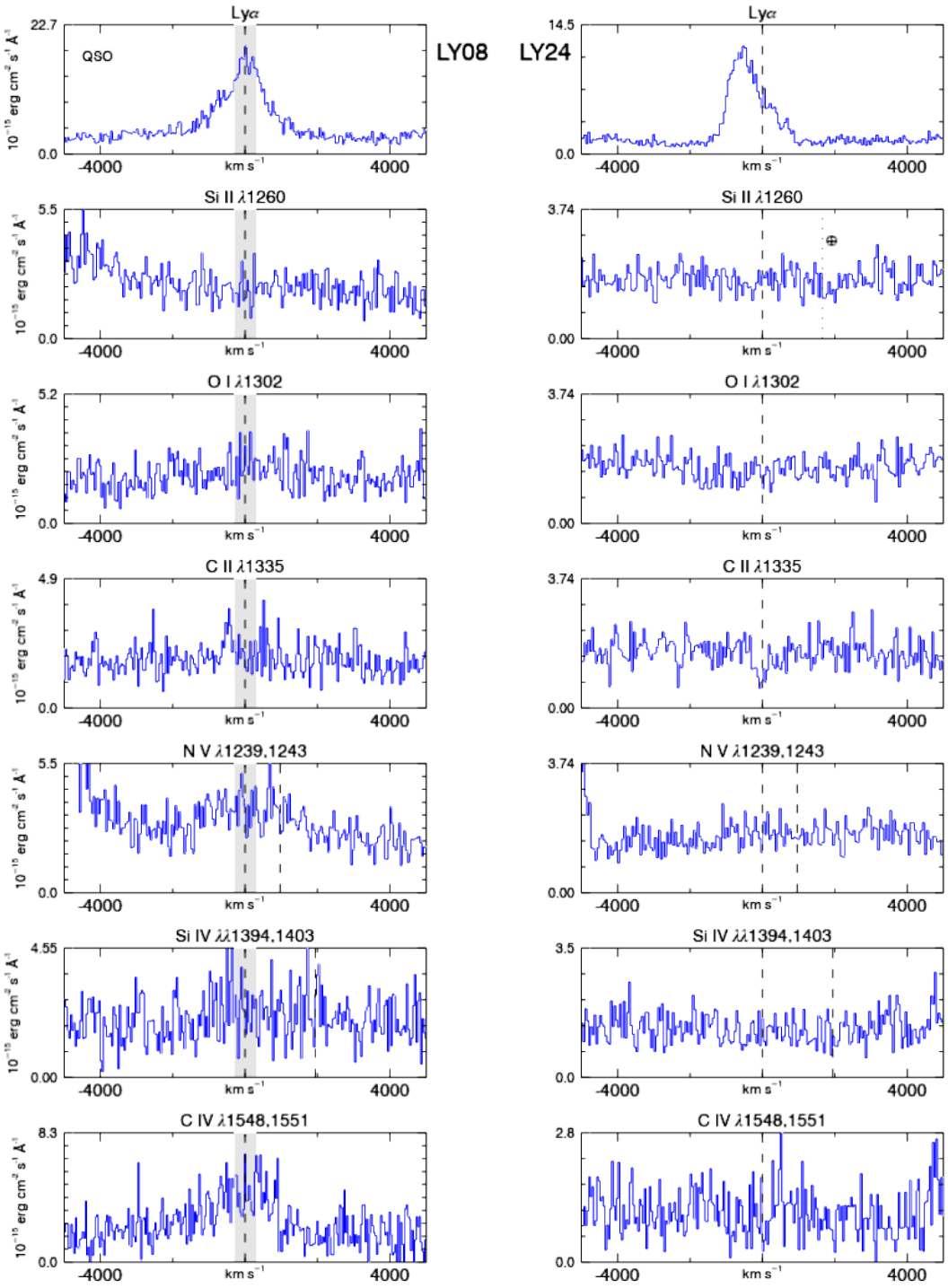
LY08
LY24
Lyα
QSO
Si II λ1260
O I λ1302
C II λ1335
N V λ1239,1243
Si IV λλ1394,1403
C IV λ1548,1551
22.7
14.5
5.5
3.74
5.2
4.9
4.55
3.5
8.3
2.8
0.0
0.00
-4000
4000
km s^{-1}
10^{-15} erg cm^{-2} s^{-1} Å^{-1}

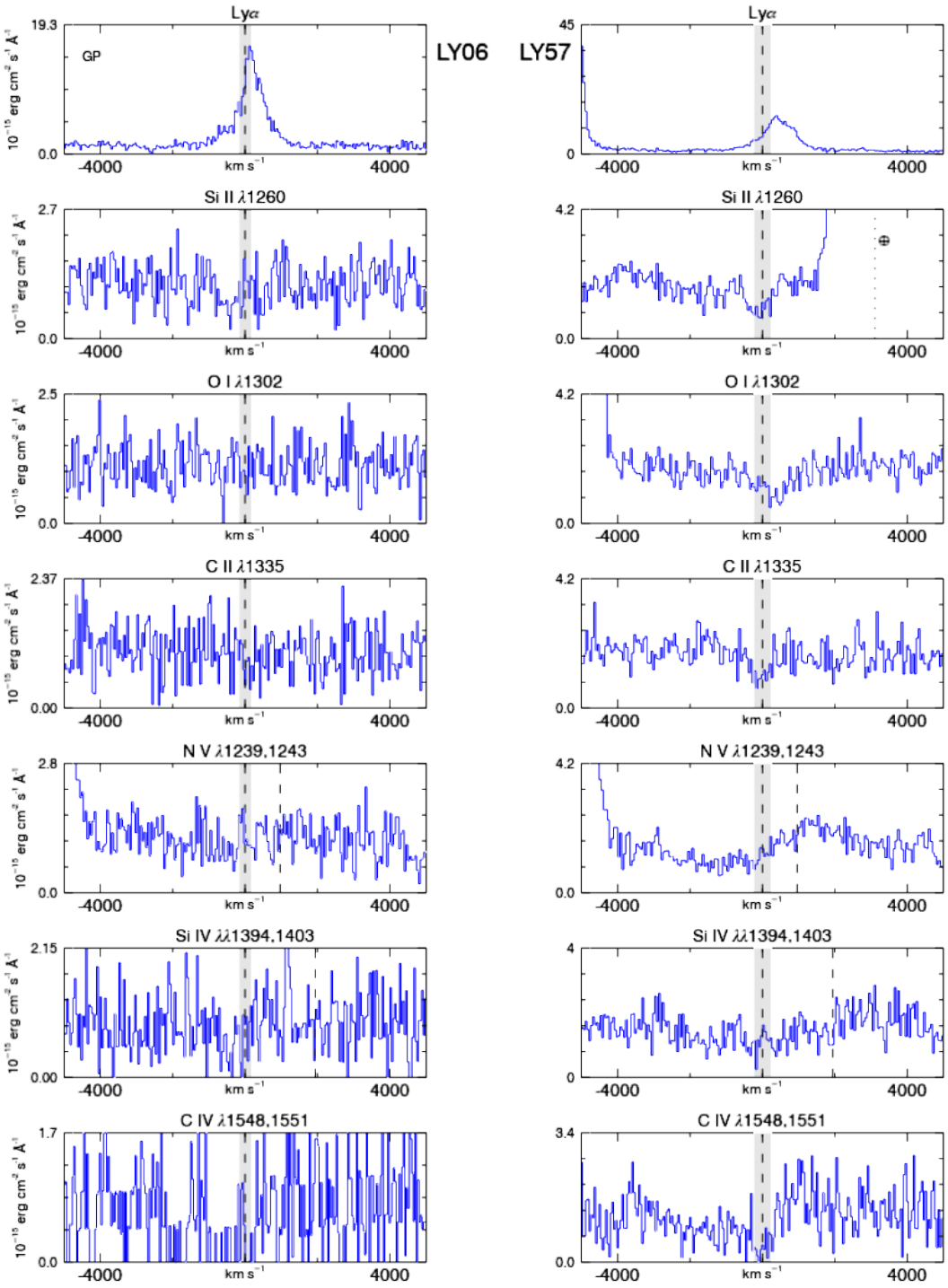
LY06
LY57
Lyα
GP
Si II λ1260
O I λ1302
C II λ1335
N V λ1239,1243
Si IV λλ1394,1403
C IV λ1548,1551
km s⁻¹
-4000
4000
0.0
19.3
45
2.7
4.2
2.5
2.37
2.8
2.15
1.7
3.4

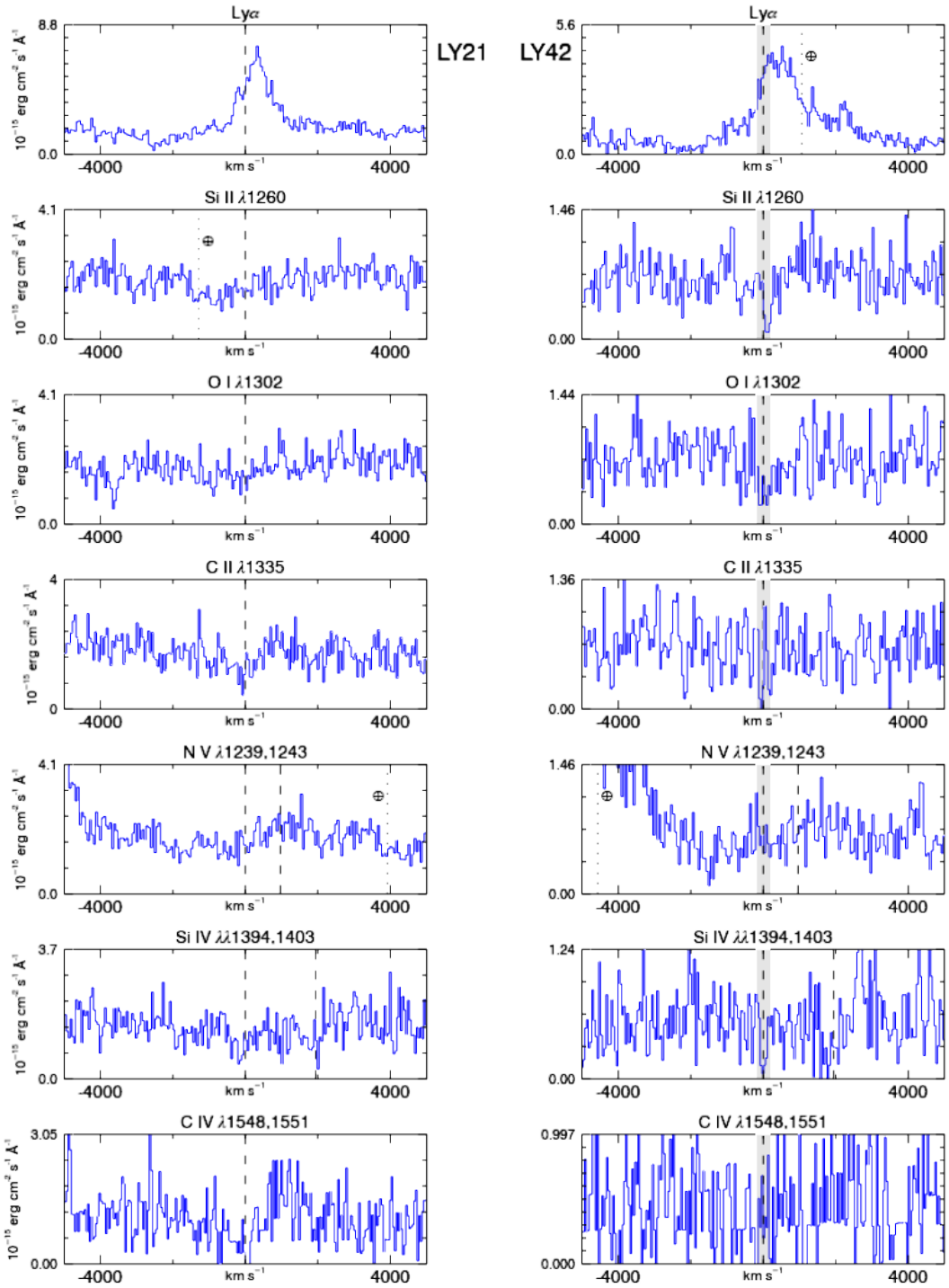
LY21
LY42
Lyα
Si II λ1260
O I λ1302
C II λ1335
N V λ1239,1243
Si IV λλ1394,1403
C IV λ1548,1551
km s⁻¹
-4000
4000
8.8
0.0
4.1
5.6
1.46
1.44
1.36
4
3.7
1.24
3.05
0.997
0.00
0.000

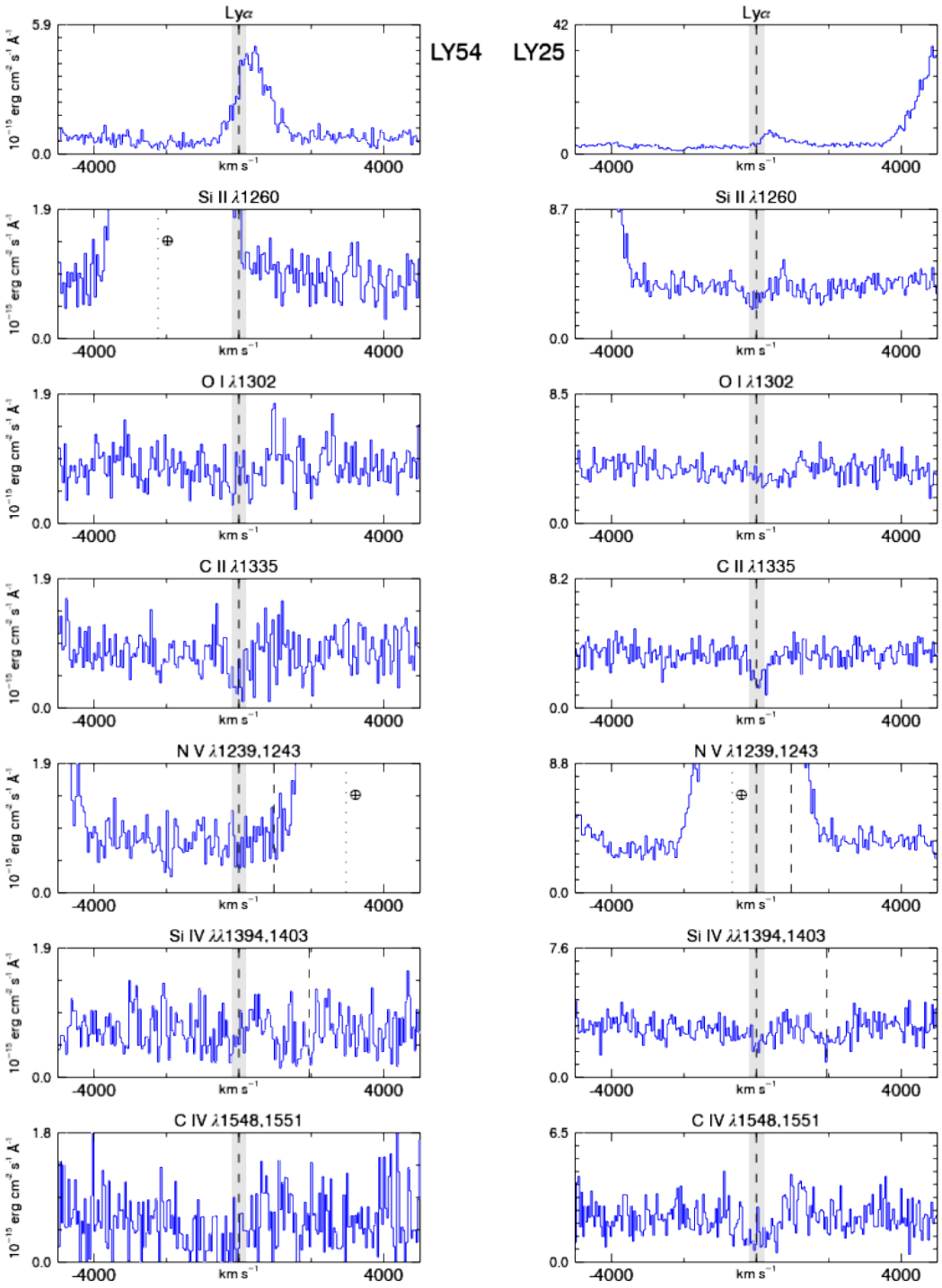
LY54
LY25
Lyα
Si II λ1260
O I λ1302
C II λ1335
N V λ1239,1243
Si IV λλ1394,1403
C IV λ1548,1551
km s⁻¹
-4000
4000
0.0
5.9
42
1.9
8.7
8.5
8.2
8.8
7.6
1.8
6.5

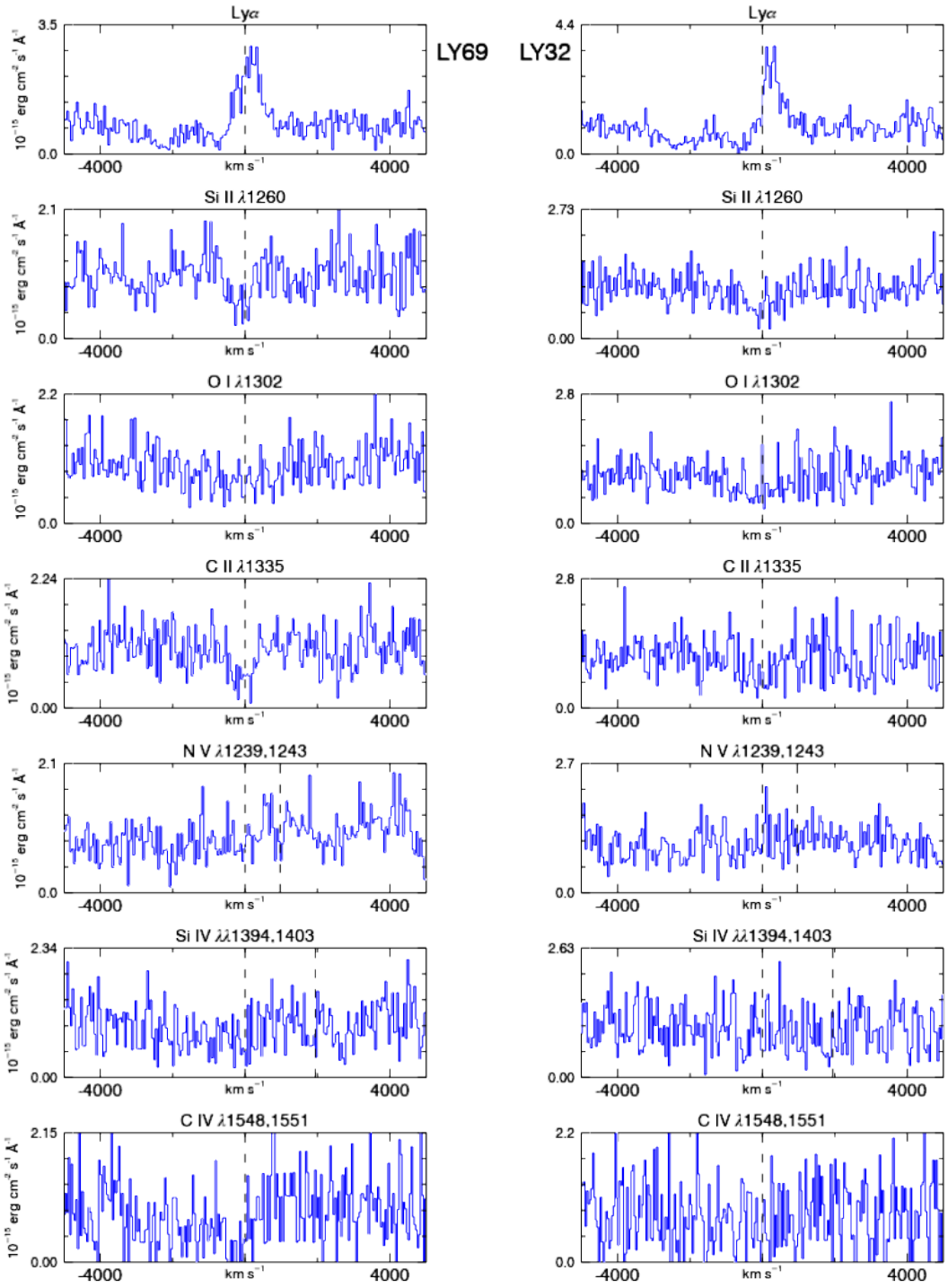
LY69
LY32
Lyα
Si II λ1260
O I λ1302
C II λ1335
N V λ1239,1243
Si IV λλ1394,1403
C IV λ1548,1551
km s⁻¹
-4000
4000
0.0
3.5
2.1
2.2
2.24
2.34
2.15
4.4
2.73
2.8
2.7
2.63
2.2

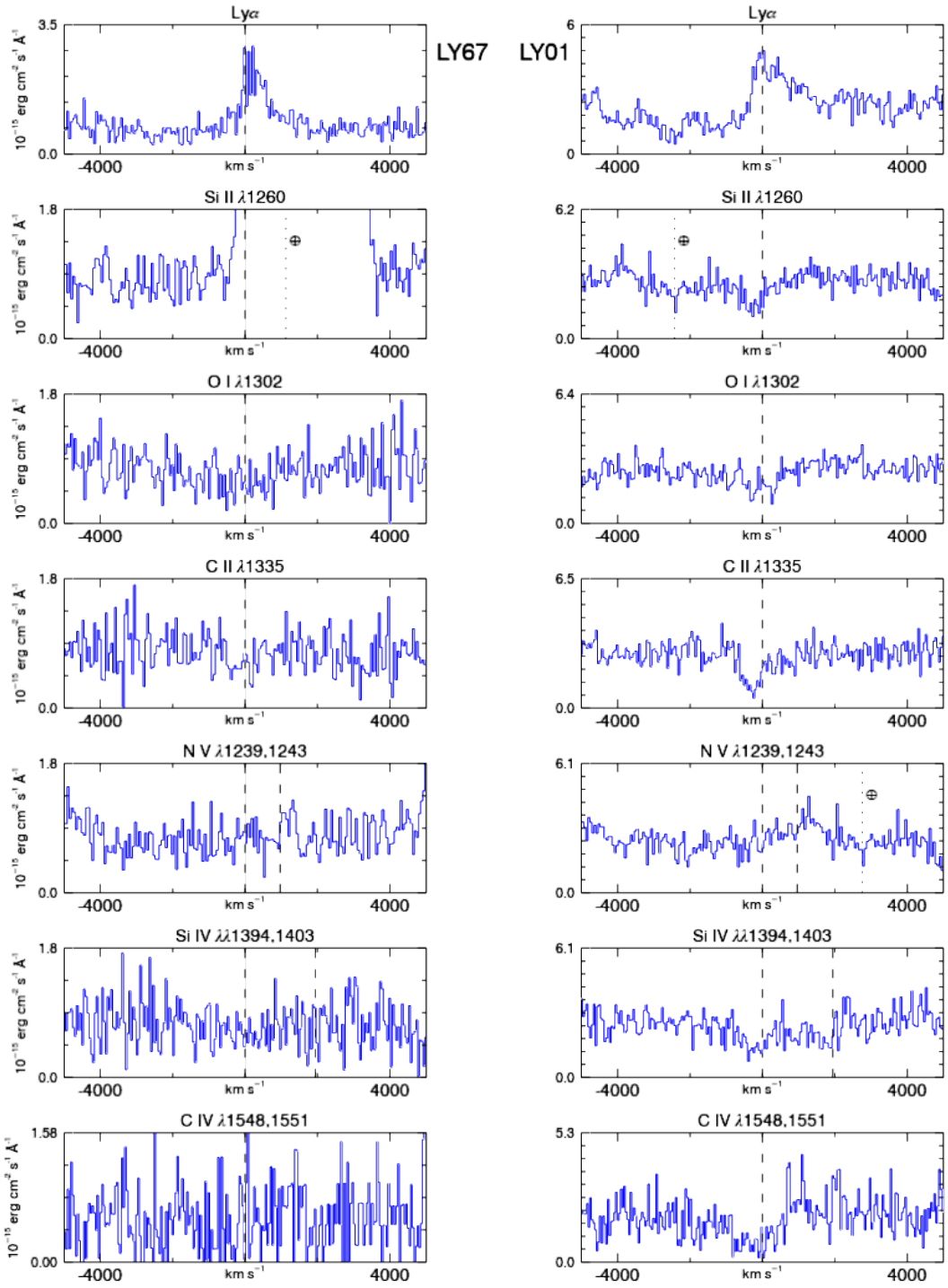
LY67
LY01
Lyα
Si II λ1260
O I λ1302
C II λ1335
N V λ1239,1243
Si IV λλ1394,1403
C IV λ1548,1551
km s⁻¹
-4000
4000
0.0
3.5
1.8
1.58
0.00
6
6.2
6.4
6.5
6.1
5.3

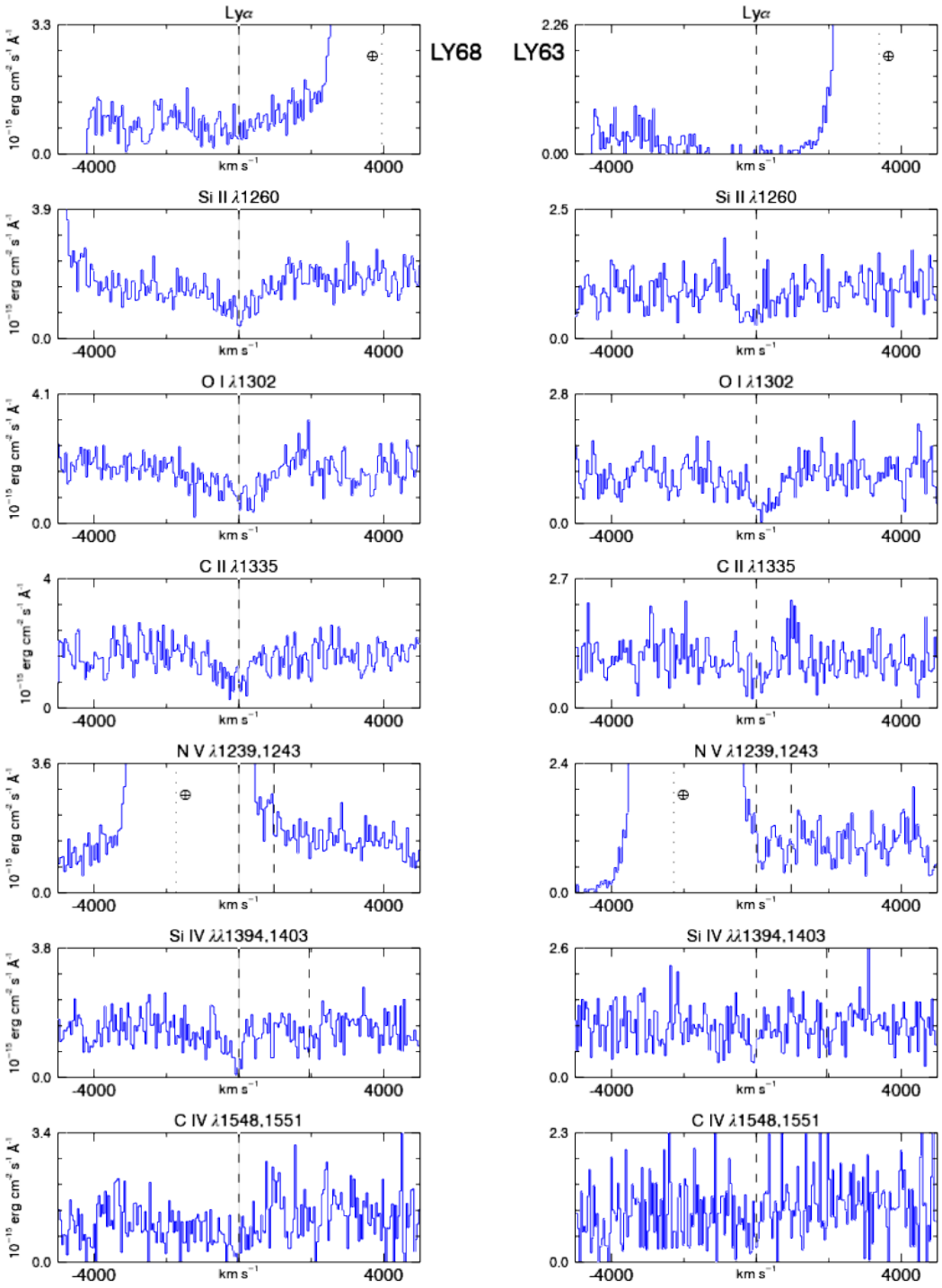
LY68
LY63
Lyα
Si II λ1260
O I λ1302
C II λ1335
N V λ1239,1243
Si IV λλ1394,1403
C IV λ1548,1551
km s⁻¹
-4000
4000
0.0
3.3
3.9
4.1
4
3.6
3.8
3.4
2.26
2.5
2.8
2.7
2.4
2.6
2.3

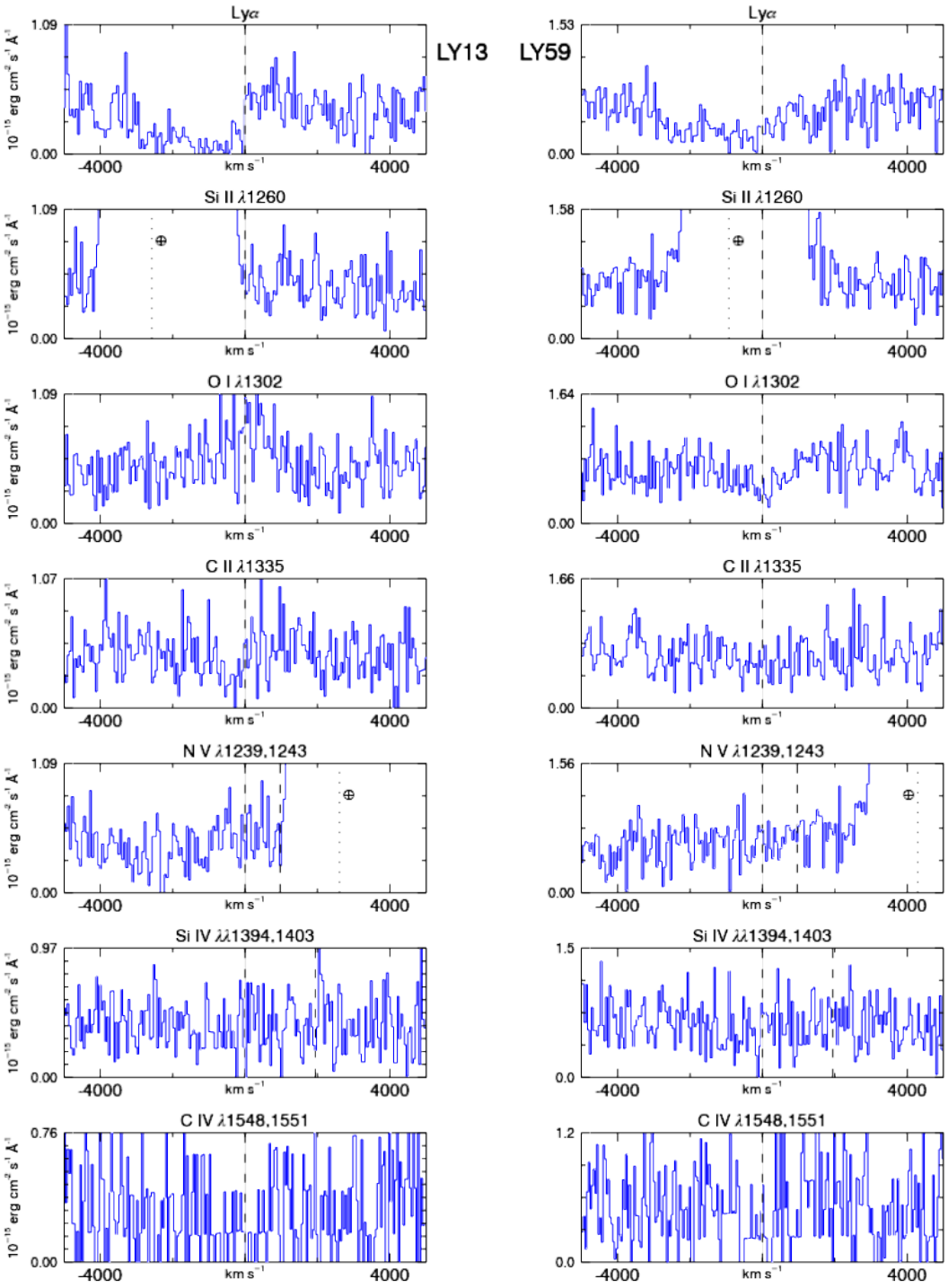
LY13
LY59
Lyα
Si II λ1260
O I λ1302
C II λ1335
N V λ1239,1243
Si IV λλ1394,1403
C IV λ1548,1551
km s⁻¹
-4000
4000
0.00
1.09
1.53
1.58
1.64
1.66
1.56
0.97
1.5
0.76
1.2
0.0

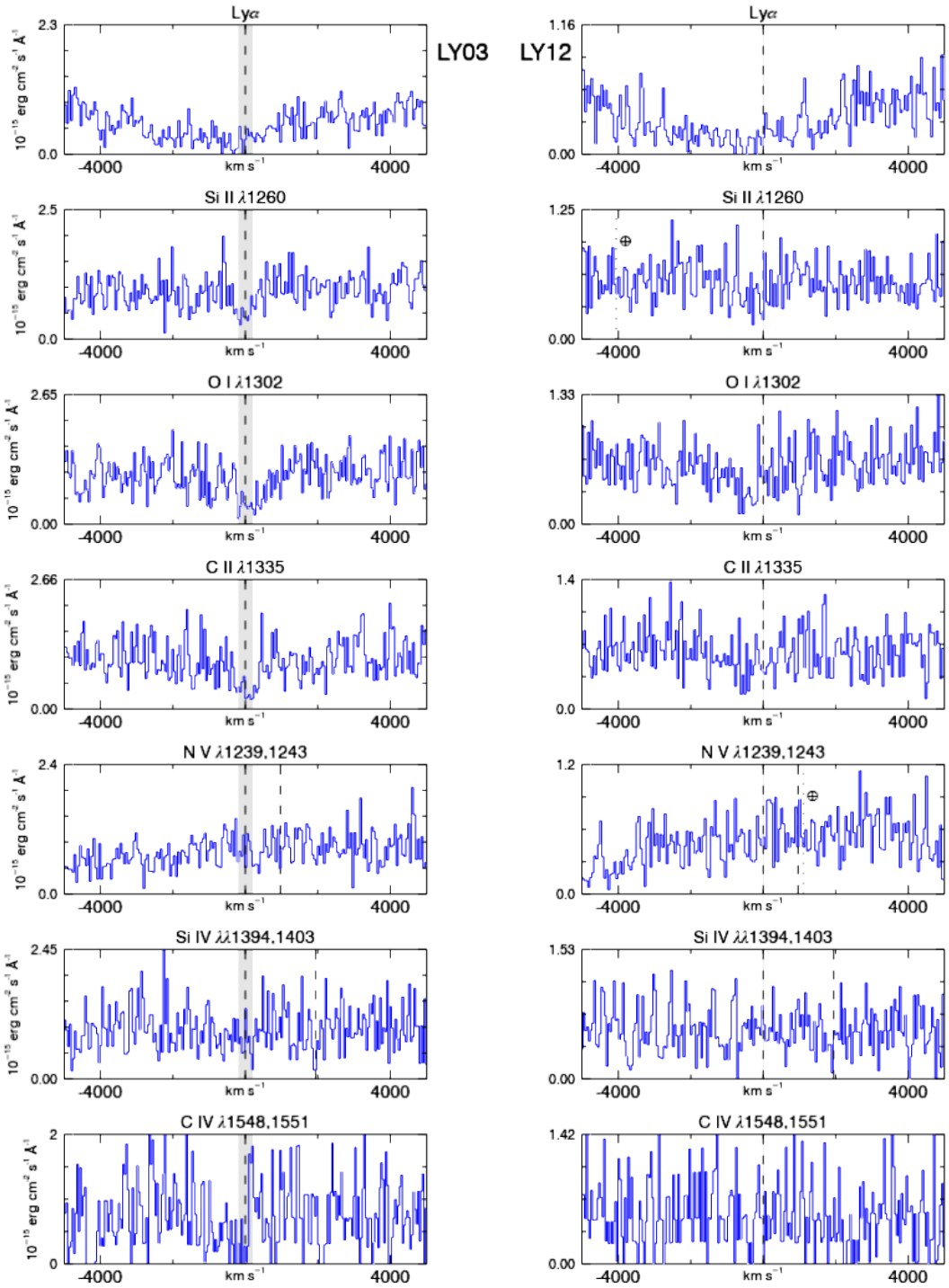
LY03
LY12
Lyα
Si II λ1260
O I λ1302
C II λ1335
N V λ1239,1243
Si IV λλ1394,1403
C IV λ1548,1551
km s⁻¹
-4000
4000

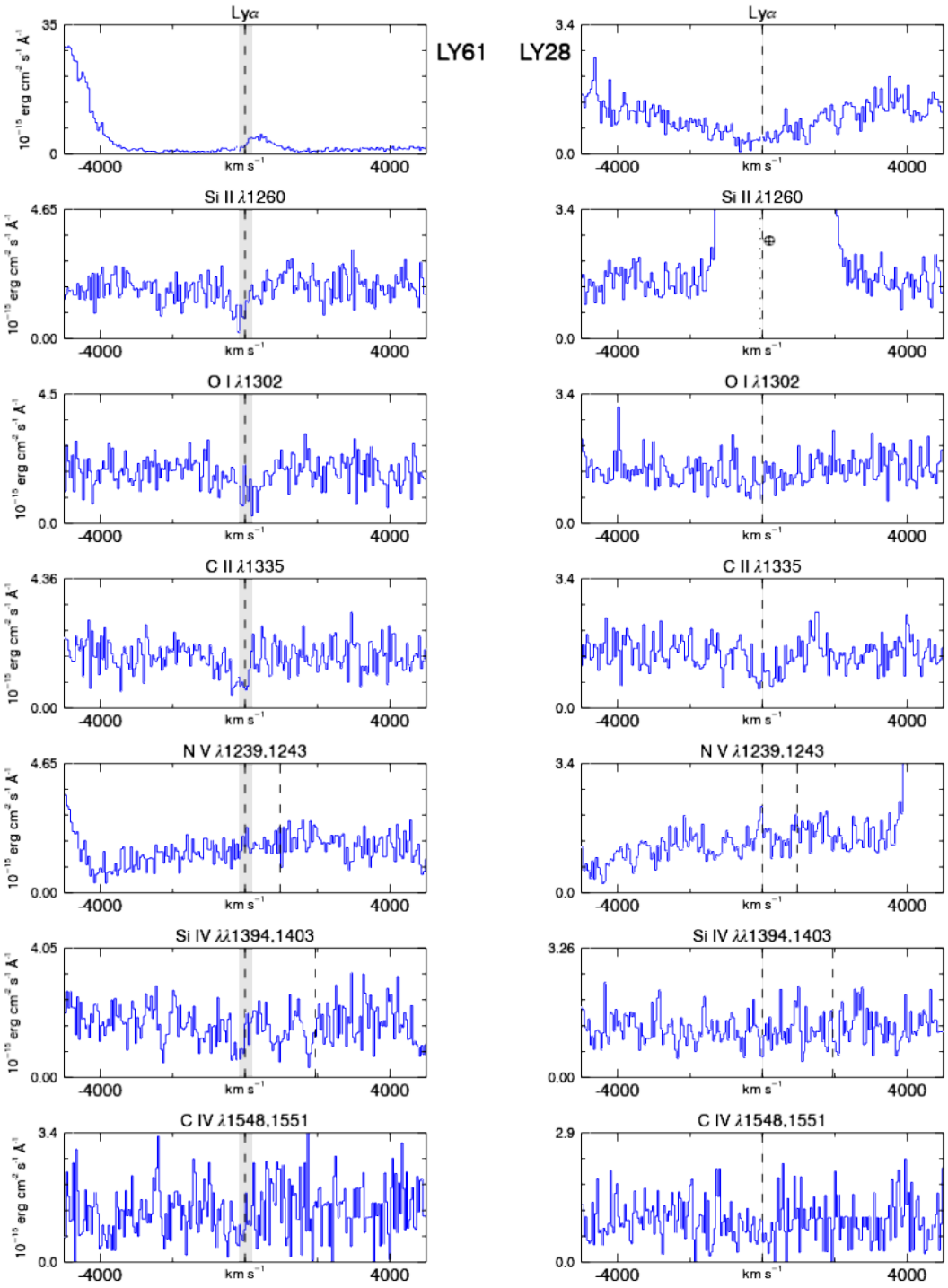
LY61
LY28
Lyα
Si II λ1260
O I λ1302
C II λ1335
N V λ1239,1243
Si IV λλ1394,1403
C IV λ1548,1551
km s⁻¹
-4000
4000

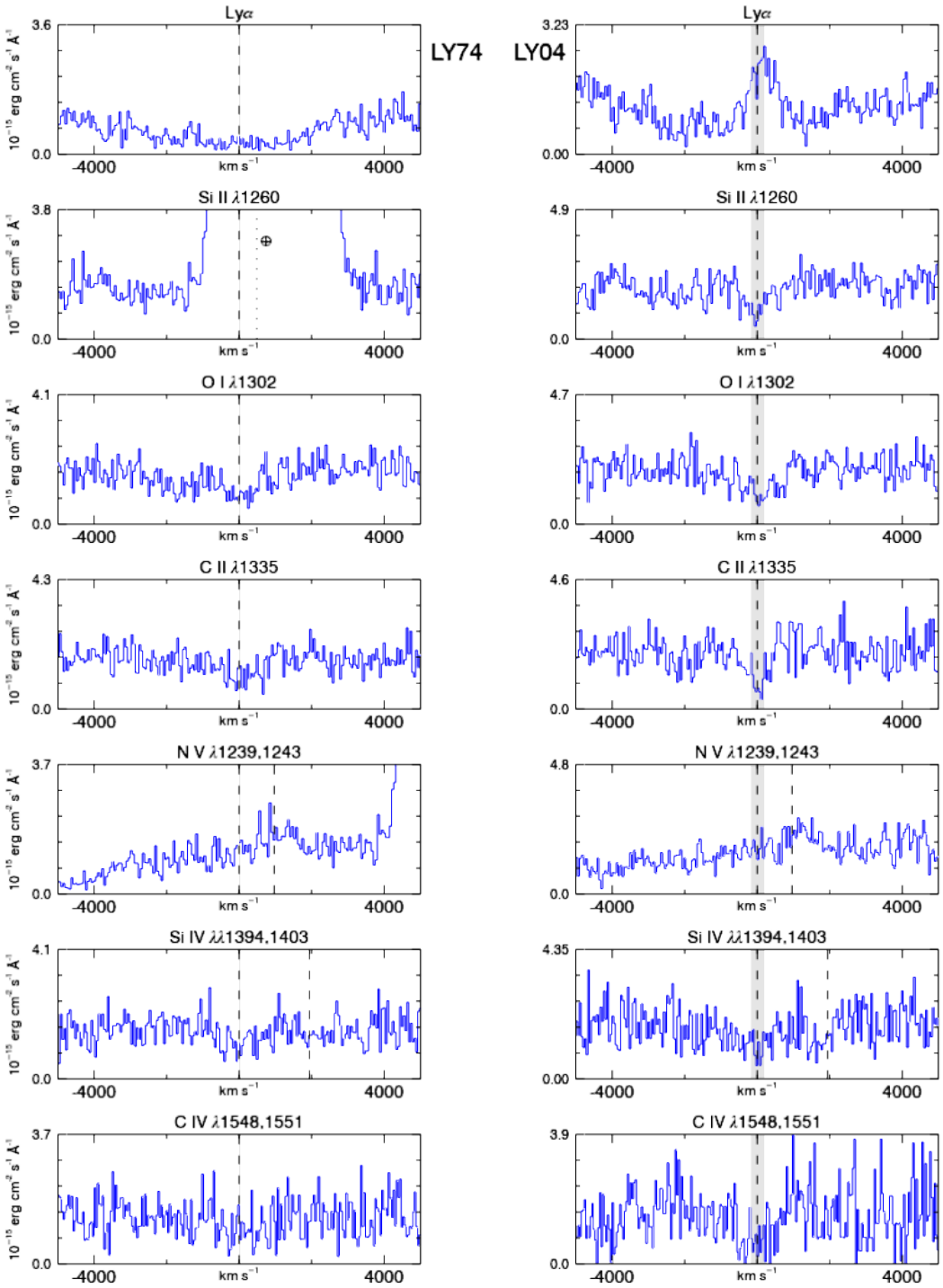
LY74
LY04
Lyα
Si II λ1260
O I λ1302
C II λ1335
N V λ1239,1243
Si IV λλ1394,1403
C IV λ1548,1551
km s⁻¹
-4000
4000
3.6
0.0
3.23
0.00
3.8
4.9
4.1
4.7
4.3
4.6
3.7
4.8
4.35
3.9

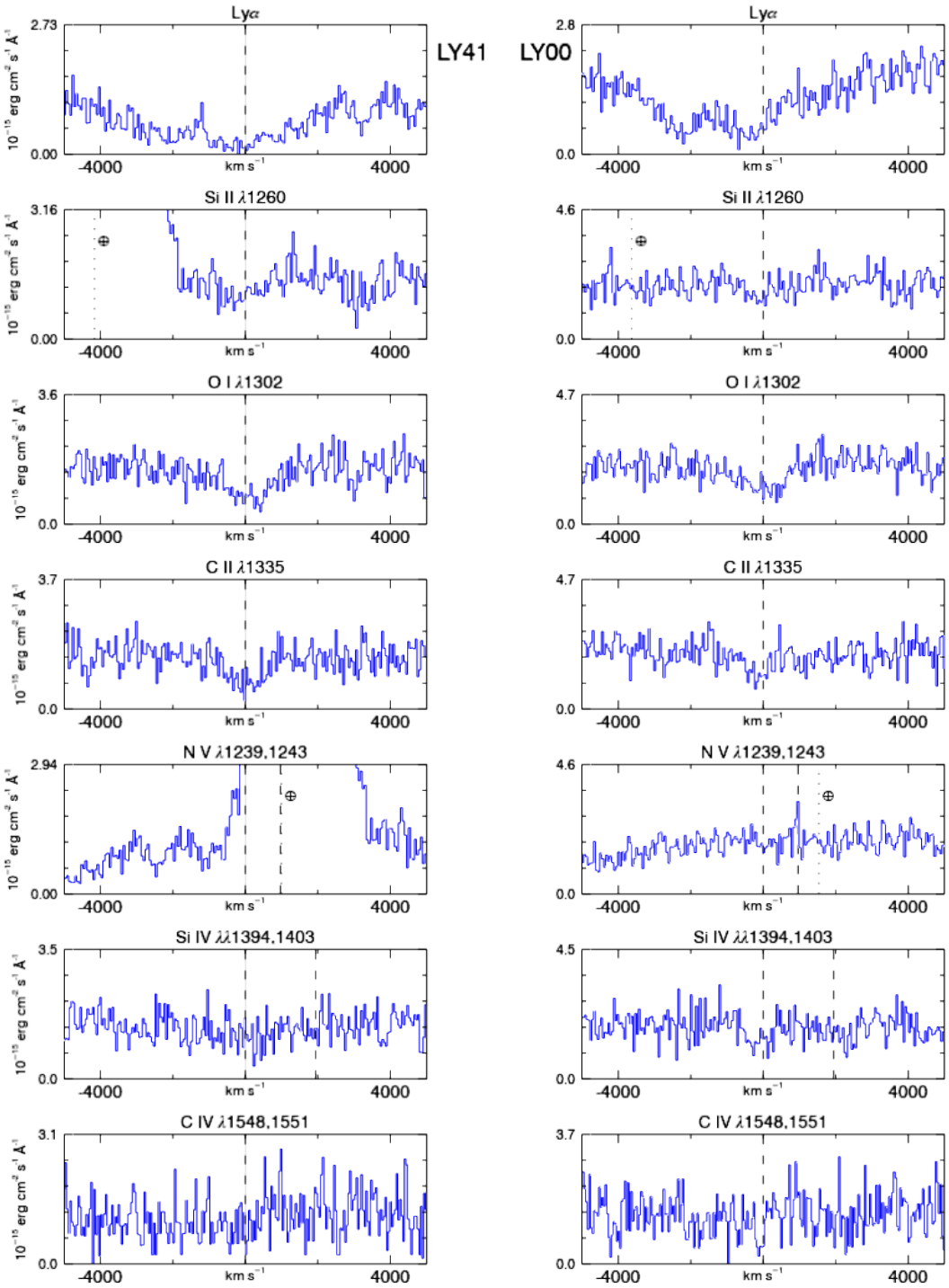
LY41
LY00
Lyα
Si II λ1260
O I λ1302
C II λ1335
N V λ1239,1243
Si IV λλ1394,1403
C IV λ1548,1551
km s⁻¹
-4000
4000
10⁻¹⁵ erg cm⁻² s⁻¹ Å⁻¹

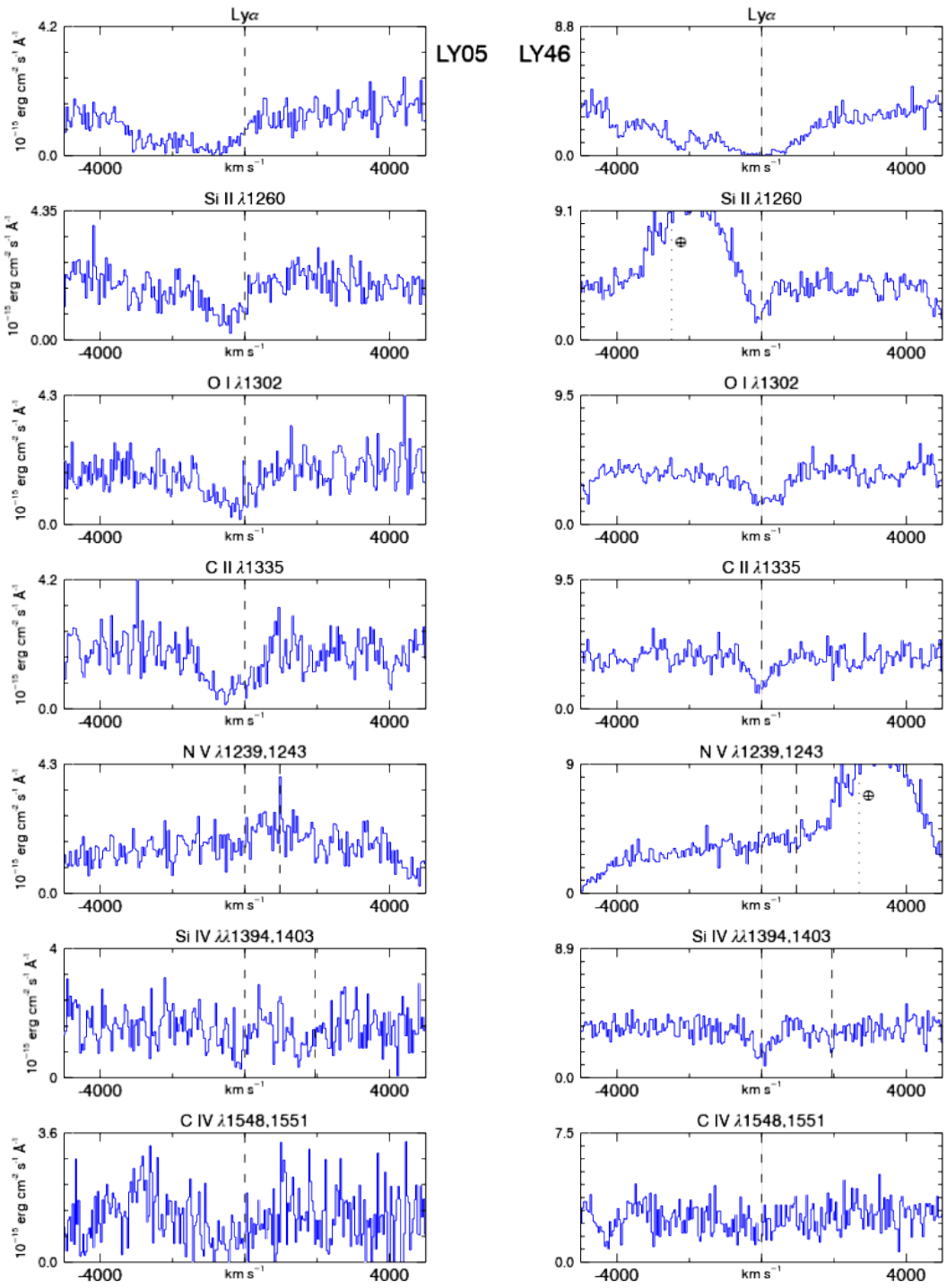
LY05
LY46
Lyα
Si II λ1260
O I λ1302
C II λ1335
N V λ1239,1243
Si IV λλ1394,1403
C IV λ1548,1551
km s⁻¹
-4000
4000

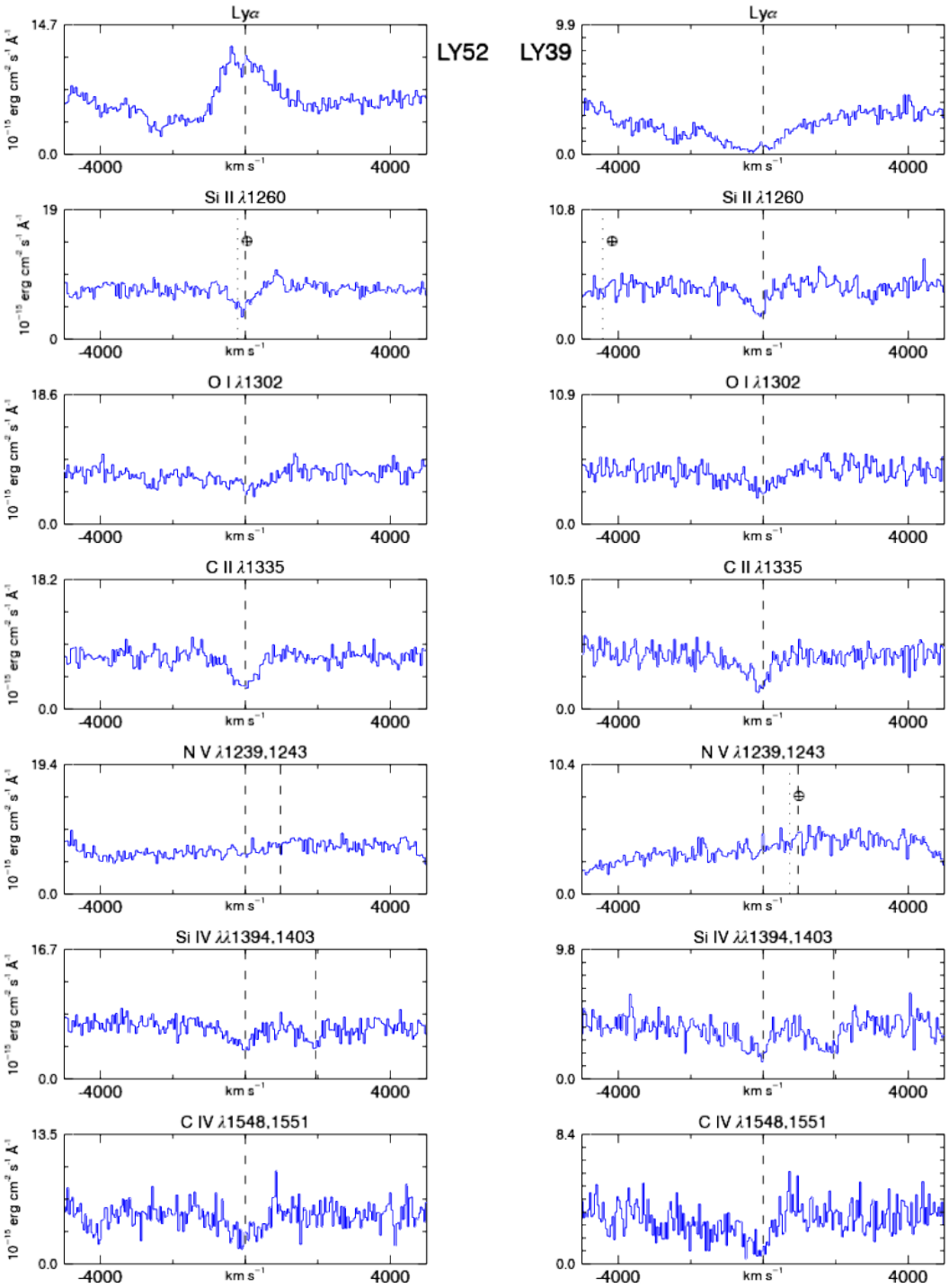
LY52
LY39
Lyα
Si II λ1260
O I λ1302
C II λ1335
N V λ1239,1243
Si IV λλ1394,1403
C IV λ1548,1551
14.7
0.0
19
0
18.6
18.2
19.4
16.7
13.5
9.9
10.8
10.9
10.5
10.4
9.8
8.4
-4000
4000
km s⁻¹
10⁻¹⁵ erg cm⁻² s⁻¹ Å⁻¹

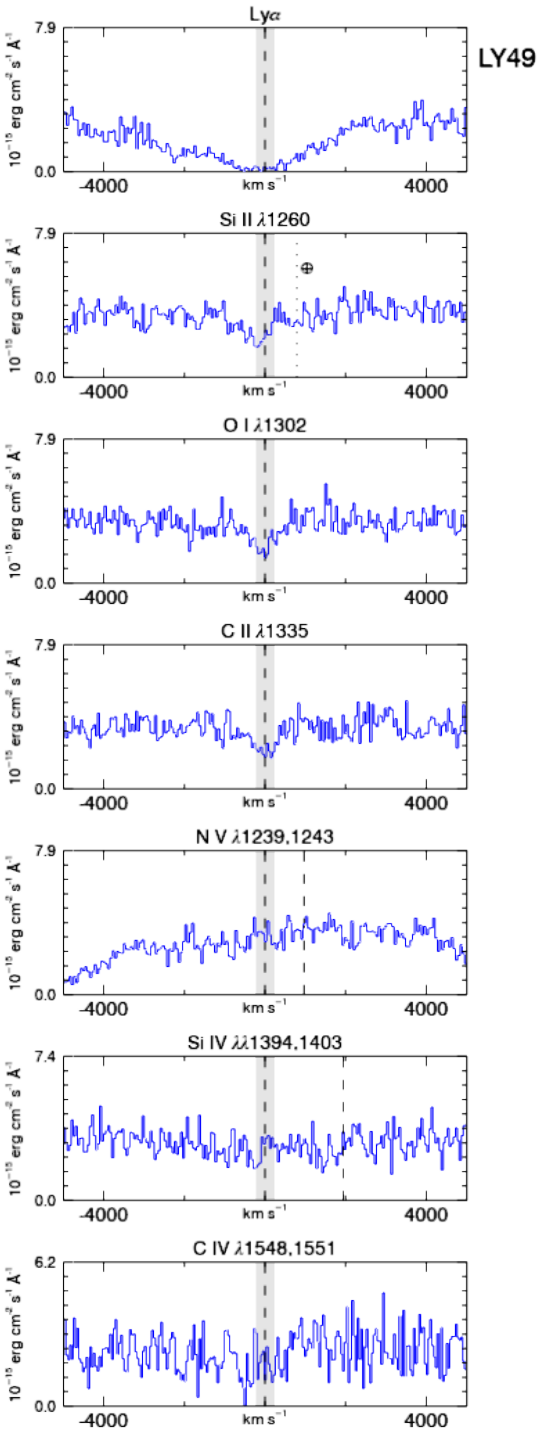
Lyα
LY49
Si II λ1260
O I λ1302
C II λ1335
N V λ1239,1243
Si IV λλ1394,1403
C IV λ1548,1551
7.9
7.4
6.2
0.0
-4000
4000
km s⁻¹
10⁻¹⁵ erg cm⁻² s⁻¹ Å⁻¹

Bibliography

[1] J. E. Gunn and B. A. Peterson, "On the Density of Neutral Hydrogen in Intergalactic Space." ApJ, vol. 142, pp. 1633–1641, Nov. 1965.

[2] R. H. Becker, X. Fan, R. L. White, M. A. Strauss, V. K. Narayanan, R. H. Lupton, J. E. Gunn, J. Annis, N. A. Bahcall, J. Brinkmann, A. J. Connolly, I. Csabai, P. C. Czarapata, M. Doi, T. M. Heckman, G. S. Hennessy, Ž. Ivezić, G. R. Knapp, D. Q. Lamb, T. A. McKay, J. A. Munn, T. Nash, R. Nichol, J. R. Pier, G. T. Richards, D. P. Schneider, C. Stoughton, A. S. Szalay, A. R. Thakar, and D. G. York, "Evidence for Reionization at z˜6: Detection of a Gunn-Peterson Trough in a z=6.28 Quasar," AJ, vol. 122, pp. 2850–2857, Dec. 2001.

[3] X. Fan, V. K. Narayanan, R. H. Lupton, M. A. Strauss, G. R. Knapp, R. H. Becker, R. L. White, L. Pentericci, S. K. Leggett, Z. Haiman, J. E. Gunn, Ž. Ivezić, D. P. Schneider, S. F. Anderson, J. Brinkmann, N. A. Bahcall, A. J. Connolly, I. Csabai, M. Doi, M. Fukugita, T. Geballe, E. K. Grebel, D. Harbeck,

G. Hennessy, D. Q. Lamb, G. Miknaitis, J. A. Munn, R. Nichol, S. Okamura, J. R. Pier, F. Prada, G. T. Richards, A. Szalay, and D. G. York, "A Survey of z¿5.8 Quasars in the Sloan Digital Sky Survey. I. Discovery of Three New Quasars and the Spatial Density of Luminous Quasars at z˜6," AJ, vol. 122, pp. 2833–2849, Dec. 2001.

[4] P. Madau, F. Haardt, and M. J. Rees, "Radiative Transfer in a Clumpy Universe. III. The Nature of Cosmological Ionizing Sources," ApJ, vol. 514, pp. 648–659, Apr. 1999.

[5] P. Madau and F. Haardt, "Cosmic Reionization after Planck: Could Quasars Do It All?" ApJ, vol. 813, p. L8, Nov. 2015.

[6] Planck Collaboration, P. A. R. Ade, N. Aghanim, M. Arnaud, M. Ashdown, J. Aumont, C. Baccigalupi, A. J. Banday, R. B. Barreiro, J. G. Bartlett, and et al., "Planck 2015 results. XIII. Cosmological parameters," A&A, vol. 594, p. A13, Sep. 2016.

[7] B. E. Robertson, R. S. Ellis, S. R. Furlanetto, and J. S. Dunlop, "Cosmic Reionization and Early Star-forming Galaxies: A Joint Analysis of New Constraints from Planck and the Hubble Space Telescope," ApJ, vol. 802, p. L19, Apr. 2015.

[8] H. Yan and R. A. Windhorst, "Candidates of z ˜= 5.5-7 Galaxies in the Hubble Space Telescope Ultra Deep Field," ApJ, vol. 612, pp. L93–L96, Sep. 2004.

[9] S. R. McCandliss, B. Andersson, N. Bergvall, L. Bianchi, C. Bridge, M. Bogosavljevic, S. H. Cohen, J.-M. Deharveng, W. Van Dyke Dixon, H. Ferguson, P. Friedman, M. Hayes, J. C. Howk, A. Inoue, I. Iwata, M. E. Kaiser, G. Kriss, J. Kruk, A. S. Kutyrev, C. Leitherer, G. R. Meurer, J. X. Prochaska, G. Sonneborn, M. Stiavelli, H. I. Teplitz, and R. A. Windhorst, "Project Lyman: Quantifying 11 Gyrs of Metagalactic Ionizing Background Evolution," *ArXiv e-prints*, Sep. 2012.

[10] S. L. Finkelstein, R. E. Ryan, Jr., C. Papovich, M. Dickinson, M. Song, R. Somerville, H. C. Ferguson, B. Salmon, M. Giavalisco, A. M. Koekemoer, M. L. N. Ashby, P. Behroozi, M. Castellano, J. S. Dunlop, S. M. Faber, G. G. Fazio, A. Fontana, N. A. Grogin, N. Hathi, J. Jaacks, D. D. Kocevski, R. Livermore, R. J. McLure, E. Merlin, B. Mobasher, J. A. Newman, M. Rafelski, V. Tilvi, and S. P. Willner, "The Evolution of the Galaxy Rest-Frame Ultraviolet Luminosity Function Over the First Two Billion Years," ApJ, vol. 810, p. 71, Sep. 2015.

[11] M. Ouchi, B. Mobasher, K. Shimasaku, H. C. Ferguson, S. M. Fall, Y. Ono, N. Kashikawa, T. Morokuma, K. Nakajima, S. Okamura, M. Dickinson, M. Giavalisco, and K. Ohta, "Large Area Survey for z = 7 Galaxies in SDF and GOODS-N: Implications for Galaxy Formation and Cosmic Reionization," ApJ, vol. 706, pp. 1136–1151, Dec. 2009.

[12] P. Madau and M. Dickinson, "Cosmic Star-Formation History," ARA&A, vol. 52, pp. 415–486, Aug. 2014.

[13] E. E. Salpeter, "The Luminosity Function and Stellar Evolution." ApJ, vol. 121, p. 161, Jan. 1955.

[14] C. Conroy, J. E. Gunn, and M. White, "The Propagation of Uncertainties in Stellar Population Synthesis Modeling. I. The Relevance of Uncertain Aspects of Stellar Evolution and the Initial Mass Function to the Derived Physical Properties of Galaxies," ApJ, vol. 699, pp. 486–506, Jul. 2009.

[15] G. Bruzual and S. Charlot, "Stellar population synthesis at the resolution of 2003," MNRAS, vol. 344, pp. 1000–1028, Oct. 2003.

[16] D. Schiminovich, O. Ilbert, S. Arnouts, B. Milliard, L. Tresse, O. Le Fèvre, M. Treyer, T. K. Wyder, T. Budavári, E. Zucca, G. Zamorani, D. C. Martin, C. Adami, M. Arnaboldi, S. Bardelli, T. Barlow, L. Bianchi, M. Bolzonella, D. Bottini, Y.-I. Byun, A. Cappi, T. Contini, S. Charlot, J. Donas, K. Forster, S. Foucaud, P. Franzetti, P. G. Friedman, B. Garilli, I. Gavignaud, L. Guzzo, T. M. Heckman, C. Hoopes, A. Iovino, P. Jelinsky, V. Le Brun, Y.-W. Lee, D. Maccagni, B. F. Madore, R. Malina, B. Marano, C. Marinoni, H. J. McCracken, A. Mazure, B. Meneux, P. Morrissey, S. Neff, S. Paltani, R. Pellò, J. P. Picat, A. Pollo, L. Pozzetti, M. Radovich, R. M. Rich, R. Scaramella, M. Scodeggio, M. Seibert, O. Siegmund, T. Small, A. S. Szalay, G. Vettolani,

B. Welsh, C. K. Xu, and A. Zanichelli, "The GALEX-VVDS Measurement of the Evolution of the Far-Ultraviolet Luminosity Density and the Cosmic Star Formation Rate," ApJ, vol. 619, pp. L47–L50, Jan. 2005.

[17] O. Cucciati, L. Tresse, O. Ilbert, O. Le Fèvre, B. Garilli, V. Le Brun, P. Cassata, P. Franzetti, D. Maccagni, M. Scodeggio, E. Zucca, G. Zamorani, S. Bardelli, M. Bolzonella, R. M. Bielby, H. J. McCracken, A. Zanichelli, and D. Vergani, "The star formation rate density and dust attenuation evolution over 12 Gyr with the VVDS surveys," A&A, vol. 539, p. A31, Mar. 2012.

[18] T. Dahlen, B. Mobasher, M. Dickinson, H. C. Ferguson, M. Giavalisco, C. Kretchmer, and S. Ravindranath, "Evolution of the Luminosity Function, Star Formation Rate, Morphology, and Size of Star-forming Galaxies Selected at Rest-Frame 1500 and 2800 Å," ApJ, vol. 654, pp. 172–185, Jan. 2007.

[19] N. A. Reddy and C. C. Steidel, "A Steep Faint-End Slope of the UV Luminosity Function at z ˜ 2-3: Implications for the Global Stellar Mass Density and Star Formation in Low-Mass Halos," ApJ, vol. 692, pp. 778–803, Feb. 2009.

[20] R. J. Bouwens, G. D. Illingworth, P. A. Oesch, M. Franx, I. Labbé, M. Trenti, P. van Dokkum, C. M. Carollo, V. González, R. Smit, and D. Magee, "UV-continuum Slopes at z ˜ 4-7 from the HUDF09+ERS+CANDELS Observations: Discovery of a Well-defined UV Color-Magnitude Relationship for z >= 4 Star-forming Galaxies," ApJ, vol. 754, p. 83, Aug. 2012.

[21] R. J. Bouwens, G. D. Illingworth, P. A. Oesch, M. Trenti, I. Labbé, M. Franx, M. Stiavelli, C. M. Carollo, P. van Dokkum, and D. Magee, "Lower-luminosity Galaxies Could Reionize the Universe: Very Steep Faint-end Slopes to the UV Luminosity Functions at z >= 5-8 from the HUDF09 WFC3/IR Observations," ApJ, vol. 752, p. L5, Jun. 2012.

[22] M. A. Schenker, B. E. Robertson, R. S. Ellis, Y. Ono, R. J. McLure, J. S. Dunlop, A. Koekemoer, R. A. A. Bowler, M. Ouchi, E. Curtis-Lake, A. B. Rogers, E. Schneider, S. Charlot, D. P. Stark, S. R. Furlanetto, and M. Cirasuolo, "The UV Luminosity Function of Star-forming Galaxies via Dropout Selection at Redshifts z ˜ 7 and 8 from the 2012 Ultra Deep Field Campaign," ApJ, vol. 768, p. 196, May 2013.

[23] D. B. Sanders, J. M. Mazzarella, D.-C. Kim, J. A. Surace, and B. T. Soifer, "The IRAS Revised Bright Galaxy Sample," AJ, vol. 126, pp. 1607–1664, Oct. 2003.

[24] T. T. Takeuchi, K. Yoshikawa, and T. T. Ishii, "The Luminosity Function of IRAS Point Source Catalog Redshift Survey Galaxies," ApJ, vol. 587, pp. L89–L92, Apr. 2003.

[25] B. Magnelli, D. Elbaz, R. R. Chary, M. Dickinson, D. Le Borgne, D. T. Frayer, and C. N. A. Willmer, "Evolution of the dusty infrared luminosity function

from z = 0 to z = 2.3 using observations from Spitzer," A&A, vol. 528, p. A35, Apr. 2011.

[26] B. Magnelli, P. Popesso, S. Berta, F. Pozzi, D. Elbaz, D. Lutz, M. Dickinson, B. Altieri, P. Andreani, H. Aussel, M. Béthermin, A. Bongiovanni, J. Cepa, V. Charmandaris, R.-R. Chary, A. Cimatti, E. Daddi, N. M. Förster Schreiber, R. Genzel, C. Gruppioni, M. Harwit, H. S. Hwang, R. J. Ivison, G. Magdis, R. Maiolino, E. Murphy, R. Nordon, M. Pannella, A. Pérez García, A. Poglitsch, D. Rosario, M. Sanchez-Portal, P. Santini, D. Scott, E. Sturm, L. J. Tacconi, and I. Valtchanov, "The deepest Herschel-PACS far-infrared survey: number counts and infrared luminosity functions from combined PEP/GOODS-H observations," A&A, vol. 553, p. A132, May 2013.

[27] C. Gruppioni, F. Pozzi, G. Rodighiero, I. Delvecchio, S. Berta, L. Pozzetti, G. Zamorani, P. Andreani, A. Cimatti, O. Ilbert, E. Le Floc'h, D. Lutz, B. Magnelli, L. Marchetti, P. Monaco, R. Nordon, S. Oliver, P. Popesso, L. Riguccini, I. Roseboom, D. J. Rosario, M. Sargent, M. Vaccari, B. Altieri, H. Aussel, A. Bongiovanni, J. Cepa, E. Daddi, H. Domínguez-Sánchez, D. Elbaz, N. Förster Schreiber, R. Genzel, A. Iribarrem, M. Magliocchetti, R. Maiolino, A. Poglitsch, A. Pérez García, M. Sanchez-Portal, E. Sturm, L. Tacconi, I. Valtchanov, A. Amblard, V. Arumugam, M. Bethermin, J. Bock, A. Boselli, V. Buat, D. Burgarella, N. Castro-Rodríguez, A. Cava, P. Cha-

nial, D. L. Clements, A. Conley, A. Cooray, C. D. Dowell, E. Dwek, S. Eales, A. Franceschini, J. Glenn, M. Griffin, E. Hatziminaoglou, E. Ibar, K. Isaak, R. J. Ivison, G. Lagache, L. Levenson, N. Lu, S. Madden, B. Maffei, G. Mainetti, H. T. Nguyen, B. O'Halloran, M. J. Page, P. Panuzzo, A. Papageorgiou, C. P. Pearson, I. Pérez-Fournon, M. Pohlen, D. Rigopoulou, M. Rowan-Robinson, B. Schulz, D. Scott, N. Seymour, D. L. Shupe, A. J. Smith, J. A. Stevens, M. Symeonidis, M. Trichas, K. E. Tugwell, L. Vigroux, L. Wang, G. Wright, C. K. Xu, M. Zemcov, S. Bardelli, M. Carollo, T. Contini, O. Le Févre, S. Lilly, V. Mainieri, A. Renzini, M. Scodeggio, and E. Zucca, "The Herschel PEP/HerMES luminosity function - I. Probing the evolution of PACS selected Galaxies to z 4," MNRAS, vol. 432, pp. 23–52, Jun. 2013.

[28] A. H. Pawlik, J. Schaye, and E. van Scherpenzeel, "Keeping the Universe ionized: photoheating and the clumping factor of the high-redshift intergalactic medium," MNRAS, vol. 394, pp. 1812–1824, Apr. 2009.

[29] J. M. Shull, A. Harness, M. Trenti, and B. D. Smith, "Critical Star Formation Rates for Reionization: Full Reionization Occurs at Redshift z 7," ApJ, vol. 747, p. 100, Mar. 2012.

[30] D. Osterbrock and G. Ferland, *Astrophysics of Gaseous Nebulae and Active Galactic Nuclei*. University Science Books, 2006.

[31] M. Shull, A. Harness, M. Trenti, and B. Smith, "Critical Star-Formation Rates for Reionization: Full Reionization occurs at z = 7," *ArXiv e-prints*, Aug. 2011.

[32] S. Borthakur, T. M. Heckman, C. Leitherer, and R. A. Overzier, "A local clue to the reionization of the universe," *Science*, vol. 346, no. 6206, pp. 216–219, 2014. [Online]. Available: http://www.sciencemag.org/content/346/6206/216.abstract

[33] Y. I. Izotov, I. Orlitová, D. Schaerer, T. X. Thuan, A. Verhamme, N. G. Guseva, and G. Worseck, "Eight per cent leakage of Lyman continuum photons from a compact, star-forming dwarf galaxy," Nature, vol. 529, pp. 178–180, Jan. 2016.

[34] C. Leitherer, S. Hernandez, J. C. Lee, and M. S. Oey, "Direct Detection of Lyman Continuum Escape from Local Starburst Galaxies with the Cosmic Origins Spectrograph," ApJ, vol. 823, p. 64, May 2016.

[35] A. E. Shapley, C. C. Steidel, A. L. Strom, M. Bogosavljević, N. A. Reddy, B. Siana, R. E. Mostardi, and G. C. Rudie, "Q1549-C25: A Clean Source of Lyman-Continuum Emission at z = 3.15," ApJ, vol. 826, p. L24, Aug. 2016.

[36] F. Haardt and P. Madau, "Radiative Transfer in a Clumpy Universe. IV. New Synthesis Models of the Cosmic UV/X-Ray Background," ApJ, vol. 746, p. 125, Feb. 2012.

[37] J. A. Kollmeier, D. H. Weinberg, B. D. Oppenheimer, F. Haardt, N. Katz,

R. Davé, M. Fardal, P. Madau, C. Danforth, A. B. Ford, M. S. Peeples, and J. McEwen, "The Photon Underproduction Crisis," ApJ, vol. 789, p. L32, Jul. 2014.

[38] F. Paresce, C. F. McKee, and S. Bowyer, "Galactic and extragalactic contributions to the far-ultraviolet background," ApJ, vol. 240, pp. 387–400, Sep. 1980.

[39] P. Madau, "Radiative transfer in a clumpy universe: The colors of high-redshift galaxies," ApJ, vol. 441, pp. 18–27, Mar. 1995.

[40] A. K. Inoue, I. Shimizu, I. Iwata, and M. Tanaka, "An updated analytic model for attenuation by the intergalactic medium," MNRAS, vol. 442, pp. 1805–1820, Aug. 2014.

[41] A. K. Inoue and I. Iwata, "A Monte Carlo simulation of the intergalactic absorption and the detectability of the Lyman continuum from distant galaxies," MNRAS, vol. 387, pp. 1681–1692, Jul. 2008.

[42] M. Stiavelli, S. M. Fall, and N. Panagia, "Observable Properties of Cosmological Reionization Sources," ApJ, vol. 600, pp. 508–519, Jan. 2004.

[43] J. Mao, A. Lapi, G. L. Granato, G. de Zotti, and L. Danese, "The Role of the Dust in Primeval Galaxies: A Simple Physical Model for Lyman Break Galaxies and Lyα Emitters," ApJ, vol. 667, pp. 655–666, Oct. 2007.

[44] D. A. Neufeld, "The transfer of resonance-line radiation in static astrophysical media," ApJ, vol. 350, pp. 216–241, Feb. 1990.

[45] D. A. Neufeld, "The escape of Lyman-alpha radiation from a multiphase interstellar medium," ApJ, vol. 370, pp. L85–L88, Apr. 1991.

[46] D. G. York, J. Adelman, J. E. Anderson, Jr., S. F. Anderson, J. Annis, N. A. Bahcall, J. A. Bakken, R. Barkhouser, S. Bastian, E. Berman, W. N. Boroski, S. Bracker, C. Briegel, J. W. Briggs, J. Brinkmann, R. Brunner, S. Burles, L. Carey, M. A. Carr, F. J. Castander, B. Chen, P. L. Colestock, A. J. Connolly, J. H. Crocker, I. Csabai, P. C. Czarapata, J. E. Davis, M. Doi, T. Dombeck, D. Eisenstein, N. Ellman, B. R. Elms, M. L. Evans, X. Fan, G. R. Federwitz, L. Fiscelli, S. Friedman, J. A. Frieman, M. Fukugita, B. Gillespie, J. E. Gunn, V. K. Gurbani, E. de Haas, M. Haldeman, F. H. Harris, J. Hayes, T. M. Heckman, G. S. Hennessy, R. B. Hindsley, S. Holm, D. J. Holmgren, C.-h. Huang, C. Hull, D. Husby, S.-I. Ichikawa, T. Ichikawa, Ž. Ivezić, S. Kent, R. S. J. Kim, E. Kinney, M. Klaene, A. N. Kleinman, S. Kleinman, G. R. Knapp, J. Korienek, R. G. Kron, P. Z. Kunszt, D. Q. Lamb, B. Lee, R. F. Leger, S. Limmongkol, C. Lindenmeyer, D. C. Long, C. Loomis, J. Loveday, R. Lucinio, R. H. Lupton, B. MacKinnon, E. J. Mannery, P. M. Mantsch, B. Margon, P. McGehee, T. A. McKay, A. Meiksin, A. Merelli, D. G. Monet, J. A. Munn, V. K. Narayanan, T. Nash, E. Neilsen, R. Neswold, H. J. Newberg, R. C. Nichol,

T. Nicinski, M. Nonino, N. Okada, S. Okamura, J. P. Ostriker, R. Owen, A. G. Pauls, J. Peoples, R. L. Peterson, D. Petravick, J. R. Pier, A. Pope, R. Pordes, A. Prosapio, R. Rechenmacher, T. R. Quinn, G. T. Richards, M. W. Richmond, C. H. Rivetta, C. M. Rockosi, K. Ruthmansdorfer, D. Sandford, D. J. Schlegel, D. P. Schneider, M. Sekiguchi, G. Sergey, K. Shimasaku, W. A. Siegmund, S. Smee, J. A. Smith, S. Snedden, R. Stone, C. Stoughton, M. A. Strauss, C. Stubbs, M. SubbaRao, A. S. Szalay, I. Szapudi, G. P. Szokoly, A. R. Thakar, C. Tremonti, D. L. Tucker, A. Uomoto, D. Vanden Berk, M. S. Vogeley, P. Waddell, S.-i. Wang, M. Watanabe, D. H. Weinberg, B. Yanny, N. Yasuda, and SDSS Collaboration, "The Sloan Digital Sky Survey: Technical Summary," AJ, vol. 120, pp. 1579–1587, Sep. 2000.

[47] C. Leitherer, D. Schaerer, J. D. Goldader, R. M. G. Delgado, C. Robert, D. F. Kune, D. F. de Mello, D. Devost, and T. M. Heckman, "Starburst99: Synthesis Models for Galaxies with Active Star Formation," ApJS, vol. 123, pp. 3–40, Jul. 1999.

[48] R. J. Bouwens, G. D. Illingworth, P. A. Oesch, M. Stiavelli, P. van Dokkum, M. Trenti, D. Magee, I. Labbé, M. Franx, C. M. Carollo, and V. Gonzalez, "Discovery of z ˜ 8 Galaxies in the Hubble Ultra Deep Field from Ultra-Deep WFC3/IR Observations," ApJ, vol. 709, pp. L133–L137, Feb. 2010.

[49] A. Verhamme, I. Orlitová, D. Schaerer, and M. Hayes, "Using Lyman-α to

detect galaxies that leak Lyman continuum," A&A, vol. 578, p. A7, Jun. 2015.

[50] R. M. Alexandroff, T. M. Heckman, S. Borthakur, R. Overzier, and C. Leitherer, "Indirect Evidence for Escaping Ionizing Photons in Local Lyman Break Galaxy Analogs," ApJ, vol. 810, p. 104, Sep. 2015.

[51] M. Dijkstra, M. Gronke, and A. Venkatesan, "The Lyα-LyC Connection: Evidence for an Enhanced Contribution of UV-faint Galaxies to Cosmic Reionization," ApJ, vol. 828, p. 71, Sep. 2016.

[52] N. Kashikawa, K. Shimasaku, Y. Matsuda, E. Egami, L. Jiang, T. Nagao, M. Ouchi, M. A. Malkan, T. Hattori, K. Ota, Y. Taniguchi, S. Okamura, C. Ly, M. Iye, H. Furusawa, Y. Shioya, T. Shibuya, Y. Ishizaki, and J. Toshikawa, "Completing the Census of Lyα Emitters at the Reionization Epoch," ApJ, vol. 734, p. 119, Jun. 2011.

[53] D. K. Erb, C. C. Steidel, R. F. Trainor, M. Bogosavljević, A. E. Shapley, D. B. Nestor, K. R. Kulas, D. R. Law, A. L. Strom, G. C. Rudie, N. A. Reddy, M. Pettini, N. P. Konidaris, G. Mace, K. Matthews, and I. S. McLean, "The Lyα Properties of Faint Galaxies at z ˜ 2-3 with Systemic Redshifts and Velocity Dispersions from Keck-MOSFIRE," ApJ, vol. 795, p. 33, Nov. 2014.

[54] G. Workman, I. Jordan, G. Chapman, A. Patterson, M. Reinhart, D. Taylor, and D. Adler, "Snapshot programs: Information, rules and guidelines for proposers and observers," Space Telescope Science Institute, January, Tech.

Rep., 2014. [Online]. Available: http://www.stsci.edu/hst/HST_overview/documents/uir/UIR_SNAP.pdf

[55] W. V. Dixon and et al., *Cosmic Origins Spectrograph Instrument Handbook, Version 3.0*, December 2010.

[56] D. C. Martin, J. Fanson, D. Schiminovich, P. Morrissey, P. G. Friedman, T. A. Barlow, T. Conrow, R. Grange, P. N. Jelinsky, B. Milliard, O. H. W. Siegmund, L. Bianchi, Y.-I. Byun, J. Donas, K. Forster, T. M. Heckman, Y.-W. Lee, B. F. Madore, R. F. Malina, S. G. Neff, R. M. Rich, T. Small, F. Surber, A. S. Szalay, B. Welsh, and T. K. Wyder, "The Galaxy Evolution Explorer: A Space Ultraviolet Survey Mission," ApJ, vol. 619, pp. L1–L6, Jan. 2005.

[57] P. Morrissey, D. Schiminovich, T. A. Barlow, D. C. Martin, B. Blakkolb, T. Conrow, B. Cooke, K. Erickson, J. Fanson, P. G. Friedman, R. Grange, P. N. Jelinsky, S.-C. Lee, D. Liu, A. Mazer, R. McLean, B. Milliard, D. Randall, W. Schmitigal, A. Sen, O. H. W. Siegmund, F. Surber, A. Vaughan, M. Viton, B. Y. Welsh, L. Bianchi, Y.-I. Byun, J. Donas, K. Forster, T. M. Heckman, Y.-W. Lee, B. F. Madore, R. F. Malina, S. G. Neff, R. M. Rich, T. Small, A. S. Szalay, and T. K. Wyder, "The On-Orbit Performance of the Galaxy Evolution Explorer," ApJ, vol. 619, pp. L7–L10, Jan. 2005.

[58] M. N. Fanelli, R. W. O'Connell, and T. X. Thuan, "Spectral synthesis in the

ultraviolet. II - Stellar populations and star formation in blue compact galaxies," ApJ, vol. 334, pp. 665–687, Nov. 1988.

[59] D. Calzetti, A. L. Kinney, and T. Storchi-Bergmann, "Dust extinction of the stellar continua in starburst galaxies: The ultraviolet and optical extinction law," ApJ, vol. 429, pp. 582–601, Jul. 1994.

[60] H. Domínguez Sánchez, M. Mignoli, F. Pozzi, F. Calura, A. Cimatti, C. Gruppioni, J. Cepa, M. Sánchez Portal, G. Zamorani, S. Berta, D. Elbaz, E. Le Floc'h, G. L. Granato, D. Lutz, R. Maiolino, F. Matteucci, P. Nair, R. Nordon, L. Pozzetti, L. Silva, J. Silverman, S. Wuyts, C. M. Carollo, T. Contini, J.-P. Kneib, O. Le Fèvre, S. J. Lilly, V. Mainieri, A. Renzini, M. Scodeggio, S. Bardelli, M. Bolzonella, A. Bongiorno, K. Caputi, G. Coppa, O. Cucciati, S. de la Torre, L. de Ravel, P. Franzetti, B. Garilli, A. Iovino, P. Kampczyk, C. Knobel, K. Kovač, F. Lamareille, J.-F. Le Borgne, V. Le Brun, C. Maier, B. Magnelli, R. Pelló, Y. Peng, E. Perez-Montero, E. Ricciardelli, L. Riguccini, M. Tanaka, L. A. M. Tasca, L. Tresse, D. Vergani, and E. Zucca, "Comparison of star formation rates from Hα and infrared luminosity as seen by Herschel," MNRAS, vol. 426, pp. 330–341, Oct. 2012.

[61] D. Calzetti, G. R. Meurer, R. C. Bohlin, D. R. Garnett, A. L. Kinney, C. Leitherer, and T. Storchi-Bergmann, "Dust and Recent Star Formation in the Core of NGC 5253," AJ, vol. 114, p. 1834, Nov. 1997.

[62] C. Leitherer, I.-H. Li, D. Calzetti, and T. M. Heckman, "Global Far-Ultraviolet (912-1800 Å) Properties of Star-forming Galaxies," ApJS, vol. 140, pp. 303–329, Jun. 2002.

[63] C. A. Tremonti, T. M. Heckman, G. Kauffmann, J. Brinchmann, S. Charlot, S. D. M. White, M. Seibert, E. W. Peng, D. J. Schlegel, A. Uomoto, M. Fukugita, and J. Brinkmann, "The Origin of the Mass-Metallicity Relation: Insights from 53,000 Star-forming Galaxies in the Sloan Digital Sky Survey," ApJ, vol. 613, pp. 898–913, Oct. 2004.

[64] C. Allende Prieto, D. L. Lambert, and M. Asplund, "The Forbidden Abundance of Oxygen in the Sun," ApJ, vol. 556, pp. L63–L66, Jul. 2001.

[65] D. P. Schneider, G. T. Richards, P. B. Hall, M. A. Strauss, S. F. Anderson, T. A. Boroson, N. P. Ross, Y. Shen, W. N. Brandt, X. Fan, N. Inada, S. Jester, G. R. Knapp, C. M. Krawczyk, A. R. Thakar, D. E. Vanden Berk, W. Voges, B. Yanny, D. G. York, N. A. Bahcall, D. Bizyaev, M. R. Blanton, H. Brewington, J. Brinkmann, D. Eisenstein, J. A. Frieman, M. Fukugita, J. Gray, J. E. Gunn, P. Hibon, Ž. Ivezić, S. M. Kent, R. G. Kron, M. G. Lee, R. H. Lupton, E. Malanushenko, V. Malanushenko, D. Oravetz, K. Pan, J. R. Pier, T. N. Price, III, D. H. Saxe, D. J. Schlegel, A. Simmons, S. A. Snedden, M. U. SubbaRao, A. S. Szalay, and D. H. Weinberg, "The Sloan Digital Sky Survey Quasar Catalog. V. Seventh Data Release," AJ, vol. 139, p. 2360, Jun. 2010.

[66] N. A. Reddy, C. C. Steidel, M. Pettini, and M. Bogosavljević, "Spectroscopic Measurements of the Far-Ultraviolet Dust Attenuation Curve at z 3," ApJ, vol. 828, p. 107, Sep. 2016.

[67] N. A. Reddy, C. C. Steidel, M. Pettini, M. Bogosavljević, and A. E. Shapley, "The Connection Between Reddening, Gas Covering Fraction, and the Escape of Ionizing Radiation at High Redshift," ApJ, vol. 828, p. 108, Sep. 2016.

[68] X. Du, A. E. Shapley, N. A. Reddy, T. Jones, D. P. Stark, C. C. Steidel, A. L. Strom, G. C. Rudie, D. K. Erb, R. S. Ellis, and M. Pettini, "The redshift evolution of rest-UV spectroscopic properties in Lyman Break Galaxies at z ˜ 2-4," *ArXiv e-prints*, Mar. 2018.

[69] A. J. Fox and et al., "Cosmic origins spectrograph instrument handbook, version 9.0," Space Telescope Science Institute, Tech. Rep., 2017.

[70] E. L. Fitzpatrick and D. Massa, "An analysis of the shapes of ultraviolet extinction curves. III - an atlas of ultraviolet extinction curves," ApJS, vol. 72, pp. 163–189, Jan. 1990.

[71] J. A. Cardelli, G. C. Clayton, and J. S. Mathis, "The Relationship between IR, optical, and UV Extinction." in *Interstellar Dust*, ser. IAU Symposium, L. J. Allamandola and A. G. G. M. Tielens, Eds., vol. 135, Dec. 1989, pp. 5–10.

[72] B. D. Savage, "Ultraviolet photometry from the Orbiting Astronomical Obser-

vatory. XX - The ultraviolet extinction bump," ApJ, vol. 199, pp. 92–109, Jul. 1975.

[73] M. J. Seaton, "Interstellar extinction in the UV," MNRAS, vol. 187, pp. 73P–76P, Jun. 1979.

[74] K. M. Pitman, G. C. Clayton, and K. D. Gordon, "The 2175 Å Extinction Bump in QSO Spectra," PASP, vol. 112, pp. 537–541, Apr. 2000.

[75] P. Massey and K. A. G. Olsen, "The Evolution of Massive Stars. I. Red Supergiants in the Magellanic Clouds," AJ, vol. 126, pp. 2867–2886, Dec. 2003.

[76] V. Zubko, E. Dwek, and R. G. Arendt, "Interstellar Dust Models Consistent with Extinction, Emission, and Abundance Constraints," ApJS, vol. 152, pp. 211–249, Jun. 2004.

[77] R. C. Bohlin, B. D. Savage, and J. F. Drake, "A survey of interstellar H I from L-alpha absorption measurements. II," ApJ, vol. 224, pp. 132–142, Aug. 1978.

[78] R. C. Kennicutt, Jr., P. Tamblyn, and C. E. Congdon, "Past and future star formation in disk galaxies," ApJ, vol. 435, pp. 22–36, Nov. 1994.

[79] M. Hayes, D. Schaerer, G. Östlin, J. M. Mas-Hesse, H. Atek, and D. Kunth, "On the Redshift Evolution of the Lyα Escape Fraction and the Dust Content of Galaxies," ApJ, vol. 730, p. 8, Mar. 2011.

[80] I. G. B. Wold, S. L. Finkelstein, A. J. Barger, L. L. Cowie, and B. Rosenwasser, "A Faint Flux-limited Lyα Emitter Sample at z $\sim$ 0.3," ApJ, vol. 848, p. 108, Oct. 2017.

[81] J. Brinchmann, S. Charlot, S. D. M. White, C. Tremonti, G. Kauffmann, T. Heckman, and J. Brinkmann, "The physical properties of star-forming galaxies in the low-redshift Universe," MNRAS, vol. 351, pp. 1151–1179, Jul. 2004.

[82] G. J. Ferland, K. T. Korista, D. A. Verner, J. W. Ferguson, J. B. Kingdon, and E. M. Verner, "CLOUDY 90: Numerical Simulation of Plasmas and Their Spectra," PASP, vol. 110, pp. 761–778, Jul. 1998.

[83] L. J. Kewley and S. L. Ellison, "Metallicity Calibrations and the Mass-Metallicity Relation for Star-forming Galaxies," ApJ, vol. 681, pp. 1183–1204, Jul. 2008.

[84] G. Denicoló, R. Terlevich, and E. Terlevich, "New light on the search for low-metallicity galaxies - I. The N2 calibrator," MNRAS, vol. 330, pp. 69–74, Feb. 2002.

[85] M. Pettini and B. E. J. Pagel, "[OIII]/[NII] as an abundance indicator at high redshift," MNRAS, vol. 348, pp. L59–L63, Mar. 2004.

[86] S. S. McGaugh, "H II region abundances - Model oxygen line ratios," ApJ, vol. 380, pp. 140–150, Oct. 1991.

[87] D. Zaritsky, R. C. Kennicutt, Jr., and J. P. Huchra, "H II regions and the abundance properties of spiral galaxies," ApJ, vol. 420, pp. 87–109, Jan. 1994.

[88] J. A. Baldwin, M. M. Phillips, and R. Terlevich, "Classification parameters for the emission-line spectra of extragalactic objects," PASP, vol. 93, pp. 5–19, Feb. 1981.

[89] L. J. Kewley, M. A. Dopita, R. S. Sutherland, C. A. Heisler, and J. Trevena, "Theoretical Modeling of Starburst Galaxies," ApJ, vol. 556, pp. 121–140, Jul. 2001.

[90] T. M. Heckman, "An optical and radio survey of the nuclei of bright galaxies - Activity in normal galactic nuclei," A&A, vol. 87, pp. 152–164, Jul. 1980.

[91] S. Komossa, "Narrow-line Seyfert 1 Galaxies," in *Revista Mexicana de Astronomia y Astrofisica Conference Series*, ser. Revista Mexicana de Astronomia y Astrofisica, vol. 27, vol. 32, Apr. 2008, pp. 86–92.

[92] H. Yang, S. Malhotra, M. Gronke, J. E. Rhoads, C. Leitherer, A. Wofford, T. Jiang, M. Dijkstra, V. Tilvi, and J. Wang, "Lyα profile, dust, and prediction of Lyα escape fraction in Green Pea Galaxies," *ArXiv e-prints*, Jan. 2017.

[93] J. C. Green, C. S. Froning, S. Osterman, D. Ebbets, S. H. Heap, C. Leitherer, J. L. Linsky, B. D. Savage, K. Sembach, J. M. Shull, O. H. W. Siegmund, T. P. Snow, J. Spencer, S. A. Stern, J. Stocke, B. Welsh, S. Béland, E. B. Burgh,

C. Danforth, K. France, B. Keeney, J. McPhate, S. V. Penton, J. Andrews, K. Brownsberger, J. Morse, and E. Wilkinson, "The Cosmic Origins Spectrograph," ApJ, vol. 744, p. 60, Jan. 2012.

[94] S. Osterman, J. Green, C. Froning, S. Béland, E. Burgh, K. France, S. Penton, T. Delker, D. Ebbets, D. Sahnow, J. Bacinski, R. Kimble, J. Andrews, E. Wilkinson, J. McPhate, O. Siegmund, T. Ake, A. Aloisi, C. Biagetti, R. Diaz, W. Dixon, S. Friedman, P. Ghavamian, P. Goudfrooij, G. Hartig, C. Keyes, D. Lennon, D. Massa, S. Niemi, C. Oliveira, R. Osten, C. Proffitt, T. Smith, and D. Soderblom, "The Cosmic Origins Spectrograph: on-orbit instrument performance," Ap&SS, vol. 335, pp. 257–265, Sep. 2011.

[95] S. R. McCandliss, K. France, S. Osterman, J. C. Green, J. B. McPhate, and E. Wilkinson, "Far-Ultraviolet Sensitivity of the Cosmic Origins Spectrograph," ApJ, vol. 709, pp. L183–L187, Feb. 2010.

[96] D. J. Sahnow, S. J. Conard, R. H. Barkhouser, J. P. Evans, S. D. Friedman, J. Kruk, H. W. Moos, and R. G. Ohl IV, "Far Ultraviolet Spectroscopic Explorer Optical System: Lessons Learned," in *Instrumentation for UV/EUV Astronomy and Solar Missions*, ser. Proc. SPIE, vol. 4139, Dec. 2000, p. 186.

[97] H. W. Moos, W. C. Cash, L. L. Cowie, A. F. Davidsen, A. K. Dupree, P. D. Feldman, S. D. Friedman, J. C. Green, R. F. Green, C. Gry, J. B. Hutchings, E. B. Jenkins, J. L. Linsky, R. F. Malina, A. G. Michalitsianos, B. D. Savage,

J. M. Shull, O. H. W. Siegmund, T. P. Snow, G. Sonneborn, A. Vidal-Madjar, A. J. Willis, B. E. Woodgate, D. G. York, T. B. Ake, B.-G. Andersson, J. P. Andrews, R. H. Barkhouser, L. Bianchi, W. P. Blair, K. R. Brownsberger, A. N. Cha, P. Chayer, S. J. Conard, A. W. Fullerton, G. A. Gaines, R. Grange, M. A. Gummin, G. Hebrard, G. A. Kriss, J. W. Kruk, D. Mark, D. K. McCarthy, C. L. Morbey, R. Murowinski, E. M. Murphy, W. R. Oegerle, R. G. Ohl, C. Oliveira, S. N. Osterman, D. J. Sahnow, M. Saisse, K. R. Sembach, H. A. Weaver, B. Y. Welsh, E. Wilkinson, and W. Zheng, "Overview of the Far Ultraviolet Spectroscopic Explorer Mission," ApJ, vol. 538, pp. L1–L6, Jul. 2000.

[98] P. Greenfield, F. Paresce, D. Baxter, P. Hodge, R. Hook, P. Jakobsen, R. Jedrzejewski, A. Nota, W. B. Sparks, and N. Towers, "In-flight performance of the Faint Object Camera of the Hubble Space Telescope," in *Space Astronomical Telescopes and Instruments*, ser. Proc. SPIE, P. Y. Bely and J. B. Breckinridge, Eds., vol. 1494, Sep. 1991, pp. 16–39.

[99] A. Boggess, F. A. Carr, D. C. Evans, D. Fischel, H. R. Freeman, C. F. Fuechsel, D. A. Klinglesmith, V. L. Krueger, G. W. Longanecker, and J. V. Moore, "The IUE spacecraft and instrumentation," Nature, vol. 275, pp. 372–377, Oct. 1978.

[100] G. A. Kriss, J. M. Shull, W. Oegerle, W. Zheng, A. F. Davidsen, A. Songaila, J. Tumlinson, L. L. Cowie, J.-M. Deharveng, S. D. Friedman, M. L. Giroux, R. F. Green, J. B. Hutchings, E. B. Jenkins, J. W. Kruk, H. W. Moos, D. C.

Morton, K. R. Sembach, and T. M. Tripp, "Resolving the Structure of Ionized Helium in the Intergalactic Medium with the Far Ultraviolet Spectroscopic Explorer," *Science*, vol. 293, pp. 1112–1116, Aug. 2001.

[101] J. M. Shull, J. Tumlinson, M. L. Giroux, G. A. Kriss, and D. Reimers, "The Fluctuating Intergalactic Radiation Field at Redshifts z = 2.3-2.9 from He II and H I Absorption toward HE 2347-4342," ApJ, vol. 600, pp. 570–579, Jan. 2004.

[102] W. Zheng, G. A. Kriss, J.-M. Deharveng, W. V. Dixon, J. W. Kruk, J. M. Shull, M. L. Giroux, D. C. Morton, G. M. Williger, S. D. Friedman, and H. W. Moos, "A Study of the Reionization History of Intergalactic Helium with FUSE and the Very Large Telescope," ApJ, vol. 605, pp. 631–644, Apr. 2004.

[103] C. Fechner, D. Reimers, G. A. Kriss, R. Baade, W. P. Blair, M. L. Giroux, R. F. Green, H. W. Moos, D. C. Morton, J. E. Scott, J. M. Shull, R. Simcoe, A. Songaila, and W. Zheng, "The UV spectrum of HS 1700+6416. II. FUSE observations of the He II Lyman alpha forest," A&A, vol. 455, pp. 91–106, Aug. 2006.

[104] J. M. Shull, K. France, C. W. Danforth, B. Smith, and J. Tumlinson, "HST/COS Observations of the Quasar HE 2347-4342: Probing the Epoch of He II Patchy Reionization at Redshifts z = 2.4-2.9," ApJ, vol. 722, pp. 1312–1324, Oct. 2010.

[105] D. Syphers, S. F. Anderson, W. Zheng, B. Smith, M. Pieri, G. A. Kriss, A. Meiksin, D. P. Schneider, J. M. Shull, and D. G. York, "He II Lyβ Gunn-Peterson Absorption: New HST Observations and Theoretical Expectations," ApJ, vol. 742, p. 99, Dec. 2011.

[106] D. Syphers and J. M. Shull, "The He II Post-reionization Epoch: HST/COS Observations of the Quasar HS1700+6416," ApJ, vol. 765, p. 119, Mar. 2013.

[107] S. T. Holland and et al., *Cosmic Origins Spectrograph Instrument Handbook for Cycle 21 v. 5.0*, Dec. 2012.

[108] J. Maki, G. Lawrence, L. Esposito, H. Lauche, and M. Ludwig, "The Cassini Hydrogen Deuterium Absorption Cell: A Remote Sensing Instrument for Atomic D/H Measurements at Titan," in *AAS/Division for Planetary Sciences Meeting Abstracts #28*, ser. Bulletin of the American Astronomical Society, vol. 28, Sep. 1996, p. 1132.

[109] L. W. Esposito, C. A. Barth, J. E. Colwell, G. M. Lawrence, W. E. McClintock, A. I. F. Stewart, H. U. Keller, A. Korth, H. Lauche, M. C. Festou, A. L. Lane, C. J. Hansen, J. N. Maki, R. A. West, H. Jahn, R. Reulke, K. Warlich, D. E. Shemansky, and Y. L. Yung, "The Cassini Ultraviolet Imaging Spectrograph Investigation," Space Sci. Rev., vol. 115, pp. 299–361, Dec. 2004.

[110] T. D. Kawahara, S. Okano, T. Abe, H. Fukunishi, and K. Ito, "Glass-type hydrogen and deuterium absorption cells developed for d/h ration measurements

in the martian atmosphere," *Applied Optics*, vol. 36, no. 10, pp. 2229–2237, April 1997.

[111] S. Werner, H. Keller, A. Korth, and H. Lauche, "Uvis/hdac lyman- observations of the geocorona during cassini's earth swingby compared to model predictions," *Advances in Space Research*, vol. 34, no. 8, pp. 1647 – 1649, 2004, planetary Ionospheres and Atmospheres Including CIRA. [Online]. Available: http://www.sciencedirect.com/science/article/pii/S0273117704006659

[112] H. Nakagawa, H. Fukunishi, S. Watanabe, M. Taguchi, Y. Tkahashi, J. Bertaux, E. Quemerais, and R. Lallement, "Studying the solar wind by simultaneous observations of the interplanetary Lyman alpha background with NOZOMI/UVS and SOHO/SWAN," *AGU Fall Meeting Abstracts*, p. A499, Dec. 2002.

[113] J. Costa, R. Lallement, E. Quémerais, J.-L. Bertaux, E. Kyrölä, and W. Schmidt, "Heliospheric interstellar H temperature from SOHO/SWAN H cell data," A&A, vol. 349, pp. 660–672, Sep. 1999.

[114] E. D. Palik, *Handbook of optical constants of solids*. Academic Press Handbook Series, New York: Academic Press, 1985, edited by Palik, Edward D., 1985. [Online]. Available: http://adsabs.harvard.edu/cgi-bin/nph-bib_query?bibcode=1985hocs.book.....P&db_key=AST

[115] S. R. McCandliss, K. France, P. D. Feldman, K. Glazebrook, G. Meurer, L. Bianchi, H. W. Moos, J. W. Kruk, W. P. Blair, and I. Baldry, "FORTIS:

pathfinder to the Lyman continuum," in *UV and Gamma-Ray Space Telescope Systems*, ser. Society of Photo-Optical Instrumentation Engineers (SPIE) Conference Series, G. Hasinger and M. J. L. Turner, Eds., vol. 5488, Oct. 2004, pp. 709–718.

[116] B. T. Fleming, S. R. McCandliss, K. Redwine, M. E. Kaiser, J. Kruk, P. D. Feldman, A. S. Kutyrev, M. J. Li, S. H. Moseley, O. Siegmund, J. Vallerga, and A. Martin, "Calibration and flight qualification of FORTIS," in *UV, X-Ray, and Gamma-Ray Space Instrumentation for Astronomy XVIII*, ser. Proc. SPIE, vol. 8859, Sep. 2013, p. 88590Q.

[117] B. W. Ballard, R. Barkhouser, B. Kean Jr, and M. Romelfanger, "The hopkins ultraviolet telescope engineering report for the astro2 mission," 09 1995.

[118] B. Fleming, "The search for lyman alpha escape from nearby starforming galaxies," Ph.D. dissertation, Johns Hopkins University, September 2013.

[119] O. Siegmund, J. Vallerga, A. Tremsin, and J. McPhate, "Microchannel plates: Recent advances in performance," in *UV, X-Ray, and Gamma-Ray Space Instrumentation for Astronomy XV*, ser. Society of Photo-Optical Instrumentation Engineers (SPIE) Conference Series, O. Siegmund, Ed., vol. 6686, San Diego, CA, September 2007.

[120] S. H. Moseley, R. G. Arendt, R. A. Boucarut, M. Jhabvala, T. King, G. Kletetschka, A. S. Kutyrev, M. Li, S. E. Meyer, D. Rapchun, and R. F.

Silverberg, "Microshutters arrays for the jwst near-infrared spectrometer," pp. 645–652, 2004. [Online]. Available: http://dx.doi.org/10.1117/12.552431

[121] S. H. Moseley, R. Arendt, R. A. Boucarut, M. Jhabvala, T. King, G. Kletetschka, A. S. Kutyrev, M. Li, D. Rapchun, R. F. Silverberg, D. Sohl, and L. Sparr, "Microshutter Arrays for the JWST NIRSpec," *IAU Special Session*, vol. 1, Aug. 2006.

[122] A. Kutyrev, S. H. Moseley, R. Arendt, R. Boucarut, T. Hadjimichael, M. Jhabvala, T. King, G. Kletetchka, M. Li, D. Rapchun, R. Silverberg, D. Sohl, L. Sparr, and Microshutter Team, "First Flight Design Microshutter Arrays for JWST NIRSpec." in *American Astronomical Society Meeting Abstracts #208*, ser. Bulletin of the American Astronomical Society, vol. 38, Jun. 2006, p. 147.

[123] L. Colina, M. L. García Vargas, J. M. Mas-Hesse, A. Alberdi, and A. Krabbe, "Nuclear Spiral and Ring Star-forming Structures and the Starburst–Active Galactic Nucleus Connection in Barred Spirals NGC 3351 and NGC 4303," ApJ, vol. 484, pp. L41–L45, Jul. 1997.

[124] E. Schinnerer, W. Maciejewski, N. Scoville, and L. A. Moustakas, "Toward the Secondary Bar: Gas Morphology and Dynamics in NGC 4303," ApJ, vol. 575, pp. 826–844, Aug. 2002.

[125] R. A. Koopmann and J. D. P. Kenney, "Hα Morphologies and Environmental Effects in Virgo Cluster Spiral Galaxies," ApJ, vol. 613, pp. 866–885, Oct. 2004.

[126] Central bureau for astronomical telegrams. [Online]. Available: http://www.cbat.eps.harvard.edu/lists/Supernovae.html

[127] P. D. Feldman, P. Z. Takacs, W. G. Fastie, and B. Donn, "Rocket Ultraviolet Spectrophotometry of Comet Kohoutek (1973f)," *Science*, vol. 185, pp. 705–707, Aug. 1974.

[128] P. D. Feldman and W. H. Brune, "Carbon production in comet West 1975n," ApJ, vol. 209, pp. L45–L48, Oct. 1976.

[129] T. N. Woods, P. D. Feldman, K. F. Dymond, and D. J. Sahnow, "Rocket ultraviolet spectroscopy of comet Halley and abundance of carbon monoxide and carbon," Nature, vol. 324, pp. 436–438, Dec. 1986.

[130] D. J. Sahnow, P. D. Feldman, S. R. McCandliss, and M. E. Martinez, "Long-slit ultraviolet spectroscopy of Comet Austin (1990 V)," Icarus, vol. 101, pp. 71–83, Jan. 1993.

[131] J. B. McPhate, P. D. Feldman, S. R. McCandliss, and E. B. Burgh, "Rocket-borne Long-Slit Ultraviolet Spectroscopy of Comet Hale-Bopp," ApJ, vol. 521, pp. 920–927, Aug. 1999.

[132] S. R. McCandliss, P. D. Feldman, H. Weaver, B. Fleming, K. Redwine, M. J. Li, A. Kutyrev, and S. H. Moseley, "Far-ultraviolet Observations of Comet C/2012 S1 (ISON) from FORTIS," AJ, vol. 152, p. 65, Sep. 2016.

[133] Z. Sekanina and R. Kracht, "Disintegration of Comet C/2012 S1 (ISON) Shortly Before Perihelion: Evidence from Independent Data Sets," *ArXiv e-prints*, Apr. 2014.

[134] L. Haser, "Distribution d'intensité dans la tête d'une comète," *Bulletin de la Societe Royale des Sciences de Liege*, vol. 43, pp. 740–750, 1957.

[135] S. A. Budzien, M. C. Festou, and P. D. Feldman, "Solar flux variability and the lifetimes of cometary H2O and OH," Icarus, vol. 107, p. 164, Jan. 1994.

[136] M. R. Combi, N. Fougere, J. T. T. Mäkinen, J.-L. Bertaux, E. Quémerais, and S. Ferron, "Unusual water production activity of comet c/2012 s1 (ison): Outbursts and continuous fragmentation," *The Astrophysical Journal Letters*, vol. 788, no. 1, p. L7, 2014. [Online]. Available: http://stacks.iop.org/2041-8205/788/i=1/a=L7

[137] D. Bockelée-Morvan, J. Crovisier, M. J. Mumma, and H. A. Weaver, *The composition of cometary volatiles*, 2004, pp. 391–423.

[138] M. A. DiSanti, M. J. Mumma, N. D. Russo, and K. Magee-Sauer, "Carbon Monoxide Production and Excitation in Comet C/1995 O1 (Hale-Bopp): Isolation of Native and Distributed CO Sources," Icarus, vol. 153, pp. 361–390, Oct. 2001.

[139] H. Weaver, M. A'Hearn, P. Feldman, D. Bodewits, M. Combi, N. Dello Russo,

and S. McCandliss, "Ultraviolet spectroscopy of comet ISON (2012 S1)," in *Asteroids, Comets, Meteors 2014*, K. Muinonen, A. Penttilä, M. Granvik, A. Virkki, G. Fedorets, O. Wilkman, and T. Kohout, Eds., Jul. 2014.

[140] N. Dello Russo, R. Vervack, H. Kawakita, A. Cochran, A. McKay, W. Harris, H. Weaver, C. Lisse, M. DiSanti, H. Kobayashi, N. Biver, D. Bockelée-Morvan, J. Crovisier, C. Opitom, and E. Jehin, "The compositional evolution of c/2012 s1 (ison) from ground-based high-resolution infrared spectroscopy as part of a worldwide observing campaign," *Icarus*, vol. 266, pp. 152–172, 3 2016.

[141] M. A. DiSanti, B. P. Bonev, E. L. Gibb, L. Paganini, G. L. Villanueva, M. J. Mumma, J. V. Keane, G. A. Blake, N. D. Russo, K. J. Meech, R. J. V. Jr., and A. J. McKay, "En route to destruction: The evolution in composition of ices in comet d/2012 s1 (ison) between 1.2 and 0.34 au from the sun as revealed at infrared wavelengths," *The Astrophysical Journal*, vol. 820, no. 1, p. 34, 2016. [Online]. Available: http://stacks.iop.org/0004-637X/820/i=1/a=34

[142] M. Li, A. Brown, A. Kutyrev, H. S. Moseley, and V. Mikula, "Jwst microshutter array system and beyond," *SPIE Proceedings*, vol. 7594, 02 2010.

[143] A. Carter, S. R. McCandliss, K. Redwine, and R. Pelton, "Wide Field Lyman alpha Geocoronal Simulator (WFLaGS) for the Far-uv Off Rowland-circle Telescope for Imaging and Spectroscopy (FORTIS)," in *American Astronom-*

ical Society Meeting Abstracts, ser. American Astronomical Society Meeting Abstracts, vol. 229, Jan. 2017, p. 238.08.

[144] D. M. Skowron, A. M. Jacyszyn, A. Udalski, M. K. Szymański, J. Skowron, R. Poleski, S. Kozłowski, M. Kubiak, G. Pietrzyński, I. Soszyński, P. Mróz, P. Pietrukowicz, K. Ulaczyk, and Ł. Wyrzykowski, "OGLE-ING the Magellanic System: Stellar Populations in the Magellanic Bridge," ApJ, vol. 795, p. 108, Nov. 2014.

[145] K. Bekki and M. Chiba, "Formation and evolution of the Magellanic Clouds - I. Origin of structural, kinematic and chemical properties of the Large Magellanic Cloud," MNRAS, vol. 356, pp. 680–702, Jan. 2005.

[146] K. Bekki, "Models for the dynamical evolution of the Magellanic System," in *The Magellanic System: Stars, Gas, and Galaxies*, ser. IAU Symposium, J. T. Van Loon and J. M. Oliveira, Eds., vol. 256, Mar. 2009, pp. 105–116.

[147] C. Yozin and K. Bekki, "Evolution of dust and molecular hydrogen in the Magellanic System," MNRAS, vol. 443, pp. 522–546, Sep. 2014.

[148] R. C. Kennicutt, Jr., D. Calzetti, F. Walter, G. Helou, D. J. Hollenbach, L. Armus, G. Bendo, D. A. Dale, B. T. Draine, C. W. Engelbracht, K. D. Gordon, M. K. M. Prescott, M. W. Regan, M. D. Thornley, C. Bot, E. Brinks, E. de Blok, D. de Mello, M. Meyer, J. Moustakas, E. J. Murphy, K. Sheth, and J. D. T.

Smith, "Star Formation in NGC 5194 (M51a). II. The Spatially Resolved Star Formation Law," ApJ, vol. 671, pp. 333–348, Dec. 2007.

[149] N. Lehner, J. C. Howk, F. P. Keenan, and J. V. Smoker, "Metallicity and Physical Conditions in the Magellanic Bridge," ApJ, vol. 678, pp. 219–233, May 2008.

[150] W. R. J. Rolleston, P. L. Dufton, N. D. McErlean, and K. A. Venn, "The chemical composition of the young, Inter-Cloud population," A&A, vol. 348, pp. 728–736, Aug. 1999.

[151] K. D. Gordon, C. Bot, E. Muller, K. A. Misselt, A. Bolatto, J.-P. Bernard, W. Reach, C. W. Engelbracht, B. Babler, S. Bracker, M. Block, G. C. Clayton, J. Hora, R. Indebetouw, F. P. Israel, A. Li, S. Madden, M. Meade, M. Meixner, M. Sewilo, B. Shiao, L. J. Smith, J. T. van Loon, and B. A. Whitney, "The Dust-to-Gas Ratio in the Small Magellanic Cloud Tail," ApJ, vol. 690, pp. L76–L80, Jan. 2009.

[152] E. B. Burgh, S. R. McCandliss, B.-G. Andersson, and P. D. Feldman, "On the Correlation between CO Absorption and Far-Ultraviolet Nonlinear Extinction toward Galactic OB Stars," ApJ, vol. 541, pp. 250–256, Sep. 2000.

[153] O. Vancura, W. P. Blair, K. S. Long, J. C. Raymond, and J. B. Holberg, "A Far-Ultraviolet Study of the Cygnus Loop Using the Voyager Ultraviolet Spectrometers," ApJ, vol. 417, p. 663, Nov. 1993.

[154] C. W. Danforth, R. H. Cornett, N. A. Levenson, W. P. Blair, and T. P. Stecher, "A Comparison of Ultraviolet, Optical, and X-Ray Imagery of Selected Fields in the Cygnus Loop," AJ, vol. 119, pp. 2319–2331, May 2000.

[155] I.-J. Kim, K.-I. Seon, Y.-M. Lim, D.-H. Lee, W. Han, K.-W. Min, and J. Edelstein, "Global Far-ultraviolet Properties of the Cygnus Loop," ApJ, vol. 784, p. 12, Mar. 2014.

[156] A. R. Sandage and M. Schwarzschild, "Inhomogeneous Stellar Models. II. Models with Exhausted Cores in Gravitational Contraction." ApJ, vol. 116, p. 463, Nov. 1952.

[157] W. H. McCrea, "Extended main-sequence of some stellar clusters," MNRAS, vol. 128, p. 147, 1964.

[158] J. G. Hills and C. A. Day, "Stellar Collisions in Globular Clusters," Astrophys. Lett., vol. 17, p. 87, Feb. 1976.

[159] F. R. Ferraro, B. Lanzoni, E. Dalessandro, G. Beccari, M. Pasquato, P. Miocchi, R. T. Rood, S. Sigurdsson, A. Sills, E. Vesperini, M. Mapelli, R. Contreras, N. Sanna, and A. Mucciarelli, "Dynamical age differences among coeval star clusters as revealed by blue stragglers," Nature, vol. 492, pp. 393–395, Dec. 2012.

[160] F. R. Ferraro, G. Beccari, E. Dalessandro, B. Lanzoni, A. Sills, R. T. Rood,

F. F. Pecci, A. I. Karakas, P. Miocchi, and S. Bovinelli, "Two distinct sequences of blue straggler stars in the globular cluster M 30," Nature, vol. 462, pp. 1028–1031, Dec. 2009.

[161] C. Knigge, N. Leigh, and A. Sills, "A binary origin for 'blue stragglers' in globular clusters," Nature, vol. 457, pp. 288–290, Jan. 2009.

[162] E. Dalessandro, F. R. Ferraro, B. Lanzoni, R. P. Schiavon, R. W. O'Connell, and G. Beccari, "Ultraviolet Observations of the Globular Cluster M10 from HST and GALEX: The BSS Population," ApJ, vol. 770, p. 45, Jun. 2013.

[163] F. R. Ferraro, N. D'Amico, A. Possenti, R. P. Mignani, and B. Paltrinieri, "Blue Stragglers, Young White Dwarfs, and UV-Excess Stars in the Core of 47 Tucanae," ApJ, vol. 561, pp. 337–345, Nov. 2001.

Vita

Keith Redwine was born in Princeton, NJ in 1988 and grew up near Boston, Massachusetts. He graduated high school in 2006 before moving to New York City to attend Columbia University. After getting an introduction into physics research working with the LIGO gravitational wave experiment, he received his B.A. degree in physics in 2010. Following enrollment at Johns Hopkins University, he balanced tinkering on sounding rockets with softball team captain duties, and hopes to continue in both space technology development and softball competition in his future.